Phase transitions in single layer and bilayer quantum Hall ferromagnets

Von der Fakultät Mathematik und Physik der Universität Stuttgart zur
Erlangung der Würde eines Doktors der Naturwissenschaften
(Dr. rer. nat.) genehmigte Abhandlung

vorgelegt von

LUTZ W. HÖPPEL

aus Nürnberg, Deutschland

Hauptberichter:	**Prof. Dr. K. v. KLITZING**
Mitberichter:	**Prof. Dr. M. DRESSEL**
Tag der Einreichung:	**16. Juni 2004**
Tag der mündlichen Prüfung:	**14. Juli 2004**

MAX-PLANCK-INSTITUT FÜR FESTKÖRPERFORSCHUNG
STUTTGART, 2004

Contents

Abbreviations and symbols

1C	one-component.
2C	two-component.
2DES	two-dimensional electron system.
2DHS	two-dimensional hole system.
a.u.	arbitrary units.
AB	anti-bonding (energy level).
AC	alternating current.
B	bonding (energy level).
BJ	Barkhausen jump.
CEO	cleaved edge overgrowth.
CF	composite fermion.
DC	direct current.
DLS	double layer system.
DOS	density of states.
DQW	double quantum well.
e.g.	exemplia gratia = "for example".
EMP	edge magneto-plasmon.
Eq.	Equation.
ESR	electron spin resonance.
et al.	et alii = "and others".
FET	field effect transistor.
Fig.	Figure.
FPT	ferromagnetic phase transition.
FQH	fractional quantum Hall.
FQHE	fractional quantum Hall effect.
FWHM	full width at half maximum.
HIGFET	heterojunction insulating gate FET.
HLR	huge longitudinal resistance.
IP	insulating phase.
i.e.	id est = "that is, that means".
LDA	local density approximation.
LED	light emitting diode.

LL	Landau level.
LLL	lowest Landau level.
LT	low temperature grown.
MBE	molecular beam epitaxy.
MOSFET	metal oxide semiconductor FET.
NMR	nuclear magnetic resonance.
PAC	pseudospin anisotropy classification.
PMMA	poly methyl methacrylate.
QW	quantum well.
QH	quantum Hall.
QHE	quantum Hall effect.
QHF	quantum Hall ferromagnetism.
RT	room temperature.
SdH	Shubnikov-de Haas.
Sec.	Section.
SHI	single heterointerface.
Subsec.	Subsection.
WC	Wigner crystal.
WQW	wide quantum well.
A	hyperfine coupling constant.
a	abundance.
α	relation between subband splitting and Coulomb correlation energy.
B	magnetic field.
$B_{\rm S}$	critical magnetic field for the spin transition.
$B_{1/2}$	magnetic field at filling factor 1/2.
$B_{\rm eff}$	effective magnetic field.
$B_{\rm ip}$	in-plane magnetic field.
$B_{\perp}$	perpendicular magnetic field.
$B_J(X)$	Brillouin function.
$B_{\rm N}$	nuclear magnetic field.
b	Fang-Howard parameter.
$C_{\rm C}$	Coulomb correlation energy prefactor.
$C_{\rm Z}$	enhancement of the Zeeman splitting.
$C_{\square}$	capacitance per unit area.
c	prefactor in Taylor expansion.
d	peak to peak distance between electron layers.
d^*	critical layer separation.
D	density of states.
$D_{\rm LL}$	degeneracy of each LL.
ΔB	magnetic field sweep rate.
$\Delta\mathrm{BAB}$	subband splitting for $\sigma \neq 0$.

$\Delta\mathrm{SAS}$	subband splitting for $\sigma = 0$.
Δn	transferred electron density.
Δn_{BG}	layer density change upon back gate bias.
Δn_{FG}	layer density change upon front gate bias.
E	energy.
$E_{0,1,2}$	energy of the subband level $0, 1, 2$.
E_{A}	activation energy.
E_{C}	intra-layer Coulomb correlation energy.
E_{d}	inter-layer Coulomb correlation energy.
ε_{F}	Fermi energy.
$E(\vec{k})$	dispersion relation.
E_{PS}	pseudospin splitting.
E_{Z}	Zeeman energy.
e	elementary charge.
ϵ	dielectric constant of AlGaAs, $\epsilon = 13.1$ for GaAs.
ϵ_0	dielectric constant in vacuum.
f	polynomial function.
$\Phi = BL_xL_y$	magnetic flux.
$\Phi_0 = h/e$	magnetic flux quantum.
g^*	effective Landé-factor.
$g^*_{\parallel}$	effective g factor for in-plane magnetic field.
$g^*_{\perp}$	effective g factor for perpendicular magnetic field.
g_{N}	nuclear effective g factor.
γ	gyromagnetic ratio.
H	Hamiltonian.
h	Planck's constant.
$\hbar$	reduced Planck's constant.
I	probing AC-current amplitude.
I_{AC}	AC-current amplitude.
I_{DC}	DC-current amplitude.
I	nuclear spin polarization.
$\hat{I}$	nuclear spin operator.
I_+	nuclear spin up-flip operator.
I_-	nuclear spin down-flip operator.
i	isotope.
J	total nuclear spin.
j	running index over electrons.
k	running index over electrons or nuclei.
k_{B}	Boltzmann's constant.
k_{F}	Fermi wave vector.
k_{x}	component of k-vector along the x direction.

k_y	component of k-vector along the y direction.
$\vec{k}$	k-vector.
L	distance between adjacent Hall probes along the Hall bar.
L_x	lateral extension of a 2DES.
L_y	lateral extension of a 2DES.
l_B	magnetic length.
$l_\mathrm{B}^\mathrm{eff}$	effective magnetic length.
λ	finite thickness of single electron layer measured as FWHM.
M	odd integer number.
m	intra-layer correlation exponent.
m'	intra-layer correlation exponent.
m''	inter-layer correlation exponent.
m_0	free electron mass.
m^*	effective mass of an electron.
μ	mobility.
μ_B	magnetic moment of an electron.
μ_N	magnetic moment of a nucleus.
μ_PS	pseudomagnetic moment.
N_e	number of electrons in one sample.
N_Φ	number of flux quanta in one sample.
n	single layer electron density.
n_AB	density of the second lowest subband.
n_B	density of the lowest subband.
n_S	critical density at the spin transition.
n_b	back layer density.
n_f	front layer density.
$n_\mathrm{b,0}$	back layer density at zero gate bias.
$n_\mathrm{f,0}$	front layer density at zero gate bias.
n_tot	bilayer (total) electron density.
ν_count	filling factor for measurement.
ν_reset	filling factor for reset.
ν	single layer filling factor.
ν_AB	filling factor of the AB subband.
ν_B	filling factor of the B subband.
ν_CF	CF filling factor.
ν_b	back layer filling factor.
ν_f	front layer filling factor.
ν_tot	bilayer (total) filling factor.
o	orbital quantum number.
P	pseudomagnetic field.
p	nominator of fractional filling factor.

Q	charge per unit area.
q	Laughlin exponent, denominator of fractional filling factor.
θ	tilt angle.
R_{xx}	longitudinal resistance.
ρ_{xx}	specific longitudinal resistance.
$\hat{S}$	electron spin operator.
S	spin quantum number.
S'	spin quantum number.
S_+	electron spin up-flip operator.
S_-	electron spin down-flip operator.
s	slope and number of pseudospin flips.
σ	imbalance.
R_{H}	Hall resistance.
$\vec{r}$	coordinate of an electron.
$r_{\mathrm{c,i}}$	cyclotron radius at orbital quantum number i.
$\rho(z)$	electron distribution along the growth axis of a heterostructure.
T	sample (electron) temperature in K.
T_{c}	crystal temperature in K.
T_1	spin equilibration time.
t	time.
t_{count}	time at ν_{count} until data point is taken.
t_{reset}	time at ν_{reset} for reset procedure.
τ	scattering time.
U	bias voltage.
U_{BG}	back gate voltage.
U_{FG}	front gate voltage.
u	prefactor in theory to in-plane magnetic fields.
V	inter-layer bias.
$V(r)$	Coulomb interaction potential.
VH	length to width ratio of a probed Hall bar area.
v	prefactor in theory to in-plane magnetic fields.
W	width of a Hall bar.
w	width of a QW or WQW.
ω_{c}	electron cyclotron frequency.
$\omega_{\mathrm{c,CF}}$	CF cyclotron frequency.
X	input parameter to the Brillouin function.
x	direction within the plane of the 2DES.
y	direction within the plane of the 2DES.
Ψ	Laughlin type wave function.
ψ	one electron envelope wave function.
z	coordinate along the growth axis of a heterostructure.

$\bar{z}$	mean electron position.
$\mathbf{z}$	complex coordinate of an electron within the plane of a 2DES.

Chapter 1

Introduction

In this thesis, the properties of ferromagnetic phase transitions under quantum Hall conditions mainly in bilayers are investigated by means of magneto-transport. A bilayer consists of two parallel two-dimensional electron systems (2DESs) arranged so close that charge carrier exchange occurs by virtue of quantum tunneling. This induces a hybridization (splitting) of the subband energies and introduces an additional energy scale, namely the subband splitting. Additional physical phenomena can occur due to this new energy scale in dependence of its magnitude compared to the system's various other energy scales. Tunneling related phenomena between the two close 2DESs were widely studied from both a fundamental point of view as well as with respect to application. Tunneling provides on the one hand access to low energetic excitations of a bilayer [1] while on the other hand the current-voltage-characteristic of a bilayer can exhibit a negative differential resistance even at high temperatures [2] due to tunneling. A bilayer can also be regarded as a resonant tunneling transistor with resonance frequencies well in the THz range [3] and can be used as a THz detector [4, 5]. A theoretical description of a bilayer involves in particular the introduction of an artificial spin (labeled isospin in this thesis), whose two orientations can be regarded as the two layers. In the past decade, the spin degree of freedom attracted a lot of interest in the field of spintronics or quantum computation. Also the isospin was proposed as a two-level system (qubit) for quantum computation [6].

The integer (IQHE) and the fractional quantum Hall effect (FQHE) are macroscopic quantum effects. They appear when a 2DES is subject to a perpendicular magnetic field and the number of electrons compared to the number of magnetic flux quanta per unit area (filling factor ν) is a magic number, *i.e.* an integer or fractional number of the form p/q where p is an arbitrary positive integer and $q = 2p \pm 1$. The condensation of the electron states into a fan-chart of Landau levels (LLs) is the physical basis of the IQHE, while the FQHE is due to many body correlation effects. The changeover from electrons to composite Fermions (CFs), however, enables one to consider the FQHE as a kind of IQHE when assuming that CF states condense into a fan-chart of LLs. Each state is characterized by several quantum numbers, which are specific for the LL. Theory connects the quantum numbers of each state to another artificial spin labeled pseudospin. Ideally, when ν is equal to a magic number, all pseudospins of each LL are aligned. In analogy to conventional ferromagnetism, this alignment can be regarded as a ferromagnetic order and therefore is referred to as quantum Hall ferromagnetism is established. When two LLs of different ferromagnetic order are tuned through their energetic resonance, a ferromagnetic phase transition (FPT) can be induced that is equivalent to how the magnetization of a conventional ferromagnet changes with magnetic field. Since quantum Hall ferromagnets can be much more ideal than conventional ferromagnets [7], they represent an excellent model system to study FPTs. A convenient way to study FPTs is through magnetotransport measurements since they allow one to probe the energy gaps (at the Fermi energy) and a FPT is indicated by the breakdown of such a gap.

Bilayers are very interesting in a FPT framework, because they provide energetic resonances of LLs (LL crossings) in the IQHE regime due to the charge carrier exchange. The FQHE regime also gives rise to FPTs, but in contrast to the IQHE regime, one of the competing energies is governed by the average inter-particle distance between the electrons. One concept presented in this work to realize a bilayer system allows for the opportunity to preferentially adjust this quantity.

Chapter 2 introduces the 2DES to study the QHE. It is argued that the IQHE is due to the appearance of an energy gap between adjacent LLs at the Fermi energy. The same argument applies in the regime of the FQHE, when the electrons are replaced by composite Fermions (CFs) ($\nu \rightarrow \nu_{\mathrm{CF}}$). It is highlighted that the relevant energy gap in the FQHE regime is entirely governed by the Coulomb interaction among the particles.

The concepts used to produce a bilayer system, namely a single wide quantum well (WQW) or two closely spaced narrow QWs (DQW) are presented in Chapter 3. Due to the requirement for a gate on both sides of the bilayer needed to adjust the two electron layers' densities individually, the techniques to fabricate gates and in particular to incorporate a gate underneath the bilayer are discussed.

The theoretical description of a bilayer is the subject of Chapter 4. The calculations presented in this chapter reveal the dependence of the subband splitting on the total electron density of the two layers and the charge distribution between them. It is furthermore illustrated that the layer separation is an important parameter controlling the correlation between both layers and the impact of the total density on the layer separation in the case of the WQW is discussed. It is shown that a bilayer in a magnetic field (IQHE regime) is characterized by two LL fan-charts, which intersect giving rise to FPTs. The concept of pseudospin is introduced to generalize the theoretical treatment of FPTs. The reason for additional FPTs in the FQHE regime is discussed.

Experimental control of a bilayer is demonstrated in Chapter 5. The properties of FPTs associated with the total filling factors $\nu_{\mathrm{tot}} = 3, 4, 5$ are discussed as a function of the total electron density and density distribution between the two electron layers. Furthermore, the observed QHE at $\nu_{\mathrm{tot}} = 1/2$ is investigated. The results are compared with data presented in the literature.

The investigation of the FPT at $\nu_{\mathrm{CF}} = 2$ ($\nu = 2/3$) with only one single 2DES confined to the WQW is subject of Chapter 6. It is shown that the FPT is due to a competition between the Zeeman energy and the Coulomb interaction energy. The parameters which influence this competition are discussed. It is pointed out that for the Zeeman energy, the effective g factor is decisive, while the Coulomb energy depends on the finite thickness of the 2DES. Both parameters are tuned in experiment. The density, on which both energies depend although in a different way, is used to compensate for this tuning and to reestablish the energetic resonance. Also studied is the influence of the nuclear magnetic field on this FPT.

Chapter 7 is dedicated to the FPT at $\nu_{\mathrm{CF}} = 2$ ($\nu_{\mathrm{tot}} = 2/3$) when a bilayer is formed in the WQW. It can be shown that this FPT is accompanied by a loss of correlation between the layers. Measurements of the energy gap by thermal activation are carried out. The results are interpreted as indication for isospin exchange interaction governing the FPT and for the formation of isospin Skyrmions. The influence of an asymmetric charge distribution on the FPT is investigated. Finally, a complete phase diagram of the ferromagnetic order at $\nu_{\mathrm{CF}} = 2$ is given.

Chapter 2

2DES, QHE and FQHE

A study of the quantum Hall effect (QHE) is usually based on the utilization of a quasi-two-dimensional layer of charge carriers, either electrons (2DES) or holes (2DHS). In this work, electron layers are predominantly used except in one case where a 2DHS is of interest. This chapter discusses how a 2DES can be formed in a solid and what are the relevant properties of such a 2DES. In particular, the effect of a magnetic field applied perpendicular to the charge layer is discussed.

2.1 Formation and properties of a 2DES

A 2DES can be achieved in several ways. The most common method is to create a highly mobile electron layer in a solid.[1] An electron layer is labeled an inversion layer when it is formed by pulling down the conduction band edge below the Fermi energy. This effect is possible in silicon[2] and other materials. The quasi-two-dimensionality of a 2DES, where the thickness of the 2DES is of the order of the de Broglie wavelength, is achieved by a discontinuity in the conduction band edge. Such a discontinuity can be created in silicon by an oxide layer which causes the conduction band edge of silicon to be pulled below the Fermi energy near the interface of silicon and silicon oxide, resulting in charges being confined at the interface. Nevertheless, if correlation effects among electrons at small energy scales are of interest, a uniform potential landscape leading to a high mobility and a long mean free path of the charge carriers is desired. Such an interface is provided by GaAs and AlGaAs heterostructures due to the lattice constants of the two different materials matching almost perfectly independent of the Al content and, as a result a virtually unstrained interface is possible. This is important, because strain can lead to crystal imperfections, *i.e.* disorder. AlGaAs material with an Al content of typically 30% is used, because it exhibits the largest direct band gap of the AlGaAs system. The AlGaAs/GaAs interface shows in this case an offset in the conduction band edge of about

---

[1] The realization of a layer of free electrons on liquid helium is also possible and is characterized by the absence of a hosting material, which otherwise imposes its properties arising from the nuclei onto the 2DES.

[2] Originally, the QHE was discovered in a silicon MOSFET [8].

0.3 eV at low temperatures (4 K). The electron effective mass in GaAs is isotropic in contrast to silicon. GaAs/AlGaAs material is grown with molecular beam epitaxy (MBE) using a GaAs wafer[3] as the substrate material.

The profile of the valence (E_{VB}) and conduction band (E_{CB}) edges along the growth axis z of a structure is displayed in Fig. 2.1b. The fundamental energy gap of GaAs is about 1.5 eV at 4 K (the gap being a function of the temperature and decreases towards higher temperatures). After a growth sequence of several GaAs/AlGaAs layers (discussed in Chapter 3 and not shown in Fig. 2.1b) a layer of GaAs is grown followed by a layer of AlGaAs so that an interface is formed between these two materials. Finally the structure is capped with a thin layer of GaAs. The Fermi energy is pinned approximately in the center of the energy gap of the cap layer due to surface states. The Fermi energy is also pinned roughly in the center of the GaAs material far below the interface but usually slightly displaced towards the valence band edge. This is due to impurities. The dominant impurity is typically carbon, which leads to p-type doping. A very thin layer of silicon (Si) is introduced within the AlGaAs material as a dopant. Because of the minimal thickness achieved this method is named delta-doping. Also a certain volume of the AlGaAs material can be doped. The dopants pin the Fermi energy to the conduction band edge causing the conduction band edge of the GaAs interface to drop below the Fermi energy due to the band offset. The dopants also provide free charge carriers by thermal ionization (activation) because their energy level within AlGaAs is only slightly (meV) below the conduction band edge. Consequently, Si acts normally as a donor for electrons and leads to an n-type doped semiconductor material.[4] Each Si atom introduces one excess electron. The excess electrons accumulate in the GaAs at the interface because they are pulled towards it due to the remaining positively charged dopants. The perpendicular extent of the charge layer is of the order of 10 nm, and the charges form a conducting channel. An incorporation of too many dopants has to be avoided. Otherwise so-called parallel conductivity can set in, *i.e.* a conducting layer parallel to the 2DES will arise, since a degenerate band can be formed by the dopants. The dopants are introduced at a certain distance from the GaAs/AlGaAs interface, separated by the spacer. This remote doping is crucial to achieve the high mobilities of the intended 2DES, because the ionized impurities can act as very efficient scatterers. If scattering due to the dopants is reduced by their set back from the interface then the residual disorder is the most limiting factor of the mobility. This kind of realization of a 2DES at a single interface formed by a heterojunction is named a single heterointerface (SHI). Alternatively, the thickness of the GaAs involved in forming the interface can be strongly reduced (to a few 10 nm) and set on top of AlGaAs so that a second and now inverted interface is formed. The result is a quantum well (QW) structure. The number of charge carriers accumulated within the channel is strongly influenced by the spacer and has been shown to vary approximately as an inverse relation of the spacer thickness [9]. The quantity of electrons is measured per unit area and termed the electron density or density; a typical value is 2.0×10^{15} m^{-2}. The trapping potential for electrons (termed the confinement potential) is determined by the conduction band profile below the Fermi energy (see Fig. 2.1c).

---

[3] Usually the surface of GaAs is the (001) plane.

[4] On other substrate orientations like GaAs(311)A Si leads to p-type doping.

In the case of an SHI, an approximately triangular potential profile along the growth axis is formed. The resulting electron distribution along the growth axis can be described by the Fang-Howard model [10] and resembles an asymmetric Gaussian. The distinct influence of the finite thickness on the correlation effects among all electrons is particularly relevant in this thesis. If desired, the electron density can be varied via a front gate which is usually formed by a metal evaporated on top of the structure. The evaporated metal leaves the position of the Fermi energy within the cap layer almost unchanged,[5] so that a Schottky barrier of about 0.7 eV is formed, which will suppress a current between the front gate and the 2DES. With a positive gate bias applied to the front gate with respect to the 2DES, the conduction band profile can be pulled down towards the Fermi energy leading to a larger inversion of the channel region and to an increase in the electron density (FET effect). The maximum positive gate bias that can be applied is limited in that the conduction band edge at the position of the dopants cannot be pulled below the Fermi energy. Exceeding this limit would result in parallel conductivity. A negative gate voltage has the reverse effect of lowering the electron density.

In the conducting channel the electrons can move freely (in so far as they are not scattered by disorder) along the interface, while their motion in the direction perpendicular to the interface is restricted due to the narrow confinement potential. This restriction leads to the quantization of allowed energy values. These energy levels $E_{0,1,2,\ldots}$ (see Fig. 2.1c) are separated by about 10 meV. But because of the unrestricted movement along the interface, a parabolic dispersion relation $E(\vec{k})$ arises for each energy level separately and the resultant Fermi contour is a circle (see Fig. 2.1d).[6] The quasi-two-dimensionality leads to a constant density of states in energy (DOS) $D(E)$ for each energy level [11]

$$D(E) = \frac{m^*}{\pi\hbar^2}, \tag{2.1}$$

where the spin degeneracy of the electrons is included and m^* is the effective electron mass (GaAs has a m^* of $0.067 \times m_0$ where m_0 being the free electron mass at a temperature close to 0 K). The given DOS results from dividing the DOS in $\vec{k}$-space (see Fig. 2.1d) by the derivative of the parabolic dispersion relation with respect to $\vec{k}$. The DOS is so large that a typical electron density can reside entirely in the lowest energy level.

2.2 2DES plus magnetic field

A magnetic field B perpendicular to the plane of the 2DES causes the electron to move in cyclotron orbits due to the Lorentz force with a cyclotron frequency of

$$\omega_\mathrm{c} = \frac{eB}{m^*}. \tag{2.2}$$

---

[5] The real situation is discussed in Sec. 3.4 and an exception is mentioned in Subsec. 6.8.3.

[6] This circular shape is modified by a magnetic field oriented along the plane of the 2DES (see Sec. 5.4).

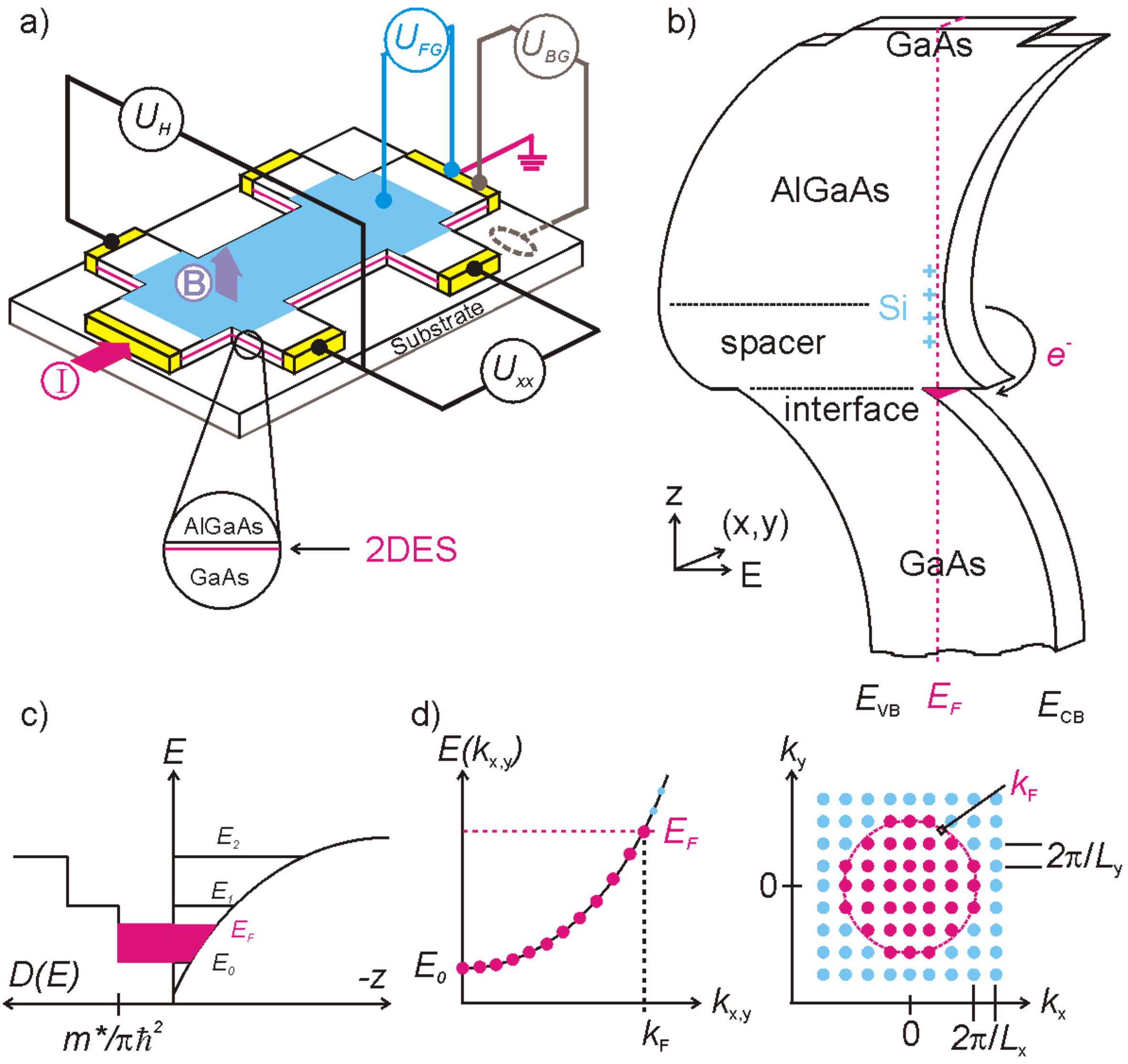

Figure 2.1: a) Mesa in Hall bar geometry with metallic front gate (blue) and back gate and the various connections to the yellow ohmic contacts. b) Schematic profile of the valence and conduction band edges of a GaAs/AlGaAs single heterointerface (SHI). c) Expansion of the interface region with the quantized energy levels and the DOS. d) Parabolic energy dispersion for the movement of the electrons along the interface (x,y) and Fermi circle. Red dots denote electrons, blue dots represent quasi-holes.

The charge of an electron is e. The radii of cyclotron orbits are quantized

$$r_{\mathrm{c,o}} = \sqrt{\frac{2\hbar}{eB}\left(\mathrm{o} + \frac{1}{2}\right)}, \tag{2.3}$$

with the orbital quantum number $\mathrm{o} = 0, 1, 2....$ and $\hbar$ the reduced Planck's constant. This quantization is due to that an electron encircling a certain area, which is threaded by a certain magnetic flux, must accumulate a quantum mechanical phase which is a multiple of 2π in one complete revolution, and is known as the Landau quantization. Each energy level $E_{0,1,2,...}$, that originates from the restricted movement perpendicular to the interface, is transferred into a set of Landau levels (LLs). The LLs (of one and the same set) are equally spaced in energy by the cyclotron energy

$$E_\mathrm{c} = \hbar\omega_\mathrm{c}. \tag{2.4}$$

Since the cyclotron energy is a linear function of the magnetic field, the energetic separation of the LLs increases linearly with the magnetic field, *i.e.* a LL fan-chart appears.[7] Also due to the additional quantization of the motion of the electrons within the plane of the 2DES the system can be considered fully quantized. Therefore, the former constant DOS (Eq. 2.1) is transformed into a series of Dirac-delta functions, which are separated by the cyclotron energy [11].

Electrons have a spin degree of freedom associated with a magnetic moment. There are two

---

[7] It is assumed here that only the lowest energy level E_0 is occupied and therefore only one LL fan-chart is considered.

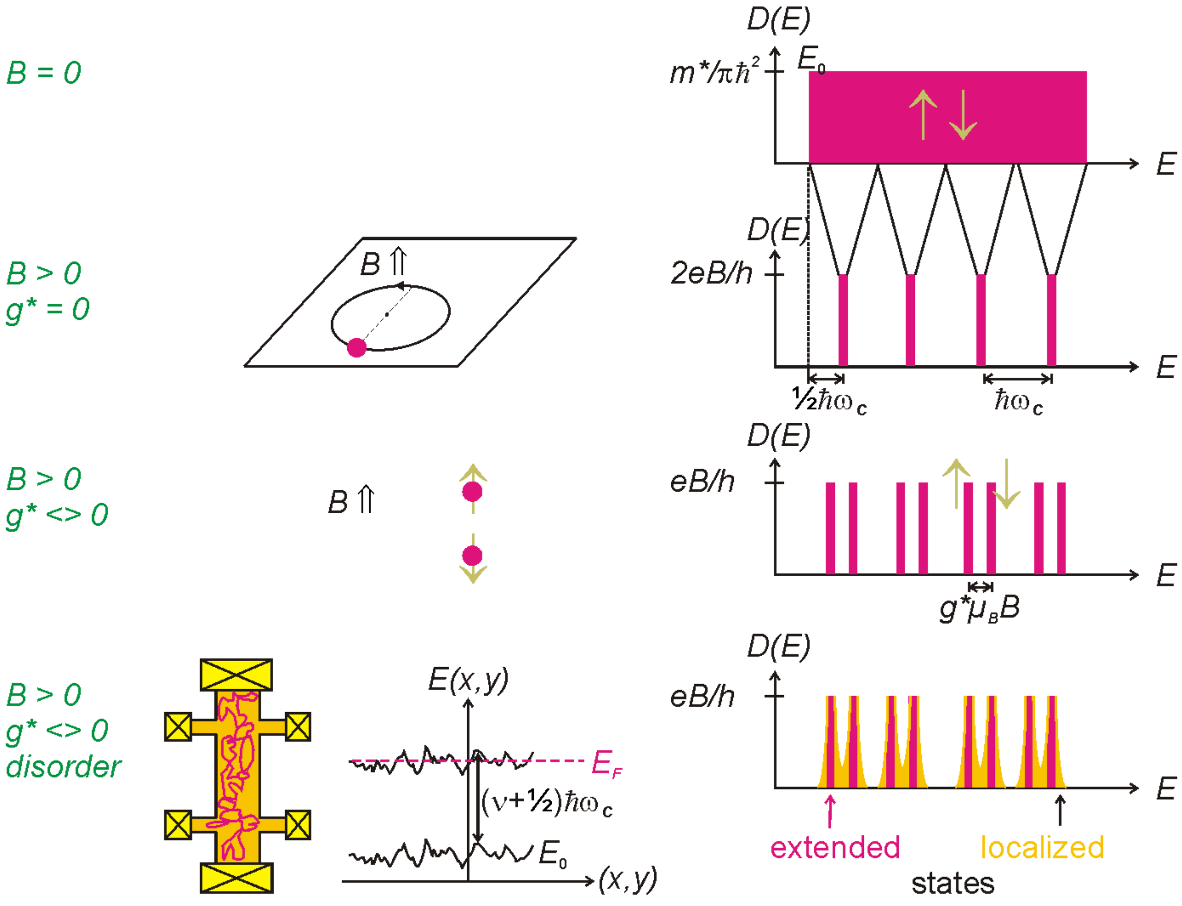

Figure 2.2: A magnetic field B applied perpendicular to a 2DES forces the electrons onto cyclotron orbits and transfers the constant DOS into Dirac-delta functions equally spaced in energy, which are further split since the spin degeneracy is lifted. Disorder leads to a broadening of the ideal Dirac-delta functions.

possible orientations of the spin with respect to the direction of the magnetic field which are different in energy and a splitting of each LL occurs. This Zeeman splitting (energy) reads

$$E_{\mathrm{Z}} = |g^*|\mu_{\mathrm{B}}B, \tag{2.5}$$

where g^* denotes the effective g factor, which is -0.44 in GaAs (at low temperatures).[8] The magnetic moment of the electrons is $\mu_{\mathrm{B}} = e\hbar/2m_0$. Because of the small effective g factor and in particular the small effective mass of the electrons in GaAs, the spin splitting is smaller by about a factor of 68 than the orbital splitting of LLs caused by the cyclotron motion. Consequently, the different energy gaps between adjacent LLs, which are alternately either orbital or spin gaps, lead to quite differently pronounced physical effects, because it is the magnitude of the energy splitting that is significant, as will be discussed below. As another consequence, each LL is characterized by two quantum numbers, the orbital quantum number (0,1,2,...) and the spin orientation (↑,↓). The degeneracy of each spin-split LL is [11]

$$D_{\mathrm{LL}} = \frac{eB}{h}, \tag{2.6}$$

so that the number of available states at each LL increases linearly with the magnetic field. The linear dependence on B arises from the fact that the difference between allowed energy values is given by the cyclotron energy.

If the energetically highest LL, which contains electrons is only partially occupied, the Fermi energy is pinned to this LL (quasi-metallic state) and is steadily raised with the increasing magnetic field. Since the degeneracy of each LL steadily increases with higher magnetic fields, the electrons are redistributed from LLs of higher energy to those of lower energy, *i.e.* the LL at the Fermi energy is successively depopulated. Once the LL at the Fermi energy is at the point of being completely depopulated by the magnetic field but the next lower LL is still fully occupied, the situation becomes similar to that of a semiconductor or insulator. The Fermi energy jumps down in energy and becomes at finite temperature[9] located in the center of the energy gap that separates these two LLs. Moving towards an even higher magnetic field results in the depopulation of the next lower LL. The Fermi energy jumps further down and is pinned to this LL. Consequently, the Fermi energy exhibits sawtooth-like oscillations, as depicted in Fig. 2.3.

The filling factor ν is defined as the number of electrons N_e divided by the number of magnetic flux quanta N_Φ present in one sample

$$\nu = \frac{N_e}{N_\Phi} = n\frac{h}{eB}. \tag{2.7}$$

Therefore, it depends linearly on the electron density n and inversely on the magnetic field B. Comparing the Eq. 2.6 with Eq. 2.7, the filling factor denotes the number of occupied LLs. An integer filling factor therefore indicates the fact that the Fermi energy resides in an energy gap

---

[8] g^* can be altered which is relevant in this thesis.

[9] At zero temperature, the Fermi energy jumps down to the next lower LL by definition.

between two adjacent LLs. When ν is an odd number a spin gap is present, while an orbital gap is indicated by an even number. The 2DES can be regarded as incompressible when the Fermi energy lies in a gap. The incompressibility of the 2DES is due to the large amount of energy necessary to add one extra electron to the system. This is in contrast to the situation in which the Fermi energy is pinned to one LL; this situation is consequently termed the compressible phase.

The technical realization of a 2DES within a sample involves disorder. The confinement potential as seen by the 2DES is therefore an energetic landscape that varies with the spatial coordinate along the interface. Consequently, the energy levels will fluctuate throughout the

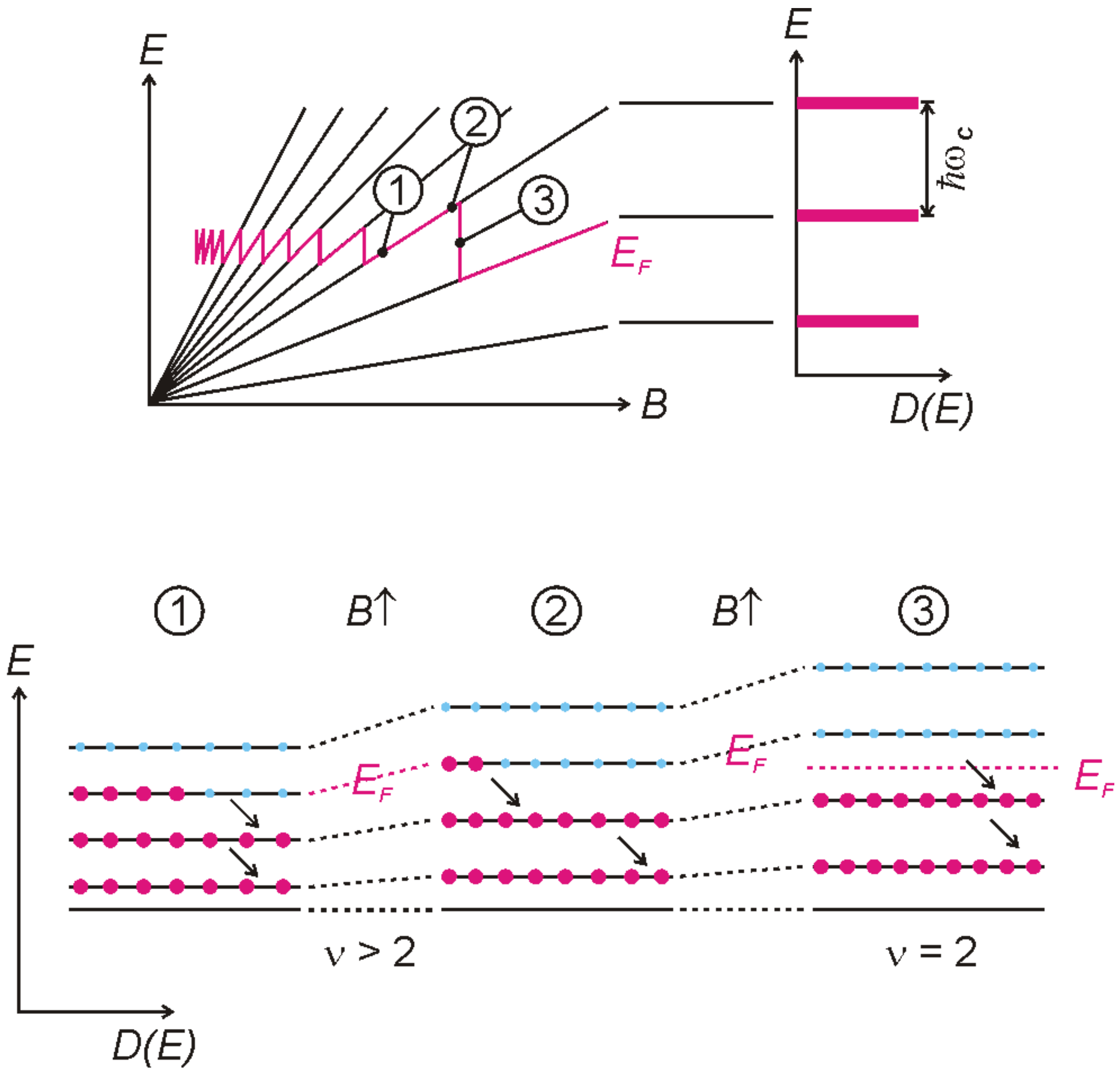

Figure 2.3: Upper panel: LL fan-chart and oscillating Fermi energy. Lower panel: Illustration of the successive depopulation of the LL at the Fermi energy with increasing magnetic field due to the increase of the degeneracy of each LL.

lateral extent of a sample. This leads to a broadening of the otherwise ideal Dirac-delta functions representing the DOS. In the absence of disorder, the energy levels would be independent of the spatial coordinate. These ideal states are therefore labeled extended states and are at the centers of the broadened Dirac-delta functions. Disorder however reduces the area where the ideal situation is present. Instead, the sample decomposes into many smaller areas (puddles) with different energetic properties. These areas regarded as puddles are bordered by extended states as shown in Fig. 2.2. Since the states of these puddles are only locally relevant they are called localized states. Further implications of disorder are discussed below.

2.2.1 The IQHE regime

One typical technique deployed to study the properties of a 2DES is magneto-transport. For this purpose a grown structure, as described in the Sec. 2.1, is processed[10] into a Hall bar[11] (sample), which restricts the 2DES to a certain area called a mesa. The Hall bar comprises ohmic contacts to the 2DES, which provide the possibility of probing the 2DES electrically. For this purpose an AC-current at low frequency (about 10 Hz), to benefit from a lock-in technique, and low amplitude (about 10 nA), to avoid sample heating, is sent through the sample along the Hall bar, and the resulting voltage drops across different contacts are measured.[12] Of principal interest are the voltage drops along and perpendicular to the current path. Hence the longitudinal resistance R_{xx}[13] and the Hall resistance R_{H} can be calculated by dividing the voltage drop along and perpendicular to the current path by the current amplitude. All Hall bar shaped samples used in this thesis have a width of $W = 100\ \mu$m and a distance between adjacent Hall probes along the Hall bar of $L = 300\ \mu$m if not otherwise stated. This yields a geometry factor $V\!H = L/W = 3$, which denotes the number of probed square areas. The longitudinal resistivity ρ_{xx} is normalized to one square. It is thus comparable for all samples independent of the actual geometry. The relation between the resistance R_{xx} and the resistivity ρ_{xx} is

$$\rho_{\mathrm{xx}} = \frac{R_{\mathrm{xx}}}{V\!H}. \tag{2.8}$$

The cryostat,[14] where the measurements are performed, provides low temperatures (<1.5 K), and it is equipped with a superconducting coil, which produces a variable and high magnetic field typically up to 20 T.

---

[10] The details of processing are described in Appendix A.1.

[11] Other geometries such as the Van der Pauw geometry are possible with a square mesa and an ohmic contact at each corner. In order to quantify the resistivity (see below) of a sample in Van der Pauw geometry a correction factor [12] different from L/W has to be considered. Van der Pauw geometry is widely used to study anisotropic effects.

[12] This technique is known as four-point measurement and eliminates the resistances of the ohmic contacts, in contrast to a two-point measurement.

[13] The index xx indicates that the current is sent along the Hall bar and the voltage drop is also measured along the Hall bar, *i.e.* along the current path.

[14] It is indicated on all data plots which cryogenic system is used. The description of the different systems can be found in Appendix A.2.

Based on the classical Drude model, R_{xx} is a constant and unaffected by the magnetic field, while the Hall resistance R_{H} is just a linear function of the magnetic field with its slope inversely proportional to the electron density n. These relations are, however, no longer true in strong magnetic fields due to the Landau quantization. The Landau quantization becomes relevant when an electron completes more than one complete revolution in a magnetic field so that a certain number of flux quanta are encircled. This requires that no scattering occurs during one complete revolution. This requirement is satisfied either when the number of scatterers is small enough to result in a sufficiently large time τ between two scattering events or when the cyclotron frequency ω_{c} is high enough. Disorder gives rise to scattering, consequently structures with a low as possible disorder density are desirable in order to increase τ. Equivalently, the mean free path for the electron motion should be long, typically of the order of several microns, which corresponds to τ of the order of several ps. The cooling of the sample to very low temperatures is most important in this context, since phonons also act as scatterers. It is also desirable to use high magnetic fields, since the cyclotron frequency increases linearly with the field strength. Altogether, the product of scattering time and cyclotron frequency must fulfill the condition

$$\omega_{\mathrm{c}}\tau > 1, \tag{2.9}$$

if more than one complete revolution without scattering is intended. This relation is equivalent to an energetic separation, *i.e.* a reduced overlap of adjacent broadened LLs, because τ is related to the width of the broadened LLs (in an inverse manner) and ω_{c} their energetic separation from center to center. Once the given condition is achieved, the onset of oscillations in R_{xx} upon a variation of the magnetic field, *i.e.* Shubnikov-de Haas (SdH) oscillations, can be observed. They reflect the variation of the density of states at the Fermi energy with magnetic field. When the Fermi energy resides between two LLs, the lowest energetic excitation of the 2DES is a promotion of one electron from the LL below the Fermi energy to the next higher LL, because excitations within and between all lower LLs are impossible, since they are fully occupied. If the temperature is low enough, so that it cannot provide the energy for an electron excitation across the Fermi energy, the condition of vanishing scattering is created. Consequently, the conductivity in the direction of the magnetic field goes to zero. But specifically for a strong magnetic field, the resistivity ρ_{xx} also goes to zero. A vanishing longitudinal resistance R_{xx} is therefore expected in magneto-transport at integer values of the filling factor, also named magic numbers. In conclusion, the occurrence of a vanishing R_{xx} requires the existence of an excitation gap. This implies in reverse that the loss of the vanishing R_{xx} value at a fixed magic number of the filling factor is an indication of a quench of the corresponding energy gap. This can happen when *e.g.* two LLs approach or even cross. Such a situation is an important aspect of this thesis.

The Hall resistance R_{H} can be expressed as a function of the filling factor ν

$$R_{\mathrm{H}} = \frac{h}{e^2}\frac{1}{\nu}. \tag{2.10}$$

At an integer value of ν, the Hall resistance is an integral part of a ratio of fundamental constants. This fact is used in metrology as realization of the unit Ohm (Ω) [13], because this phenomenon

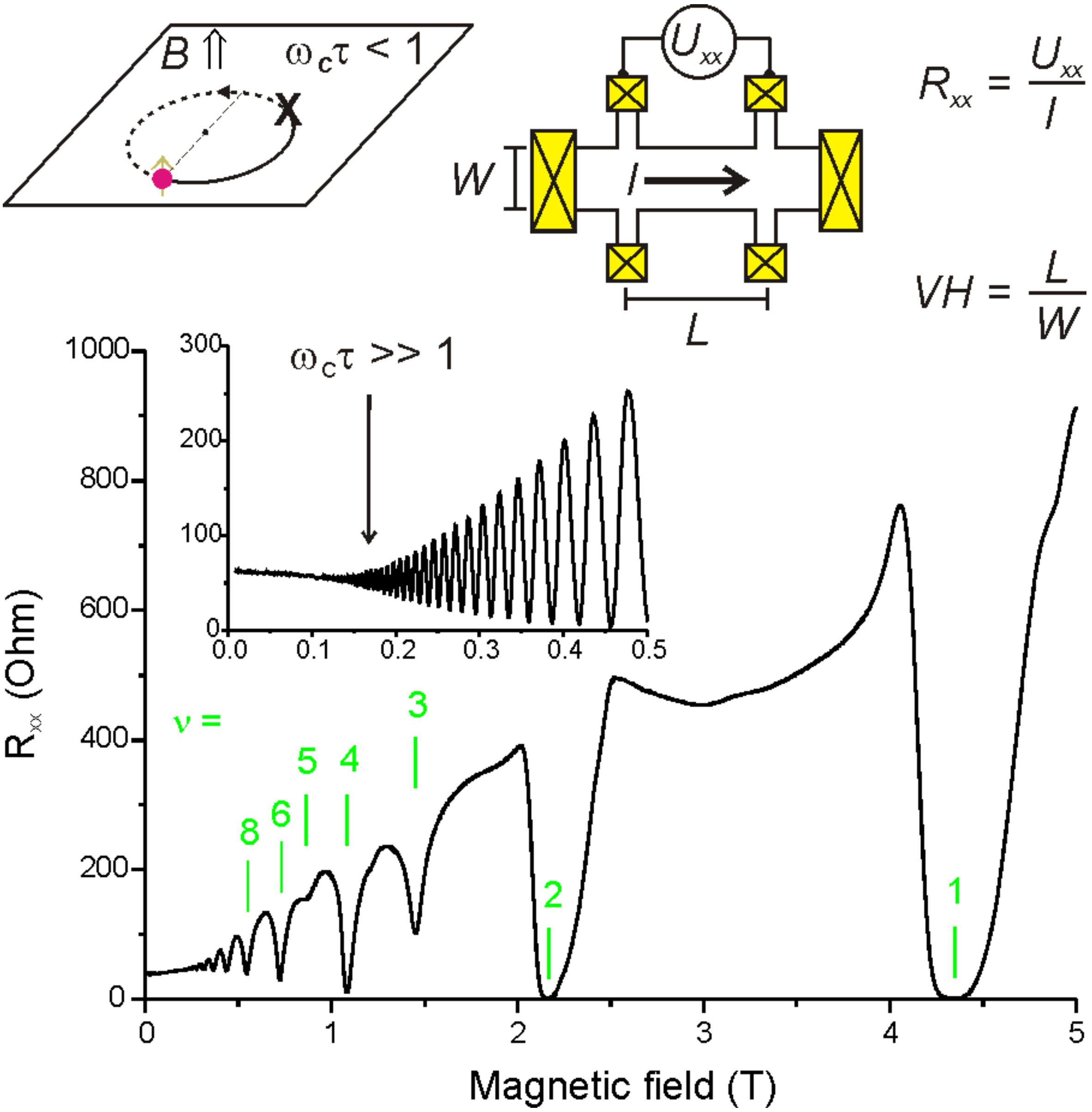

Figure 2.4: When the electrons can perform more than one complete revolution ($\omega_c\tau \gg 1$), the condition for the observation of SdH oscillations is satisfied. The longitudinal resistance R_{xx} vanishes at integer values of the filling factor ν. R_{xx} is measured as indicated in the upper right panel.

is independent of the actual sample, its geometry, and other boundary conditions. Since the localized states also need to be depopulated with an increasing magnetic field, they also pin the Fermi energy but now within the gap. The Fermi energy does not immediately jump from one to the next LL upon a variation of the magnetic field in the vicinity of an integer filling factor, as outlined above. This leads to a finite magnetic field or filling factor range for which a vanishing R_{xx} can be observed. Astonishingly, the Hall resistance remains quantized to an integral part of h/e^2 throughout this finite magnetic field or filling factor range. This effect is therefore named the quantized Hall effect (QHE) and the magnetic field or filling factor range with constant R_{H} is termed the "plateau region", since the Hall resistance exhibits a plateau. The actual width of the plateau region depends on the filling factor, the temperature and the sample quality. The width is larger towards lower filling factor, lower temperature and poorer sample quality. But if the sample quality is too poor, the QHE disappears, because the decisive energy gap between adjacent LLs is destroyed by a too strong overlap between them. It is mainly in this sense that the disorder is a relevant aspect in this thesis, because it prevents a vanishing R_{xx}, in particular at low magnetic fields where the LL splitting is already small.

The resistivity ρ_{xx} is important in order to calculate the mobility of a sample, which is a measure of the quality of a structure (or sample). The mobility μ is defined as

$$\mu = \frac{1}{ne\rho_{\mathrm{xx}}(B=0)}. \tag{2.11}$$

This relation represents, however, just the mobility at zero magnetic field. Of more interest is the mobility or quality of a sample at high magnetic fields, which is not necessarily directly related to the zero field mobility. As an indication for a high quality can be regarded the formation of QHEs in particular at odd filling factors where the small spin gap is decisive. Also the width of the plateau region can be seen as a measure of the sample quality. Since the mobility according to the Drude model (which is valid at zero field) is also defined as

$$\mu = \frac{e\tau}{m^*}, \tag{2.12}$$

the mobility increases towards lower temperature, because the scattering time τ[15] increases due to a reduction of scattering by phonons. So the mobility is a function of the temperature and is here usually given for 1.5 K. Towards even lower temperature, the increase in the mobility is negligible. The scattering time τ is then limited by the sample quality, which determines the width of the broadened LLs. Consequently, τ (as already mentioned) and therefore μ is to some extent a measure for the width of the plateau region. A reduced plateau width, equivalent to an effectively enhanced gap, can be expected when the zero field mobility is higher. An effectively larger gap between adjacent LLs due to reduced disorder leads to a pronounced strength of QHEs. A greater strength means that the QHEs are observable at lower densities and higher temperatures. Or, sen the other way around, the implications of smaller energy gaps become apparent in experiment.

2.2.2 The Laughlin description of the FQHE regime

At very high magnetic fields, beyond filling factor one, all electrons reside in the lowest LL (LLL) with the orbital quantum number $\mathrm{o} = 0$ and have a theoretically uniform spin orientation. Since the degeneracy of the LLL increases steadily towards higher magnetic fields, so that the

---

[15] Note, this scattering time is in reality not identical to the scattering time used in Eq. 2.9, although they are equally labeled. But both times exhibit qualitatively comparable dependencies and the discussion here is thought qualitatively.

LLL is only partially occupied, which consequently pins the Fermi energy, no further energy gaps and therefore QHEs are expected to appear. However, quantized values of R_H are found experimentally at fractional filling factors (fractional QHE (FQHE)) accompanied by vanishing of R_xx. A typical measurement is shown in Fig. 2.5. The so far used single particle picture of the IQHE regime however fails to account for the FQHE regime.

In the LLL all electrons precess with the same cyclotron radius,

$$r_{\mathrm{c},0} = \sqrt{\frac{\hbar}{eB}} = l_\mathrm{B}, \tag{2.13}$$

which is called magnetic length l_B. Since the associated kinetic energy is equal for all electrons, it is effectively frozen out. Instead, the Coulomb interaction among *all* the electrons is relevant.[16] Therefore, a many particle picture is necessary to describe the regime of the FQHE.

The appearance of QHEs, although at fractional filling factors, indicates the formation of energy gaps in the LLL. In the following it is briefly outlined how the formation of these energy gaps can be imagined and how the situation can be transferred to a single particle picture, which allows to simplify the discussion of physical phenomena related to the FQHE regime.

A downward cusp in the energy density in dependence of the magnetic field (see [14, 15]) leads to a discontinuity (jump) of the Fermi energy, because the Fermi energy is the derivative of the energy density with respect to the electron density. Referring to the jumps of the Fermi energy whenever a LL is completely depopulated, a downward cusp in the energy density must be present at integer filling factors, *i.e.* when the condition for a QHE is satisfied. Because of this downward cusp in the energy density, QHEs are preferred states. Laughlin proposed a wave function [16], which provides a downward cusp in the energy density whenever the 2DES is threaded by an odd number of flux quanta per electron, *i.e.* the filling factor is $\nu = 1/q$ with $q = 3, 5, ...$[17] [18] The trial wave function proposed by Laughlin

$$\Psi_{\nu=1/q}(\mathbf{z}_1, ..., \mathbf{z}_{N_e}) = \prod_{j<k}^{N_e} (\mathbf{z}_j - \mathbf{z}_k)^q \prod_{j}^{N_e} e^{\frac{-|\mathbf{z}_j|^2}{4l_\mathrm{B}^2}}, \tag{2.14}$$

with $\nu = 1/q$ and the complex coordinate of each electron $\mathbf{z}_{j,k}$, matches very well with the ground state found in diagonalization studies of few particle systems. Since typically $N_e \approx 10^{10}$ electrons are involved, no exact solution can be given for such a problem. It is important to note that the filling factor ν enters in the wave function via the exponent q.

To understand the origin of this wave function, a short excursion to $\nu = 1$ is necessary. The single particle wave function at $\nu = 1$ is

$$\Psi_{\text{single particle},\nu=1}(\mathbf{z}) = f(\mathbf{z}) e^{\frac{-|\mathbf{z}|^2}{4l_\mathrm{B}^2}}, \tag{2.15}$$

---

[16] This Coulomb interaction is certainly also present in the regime of the IQHE and consequently, QHEs at fractional filling factors larger than one can be found.

[17] Laughlin actually wanted to account for an emerging minimum in R_xx at $\nu = 1/3$ [17].

[18] Towards even smaller filling factors, other collective states such as the Wigner crystal (WC) become energetically more preferred and takeover the FQHE [15].

where $f(\mathbf{z})$ is a polynomial of the order of the number of flux quanta N_Φ. The complex coordinates at which $f(\mathbf{z})$ goes to zero can be regarded as the positions of the flux quanta. The total particle wave function at $\nu = 1$ results from a Slater determinant (anti-symmetrization) of all single particle wave functions of all electrons, which yields

$$\Psi_{\nu=1}(\mathbf{z}_1, ..., \mathbf{z}_{N_e}) = \prod_{j<k}^{N_e} (\mathbf{z}_j - \mathbf{z}_k) \prod_{j}^{N_e} e^{\frac{-|\mathbf{z}_j|^2}{4l_\mathrm{B}^2}}, \tag{2.16}$$

where the first product is again a polynomial but now of the order of the number of electrons N_e. But since the filling factor is $\nu = 1$, N_e and N_Φ are equal, the role of the flux quanta with respect to the introduction of zeros in the single particle wave function can be attributed to the consequence of the Pauli exclusion principle in the case of the many particle wave function. Therefore, the first product ensures that the electrons stay optimally separated, *i.e.* electrons avoid the positions of other electrons.[19]

In the case of $\nu = 1/3$ the Laughlin wave function can be rewritten as

$$\Psi_{\nu=1/3}(\mathbf{z}_1, ..., \mathbf{z}_{N_e}) = \prod_{j<k}^{N_e} (\mathbf{z}_j - \mathbf{z}_k) \prod_{j<k}^{N_e} (\mathbf{z}_j - \mathbf{z}_k)^2 \prod_{j}^{N_e} e^{\frac{-|\mathbf{z}_j|^2}{4l_\mathrm{B}^2}}. \tag{2.17}$$

The different contributions to the Laughlin wave function at $\nu = 1/3$ can be understood as follows. Neglecting for a moment the second product, the rest of the wave function is identical to the many particle wave function at $\nu = 1$, so that the first product can be said to originate from the Pauli exclusion principle. The single particle wave function demonstrates that each flux quantum per electron introduces a polynomial of the order of the number of flux quanta per electron, which leads to zeros (named vortices) in the wave function. The second product in the Laughlin wave function at $\nu = 1/3$ is due to the two additional flux quanta per electron when the filling factor is changed from $\nu = 1$ to $\nu = 1/3$, because two additional vortices (zeros) per electron have to be included in the wave function. These vortices have to be positioned for each electron such, that the energy density is minimized. The most obvious choice is to put them at the positions of the vortices, which are already present due to the Pauli exclusion principle. Consequently, the first and the second products are equivalent. In other words, the two additional flux quanta seem to be located at the positions of the electrons.

Due to the downward cusp in the energy density at $\nu = 1/q$, the electrons condense into a quantum Hall fluid, which is a preferred state. Therefore, tuning the magnetic field away from $\nu = 1/q$ leads to the creation of a large number of quasi-particles. The experiment also reveals FQHEs away from $\nu = 1/q$. So the goal is to correlate the positions of these quasi-particles, *i.e.* to fulfill the Pauli exclusion principle and to condense into a quantum Hall fluid at a critical density. It can be shown that the given trial wave function has certain excitations away from $\nu = 1/q$, which again have a downward cusp in energy at the fractional filling factors $\nu = p/q$, where p is an arbitrary positive integer and $q = 2p \pm 1$. They correspond *e.g.* to the many FQHEs found in experiment between $\nu = 1$ and $\nu = 1/3$.

---

[19] When the complex coordinates of two electrons equal, *i.e.* two electrons merge, Ψ goes to zero.

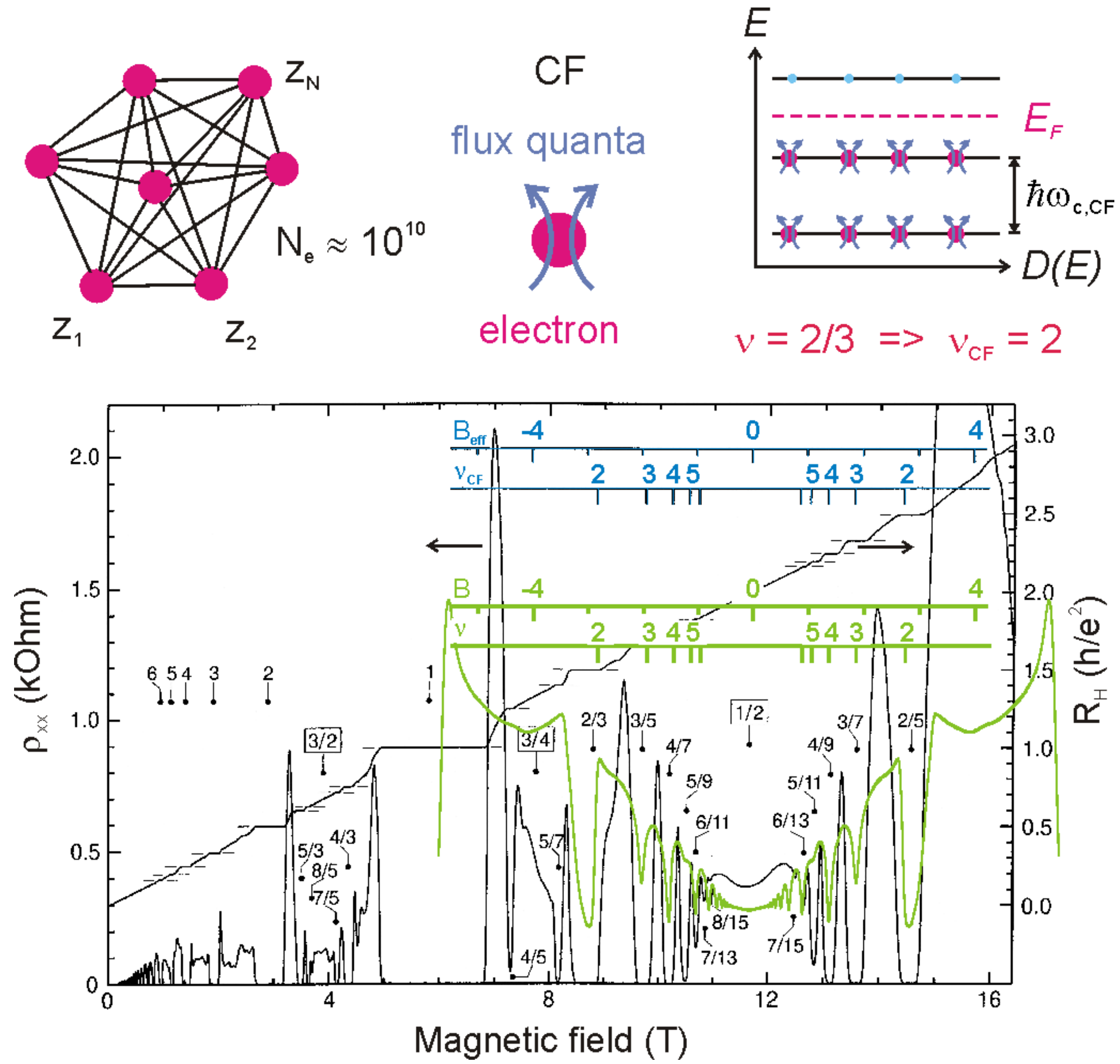

Figure 2.5: The black traces represent magneto-transport measurements of ρ_{xx} and R_{H} of a high mobility sample at very low temperatures. The range of the magnetic field spans well beyond $\nu = 1$ so that the various FQHEs are visible. The integer and fractional filling factors are indicated. The superimposed green trace is the result of a magneto-transport measurement in the IQHE regime; corresponding magnetic field values and filling factors are given. The IQHE trace is placed such that $B = 0$ and $B_{\mathrm{eff}} = 0$ coincide. The blue axes represent the effective magnetic field and CF filling factors according to the given gauge transformation. The similarity between IQHEs and FQHEs on the basis of B_{eff} is clearly apparent. Displayed above is how to regard the many particle interactions, the figurative definition of a CF, and the situation at $\nu = 2/3$, which can be mapped to $\nu_{\mathrm{CF}} = 2$ when the picture of LLs occupied with CFs is applied.

2.2.3 The composite Fermion (CF) description of the FQHE regime

The symmetry of FQHEs around $\nu = 1/2$, and the SdH-like oscillations of R_{xx} towards higher as well as lower magnetic field around $\nu = 1/2$ (see Fig. 2.5), led Jain to the proposal of the composite fermion (CF) [18] as a new and in the FQHE regime relevant quasi-particle. It results from the attachment of two flux quanta to one electron. This attachment is also related to the fact that the flux quanta seem[20] to be located at the positions of the electrons. To account for this attachment of flux quanta, an effective magnetic field B_{eff} has to be defined, which is obtained by a gauge transformation based on the condition that B_{eff} is zero at $\nu = 1/2$,

$$B_{\text{eff}} = B - B_{1/2}, \tag{2.18}$$

where $B_{1/2}$ is the magnetic field at $\nu = 1/2$. The CFs experience only the effective magnetic field. Tuning the external magnetic field through $B_{1/2}$ changes the sign of B_{eff}. Figure 2.5 shows a comparison between a magneto-transport measurement in the IQHE regime (green trace) and the already mentioned exemplary measurement in the FQHE regime. In order to highlight the similarity between the two traces, the magnetic field axis of the IQHE trace is shifted so that $B = 0$ and $B_{\text{eff}} = 0$ fall on top of each other. Furthermore, the IQHE trace is extended to positive as well as negative values of B. As can be seen, the positions of the R_{xx} minima of both IQHE and FQHE trace coincide. Considering the effective magnetic field axis (blue scale) it seems, as if the FQHEs can be regarded as IQHEs on the basis of CFs. The series of FQHEs around $\nu = 1/2$ is therefore called the Jain series.[21] This mapping reestablishes a single particle picture. The fact that the CF is indeed the relevant quasi-particle has been proven *e.g.* in magnetic focussing experiments [21].

In the IQHE regime, a vanishing R_{xx} is associated with an energy gap between adjacent LLs. An adaption of this picture leads to the postulation of energetically separated LLs, which are occupied by CFs (CF LLs). The application of the above gauge transformation to the fractional filling factors ν associated with electrons leads to the integer filling factors ν_{CF} associated with CFs

$$\nu_{\text{CF}} = \frac{\nu}{|1 - 2\nu|}. \tag{2.19}$$

Examples of this mapping are: $\nu = 1, 2/3, 3/5, 4/7, ...$ goes to $\nu_{\text{CF}} = 1, 2, 3, 4, ...$ towards negative B_{eff}, and equivalently to positive B_{eff}. The energy gap between the CF LLs arises entirely from the Coulomb interaction among all electrons. The associated Coulomb correlation[22] energy is written like the conventional Coulomb energy between two charged particles separated by a certain distance

$$E_{\text{C}} = \frac{e^2}{4\pi\epsilon\epsilon_0 l_{\text{B}}}, \tag{2.20}$$

with the magnetic length as the natural length scale since the electrons in the LLL precess on cyclotron orbits at a radius governed by l_{B}. The actual energy splitting $\hbar\omega_{\text{c,CF}}$ between adjacent

---

[20] It has been shown that the flux quanta are indeed not exactly located at the positions of the electrons [19].

[21] There exist further Jain-series towards higher magnetic fields around $\nu = 1/4$, $\nu = 1/6$ and so on, which are based on CFs with 4, 6, and so on, flux quanta attached to one electron. They are visible in samples of very high quality [20].

[22] The term correlation is typically used in the literature and indicates the many particle character in conjunction with the presence of a magnetic field.

CF LLs must scale with the Coulomb correlation energy

$$\hbar\omega_{\mathrm{c,CF}} = C_{\mathrm{C}} E_{\mathrm{C}}, \tag{2.21}$$

where the prefactor C_{C} sets the scale E_{C} to the actual value of an energy gap. Current theory finds for an ideal 2DES $C_{\mathrm{C}} \approx 0.092$ [22]. This energy gap can be regarded as the cyclotron energy of CFs and is equivalent to the cyclotron energy of electrons but with the difference, that $\hbar\omega_{\mathrm{c,CF}}$ scales with the square root of the external magnetic field and not linear as in the case of electrons. If this energy gap goes to zero, *i.e.* two CF LLs approach each other or even cross, the FQHE will disappear in a manner equivalent to the similar incident in the IQHE regime. This characteristic is used in this thesis to identify crossings of CF LLs. The energy gaps leading to the IQHEs and the FQHEs are fundamentally different in origin and therefore different in magnitude. The energy gaps relevant in the FQHE regime are typically much smaller than in the IQHE regime. Therefore, both a better sample quality as well as lower temperatures are needed to observe them, because disorder and temperature have the same influences on fractional QHEs as have been already explained above for QHEs at integer filling factors. CFs have the same spin as electrons and consequently the Zeeman splitting still applies. Adjacent CF LLs can have different spin orientation so that, the spin degree of freedom is not necessarily frozen out, in contrast to the expected implication of the LLL, which still applies although CF LLs are introduced. The different variation of CF cyclotron energy and Zeeman energy with magnetic field governs the relevance of the spin. The importance of this fact is demonstrated in this thesis by means of one example.

Chapter 3

Realization of a bilayer

There exist two different methods to realize a bilayer. The first is to use a double quantum well (DQW) structure, *i.e.* two close and either equal or different [23] QWs with a width of about 20 nm. DQW structures have been fabricated by several groups *e.g.* at Bell-Labs/Caltech [24], NTT [25], Univ. Cambridge [26, 27], Univ. Sydney [28], Sandia National Laboratories [29]. DQW structures offer a wide range of coupling regimes between the two layers by varying the barrier thickness and its energetic height. In the case of regular AlGaAs with an aluminum content of about 30% for the barrier material, tunneling, *i.e.* charge carrier exchange between the QWs, becomes noticeable below a barrier thickness of approximately 9 nm [30]. This charge carrier exchange is the main difference between a bilayer and a system known as double layer system (DLS) in the literature. This thesis is concerned solely with structures giving rise to bilayers. The charge carrier exchange implies, that the two charge layers cannot be contacted independently as is possible in the case of DLSs.

The second method to produce a bilayer is the use of a single wide quantum well (WQW) with a typical width of 50 to 100 nm within which a bilayer naturally forms above a critical electron density due to Coulomb repulsion. This critical density increases as the WQW narrows, because the repulsion must be stronger the more the electrons are squeezed together along the growth direction. Such an approach has so far only been taken by the group of M. Shayegan at Princeton University. It was originally intended to be used for studying the influence of finite thickness on the energy gaps of fractional quantum Hall states by thermal activation measurements [31]. Here, a WQW structure with a width of 77 nm is chosen. Based on a detailed study of WQW structures with widths varying from 60 nm to 96 nm [32, 33], this WQW width appears best suited to bring out the QHE at total filling factor $\nu_{\mathrm{tot}} = 1/2$,[1] a ground state of some significance in this thesis.

The fabrication of a versatile system for experiments involves the careful consideration of many design aspects such as the incorporation of back and front gates, the type and position of the doping with respect to the active region, *i.e.* the actual DQW or WQW, the intention to

---

[1] In general, the total filling factor is the sum of the filling factors of the individual charge layers. The notation total filling factor is used whenever a bilayer is the subject of the underlying discussion. The same implies for the term density versus total density.

use or avoid illumination of the sample to reach the appropriate carrier density etc. All these facts have an influence on the distance of the bilayer from the top surface, which is a crucial design parameter. This is discussed in the following. Details about the processing procedure of samples are given in Appendix A.1.

3.1 Design of a WQW and a DQW structure

The WQW and DQW structures for the studies here are produced with molecular beam epitaxy (MBE) on GaAs(001) at the Walter Schottky Institute (WSI) in Garching. The layer sequence of the WQW (03-15-01.1[2]) and the DQW (06-05-01.1) structures are shown in Fig. 3.1. Both structures are intentionally designed to exhibit a QHE at $\nu_{\mathrm{tot}} = 1/2$. The width of the WQW is chosen based on previous work reported by Suen *et al.* [32]. They found this QH ground state to be most pronounced for a nominal width of 77 nm [33]. The design of the DQW structure is adopted from work by Eisenstein *et al.* [34]. The QWs are nominally 18 nm wide and separated by a 3.1 nm thick barrier. However, as opposed to the Eisenstein device all barrier material consists of AlGaAs with an aluminum content of 30% instead of 15% as in the original publication. Quantum Hall investigations at $\nu_{\mathrm{tot}} = 1/2$ are the subject of Sec. 5.4.

The general arrangement of doped regions, spacer, cap, etc. is based on experience gathered on double layer systems (DLSs) by the group of Prof. Dietsche (Max Planck Institute for Solid State Research, Stuttgart). As a matter of fact, a successful double layer structure (11-17-97.2), in which charge carrier exchange between the two QWs (20 nm thick barrier) is avoided, served here as starting point. The active region is replaced by the above described DQW or the WQW. In addition, spacer thicknesses between doped regions and the active region are adjusted to obtain a total density of approximately 2.0×10^{15} m^{-2} without the need for illuminating (see below) the sample. The electron density is inversely proportional to the spacer thickness [9]. For tunability purposes, both structures include an *in situ* grown back gate. This back gate exhibits an unacceptable large leakage current to the 2DES if the structure is illuminated with a red LED at low temperatures, a common procedure used to enhance the carrier density and improve the mobility. Volume-doping is preferred over delta-doping, since it tends to be easier to control the final carrier density if no illumination is desirable. The doped regions are introduced on either side of the active region to achieve an approximately symmetric conduction band profile, which simplifies the control of the bilayer. The lower doped region is separated from the bilayer by a larger spacer, to take into account the surface segregation of Si dopants during the subsequent growth process. The upper doped region is wider as it must not only supply electrons to the bilayer but also compensate the surface states. The thickness of the GaAs cap layer and this doped region define here a delicate balance. The back gate is separated from the active region with an AlGaAs/GaAs superlattice. The properties of the back gate and the purpose of the LT-GaAs layer (LT = low temperature grown), covering it, are discussed in Sec. 3.3. An important

---

[2] This number is the internal labeling for structures grown at the WSI according to the scheme Month-Day-Year.Run.

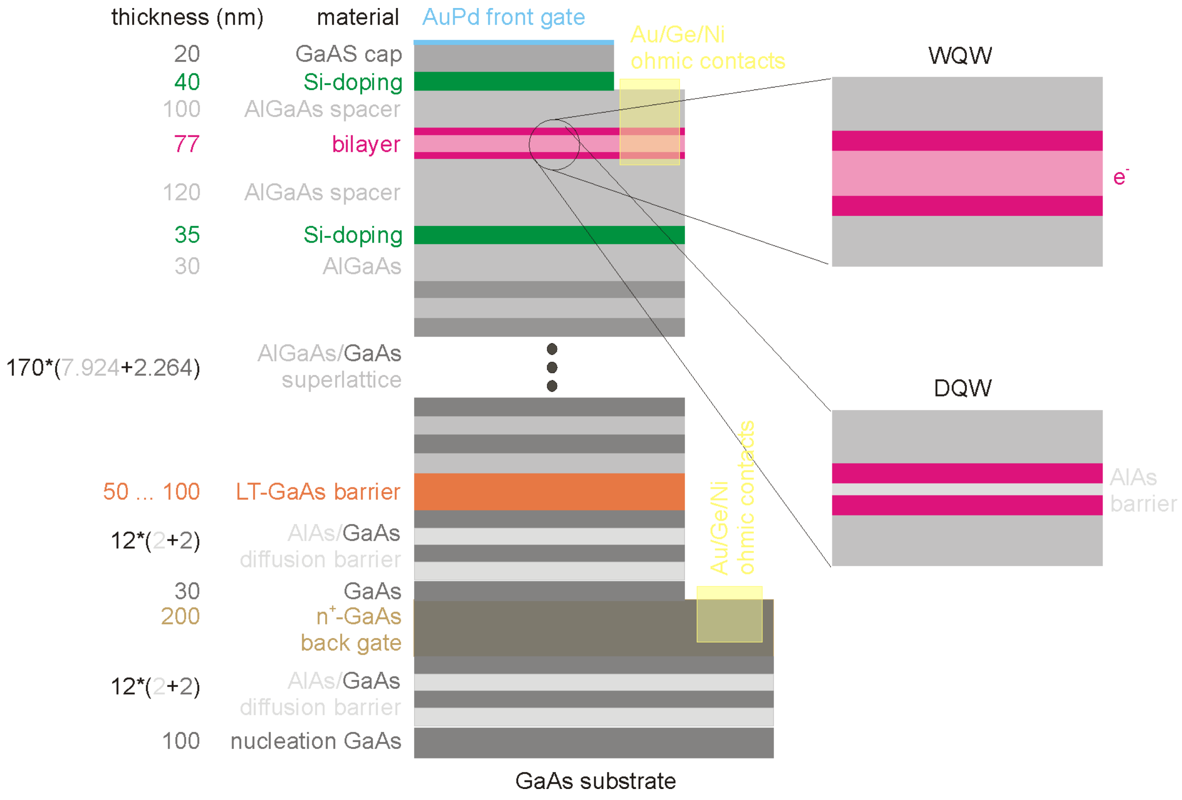

Figure 3.1: Layer sequence of the WQW and DQW structures. The growth direction is from the bottom to the top.

advantage of the volume doping is the excellent reproducibility of the density and distribution of the electrons between different cool downs. The external parameter values, *i.e.* gate voltages, to set a certain charge density and distribution, vary only by a few mV. The relevant parameters of bilayer structures, used by other groups for experiments very similar to those presented in this thesis, are listed in Tab. 3.1.

Label	Type	Dim. (nm)	Al-cont. (%)	ΔSAS (K) at n_{tot} (10^{15} m^{-2})	μ (m^2/Vs) at n_{tot} (10^{15} m^{-2})	Ref.
M1	WQW	40	30/0/30	60 - 80, 78 at 2.85	400	[35]
M2	DQW	20/1.0/20	33/0/33/0/33	17 at 4.0, 32 at 1.0	80 at 1.0	[36]
M3	DQW	20/3.1/20	33/0/33/0/33	≈ 10.9	200 at 2.0	[37]
M4	DQW	20/3.1/20	33/0/100/0/33	≈ 1	200 at 2.0	[38]
E1	DQW	18/3.1/18	15/0/100/0/15	< 0.9	50 at 1.0	[34]
S1	WQW	77	35/0/35	11.6 at 1.03	100 at 1.0	[32]

Table 3.1: The sample parameters of similar bilayer systems used by other workers in this field.

3.2 Simulation

The as-grown band structure and electron distribution of the fabricated WQW and DQW structures are simulated with a self consistent Poisson-Schrödinger solver.[3] The results are shown in Fig. 3.2. The necessary input parameters, *i.e.* the layer sequence and the dopants (including their density) along the growth axis have been slightly modified compared with the nominal values. They are adjusted so that for every pair of gate voltages, applied to the front and back gates in the experiments of Sec. 6.2, the calculated densities differ by less than 3% compared with the measured values. The accuracy of the simulations is necessary, since such simulations will be used to determine the finite thickness (λ) of the electron distribution as defined by any pair of gate voltages. The parameter λ will play an important role for the discussion of the results presented in Sec. 6.2.

The conduction band profile as well as the electron distribution for the WQW and DQW structures are displayed in Fig. 3.2. In the case of the WQW structure the deep dip in the electron distribution along the growth axis can be intuitively thought of as due to Coulomb repulsion among the electrons. Note that the probability of finding an electron in between the two charge peaks remains finite and charge carrier exchange is possible, an essential feature of bilayer systems. A similar charge distribution with an even deeper dip in the electron distribution is achieved with the help of a thin barrier in the case of the DQW structure. It is also apparent that the as-grown electron density of the lower layer is slightly larger than of the upper layer.

3.3 Back gate and LT-GaAs

For the bilayer systems described here the densities of the two layers are intended to be controlled individually. The front (back) gate only alters the density of the top (bottom) layer. The density of the bottom (top) layer is unaffected as the front (back) gate is screened by the top (bottom) layer. Consequently, two gates are necessary, one above (front gate) and one below the bilayer (back gate). The front gate is discussed in Section 3.4.

3.3.1 Incorporation of a back gate

The convenience and reproducibility of the back gate operation is improved, when the back gate is brought close (of the order of microns) to the bilayer and grown by molecular beam epitaxy (MBE). To this end a highly Si-doped layer of GaAs is buried below the active region. Two alternatives exist to bury this back gate. Either the back gate layer is grown together with the remainder of the heterostructure in one MBE step, or else the back gate layer is grown in a first MBE step, the back gate is patterned *ex situ*, and finally the WQW or DQW structure is grown in a second MBE step. The disadvantage of the first method is, that ohmic contacts to the bilayer can inadvertently also make contact with the back gate underneath thereby shortening

---

[3] This free program was written by Gregory L. Snider, Univ. Notre Dame, http://www.nd.edu/˜gsnider.

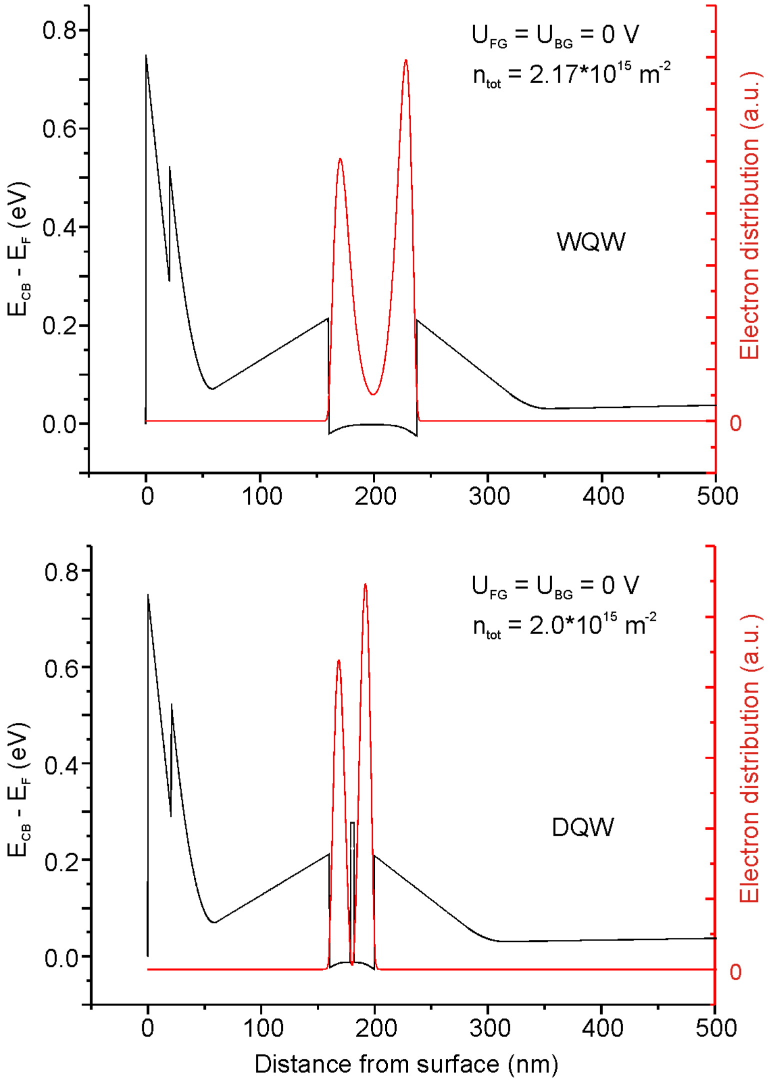

Figure 3.2: The self-consistently calculated electron distribution of the fabricated WQW and DQW structures at zero gate bias, *i.e.* as-grown.

the bilayer. However, this approach does also posses significant advantages: It avoids the more complex procedures required for overgrowth and, owing to the uninterrupted growth process, a higher sample quality is achieved. Furthermore, the desired Hall bar or device geometry is not restricted to any layout otherwise defined by the pattern of the back gate. The main advantage of a pre-patterned back gate is, that a short-circuit or an undesirable high leakage current between the back gate and the bilayer via the ohmic contacts can be reliably avoided. This is because the *ex situ* patterning process is intended to remove the back gate from areas which are later reserved for ohmic contacts to the bilayer. Both approaches are realized here. The pre-patterned back gate structures turn out to be essential for time-resolved measurements.[4] The procedure

---

[4] This thesis was originally intended to perform time-resolved transport measurements on bilayers as a continuation of the work of G. Ernst [39]. For that purpose a completely new setup had to be realized as well as bilayer

to pre-pattern back gates and prepare them for overgrowth is described in [41] and references therein. It should be noted, that other groups (*e.g.* Eisenstein *et al.* at Caltech [24], Shayegan *et al.* at Princeton University [42]) produce a back gate by thinning the processed sample from the back side down to a thickness of about 100 μm. Subsequently they evaporate a metal onto the exposed surface. The distance between back gate and the bilayer is then much larger as here requiring much larger back gate voltages of the order of 100 V, but in principle the same functionality is achieved. Still, the quality, *i.e.* number of defects and impurities of the original wafer material between back gate and active region, can significantly perturb the reproducibility of the back gate action. This holds particularly for samples from the Walter Schottky Institute (see Subsec. 6.8.2). This procedure is therefore not desirable for the samples under consideration and hence the use of the buried back gate concept is essential here.

Initially, WQW and DQW structures are fabricated with an *in situ* grown back gate. To avoid any short-circuit and sufficiently reduce the leakage current between the bilayer and the back gate, it turns out to be crucial to utilise a special recipe for the ohmic contact materials. Instead of the, in our laboratory, usual sequence of Au/Ge/Ni layers (see the reviews [43] and [44]) the order Ni/Ge/Au/Ni has to be used. The Ge layer is half as thick as the Au layer to obtain the appropriate eutectic mixture and the thickness of the Au layer is chosen to be equal to the depth of the bilayer below the crystal surface. A too thin Au layer yields difficulties at low temperatures and contacts freeze out. Ni serves as a wetting layer and forms a diffusion barrier for Au by forming NiGa clusters [45], so that Au spikes are avoided. A threshold behavior for this effect is observed with a minimum Ni thickness of about 5 nm, as shown in the upper panel of Fig. 3.3. Below this thickness, a nearly ohmic contact to the back gate results. Above this thickness however, leakage current is suppressed and saturates towards larger back gate voltages. The thicker the Ni layer is chosen the more the residual leakage current is reduced. These leakage current measurements have to be performed at liquid helium temperature or below. At higher temperatures the back gate always seems to display quasi-ohmic behavior.

---

structures. The bilayer structures were soon fabricated successfully while the development and implementation of the setup proved to be a much longer lasting and continuous process. Meanwhile the bilayer structures were being studied extensively, which finally led to all the results that make up this thesis. Nevertheless, the time-resolved project was promoted at every stage of the thesis and brought in operation. A setup has been realized that is capable of a time resolution of 150 ps. The excellent quality of the high frequency transmission has been demonstrated and a few experiments on the bilayer using the WQW structure were carried out for different configurations at 1.5 K. It turned out that in the case of the WQW structure with the un-patterned back gate no useful signal transmission could be achieved. Therefore, pre-patterned WQW structures were realized in collaboration with the MBE-group at the Max Planck Institute for Solid State Research in Stuttgart. It could be shown, that the transmission of a voltage pulse along the edge of a Hall bar under quantum Hall conditions is much faster, when the charge distribution is strongly confined to one of the interfaces of the WQW than for a symmetric electron distribution with the same density. Time-resolved measurements were intended, because they can distinguish between the different types of wave functions proposed for the QHE at $\nu_{\mathrm{tot}} = 1/2$ [40].

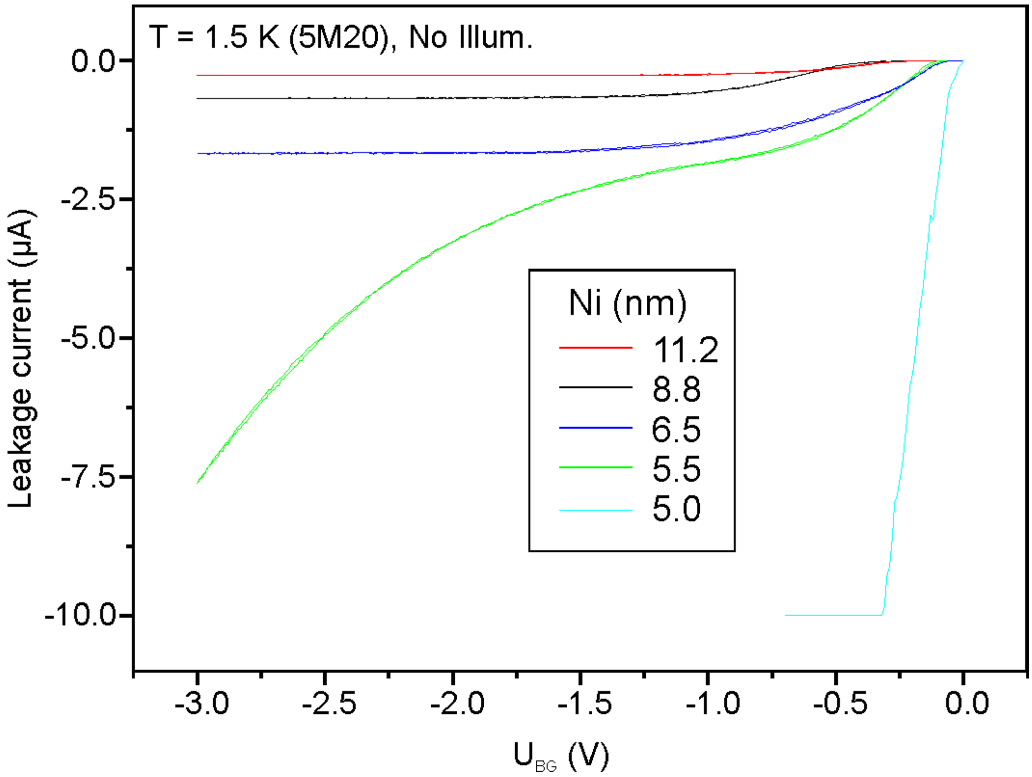

Figure 3.3: Leakage current of the back gate in dependence of the back gate voltage for different thicknesses of the Ni wetting layer underneath the ohmic contacts to the bilayer. A larger thickness of the Ni wetting layer reduces the leakage current. A saturation towards lower back gate bias is only achieved above a thickness of about 5 nm. The measurements are obtained on samples without LT-GaAs between back gate and bilayer, wherefore the leakage current is of the order of several 100 nA, even for the largest thickness of the Ni wetting layer.

3.3.2 The role of LT-GaAs

A satisfactory small leakage current is only achieved if in addition a layer of low temperature grown GaAs (LT-GaAs) is introduced between the back gate and the bilayer. A typical growth temperature for LT-GaAs is approximately 250°C. It should be noted that an accurate measurement of the temperature at these low values is difficult as the calibrated pyrometer does not work properly in this temperature regime. Usually, LT-GaAs is avoided in high mobility samples since its morphology is characterized by a rather high defect density. However, the coverage with a reasonable thick superlattice can terminate most of the induced defects and very high mobilities are again possible. The LT-GaAs is intended to introduce a Schottky barrier-like behavior between the back gate and the bilayer. The low growth temperature leads to the incorporation of excess As and As-clusters form upon a high temperature anneal. These As-clusters create energy levels close to the middle of the band gap of GaAs. These deep levels pin the Fermi energy and act as traps for charge carriers. As a consequence of this hopping transport dominates. When cooled to low temperatures, electrons can no longer thermally escape from the traps and current through the layer is exponentially suppressed. The impact of the LT-GaAs is only apparent at low temperatures. Already the procedure of trap formation indicates that the annealing process after the growth of the LT-GaAs is quite important. It is done at the regular growth temperature of 620°C. The longer the duration of the anneal the more excess As is converted in As-clusters and the insulating behavior improves. The time should be well above 4 minutes and is typically 10 minutes. A thickness of the LT-GaAs of typically 50 to 100 nm is sufficient. These parameters are optimized with the help of several test structures.

A comparison of two identical samples with and without LT-GaAs shows that the structure with LT-GaAs exhibits a reduced density in the lower layer. However, this density reduction can be compensated by a positive back gate voltage of approximately +0.5 V. This confirms, that LT-GaAs indeed pulls up the conduction band and pins the Fermi energy approximately 0.5 eV below the conduction band.

It should be noted, that for samples grown in some other MBE machines (*e.g.* at Bell-Labs, Weizmann Inst., NTT) no LT-GaAs is necessary to obtain a sufficiently low leakage current. Only the alloying temperature for the ohmic contacts to the electron system had to be reduced and in fact, 400°C seemed satisfactory [25]. Several tests with varying alloying temperature for the ohmic contacts on a WQW structure with an *in situ* grown, un-patterned back gate and without LT-GaAs are carried out. The basic idea is, to reduce the diffusion depth as it depends exponentially on temperature.[5] A reduction of the temperature even below 370°C does not lead to any improvement of the leakage current. Finally, an alloying temperature of 440°C is used (in conjunction with LT-GaAs) since this temperature resulted in the lowest contact resistances of about 25 Ω for a contact area of 80×80 μm^2.

The Si-doped back gate is sandwiched between a short period AlAs/GaAs superlattice. It is intended to impede surface segregation of Si dopants into the adjacent layers during the subsequent growth process. It also prevents diffusion of the excess As contained in the LT-GaAs layer.

3.3.3 Operation and performance of the back gate

To ensure ohmic contacts to the back gate, holes of 100×100 μm^2 are etched prior to the deposition of the ohmic contact material, which is almost the same as for the ohmic contacts to the bilayer. Just the thickness of the Ni wetting layer is reduced to only a few nm. The etch depth is chosen to make sure the LT-GaAs is entirely removed. On top of all ohmic contacts a 36 nm thick Ni layer is deposited. It is crucial to obtain a smooth surface of the contacts after the alloying procedure. This is mainly relevant for the self aligned contacts in the case of a HIGFET.[6] The thickness of the back gate layer is 200 nm. At least two contacts are bonded

---

[5] This dependency follows from a theoretical model of thermally induced diffusion. The diffusion depth depends only on the square root of the actual alloying time.

[6] HIGFET: heterojunction insulating gate field effect transistor. This special structure does not include any dopants. The original idea for its invention [46] was to check, if the absence of any remote ions would further increase the mobility, but surprisingly, the mobility of a HIGFET structure compared to the equivalent SHI structure

to the back gate to be able to test the conduction properties of the back gate. The two point resistance between two back gate contacts about 1 mm apart is typically 1 kOhm and does not noticeably change at low temperatures indicating its quasi metallic character. If not properly contacted the two point resistance increased to several 100 kΩ at 250 mK and finally to several MΩ at base temperature. The resulting extremely long response times up to hours for the carrier density to settle upon changing the gate bias is impracticable for any experiment.

A pre-patterned and overgrown back gate exhibits the best performance with respect to low leakage current. Such a structure (12-7-00.1[7]) without any LT-GaAs but with all the contacts free of any back gate material directly underneath them is successfully tested. The leakage current is of the order of 10 pA prior to the break through of the back gate. Break through happens at back gate voltages below -6 V and above +2 V. The latter value is reduced to about +1.4 V after illumination. It should be noted, that the actual gate voltages are heterostructure specific since the electric fields are relevant. These tests allow to conclude that the positioning of contacts directly above the back gate material indeed increases the leakage current significantly and that a break through happens indeed from the contacts to the back gate and not just from any site within the Hall bar. Of course this is only true if no defects within the Hall bar already cause an electrical connection between the bilayer and the back gate. Large Hall bars are more prone to such problems in view of the finite defect density per unit area. In the case of an unpatterned back gate the break through appears typically below -4 V and above +0.3 V. A typical value for the leakage current is -400 pA at -3 V and a temperature of 250 mK. Illumination immediately leads to an almost ohmic contact behavior between the bilayer and the back gate. The separation between the ohmic contacts to the bilayer and the back gate underneath can be as small as 400 nm while a short-circuit or leakage current is still efficiently avoided.[8] At temperatures typical for experiments (< 1.5 K), the leakage current is even further suppressed by increasing the magnetic field.

Nevertheless, although the leakage current is sufficiently low, it remains a critical aspect. For some applications (see Sec. 6.4) it is necessary to change the front gate voltage instantaneously

---

is always slightly lower. Because of the absence of dopants, charge carriers are entirely induced by a positive gate bias on the front gate. It consists of an *in situ* grown highly Si-doped layer of GaAs. This requires, that the ohmic contacts to the channel are self-aligned to the gate, because otherwise the induced charge layer would not reach all the way to the contacts. This leads to a very narrow process window. The main advantage of a HIGFET, however, is that with the help of the positive gate bias, a very high electron density $> 7 \times 10^{15}$ m^{-2} can be achieved [47]. This is not possible in most other structures, because the doped region will be pulled down below the Fermi energy quite soon leading to parallel conductivity. The alternative is to reduce the spacer thickness, but this leads to a reduction of the mobility [48]. It appears that some experiments here need higher as-grown electron densities, and one alternative would be to use a HIGFET. Consequently, a HIGFET compatible process was developed and a WQW structure including a front gate and back gate was realized. Magneto-transport experiments reveal the same features known from the regular WQW structure. The leakage current to the Si-doped front gate is sufficiently low when incorporating a thin layer of LT-GaAs. The buried back gate also operated properly, although only a limited positive gate bias (< 0.5 V) on the back gate can be used before break through occurs. This finally prevented the use of the HIGFET structure for further investigations.

[7] DQW structure without tunnel coupling. The lower QW is separated 628 nm from the back gate [49].

[8] This is successfully tested using an accordingly designed heterostructure (11-17-97.2).

by several 100 mV. This implies roughly one order of magnitude larger voltage jumps for the back gate if comparable experiments are intended using the back gate. However, large and sudden changes of the back gate bias lead to break down and a leakage current of several hundred nA. Hence, the back gate voltage should always be ramped slowly.

3.4 Front gate

To tune the density of the upper electron layer individually or that of the lower 2DES once the upper is depleted, a thin metallic front gate is evaporated. Because of its smoothness a mixture of AuPd with a Pd content of 40% is best suited for the purpose. For all samples a thickness of 8.5 nm is chosen, just slightly above the critical thickness of 5 to 6 nm for which a closed metal layer is formed. This small thickness is preferred for two reasons. First, it is intended to still be able to illuminate the sample through the front gate with the help of a red LED. Second, it is desirable to minimize the negative impact of the front gate on the high field transport properties of the bilayer such as a reduced mobility and weakened fractional quantum Hall effects. Fig. 3.4 shows a comparison for exactly the same Hall bar with and without such a front gate. With front gate, the density is slightly reduced by approximately 6% due to a renormalization of the surface potential. It can be compensated for by applying a positive front gate voltage of 28 meV. The mobility is reduced from 840 m^2/Vs to 790 m^2/Vs. The mobility of the uncovered structure is nearly recovered when correcting the density. It indicates no significant negative influence of the thin metallic front gate on the transport properties. This is supported by the fact, that almost no change in the different FQH states is observed. Contingently, the energy gaps are slightly reduced as signalized by the depth of the minimum at $\nu = 4/7$ after evaporation of the front gate. In the magnetic field regions between any of the magic filling factors, the longitudinal resistance is consistently somewhat higher for gated samples.

The single QW structure (11-27-01.4) used here to test the influence of a metallic front gate on magneto-transport properties is, apart from the QW width (22 nm), identical to the WQW structure. It has an as-grown mobility of over 800 m^2/Vs. We do not exclude the possibility that some finite parallel conductivity most probably introduced by the lower volume doping is responsible for the exceptional quality obtained. Such a parallel conduction layer may also screen disorder potential. The effect is similar to what happens in delta doped samples after illumination. The conduction band edge is pulled down towards the Fermi energy at the location of the dopants. Thus the onset of parallel conduction is quite close and the mobility rises significantly. This effect might also be present in the WQW structure, where the lower interface exhibits an even higher mobility than the upper one, although it is an inverted interface which usually exhibits a lower mobility. The transport properties are discussed in Chapter 5.

There have been studies that show that thicker front gates can wash out[9] the fractional quan-

---

[9] Several mechanisms are discussed, why the FQHE is usually weaker when a front gate is evaporated. Screening of the long range Coulomb interaction by the highly conducting gate may modify the FQHE. Also induced stress when cooling down, because the metal has a different thermal expansion than the semiconductor, has been

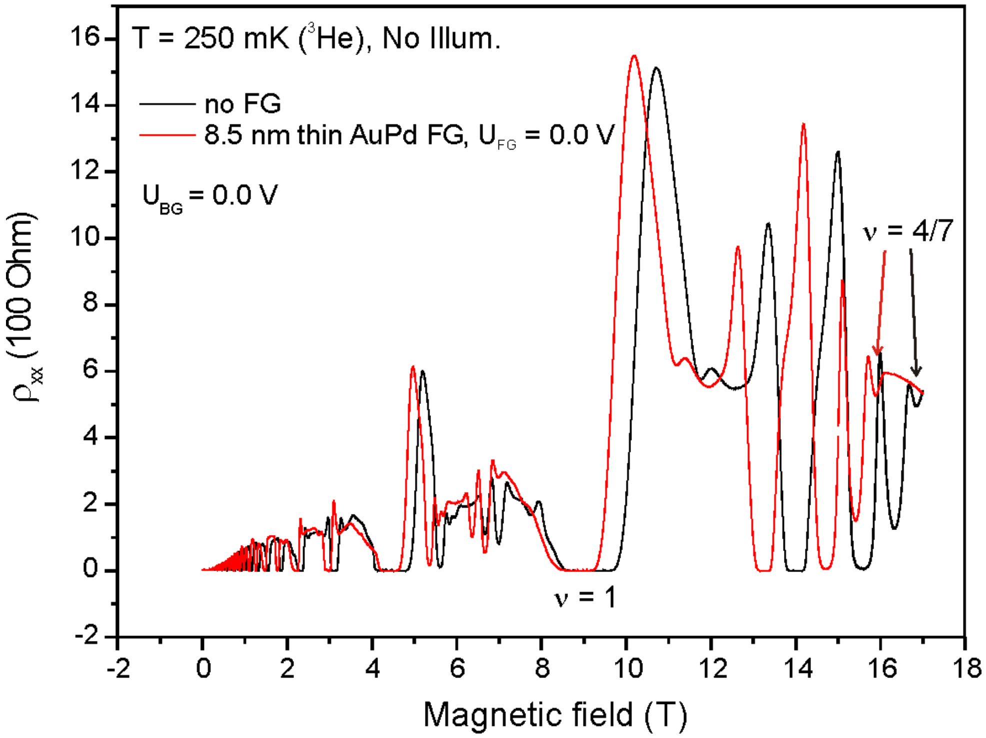

Figure 3.4: Magneto-transport measurement of one and the same Hall bar of a 22 nm wide QW structure with and without a 8.5 nm thin AuPd front gate. The front gate reduces the density slightly due to the renormalization effects of the surface potential. The quality of the sample as indicated by the appearance of certain FQH states is not noticeably affected by the additional front gate.

tum Hall effect [53, 54] and only a much larger spacer between the electron layer and the front gate can avoid this effect [55]. Here, a small distance between the front gate and the bilayer is preferred because screening effects slow down the propagation of edge magneto-plasmons (EMPs). In fact, the reduction of their propagation velocity is more pronounced if the gate is closer to the electron layer, since the velocity follows a logarithmic dependency on the distance between the electron layer and the metallic front gate [56] for intermediate distances of the

---

invoked as a potential source of difficulties. The first argument should not be crucial since the thin front gate here has a negligible effect. The second argument is supported by the observation, that thicker front gates successively wipe out the FQHE. To avoid this an all semiconductor front gate as in the case of the HIGFET (see footnote on page 40) can be used. But the HIGFET has several other disadvantages. Most of all complex processing sequences. An alternative all-semiconductor front gate can be achieved with p-type doped GaAs on top of a regularly doped structure. The p-type doped GaAs compensates the regular donors and fully depletes the channel. The gated mesa region is defined by patterning the p-type doped GaAs, which immediately reestablishes a conducting channel in the etched region so that there is no need for self-aligned ohmic contacts as in the case of the HIGFET. The leakage current is negligible because of the enlarged Schottky barrier. Such a structure is here successfully processed and tested. The problem is, that most high mobility MBE machines do not have the possibility of p-type doping using GaAs(001) substrates. The idea of an all-semiconductor p-type front gate was introduced to realize extremely narrow lateral conduction channels very accurately [50–52].

order of 150 nm. This deceleration is desirable when performing time-resolved measurements in an all-electronic fashion as here originally intended (see the footnote on page 37). Otherwise the available time resolution would not be sufficient to resolve any propagating modes. It is the main reason why the WQW structure here has a much smaller distance from the surface (250 nm) than that of the group of M. Shayegan at Princeton University (structure S1 of Tab. 3.1). Their active region is buried more than 400 nm below the surface [42].

Since the thickness of the front gate is much less than the height of the mesa (typically 90 nm because at least the cap and the doped layer have to be removed with a wet chemical etching process, see Appendix A.1 for details) it is very likely that the evaporated gate is disconnected at the mesa edge. This is even true if the gate is evaporated under a certain angle to the surface (*e.g.* 45°) because mesa edges usually have an undercut [57]. Some etch solutions provide mesa flanks that are not undercut [58]. Reliable contacts to thin front gates localized beyond the mesa are then possible. But apparently this etch solution has, for as yet unknown reasons, a detrimental effect on the sample quality. As a result a different method is introduced to ensure a reliable contact to the front gate. First, the lateral shape of the mesa is extended with two additional voltage probes on which no ohmic contacts are deposited. Instead the front gate is expanded to cover them. There, the front gate is contacted. If no additional bond pad is realized on top of the two voltage probes, the gold bond wire can only be attached by glueing it with two-component silver paint. If bonding is preferred, then the bond pad material (CrAu or TiAu) has to be deposited first prior to evaporating the AuPd front gate material, since AuPd does not inhere very well on GaAs. With two contacts to the front gate, its resistance and its functionality can be tested. A typical two point resistance across the front gate is of the order of 2.5 kΩ and independent of temperature.

Chapter 4

Theoretical description of a bilayer

In order to explain the various effects which are presented in the next chapters, it is necessary to understand the variation of the energy levels in a bilayer system as a function of the electron density, the tilt or imbalance of the WQW/DQW potential, the magnetic field etc. These points are discussed in the following sections.

4.1 Important parameters of a bilayer system

4.1.1 Bilayer formation in a WQW and its zero field properties

By definition a bilayer is a system consisting of two parallel, contiguous layers of equal charge carriers (here electrons, but they could equally be holes) between which a small but finite charge carrier exchange can take place by virtue of quantum tunneling.

When two single heterointerfaces (SHIs), one of which is inverted, approach, a wide quantum well (WQW) structure is achieved. Charge carrier exchange appears between the two electron layers, which reside at each of the interfaces, when they are brought sufficiently close together. The onset depends on the extent of each wave function, which is a function of the carrier density at each interface. Smaller densities imply a broader wave function [10] as described in good approximation by the Fang-Howard model. This means that if the width of the WQW is fixed, the charge carrier exchange is determined in an inverse manner by the total charge density (for simplicity at first an equal distribution of the charges among the two electron layers is assumed). Exchange causes hybridization of the energy levels at the two interfaces and the levels are split to so-called symmetric (S) and anti-symmetric (AS) states. In the case of unequal electron densities in the two electron layers it is customary in the literature [59, 60] to speak of bonding (B) and anti-bonding (AB) states instead. It is assumed, that the density at each SHI (or in each QW) is small enough to reside entirely within the lowest quantized energy level E_0 if considered isolated. This usually holds for densities well below 5×10^{15} m^{-2} [61], which is always the case here. Then, only the hybridization or subband splitting of the lowest energy level is relevant and is referred to as $\Delta\mathrm{SAS}$ or $\Delta\mathrm{BAB}$ if the total electron density is not equally distributed among the two layers. This is schematically displayed in Fig. 4.1.

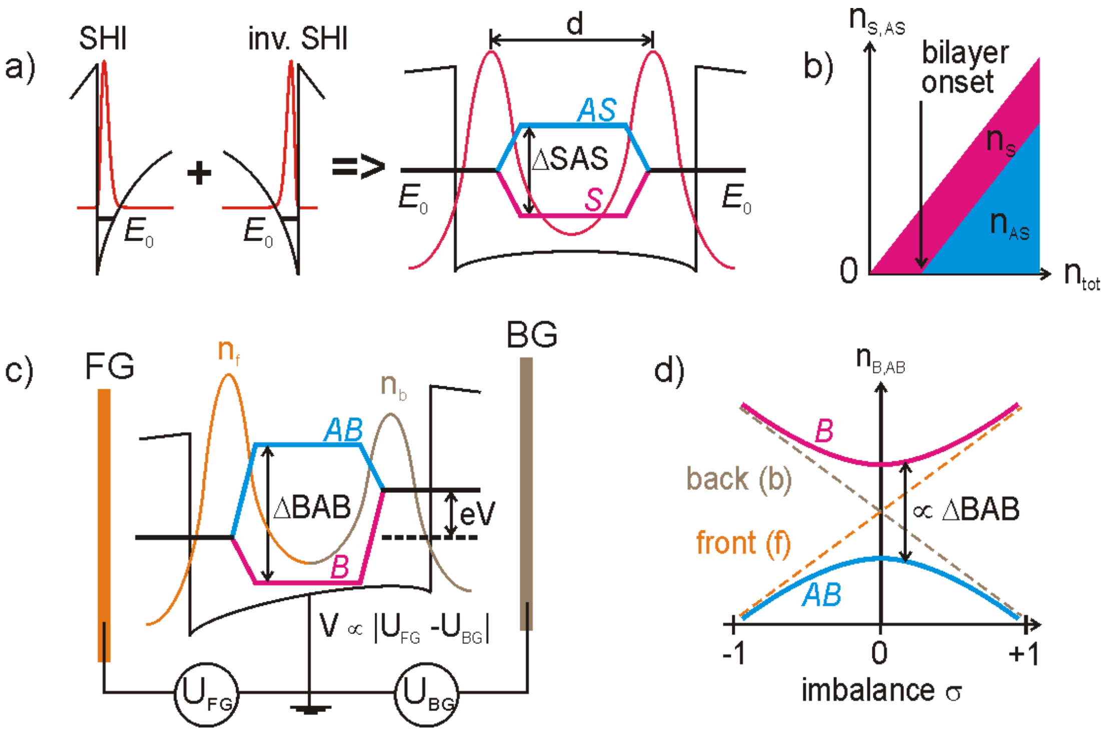

Figure 4.1: a) Two SHIs are joint together forming a WQW. A finite overlap of the individual electron distributions leads to a hybridization of the occupied energy level E_0 resulting in symmetric (S) and anti-symmetric (AS) subbands. b) Change of the different densities associated with the S and AS subbands as a function of the total density. The bilayer onset is due to the occupation of the AS subband. c) The WQW potential can be arbitrarily tilted with the help of the front and back gate. The potential asymmetry enhances the subband splitting. d) Schematic variation of the front and back layer densities (n_f, n_b) as well as the densities associated with the B and AB subbands (n_B, n_AB) as a function of the imbalance σ.

If the total charge carrier density is small, the electron distribution across the WQW does not exhibit a clear minimum at its center and the system behaves as a single layer. But with increasing total density two charge peaks develop separated by a clear dip. This is the onset of the bilayer regime. At still higher total densities the two charge peaks are pushed further to the interfaces and the relative depth of the minimum in the electron distribution becomes deeper, *i.e.* the layers separate more and more. In addition to the above mentioned inverse dependence of the extent of each electron layer on the density, this progressive separation can be intuitively understood as a result of Coulomb repulsion among the electrons. So just by sweeping the total carrier density the whole system can be tuned from a single layer over a strongly interacting bilayer to a weakly coupled bilayer system while maintaining a symmetric electron distribution in all cases. Due to the increasing distance of the electron layers towards higher total density, the tunneling strength, *i.e.* the charge carrier exchange is reduced and consequently the subband splitting drops.

The onset of a bilayer is identical (at least at zero magnetic field) to the occupation of the anti-bonding energy level. It is quite important to distinguish between the densities of the front (n_f) and back (n_b) layer (the assignment is based exclusively on the distribution in real space) and the densities that occupy the two subbands (n_B, n_AB). Because of the small but finite subband splitting $\Delta\mathrm{SAS}$ the subband densities are no longer equal even if the densities in the front and back layers are equal (the so-called balanced case). A charge transfer between the layers is called an imbalance and results from a tilt of the potential of the WQW by applying appropriate bias voltages to the front and back gates. It is intuitive as well as useful to define an imbalance parameter σ as the normalized charge difference between the layers

$$\sigma = \frac{n_\mathrm{f} - n_\mathrm{b}}{n_\mathrm{f} + n_\mathrm{b}}. \tag{4.1}$$

The imbalance σ is positive if more electrons are located in the front than in the back side of the WQW and negative if the other way round. How the different densities are related is shown in Fig. 4.1. The imbalance is a direct measure of the tilt of the WQW potential. The densities of the bonding and anti-bonding levels n_B and n_AB display a kind of anti-crossing behavior with respect to the densities of front and back layer n_f and n_b as the imbalance is tuned. The density difference between n_B and n_AB is related to the subband splitting as follows

$$\Delta\mathrm{BAB} = \frac{\pi\hbar^2}{m^*}(n_\mathrm{B} - n_\mathrm{AB}). \tag{4.2}$$

(This relation becomes apparent from the bilayer density of states as displayed in Fig. 4.7.) Since a tilt of the WQW potential raises the occupation difference, the subband splitting increases with larger imbalance values. By definition $\Delta\mathrm{SAS}$ equals $\Delta\mathrm{BAB}(\sigma = 0)$.

In order to derive more detailed information about the properties of a bilayer in a WQW quantum mechanical calculations are carried out. The results discussed here are obtained from a program written by S.-J. Cheng [62]. The calculations include exchange correlation effects in a local density approximation (LDA). How exchange interaction alters the potential and the electron distribution compared to the Hartree approximation, which neglects the exchange interaction, is displayed in Fig. 4.2. The overlap between the two electron layers is slightly reduced. In Fig. 4.3 the electron distribution for both subbands is shown. These calculations show that above a total density of about 0.4×10^{15} m^{-2} two charge peaks close to the edges of the WQW start to develop. The electron density in the middle of the WQW remains finite and is entirely due to the contribution of the symmetric subband, because the wave function of the anti-symmetric subband has a node at the center of the WQW in contrast to the wave function of the symmetric subband. Note that the square of the absolute value of the wave function yields the electron distribution function.

Above the bilayer onset, the separation d between the two electron layers, defined as the distance between the two maxima in the electron distribution function, increases steadily towards higher total density as seen in Fig. 4.4, because of a further enhancement of the Coulomb repulsion. Slightly above the bilayer onset, d rises rapidly. Towards higher total density, the layer separation saturates as the influence of the physical boundaries of the WQW gains in importance. Also displayed in Fig. 4.4 is the subband splitting $\Delta\mathrm{SAS}$ for the balanced case. It

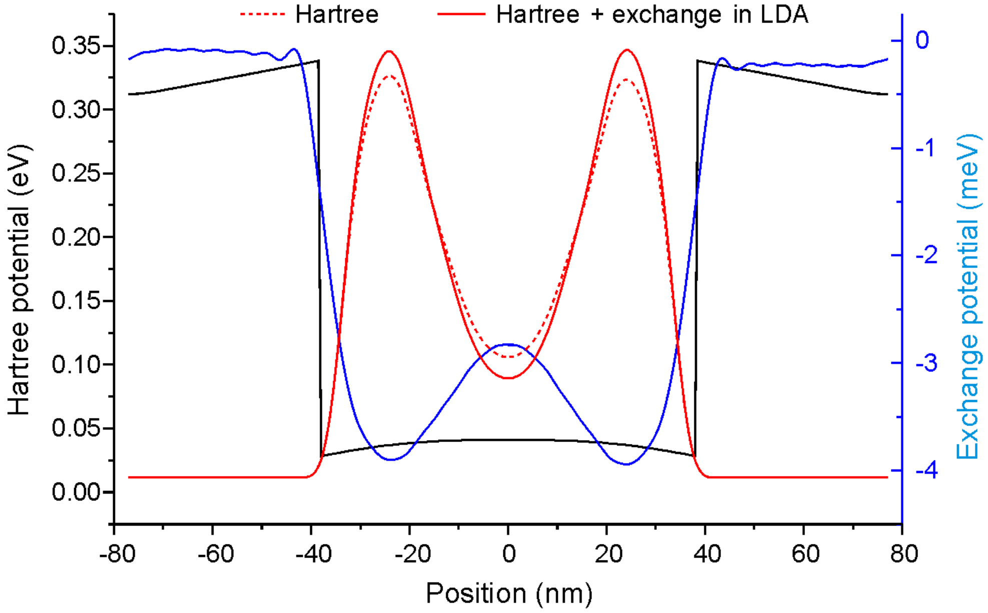

Figure 4.2: Implications of the inclusion of exchange interaction on the potential and electron distribution. The potential is stronger lowered at the positions of the charge peaks than in the middle of the WQW thus amplifying the layer separation. The overall effect is small. However, the impact on the comparable small subband splitting is significant, as explained in the text.

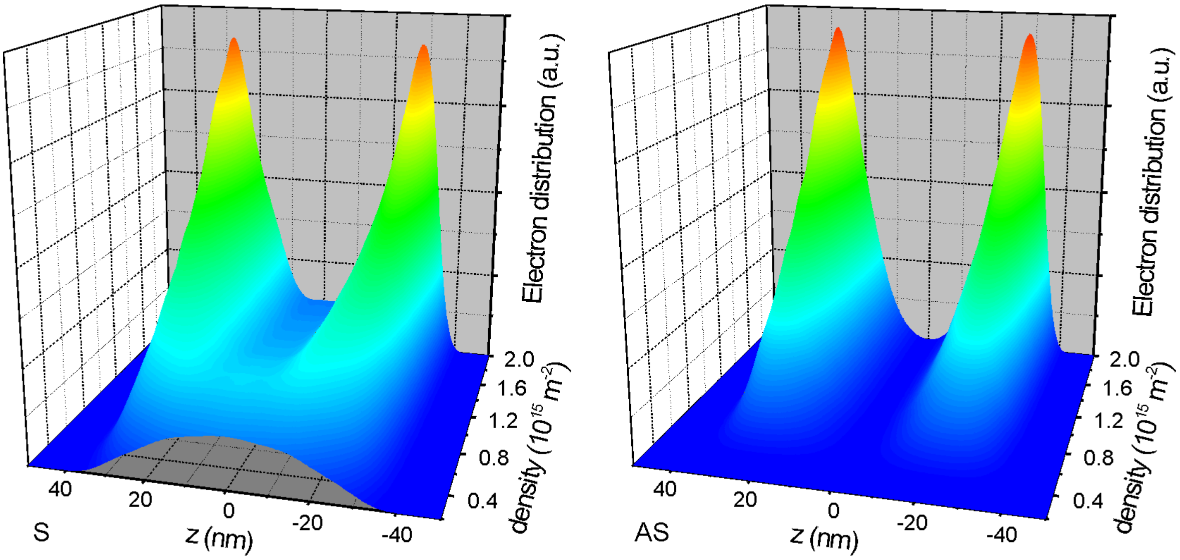

Figure 4.3: Electron distribution in the 77 nm wide WQW calculated for each subband (left: S, right: AS) individually in dependence of the (balanced) total density. Above about 0.4×10^{15} m^{-2} two charge peaks emerge leading to the formation of a bilayer. The density at the center of the WQW remains finite for the S subband whereas zero in the case of the AS subband due to a node in the AS wave function. The total density is the sum of the individual densities and is displayed in Fig. 4.4.

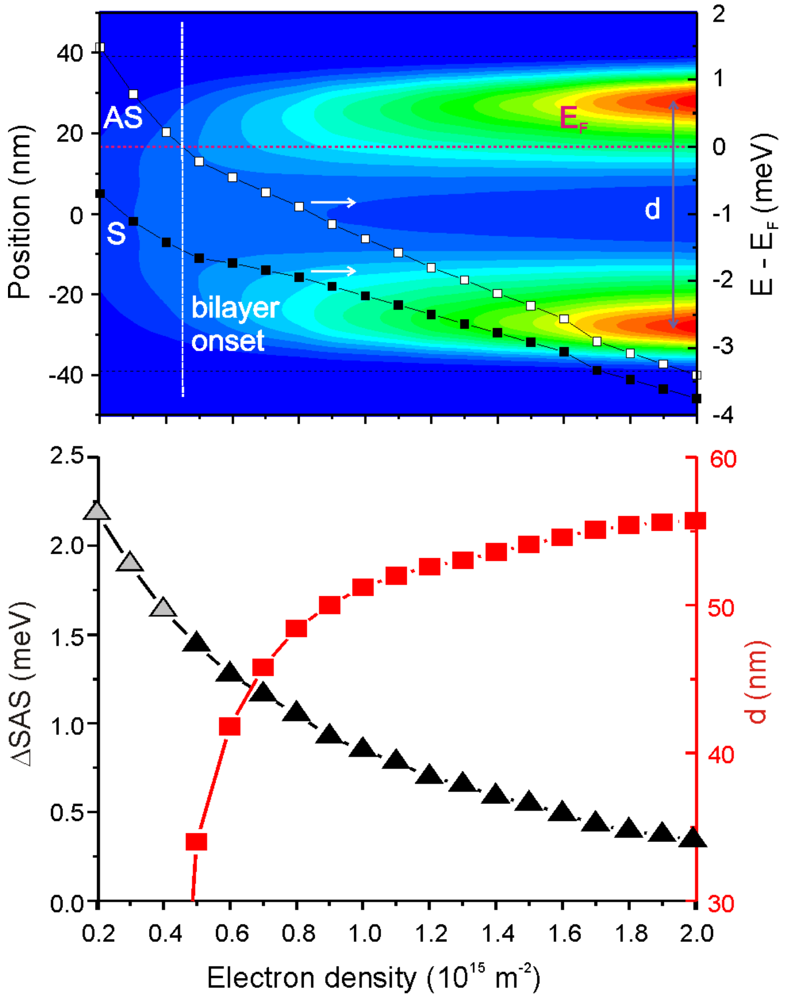

Figure 4.4: Upper panel: Color plot of the electron distribution in the WQW as a function of the total density for the balanced case. Also shown are the energies of the S and AS subbands with respect to the Fermi energy E_F. The white vertical line marks the bilayer onset. Lower panel: Layer separation d and subband splitting $\Delta\mathrm{SAS}$ as a function of the total density n_tot for the balanced case. The layer separation is defined as the distance between the two maxima of the electron distribution function. It drops to zero below a total density of approximately $n_\mathrm{tot} = 0.4 \times 10^{15}$ m^{-2}, which represents the boundary between the bilayer and single layer regimes in the case of an untilted WQW potential. An energy of 1 meV corresponds to 11.6 K.

decreases monotonously with total density as previously mentioned. The subband splitting is generally smaller if exchange interaction is included. Exchange interaction favors layer separation thereby producing a smaller tunneling strength between the layers and, hence, subband splitting. Compared to the experimentally determined values here, which are presented in Sec. 5.2, the calculated values for the subband splitting are slightly off. Without exchange correction, the gap is overestimated by about 10% or 1.5 K at a density of 1.0×10^{15} m^{-2}. With exchange correction, the gap is underestimated by about 30%. This is however not surprising, because calculating such small energy differences accurately is difficult [63].

If the WQW potential is tilted (imbalanced), the level splitting $\Delta\mathrm{BAB}$ increases approximately with the square of the imbalance σ, as shown in Fig. 4.5. This functional dependence can be immediately understood, when considering the influence of a detuning of the hybridizing energy levels on their actual splitting. The altered level splitting is given by (see Fig. 4.1)

$$\Delta\mathrm{BAB} = \sqrt{\Delta\mathrm{SAS}^2 + (eV)^2}, \tag{4.3}$$

where V is the voltage drop between the location of the electron distribution maxima due to externally applied gate voltages, which tilt the WQW potential. The problem may be treated as a parallel plate capacitor (albeit with identical charges on both plates) with a capacitance per unit area

$$C_\square = \frac{\epsilon\epsilon_0}{d}, \tag{4.4}$$

where d is the distance over which charges are transferred when tilting. For a parallel plate capacitor, the general relation

$$C_\square = \frac{Q}{U}, \tag{4.5}$$

is valid where U is the applied voltage between the two plates of the capacitor (here $U = V$) and Q the charge (per unit area), which is transferred by this voltage (here $Q = e\Delta n$). The transferred electron density Δn is related to the imbalance σ

$$\Delta n = \frac{1}{2}(n_\mathrm{f} - n_\mathrm{b}) = \frac{1}{2} n_\mathrm{tot}\sigma. \tag{4.6}$$

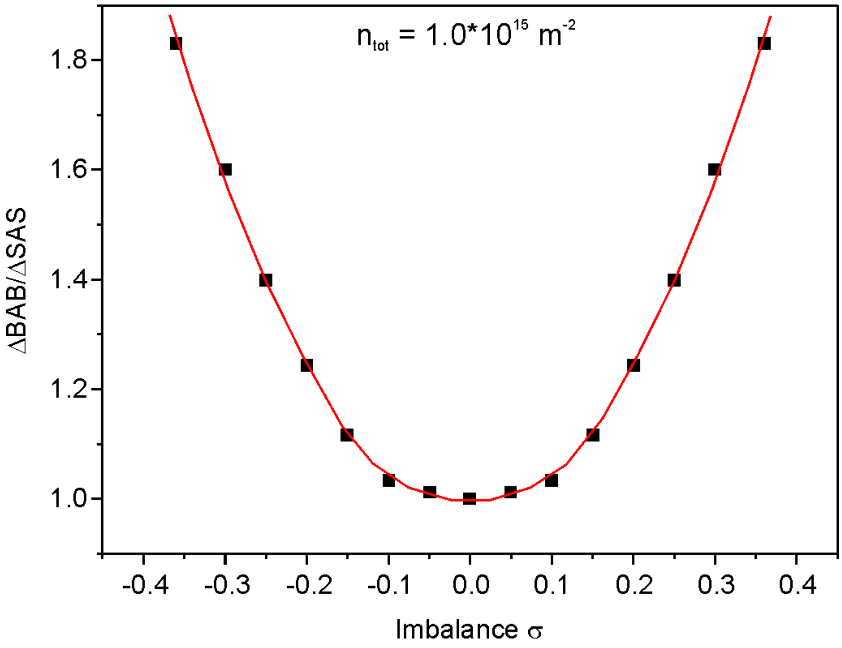

Figure 4.5: Calculated variation of the subband splitting $\Delta\mathrm{BAB}$ with imbalance at a fixed total density of 1.0×10^{15} m^{-2}. The red line is included as a guide to the eye. The subband splitting increases in good approximation with the square of the imbalance.

It follows

$$V = \sigma \frac{e n_{\mathrm{tot}} d}{2\epsilon\epsilon_0}, \tag{4.7}$$

and $\Delta\mathrm{BAB}$ takes on the form

$$\Delta\mathrm{BAB} = \Delta\mathrm{SAS}\sqrt{1+(c\sigma)^2} \approx \Delta\mathrm{SAS}\left(1+\frac{1}{2}(c\sigma)^2\right). \tag{4.8}$$

Here, c is a constant. The first term of the Taylor expansion is sufficient for a small imbalance. It is proportional to the square of the imbalance in agreement with numerical calculations. The same result was found by Hu and Heitmann [64].

With an imbalance, the contribution of the bonding subband to the total electron distribution is shifted to that side of the WQW which is energetically pulled down by the tilt of the WQW potential, whereas the contribution of the anti-bonding subband is shifted to the opposite side. This originates from the orthogonality requirement of the wave functions of the B and AB subbands. In Sec. 3.2 the program Poisson-Schrödinger solver was used to calculate the electron distribution across the WQW because contrary to the program of S.-J. Cheng, gate biases can be included. This is necessary to discuss the experimental results of Subsec. 6.2.5.

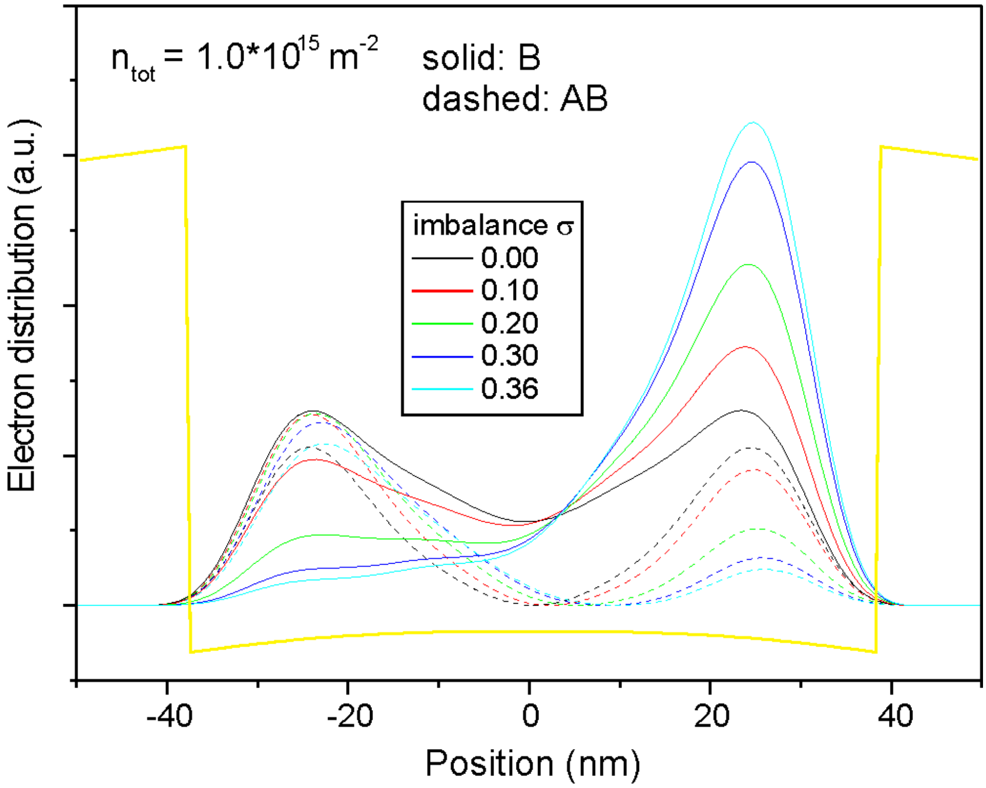

Figure 4.6: Calculated contributions of the B and AB subbands to the total electron distribution for some imbalance values. Note the overall slight shift of the preferred electron layer towards the boundary of the WQW potential, indicated by the yellow line, with increasing imbalance.

4.1.2 Bilayer formation in a DQW and its zero field properties

The properties presented so far for the WQW are partly altered in the case of a DQW. There, the distance d between the layers is fixed by the width of the barrier and the QWs. The layer distance is much smaller compared to the WQW in order to ensure charge carrier exchange through the additional barrier by virtue of quantum tunneling. The introduction of a physical barrier between the two electron layers generally suppresses quantum tunneling leading to a reduced subband splitting. The tunnel coupling is determined by the thickness of the barrier as well as its energetic height. The reduction of $\Delta\mathrm{SAS}$ with total density n_{tot} is less, because the extent of the individual electron distributions is fixed by the QW width and the impact of an imbalance σ is also reduced. Referring to Tab. 3.1, one finds that in the case of a 1 nm thick AlGaAs barrier with an Al content of 33% between two 20 nm wide QWs (structure M2), even though there is still a noticeable dependence of the subband splitting on the density from 32 K at 1.0×10^{15} m^{-2} to 17 K at 4.0×10^{15} m^{-2}, it is reduced by more than a factor of two compared with a 40 nm broad WQW (structure M1) without a barrier and a subband splitting of 80 K at about 3.0×10^{15} m^{-2}. For a DQW structure (20 nm QWs) with a 3.1 nm barrier out of AlGaAs with an Al content of 33% (structure M3) the subband splitting is further reduced to about 10 K and is already nearly independent of the actual density and imbalance. $\Delta\mathrm{SAS}$ finally shrinks to about 1 K if the barrier consists of pure AlAs (structure M4).

4.2 Energy levels of a bilayer in a perpendicular magnetic field

In a perpendicular magnetic field B the density of states (DOS) associated with each subband is discretized into a set of LLs as depicted in Fig. 4.7. So two LL fan-charts coexist and are offset by the subband splitting. Every LL is unambiguously described by three quantum numbers: the subband index (B,AB), the orbital quantum number (0,1,2,...) and the spin orientation (↑,↓). Since only the two lowest subbands are relevant, the subband index can be effectively treated as an isospin, *i.e.* a generalized spin applied to a two-level system.[1] As described in Sec. 2.2 the LLs are successively depopulated with increasing magnetic field. Since the wave functions associated with B and AB subband index (refer to Fig. 4.4) are different, the electron distribution function is permanently changed to a minor degree during this depopulation process [66].

Transport experiments at low B will be characterized by beating Shubnikov-de Haas oscillations (SdHs) due to two different $1/B$-periodicities, which correspond to the different subband densities n_{B} and n_{AB}. They can be extracted from a Fourier analysis and yield according to Eq. 4.2 a direct measure of the subband splitting. This correlation is used experimentally in Sec. 5.2 to determine the subband splitting.

The two offset LL fan-charts penetrate each other and crossings of LLs occur. The critical magnetic field (or density) of any crossing point between a pair of LLs belonging to different

---

[1] Some theoretical descriptions relate the two isospin orientations to the two layers [65].

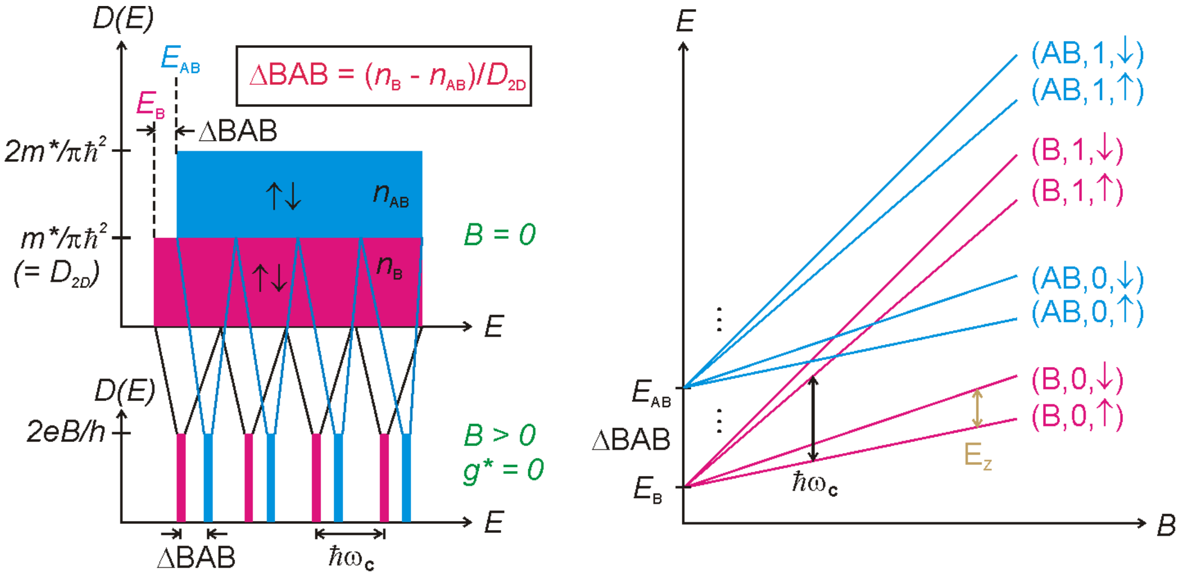

Figure 4.7: Left panel: Transformation of the constant DOS function of each subband into Dirac-delta functions due to the application of a magnetic field perpendicular to the bilayer. Right panel: Due to two occupied subbands two LL fan-charts are formed, which are offset by the subband splitting $\Delta\mathrm{BAB}$, wherefore the two fan-charts penetrate each other and cause LL crossings. Each LL is unambiguously labeled by a set of three quantum numbers (subband index, orbital quantum number, spin) as indicated.

fan-charts is controlled by the energetic offset $\Delta\mathrm{BAB}$. Since the subband splitting is a function of the imbalance σ, these crossing points can be shifted along the magnetic field axis or to a certain density by tilting the WQW potential. With $\Delta\mathrm{BAB}$ being smallest for zero imbalance, the crossing points are found at the lowest magnetic field value for the balanced case. According to Fig. 4.5 the subband splitting $\Delta\mathrm{BAB}$ is enlarged in a quadratic manner with increasing imbalance so that to first order an equivalent shift of the crossing point to higher density or magnetic field is expected.

4.2.1 The pseudospin description of LL crossings

The character of a LL can be described with a pseudospin. The pseudospin is the collection of the three quantum numbers of all particles residing within a LL. In order to describe the crossing of two LLs it is sufficient to take into account the two involved LLs and ignore all others. This is justified, since the LL of the pair which is occupied, defines in good approximation the ground state of a 2DES (or bilayer). The ground state is labeled as a quantum Hall ferromagnet, when the pseudospin of this LL is completely aligned. Complete alignment means, that all particles are characterized by the same set of quantum numbers. It requires a full occupation of the LL and consequently a magic filling factor. The term quantum Hall ferromagnet originates from the equivalence to a preferred spin orientation in ferromagnetic materials[2] in conjunction with a magic filling factor. Passing a crossing point of two LLs leads to a reorientation of the pseudospin because several quantum numbers are changed. If the full alignment of the pseudospin is given to both sides of the crossing point, a ferromagnetic phase transition (FPT) takes place. At the crossing point, the energy gap between adjacent LLs with different pseudospin orientation vanishes.[3] Since the Fermi energy intersects the crossing point, the coincidence shows up in transport by the disappearance of the QHE at this filling factor. Therefore LL coincidences are interesting because they allow to study FPTs quite easily.

Analogous to the Zeeman splitting, the energy splitting between adjacent LLs with different pseudospin orientation can be regarded as pseudospin splitting mediated by a corresponding pseudospin field

$$E_{\mathrm{PS}} = \mu_{\mathrm{PS}} P, \tag{4.9}$$

with μ_{PS} the pseudospin magnetic moment and P the pseudospin (or pseudomagnetic) field. The pseudospin field is a combination of all the parameters that affect the energy of the pseudospin.[4] The two different pseudospin orientations involved in a crossing can be thought of for the sake of simplicity to be up and down (see Fig. 4.8a). They are energetically degenerate at the crossing point, *i.e.* the pseudospin splitting is theoretically zero and the pseudospin field is also zero. Because of this energetic degeneracy, the density of states is *twice* as large as the number of particles that can occupy these states, so that the system has to decide how to distribute the particles among the states and what pseudospin orientation to assign to them.

For each strength of the pseudospin field, the pseudospin orientation is determined by minimizing the total energy of the system. How the pseudospin orientation develops as the pseudospin field is tuned to drive the system across a coincidence depends on the so-called anisotropy energy associated with the different pseudospin orientations [68]. Three types of anisotropy can be distinguished: easy-plane and easy-axis anisotropy and no anisotropy (isotropic) representing the border case between the two previous types.

If there exists an energetic minimum for a coherent superposition of the two pseudospin orientations close to the coincidence point then easy-plane anisotropy is present. The overall orientation of the pseudospin is then within the plane (the up and down orientations of the pseudospin define the normal axis to the plane). The system is referred to as an XY-ferromagnet (XY according to the axes of the plane; see Fig. 4.8c). The isotropic case is reached when no specific pseudospin orientation or superposition is preferred. Easy-axis anisotropy emerges when two energetic minima occur for complete pseudospin polarization, either up or down. In this case, the system prefers one and the same pseudospin orientation being along the normal

---

[2] But quantum Hall ferromagnetism is not established due to long range order as in the case of conventional ferromagnets.

[3] At least theoretically in this description. The actual energy gap can remain finite (see below).

[4] For example, for the above introduced isospin, *i.e.* the subband index, the imbalance or more precisely an inter-layer bias, which is zero for the balanced case, is the effective isospin field and the characteristic isospin splitting energy is the reduced level splitting $\Delta\mathrm{BAB} - \Delta\mathrm{SAS}$, which is zero for zero isospin field (balanced condition) [67].

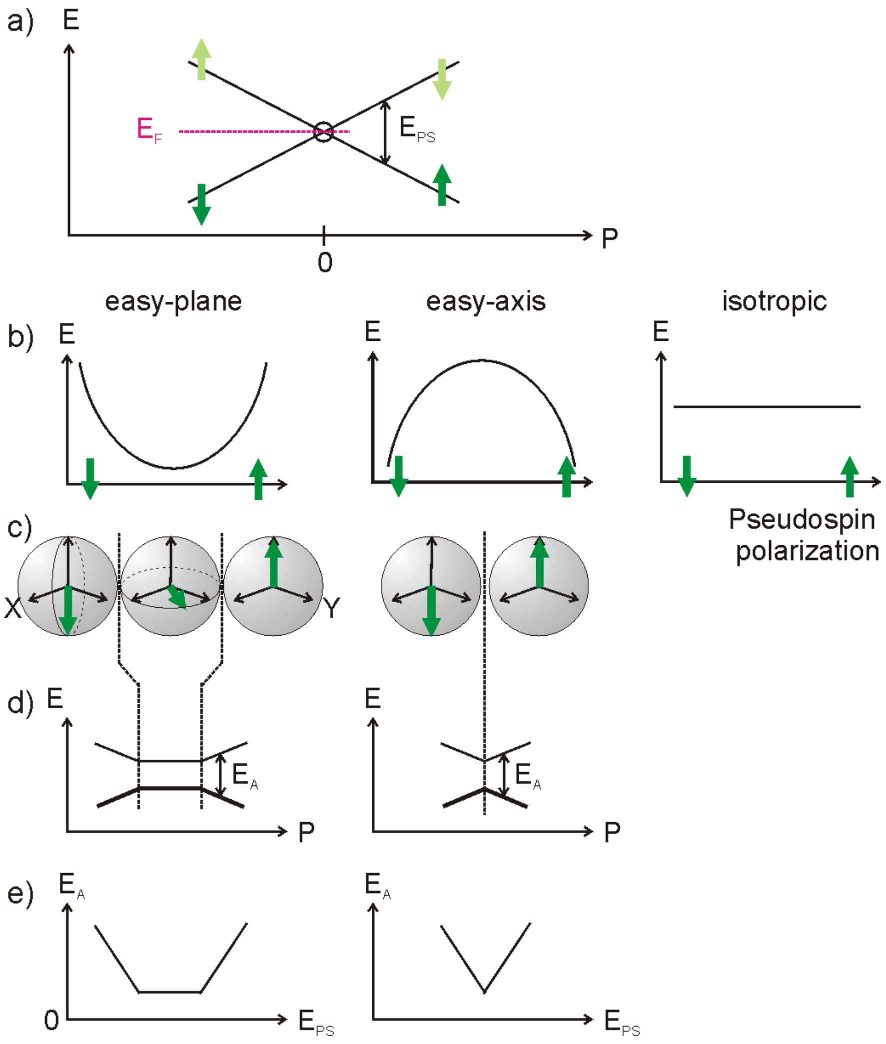

Figure 4.8: a) Two crossing LLs are identified by two different orientations of the pseudospin. Under quantum Hall conditions (the Fermi energy intersects the crossing point) the pseudospin is reoriented when the pseudospin field P is tuned through zero. The bulky arrows denote the pseudospin orientation; light green denotes unoccupied states. The reorientation process depends on the anisotropy energy of the different pseudospin orientations. Three different cases can be distinguished: easy-plane and easy-axis ansiotropy and the isotropic case. b) Schematic dependence of the anisotropy energy on a continuous reorientation of the pseudospin for different types of pseudospin anisotropy. c) Schematic representation of the pseudospin orientation. Easy-plane anisotropy prefers a coherent superposition of the two principal pseudospin orientations, which point perpendicular to the XY-plane, so that the resulting pseudospin is oriented within the XY-plane. Easy-axis anisotropy prefers an always pseudospin polarized state. d) Variation of the individual LL energies with pseudospin field when including the pseudospin anisotropy (exchange) energy. e) Expected variation of the activation energy with the pseudospin splitting E_{PS}.

axis. It is customary in the literature to speak of an Ising-ferromagnet according to the Ising model of a spin ferromagnet in two dimensions with the two possible spin orientations perpendicular to the plane. In the case of easy-axis anisotropy, the change of the pseudospin from one orientation to the other at exactly one point of the pseudospin field if a perfect homogeneous system is assumed. Therefore, a very narrow transition region, *i.e.* range of the pseudospin field or of any parameter that influences the pseudospin field, is expected in contrast to a system with easy-plane anisotropy. This is shown in Fig. 4.8. Due to pseudospin exchange interaction, the energy is independent of the pseudospin field P throughout the transition region in the case of easy-plane anisotropy [69].

When the system under investigation is not fully homogeneous, *i.e.* fluctuations of the potential landscape are present, the peudospin field will be a function of the spatial coordinate and the change of the pseudospin will happen for slightly different values of those external parameters, which allow to tune the pseudospin field. So the inhomogeneity of a real sample will affect the width of the transition region as experimentally accessible by tuning certain parameters. The inhomogeneity also supports the coexistence of areas, *i.e.* domains, within the sample with different pseudospin orientation throughout the transition region. However, the existence of potential fluctuations is not necessary for the formation of domains [70] if the temperature is finite but below a certain critical value. Specific to easy-axis anisotropy, hysteresis in the pseudospin orientation[5] upon a variation of the pseudospin field P is expected and its magnitude is governed by the strength of the anisotropy energy [68]. This energy can be thought of as originating from the pseudospin exchange interaction.

The type of anisotropy at a certain LL crossing point of a bilayer in the IQHE regime is according to Jungwirth and MacDonald [71] directly determined by the quantum numbers characterizing the two crossing LLs. The classification is displayed in Fig. 4.9. The connection to the single particle quantum numbers is possible, since they are equal for all particles of each LL involved in a crossing. However, as can be seen from the table, in one instance the type of anisotropy depends additionally on the imbalance σ and in another case on the layer separation d compared to a critical layer separation d^*, which itself is a function of the imbalance. The critical layer separation diverges when $\sigma = 0$. This classification scheme was only calculated in a single particle picture and is thus just true for the IQHE regime.

Each time when passing a crossing point in the regime of the IQHE at least two quantum numbers are changed: subband index (isospin) and orbital quantum number. The third quantum number, the spin, is altered only in the case of an even filling factor. This is a result of the linear dependencies on the magnetic field of the cyclotron energy $\hbar\omega_c$ and the Zeeman energy E_Z. For example, in the case of $\nu_\mathrm{tot} = 4$ there exist two equivalent crossing points as can be seen from Fig. 4.7 at which all three quantum numbers are changed. It is apparent from this figure that the crossing points can be passed by tuning the external magnetic field B while keeping the total filling factor ν_tot fixed, which requires to tune the total density n_tot equivalently. This kind of tuning of the pseudospin field is used to drive ferromagnetic phase transitions in Sec. 5.3 at

---

[5] The pseudospin orientation can be regarded as the pseudospin magnetization if compared to conventional ferromagnets.

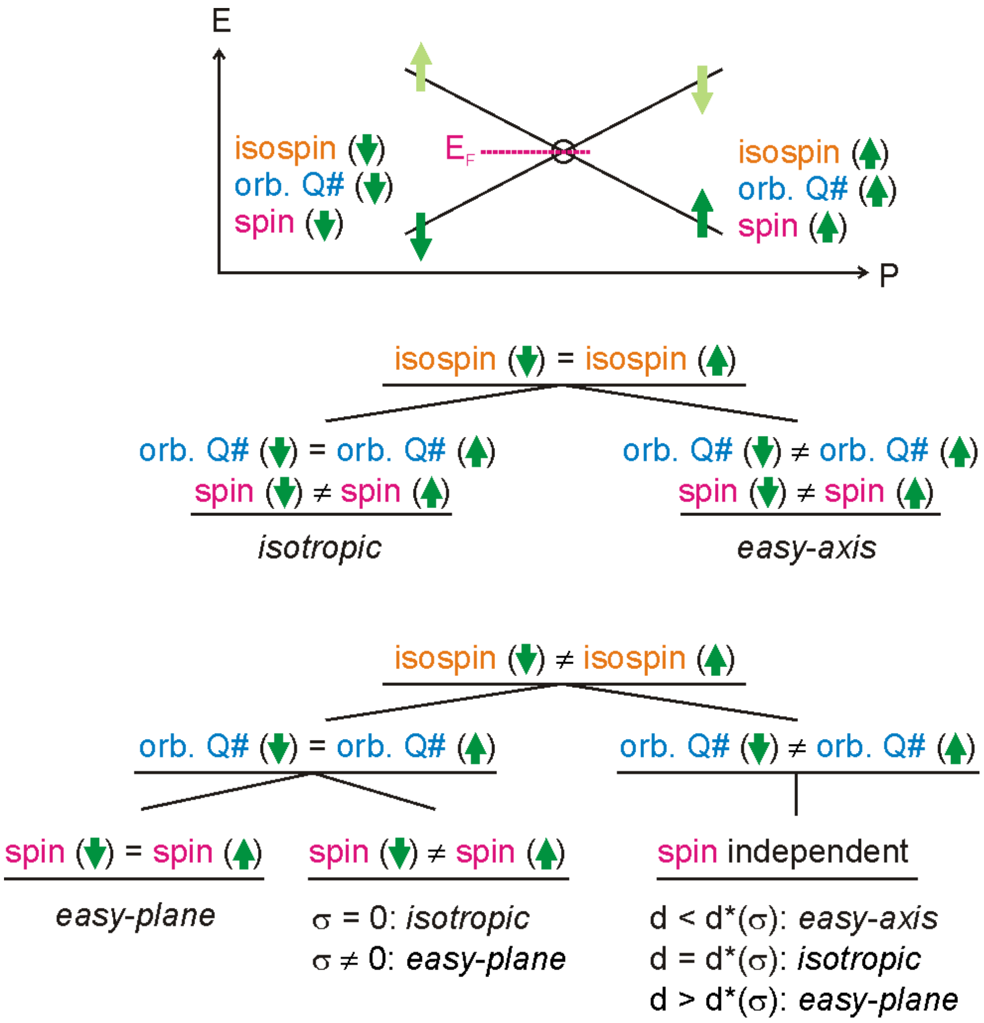

Figure 4.9: The pseudospin anisotropy classification of LL crossings in the IQHE regime after Jungwirth and MacDonald [71]. The bulky arrows denote the different pseudospin orientations. The relevant type of anisotropy is determined by the quantum numbers of the two coinciding LLs. In two cases the type of anisotropy depends additionally on the imbalance or the layer separation d compared to a critical layer separation d^*, which is a function of the imbalance.

several integer total filling factors. Although a change of B together with n_{tot} effectively tunes the pseudomagnetic field P, neither of the two parameters is identical to P since there are a number of parameters which can influence P.

The activation energy E_{A} can be defined as a certain multiple s of the pseudospin splitting energy

$$E_{\text{A}} = sE_{\text{PS}}. \tag{4.10}$$

A useful analysis is to plot the activation energy E_{A} as determined from experiment versus the theoretical gap (pseudospin splitting) E_{PS} and extract the slope

$$\left|\frac{\partial E_{\mathrm{A}}}{\partial E_{\mathrm{PS}}}\right| = s \tag{4.11}$$

which is a direct measure of s. This slope represents the number of flipped pseudospins per particle added to or subtracted from the system [72, 73]. Based on a single particle picture the slope should be unity far away from a crossing point, since a single pseudospin flip is the lowest lying excitation of the system. But as indicated in Fig. 4.8e, in the case of easy-plane anisotropy a vanishing slope throughout the transition region is expected, because the coherent superposition of the two different pseudospin orientations minimizes the total energy of the system and forbids for a certain range of the pseudospin field any pseudospin flip. In the case of easy-axis anisotropy, a slope much larger than one is possible. This is not a contradiction but denotes, that a single particle description fails here and the situation can only be understood as a many particle problem. The introduction of an additional particle with a reversed pseudospin compared to the surrounding pseudospin polarized collection of particles, *i.e.* the procedure when exciting the system, provokes a modification of the pseudospin orientation of several other particles. This happens, when the system prefers a gradual change of the pseudospin orientation of several spatially adjacent pseudospins instead of neighboring pseudospins with opposite orientations. Such formations are named Skyrmions (in the pseudospin space) [67, 72, 74–82]. They are not related to domains nor does their formation rely on disorder. Skyrmions carry charge and the Coulomb interaction prefers to smear out this charge over a large area. But this would produce a large number of misaligned pseudospins. The pseudospin exchange interaction however tends to minimize the number of misaligned spins. This competition determines the extent of a Skyrmion, *i.e.* the number of flipped pseudospins s when exciting the system.

At the coincidence near a certain total filling factor the pseudospin gap goes to zero. Therefore, a vanishing of the associated QHE or equivalently the appearance of a finite R_{xx} is expected. The course of finite R_{xx} values with P or with any tune parameter governing P (*e.g.* B) is labeled transition peak. The height of the transition peak will depend on the sample temperature and its width reflects the type of anisotropy. Referring to B as tune parameter, the plateau region has a finite width due to localized states, but the transition peak must not necessarily extend over the entire plateau width. Even the absence of a transition peak is possible, which suggests the formation of a sufficiently finite energy gap E_{A}; some experimentally observed transition peaks are listed in Tab. 6.1. In order to account for several of these experimental observations, the energy gap E_{A} between the two crossing LLs is indicated in the schematic sketch of Fig. 4.8d/e to remain finite throughout the transition region. The pseudospin exchange interaction is one possible reason [68]. Skyrmion theory suggests in the case of easy-axis anisotropy a reduction of the energy gap by 50% at the center of the transition region. A nevertheless observed transition peak is attributed to the formation of domains. Their walls, which can be regarded as one-dimensional conducting channels, contribute to the reduced gap but also lead to dissipation so that R_{xx} remains finite [70]. The size of domains and thus the length of domain walls is theoretically a function of the magnetic length so that towards higher magnetic fields domains become smaller and dilute, which lowers the dissipation and thus the height (even vanishing is possible) of the transition peak. Since it is argued that the formation of domains depends on the temperature, it is expected that a lower temperature has the same influence. Since in magneto-transport a ferromagnetic phase transition is identified by the break-down of the associated QHE, it is important to note these different influences on R_{xx} at a LL coincidence.

4.2.2 Extension to the FQHE regime

In stronger magnetic fields in the regime of the FQHE the orbital degree of freedom is identical for all electrons and is thus effectively frozen out. Within the framework of CFs the FQHE is also described as the successive depopulation of CF LLs (see Sec. 2.2). Instead of the very large electron cyclotron energy $\hbar\omega_c$ the CF cyclotron energy $\hbar\omega_{\mathrm{c,CF}}$ is important which is related to the many particle Coulomb correlation energy E_{C}. It scales with the square root of the magnetic field (or the density when the filling factor is fixed) and hence differently than the Zeeman energy. The CF LLs are characterized also by three quantum numbers: the subband index (isospin) governed by the subband splitting $\Delta\mathrm{BAB}$, the CF LL index or orbital degree of freedom associated with $\hbar\omega_{\mathrm{c,CF}}$, and the spin degree of freedom controlled by E_{Z}. The different functional dependencies on the magnetic field already produce CF LL crossings even for LLs with the same subband index but different spin polarization. Since with the introduction of CFs a single particle picture is reestablished and the quantum numbers of CF LLs are the same as for the IQHE regime, it might be justified to apply the anisotropy classification of Fig. 4.9 at least qualitative to the FQHE regime. This is discussed by means of some examples.

4.2.3 Methods of investigation

There exist several approaches to induce (CF) LL coincidences. In the case of a single 2DES all methods start from the fact, that the coincidence is due to a competition between the electron (IQHE) or CF (FQHE) cyclotron energy and the Zeeman energy. The Zeeman energy can be enhanced with an in-plane magnetic field or altered by influencing the effective g factor of electrons or CFs. This allows to increase and adjust the Zeeman energy to the electron or CF cyclotron energy (because the Zeeman splitting is typically much smaller than the electron or CF cyclotron energy) by tilting the magnetic field [83] thus forcing coincidences between (CF) LLs belonging to adjacent orbital quantum numbers. Alternatively, the effective g factor can be tuned through zero by applying a hydrostatic pressure [73, 84] thus forcing coincidences between (CF) LLs with the same orbital quantum number. Exclusively the condition of the FQHE regime [85] allows to force CF LL coincidences simply by sweeping the magnetic field at fixed filling factor since the CF cyclotron energy has a different functional dependence on the magnetic field than the Zeeman energy as already mentioned. Changing to a bilayer allows to induce LL crossings by sweeping the magnetic field at fixed filling factor even in the IQHE regime due to the appearance of two LL fan-charts which penetrate.

In the following chapters, ferromagnetic phase transitions are induced by sweeping the magnetic field (or density equivalently) in the IQHE as well as in the FQHE regime. For the FQHE regime two cases are discussed. One coincidence appears due to the crossing of CF LL which belong to the same CF LL fan-chart and the second is due to a mixing of the two CF LL fan-charts.

4.3 The one-component to two-component phase transition

4.3.1 Importance of the layer separation for the WQW

In the bilayer regime, *i.e.* for a density so high that a distinct minimum of the electron distribution is present in the center of the WQW (balanced case), two different contributions to the Coulomb correlation energy may be distinguished. The first is the intra-layer Coulomb correlation energy E_C within each layer and the second is the inter-layer Coulomb correlation energy E_d. They are characterized by the magnetic length scale l_B and the layer separation d, respectively:

$$E_\mathrm{C} = \frac{e^2}{4\pi\epsilon\epsilon_0 l_\mathrm{B}}, \tag{4.12}$$

and

$$E_\mathrm{d} = \frac{e^2}{4\pi\epsilon\epsilon_0 d}. \tag{4.13}$$

The ratio of these two energy scales

$$\frac{E_\mathrm{C}}{E_\mathrm{d}} = \frac{d}{l_\mathrm{B}}, \tag{4.14}$$

is of particular importance for correlation effects within the bilayer. As can be seen from Fig. 4.4, the distance d between the two electron layers confined to a WQW increases towards higher densities. Due to this variability of d the ratio $E_\mathrm{C}/E_\mathrm{d}$ is a function of the total density as well as the magnetic field via l_B.

Above a certain layer separation, *i.e.* a certain critical total density, the inter-layer Coulomb correlation energy will loose against the intra-layer Coulomb correlation energy and a changeover from a strongly correlated to a weakly correlated bilayer occurs. It is accompanied by a loss of coherence between the two charge layers, although a non vanishing overlap between the electron layers still exists. The subband splitting $\Delta\mathrm{SAS}$ characterizes this overlap and is non-zero but represents now the smallest energy scale. The associated phase is labeled the two-component regime (2C) while below the critical total density the electron system is in the one-component (1C) regime. In the latter case, the "bilayer" can be regarded as a single 2DES even though a dip in the electron distribution is present. Correlation effects occur due to the Coulomb interaction among all electrons in the WQW including those located in different layers. The rather broad spatial extent of the quasi 2DES in the z-direction becomes evident in the reduced activation energies of all FQHEs in comparison to an ordinary 2DES formed at an SHI [31], because the activation energy is a function of the finite thickness [86].

Due to the dominating intra-layer Coulomb correlation energy in the 2C regime, correlation effects like FQHEs no longer occur within the bilayer as a whole but in each layer individually. For the balanced case this implies, that any FQHE with odd nominator of the total filling factor vanishes beyond the 1C-2C phase transition. Those with even nominator change their nature (topological order). Due to the important issue layer separation, the critical total density is quite similar for all FQHEs.[6] The differences are mainly associated with the dependence of l_B on the magnetic field B, which is different for every filling factor at a given density.

Once in the 2C regime, it is appropriate and convenient to refer to the individual layer filling factors ν_f and ν_b of the front and back layer. As already discussed, FQH liquids form in each layer separately and may even have different filling factors when the electron distribution is imbalanced. The relation to the imbalance σ is given by

$$\sigma = \frac{n_\mathrm{f} - n_\mathrm{b}}{n_\mathrm{tot}} = \frac{\nu_\mathrm{f} - \nu_\mathrm{b}}{\nu_\mathrm{tot}}. \tag{4.15}$$

As a function of imbalance, one or even both layers can reach a fractional filling factor leading to a correlated state. The system however consists of two different phases. A correlated state in one of the layers will manifest in the transport properties since the vanishing longitudinal

---

[6] It has been shown, that an increasing electron density in a WQW (as well as in a DQW) leads to missing IQHEs [87, 88] with odd filling factor. So both FQH states and IQH states experience the 1C-2C phase transition.

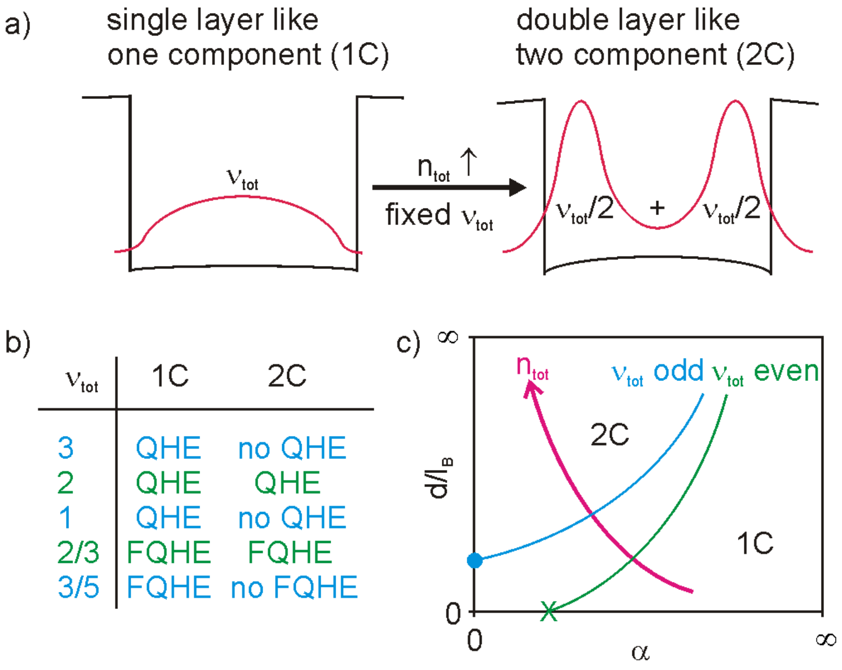

ν_tot	1C	2C
3	QHE	no QHE
2	QHE	QHE
1	QHE	no QHE
2/3	FQHE	FQHE
3/5	FQHE	no FQHE

Figure 4.10: a) Density driven layer separation and 1C to 2C phase transition in a WQW. b) All filling factors are affected by this phase transition but differently. Those with odd numerator loose the QHE and those with even numerator change their nature of the ground state. c) Phase diagram for (F)QHEs in a bilayer in the tunneling strength-distance-plane after [87] and [65]. With increasing total density n_tot the phase boundary from the 1C to the 2C phase is crossed.

resistance of one layer partly short-circuits the other layer so that a minimum in R_{xx} will show up. If both layers approach a fractional filling factor (compound quantum Hall state), the effect is more pronounced. Large imbalance values generally destroy the 2C regime and reestablish the 1C regime. The threshold value increases towards higher total density.

4.3.2 Importance of the magnetic length for the DQW

At first glance, it seems impossible to force the 1C-2C phase transition just by varying the total density in a DQW with an almost fixed layer separation. However, since $E_{\mathrm{C}}/E_{\mathrm{d}}$ contains the magnetic length l_{B} a change of the total density at fixed total filling factor still leads to a change of this ratio. Hence, a 1C-2C phase transition can also be found in a DQW even though this transition is more difficult to realize in experiment for specific filling factors. The most striking data have been reported by the group of J. Eisenstein at Caltech [1, 89–91] using a DQW with a 9.9 nm thick barrier separating the two 18 nm wide QWs. This thickness of the barrier ensures that the tunneling current between both layers is of the order of pA and hence both layers can be separately contacted. At a high total density (*e.g.* 1×10^{15} m^{-2}), no QHE at total filling factor one is present indicating the independence of the electron layers. Because with $\nu = 1/2$ for each layer individually no QHE is expected. But at a sufficiently low total density (< 0.4×10^{15} m^{-2}) the average intra-layer distance of the electrons becomes larger than the inter-layer distance d. As a consequence the 1C regime is entered and the QHE at $\nu_{\mathrm{tot}} = 1$ appears. Although the layers are physically separated, the coherence between them leads to the single layer like behavior. This coherent connection of the electrons across an opaque barrier is similar to loss-free tunneling of superconducting current through a non-superconducting barrier. This equivalence is justified since both phenomena can theoretically be treated very similar, as shown by S. Girvin [92].[7]

Note that for vanishing tunneling, *i.e.* $\alpha = \Delta\mathrm{SAS}/E_{\mathrm{C}} \rightarrow 0$, the critical layer separation below which coherence appears remains non-zero [87, 94] (the dot in the phase diagram of Fig. 4.10c), since the long range Coulomb interaction is responsible for coherence, not tunneling. This argument however is just valid for odd filling factors or fractional filling factors with odd nominator. For even filling factors and fractional filling factors with even nominator, which can form a correlated state even for $d \rightarrow \infty$ due to intra-layer correlation in each layer separately, the situation is the other way round. Even if the layer separation tends to zero, no coherence between the layers exists unless finite tunneling is allowed (the X in the phase diagram of Fig. 4.10c). The reason is that a higher correlation with a lower filling factor in each layer separately is accompanied by a larger energy gap (in the IQHE regime), wherefore the 2C phase is preferred to the 1C phase. However, 2C states are destroyed with an increasing tunneling.

---

[7] Analogies to even other physical phenomena are discussed, as summarized in [93].

Chapter 5

Characterization of a bilayer in a magnetic field

In this chapter the different physical phenomena observed in transport of the previously described bilayer realized in a 77 nm wide WQW are discussed. Almost everything related to the total filling factor $\nu_{\mathrm{tot}} = 2/3$ is excluded here and is separately discussed in the next chapters.

5.1 Features at zero gate bias

Figure 5.1 displays a measurement of the longitudinal resistance R_{xx} in dependence of the magnetic field at temperatures of 1.5 K and 250 mK, using the WQW structure with zero bias applied to both gates. Details of the measurement technique are given in Appendix A.2. The mobility is 530 m^2/Vs at a density of 2.15$\times 10^{15}$ m^{-2}. The measurement reflects the total density n_{tot}, since the ohmic contacts of the WQW contact both layers. The discrepancy of the R_{xx} trace with SdH oscillations in a regular single 2DES is due to the occupation of two subbands with different densities n_{B} and n_{AB}. The different subband densities lead to beating SdH frequencies. In particular, due to total filling factor $\nu_{\mathrm{tot}} = 4$ at 2.25 T a minimum value of R_{xx} is expected. Instead, a maximum R_{xx} is apparent. In Sec. 5.3 it is shown that the appearance of this peak is due to a crossing of LLs, as already theoretically described in Sec. 4.2. The crossing happens by chance at this density and imbalance. The exact imbalance is not known, because the WQW is not necessarily balanced with zero bias applied to both gates.

In order to draw a definite statement about any level crossing or more generally, to be able to adjust the bilayer specifically and reliably, the as grown electron distribution and the way it changes with the two gate voltages needs to be known. How these fundamental parameters can be determined is discussed in the next section. The parameters used for the simulation of the conduction band profile given in Fig. 3.2 are adjusted that way so that the calculated electron density and its distribution agree with the experimental results.

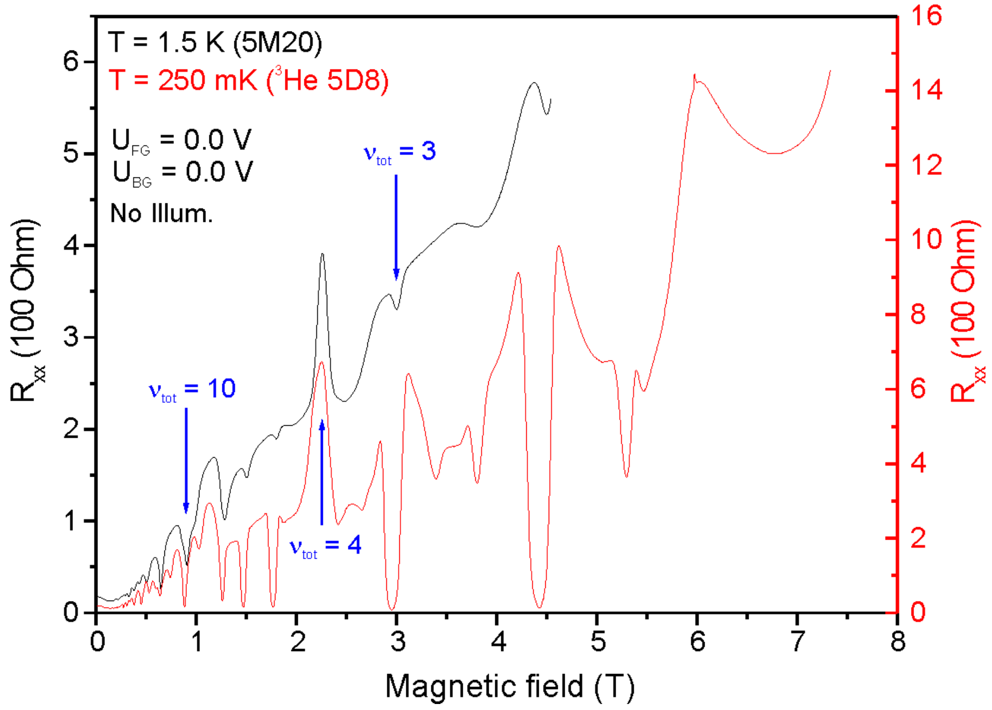

Figure 5.1: Magneto-transport measurement of a processed WQW sample at temperatures of 1.5 K and 250 mK with both gates held at zero bias. Most surprisingly, a peak at total filling factor $\nu_{\mathrm{tot}} = 4$ is present instead of a minimum indicating a LL coincidence, which will be discussed in this chapter. An equivalent reason is responsible for the absence of the QHE at $\nu_{\mathrm{tot}} = 8$, which is explained in the footnote on page 75.

5.2 Experimental determination of basic bilayer parameters

The best characterization of the bilayer confined in the WQW can be achieved at a sample temperature of 250 mK. First, it has to be established how a voltage applied to one of the gates changes the electron density of the layer next to this gate, *i.e.* the density change per gate voltage Δn_{FG} and Δn_{BG} for the front and back gate. This is achieved by measurements of R_{xx} with magnetic field typically in the range from 0 T to 2.5 T and a stepwise depletion of the electron density in one of the layers for each sweep. An evaluation of the data with respect to changes of the magnetic field along lines of constant total filling factor yields the desired parameters. They can be compared with the theoretical values

$$\Delta n_{\mathrm{FG,BG}} = \frac{\epsilon\epsilon_0}{e d_{\mathrm{FG,BG}}}, \tag{5.1}$$

according to the charging properties of a capacitor. A capacitor is formed between the charge layer and the gate. d_{FG} (d_{BG}) is the distances between the front (back) gate and the peak of the nearest electron layer. These distances are not only given by the nominal distances between the gate and the nearest WQW interface, but are also increased since the charge layers are slightly set back from the interfaces. This set back is approximately 12 nm. The set back is particularly important for the front gate, because it represents about 2% compared to the nominal distance of the front gate from the upper interface of the WQW. Due to the much greater distance of the back gate from the lower interface of the WQW, Δn_{BG} is approximately one order of magnitude smaller than Δn_{FG}. With the known density change per gate voltage, magnetic field sweeps can be carried out with an increasing density in one layer and an equally decreasing density in the other layer. This procedure corresponds to a stepwise variation of the imbalance σ.[1] Since the total density remains now constant, the R_{xx}-pattern should display QHEs at always the same magnetic field. If the filling factors do not remain at a certain magnetic field, but drift with varying imbalance, the ratio between the two parameters Δn_{FG} and Δn_{BG} has to be refined. Typical values for the WQW are $\Delta n_{\mathrm{FG}} = 3.75 \times 10^{15}$ m^{-2}/V and $\Delta n_{\mathrm{FG}}/\Delta n_{\mathrm{BG}} = 11.37$.

Traces of R_{xx} recorded for constant total density but different imbalance look like mirror images of each other with respect to a certain pair of front and back gate voltages. This pair of gate voltages defines the balanced case for this particular total density. Equal traces for the same absolute imbalance values, independent of their actual sign, are expected, because imbalancing the WQW is in principle a symmetric problem, apart from the fact that the lower inverted interface usually has a lower mobility. This typical property, however, could not be confirmed here. In fact, the lower interface seems to have a slightly higher mobility. If a pair of gate voltages U_{FG} and U_{BG} giving rise to the balanced case is determined at a certain total density $n_{\mathrm{tot}} = 2n_{\mathrm{f}} = 2n_{\mathrm{b}}$, where n_{f} and n_{b} are the front and back layer densities, respectively, the as-grown densities $n_{\mathrm{f},0}$ and $n_{\mathrm{b},0}$ of each layer can be calculated using

$$\begin{aligned} n_{\mathrm{f}} &= n_{\mathrm{f},0} + \Delta n_{\mathrm{FG}} U_{\mathrm{FG}}, \\ n_{\mathrm{b}} &= n_{\mathrm{b},0} + \Delta n_{\mathrm{BG}} U_{\mathrm{BG}}, \end{aligned} \tag{5.2}$$

and can be determined to an accuracy of about 1%. It is found that $n_{\mathrm{f},0} = 0.91 \times 10^{15}$ m^{-2} and $n_{\mathrm{b},0} = 1.26 \times 10^{15}$ m^{-2}. However, it should be noted that because of the density dependent layer separation d (see Fig. 4.4), which is in fact small but still about 4 nm in the total density range from 1.0$\times10^{15}$ m^{-2} to 2.0$\times10^{15}$ m^{-2}, the parameters Δn_{FG} and Δn_{BG} are a function of the density (and of the imbalance as well). While the variation of Δn_{BG} is absolutely negligible, because it is of the order of one thousand, Δn_{FG} changes by about 1% within the mentioned density range and even more towards lower total densities. This influence has to be considered. If n_{f} and n_{b} are known as a function of U_{FG} and U_{BG}, the imbalance σ can then be calculated and the R_{xx} traces can be plotted versus σ, as is done in the right top panel of Fig. 5.2. The electron density and its distribution in the WQW are then fully under control.

The origin of the pattern of vanishing and reappearing QHEs in Fig. 5.2 is due to crossings of LLs. They occur because of two superimposed SdH oscillations, each reflecting one LL fan-chart associated either with the bonding or anti-bonding subband energy. Since the decisive

---

[1] Initially, for this procedure sufficiently negative gate voltages should be used so that no positive gate voltage is ever applied which would pull down the doped region below the Fermi energy. This pull down already happens at voltages of about +50 mV and +600 mV for the front and back gate, respectively, and is indicated *e.g.* by suddenly negative values of R_{xx} throughout the plateau regions. Furthermore, a positive back gate bias can lead to a break through of the back gate, as discussed in Sec. 3.3.

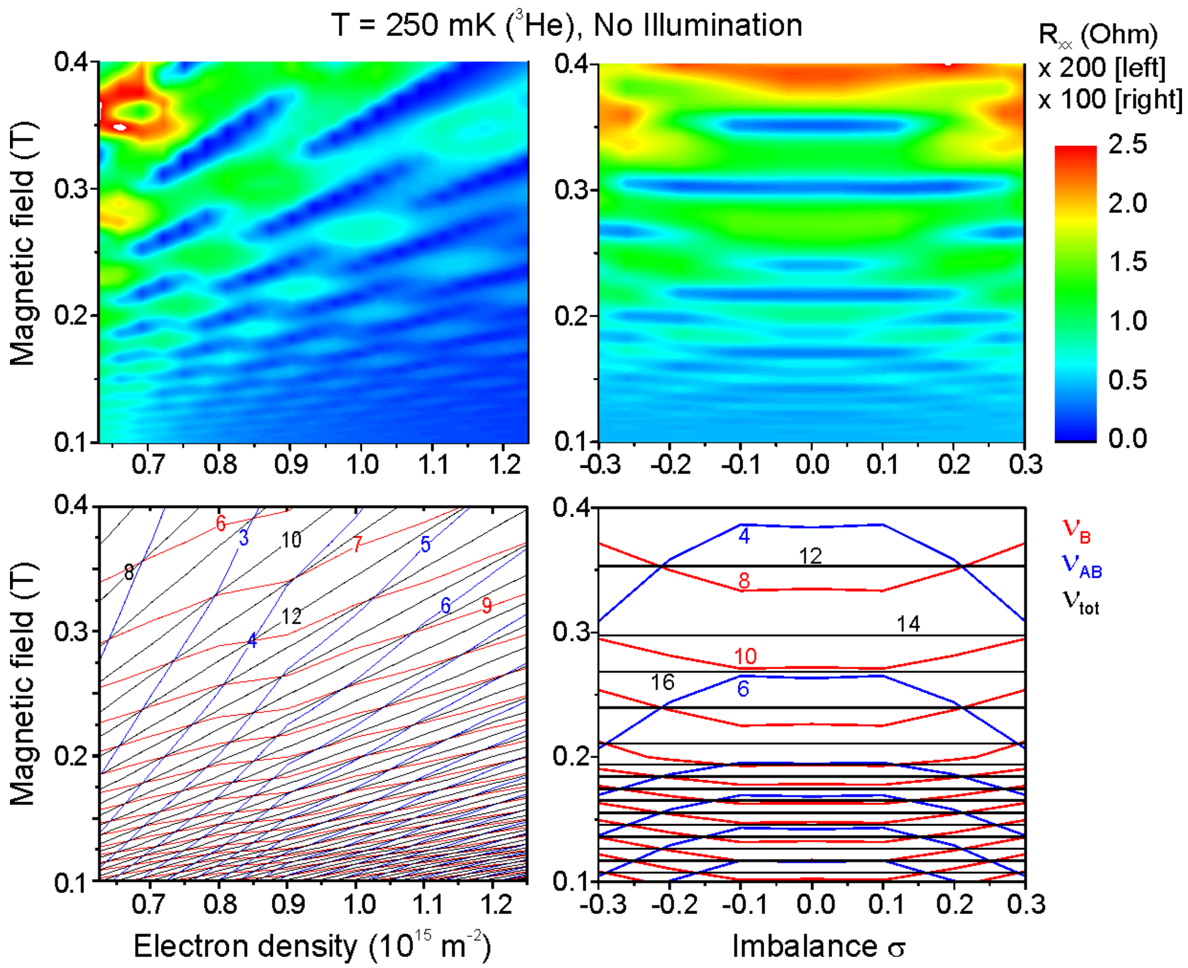

Figure 5.2: Magneto-transport measurement of the WQW structure at low magnetic fields, either with variable balanced total density (upper left panel) or variable imbalance but constant total density (upper right panel). Both R_{xx}-patterns are compared to the theoretically expected variation of the lines of constant filling factors of the bonding (ν_{B}) and anti-bonding (ν_{AB}) subband and their sum ν_{tot}. As can be seen, the points or ranges of vanishing QHEs are due to LL crossings.

subband densities n_{B} and n_{AB} are different, the SdH oscillations have different periodicities if plotted versus the inverse magnetic field. The individual densities can be extracted from a Fourier analysis of R_{xx} traces at low magnetic fields.[2] Typically the magnetic field range from 0.05 T to 0.5 T is used. Sweeps and the results of the Fourier analyses are displayed in Fig. 5.3. The two maxima of the Fourier analyses correspond to the two different subband densities n_{B} and n_{AB}. The subband densities are least different for the balanced case according to the theory shown in Fig. 4.1d. These densities allow to quantify the subband splitting $\Delta\mathrm{SAS}$, since it is a function of the occupation difference $n_{\mathrm{B}} - n_{\mathrm{AB}}$ (see Eq. 4.2). A subband splitting of 12.4 K is

---

[2] The relation between the inverse magnetic field periodicity of SdH oscillations and the subband density is $\Delta(1/B) = 2e/hn$ [42].

found at a total density of 1.4×10^{15} m^{-2}. Compared to the calculated value (see Fig. 4.4) the theory underestimates the subband splitting by about 30%.

Starting with a pair of gate voltages, which ensure a balanced electron distribution, further sweeps of the magnetic field can be carried out. The same sign of the gate voltage change is used at both gates, so that $\sigma = 0$ is maintained and only the total density varied. When following the lines of constant total filling factor total density points (or ranges) can be identified at which the QHE vanishes (see the top left panel of Fig. 5.2). This feature is again due to beating SdH frequencies. The points of vanishing QHE can be described quantitatively with LL crossings of the two LL fan-charts. The subband filling factors[3] ν_{B} and ν_{AB} involved can be identified by comparison with calculations. These calculations are possible if the dependence of the decisive

---

[3] They should not be confused with the individual layer filling factors, which are only relevant at higher total density when the 2C regime is entered.

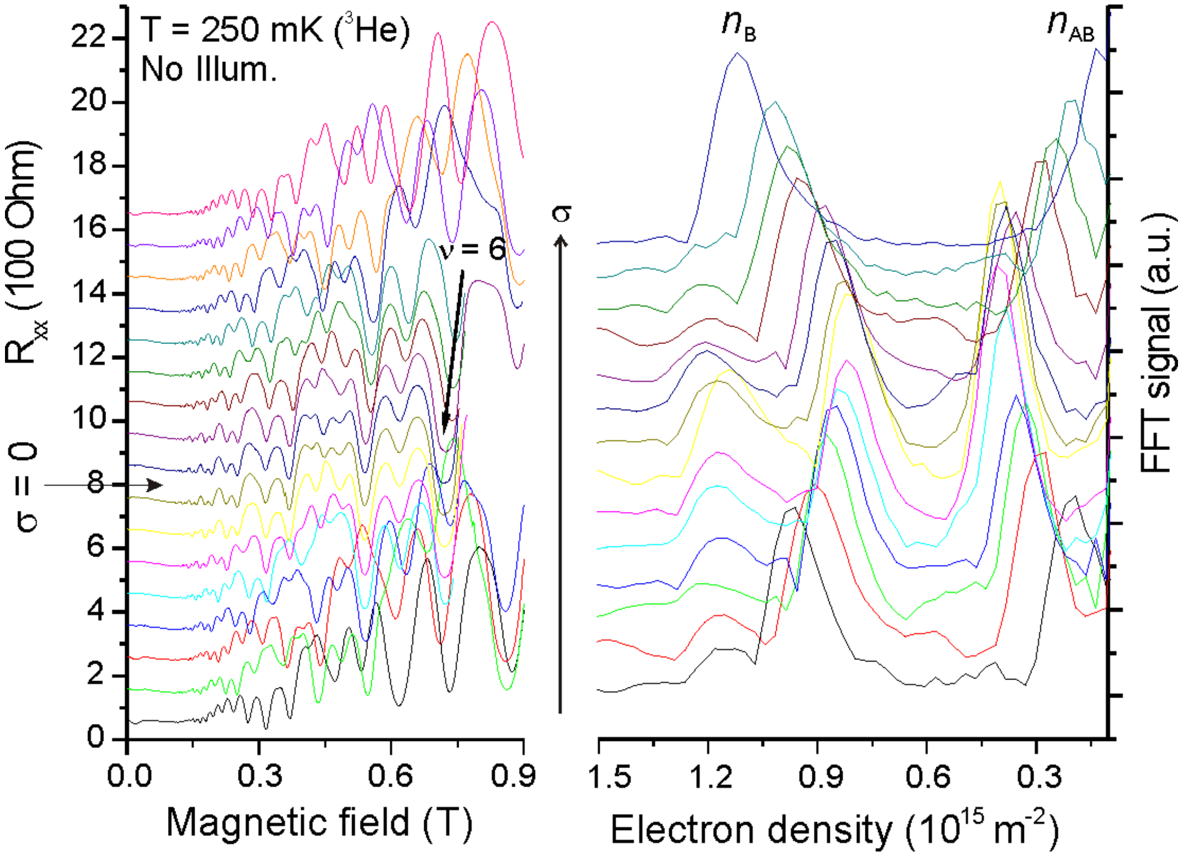

Figure 5.3: SdH oscillations over a wide imbalance range but constant total density (left panel). Each trace is offset vertically by 100 Ω for clarity. As can be seen, the traces are mirror images with respect to a certain trace indicating the balanced case ($\sigma = 0$). The Fourier analyses of the SdH oscillations (right panel) using the magnetic field range from 0.05 T to 0.5 T are characterized by two peaks which correspond to the two different subband densities n_{B} and n_{AB}, which are least different at $\sigma = 0$ as expected.

electron densities n_{B} and n_{AB} on the total density and/or the imbalance is known. When the layer separation is large and any QHE appears in each layer separately (2C regime), the measurements of R_{xx} in the total density-imbalance-plane can be plotted in a two-dimensional color plot, whose axes represent the individual front and back layer filling factors (see Fig. 5.4).

As previously mentioned in Sec. 3.1, the density and the distribution are found to be almost equal for different cool downs. Thus, the necessary pair of gate voltages to tune the WQW structure to a certain regime varies only by a few mV. This is the advantage of using volume-doping, which avoids the necessity of illuminating the sample. In contrast, the illumination always leads to slightly different densities for each cool down.

5.3 LL crossings at the total filling factors 3,4, and 5

As noted in Sec. 5.1, an LL crossing at filling $\nu_{\mathrm{tot}} = 4$ is present without bias on the gates. In the following are discussed the theory of this and other LL crossings and the results of experiments carried out at a sample temperature of 250 mK.

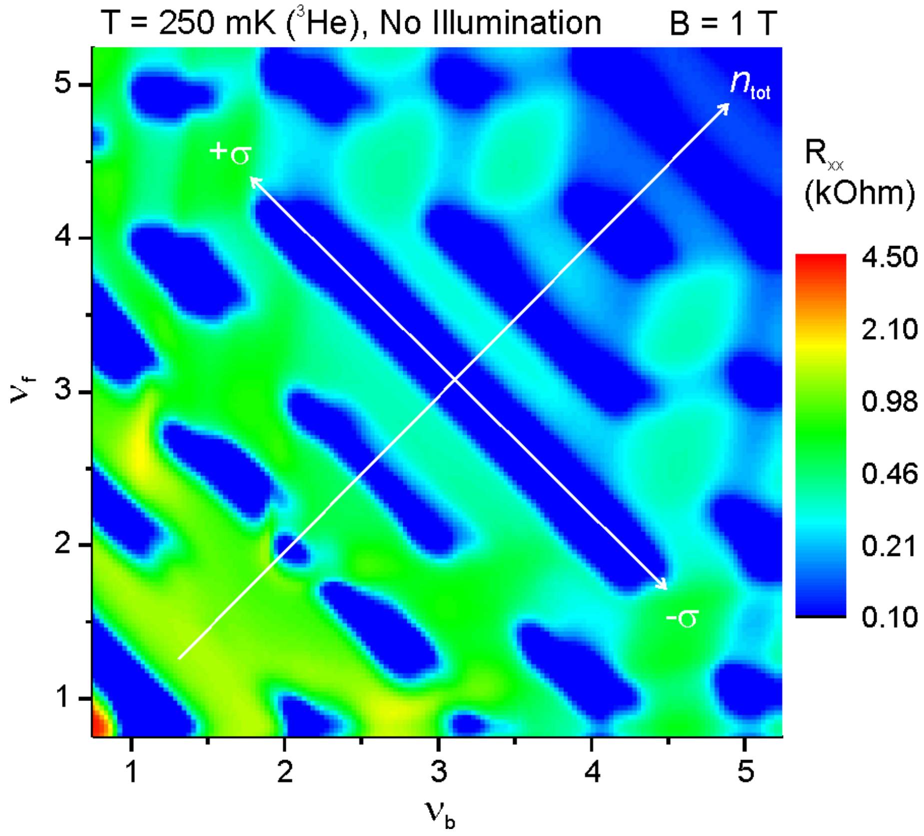

Figure 5.4: Presentation of scans of the total density and the imbalance in dependence of the individual front and back layer filling factors ν_{f} and (ν_{b}). The lines indicate increasing total density and varying imbalance. The very different stabilities of QH states of different total filling factors (sum of ν_{f} and ν_{b}) with respect to a slight imbalance is discussed in [65].

5.3.1 Theoretical discussion

Figure 5.5 is a magnification of the intersecting LL fan-charts of Fig. 4.7. Altogether four crossing points can be identified; they correspond to the total filling factors $\nu_{\mathrm{tot}} = 3$, two times $\nu_{\mathrm{tot}} = 4$, and $\nu_{\mathrm{tot}} = 5$. At the four different crossing points the LLs with the following quantum numbers are involved:

ν_{tot}	quantum numbers of coinciding LLs
3	(B,1,↑)(AB,0,↑)
4	(B,1,↓)(AB,0,↑) or (B,1,↑)(AB,0,↓)
5	(B,1,↓)(AB,0,↓)

For each total filling factor the first set of three quantum numbers (pseudospin) represents the ground state at a magnetic field or total density lower than the critical one. The last set of three quantum numbers represents the ground state towards higher magnetic field or total density. The pass of one of the coincidence points changes the ground state, because quantum numbers are changed, *i.e.* the pseudospin is reoriented. Here, because of the IQHE regime, the subband index (isospin) and the orbital quantum number always change. Whether the spin orientation changes depends additionally on the total filling factor. For $\nu_{\mathrm{tot}} = 4$, the spin orientation changes, while for $\nu_{\mathrm{tot}} = 3$ and $\nu_{\mathrm{tot}} = 5$, it does not. According to the pseudospin anisotropy classification by Jungwirth and MacDonald [71] (see Fig. 4.9), all three cases of LL crossings can exhibit either easy-axis or easy-plane anisotropy, or be isotropic, depending on the layer separation d. For a smaller layer separation than a certain critical distance d^*, easy-axis anisotropy is present, while a larger separation causes easy-plane anisotropy. When the layer separation coincides with the critical distance the system becomes isotropic. The critical distance is a function of the subband splitting $\Delta\mathrm{SAS}$ and the inter-layer bias, which is directly related to the imbalance σ of the bilayer (see Fig. 4.1c). In the case of the spin change as it happens at $\nu_{\mathrm{tot}} = 4$, the critical layer separation diverges towards $\sigma = 0$. It follows that easy-plane anisotropy is impossible when the bilayer is balanced and the spin is changed [71]. Consequently, for $\nu_{\mathrm{tot}} = 4$ easy-axis anisotropy applies at $\sigma = 0$, while all types of anisotropy are still possible at $\nu_{\mathrm{tot}} = 3$ and $\nu_{\mathrm{tot}} = 5$ independent of σ.

5.3.2 Experimental result

Figure 5.6 displays a measurement of R_{xx} of the balanced ($\sigma = 0$) WQW structure covering a larger range of the total density and the magnetic field. LL coincidences can be identified by a disruption of the different lines of constant total filling factor due to a disappearance of the QHE. The coincidences of interest are marked with circles. The total electron density or the magnetic field ranges (transition regions) of the coincidences involving $\nu_{\mathrm{tot}} = 3$ and $\nu_{\mathrm{tot}} = 5$ is much more extended than those of both coincidences associated with $\nu_{\mathrm{tot}} = 4$. According to theory, different developments of the pseudospin orientation throughout the transition region due to different types of anisotropy lead to differently large ranges of the pseudospin field, *i.e.* differently wide transition regions (see Fig. 4.8). Therefore, it can be concluded, that the type

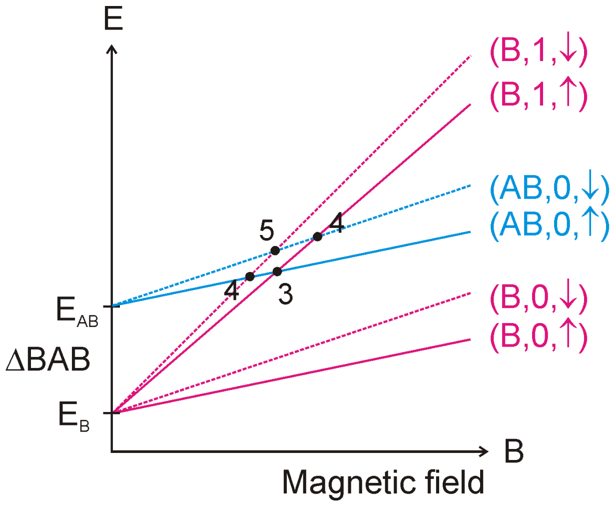

Figure 5.5: Variation of the energies of the lowest LLs with magnetic field. Color and style of the different LLs is adapted to the different quantum numbers, which characterize each LL. Each crossing point is denoted by the total filling factor concerned.

of anisotropy present at $\nu_{\rm tot} = 3$ and $\nu_{\rm tot} = 5$ is most probably different to that at $\nu_{\rm tot} = 4$, and hence of the easy-plane type.

As schematically shown in Fig. 5.7, an intuitive explanation for the different types of anisotropy arises from the fact that the two crossing points at total filling factor $\nu_{\rm tot} = 4$ differ from those at $\nu_{\rm tot} = 3$ and $\nu_{\rm tot} = 5$ by an additional flip of the spin. Therefore, the exchange interaction plays an important role at $\nu_{\rm tot} = 4$ favoring a fully spin and thus pseudospin polarized ground state throughout the transition region. Consequently, the pseudospin reorientation is preferred to happen suddenly and for the total system at once, which is the source of easy-axis anisotropy. This results in a narrow transition region. At $\nu_{\rm tot} = 3$ and $\nu_{\rm tot} = 5$, however, the spin is maintained, so that exchange interaction is in fact present, but does not govern the pseudospin reorientation. Instead, both pseudospin orientations are equally preferred and a coherent superposition of both is established, leading to a broad transition region. A change of the subband index (isospin) as present at all four crossing points requires a spatial redistribution of the charges within the WQW. A switch-over from a bonding to an anti-bonding level, *i.e.* change of the isospin, involves a transfer of charges from the center of the WQW towards the peaks of the charge layers, due to the different wave functions associated with the isospin. This redistribution is possible without any change of the associated isospin field, *i.e.* the imbalance, since the redistribution happens symmetrically with respect to the center of the WQW, *i.e.* σ is conserved.

In addition to these coincidences, there are many more crossings of LLs and hence ferromagnetic phase transitions as is immediately apparent from the resistance pattern in Fig. 5.2. This holds also in the regime of the FQHE, and two examples are discussed in the following chapters.

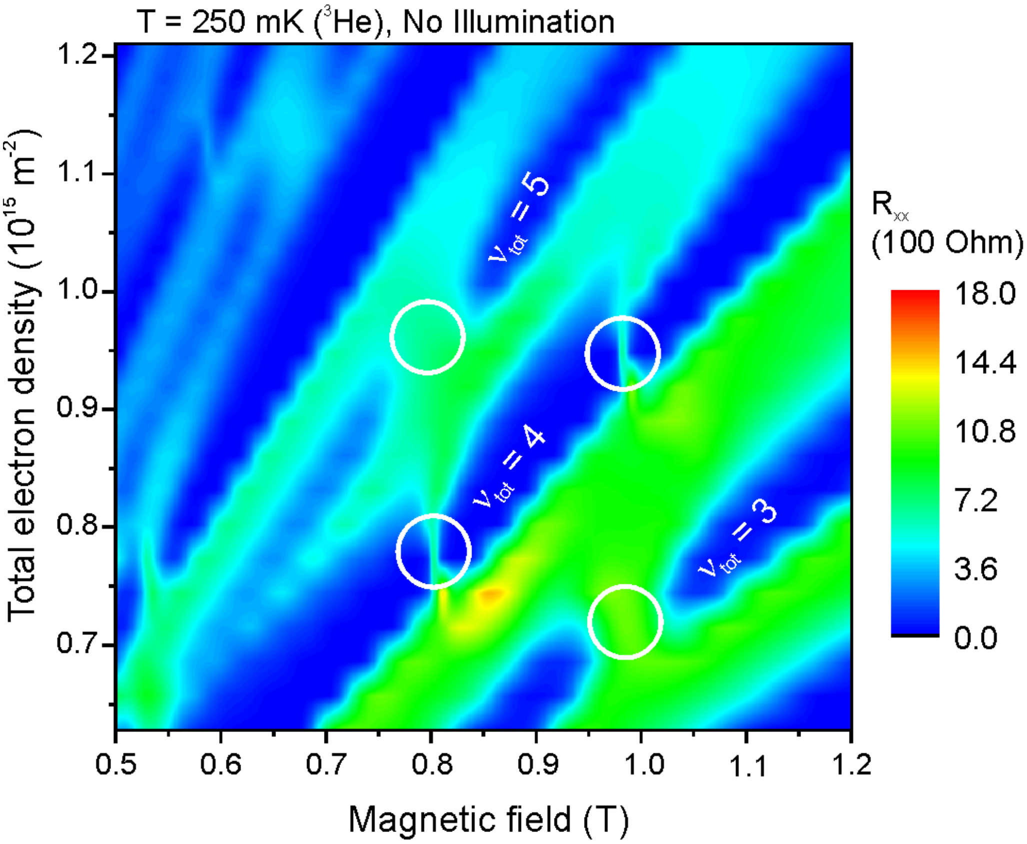

Figure 5.6: Magneto-transport measurements with variable but balanced total density. Relevant lines of constant total filling factor are denoted. The four LL crossing "points" (transition regions) of Fig. 5.5 are indicated by circles. The transition regions involving $\nu_{\rm tot} = 3$ and $\nu_{\rm tot} = 5$ are much broader than those of $\nu_{\rm tot} = 4$. This is discussed in the text.

5.3.3 Impact of an imbalance

With an increasing imbalance σ, the subband splitting ΔBAB is enhanced according to Fig. 4.5 with a quadratic dependence on σ. Therefore, a relocation of the crossing points to higher total densities also with a quadratic dependence on σ is expected, because the competing energies associated with the other quantum numbers are in first order not affected by the tilt of the WQW potential. Experimentally, the total density is increased stepwise keeping the total filling factor fixed by adjusting the magnetic field accordingly, and for every step the imbalance is swept. The experiment covering both coincidences at $\nu_{\rm tot} = 4$ is shown in Fig. 5.8. Data for $\nu_{\rm tot} = 3$ and $\nu_{\rm tot} = 5$ are shown in Fig. 5.9. The quadratic increase of the critical total density with imbalance can be seen in all four cases. Also apparent are the very narrow transition regions in both cases of $\nu_{\rm tot} = 4$ which, however, broaden with imbalance. As mentioned above, the pseudospin classification by Jungwirth and MacDonald [71] results in three different types of anisotropy, depending on the layer separation d with respect to a critical value d^*. Since this critical distance is a function of the subband splitting ΔSAS and any inter-layer bias, which is related to the imbalance σ (theoretically one can assume that ΔSAS is independent of σ),

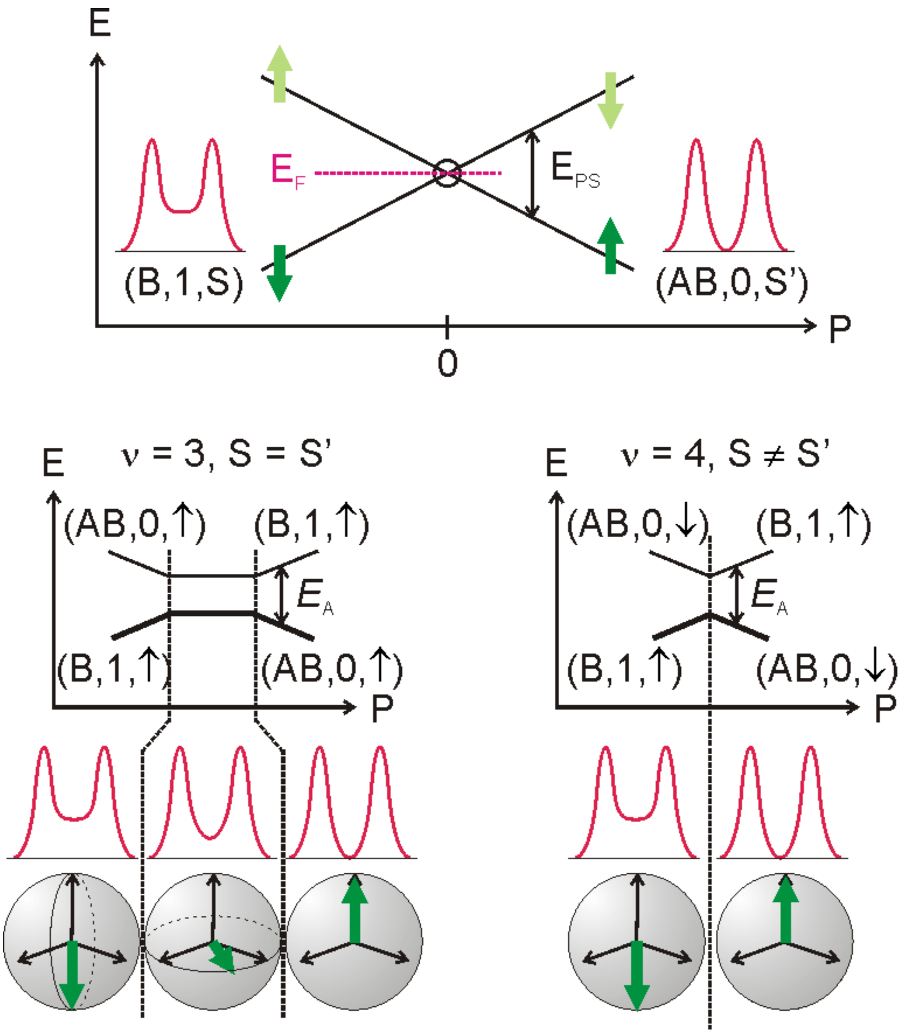

Figure 5.7: Upper panel: Schematic variation of the energy of two crossing LLs with the pseudospin field P (see also Fig. 4.8). The wave function and the quantum numbers of the occupied LL are indicated. S and S' denote the spin. Lower panels: Application of the pseudospin anisotropy to the LL crossings at total filling factor $\nu_{\rm tot} = 3$ (equivalent to $\nu_{\rm tot} = 5$) and $\nu_{\rm tot} = 4$ (at higher total density). When the spin is conserved ($S = S'$), a broad transition region is found, due to a coherent superposition of the two pseudospin orientations (easy-plane anisotropy). A change of the spin $S \neq S'$ causes a narrow transition region, due to exchange interaction, which favors a pseudospin polarized ground state (easy-axis anisotropy).

the type of anisotropy can be tuned with increasing imbalance from easy-axis to easy-plane crossing the isotropic line [71]. Accepting a broad transition region as an indication of easy-plane anisotropy in contrast to a narrow one indicating easy-axis anisotropy, as discussed above by comparing $\nu_{\rm tot} = 3$ and $\nu_{\rm tot} = 5$ to $\nu_{\rm tot} = 4$, the broadening of the transition regions in Fig. 5.8 with increasing imbalance might be an indication of a changeover from easy-axis to easy-plane anisotropy. The broadening of the transition region at lower total density is found to be much less with imbalance as is the case for the second transition region at higher total density. This difference is consistent with the theoretical prediction [71] that at smaller layer separation, which applies in the case of a WQW at smaller total density, a larger imbalance is necessary to achieve a changeover from easy-axis to easy-plane anisotropy. The equivalently much less pronounced increase of the critical total density with imbalance is again due to the smaller total density, which causes a larger subband splitting. The increase of $\Delta\mathrm{BAB}$ is less on a relative basis at small total densities, due to a smaller tilt of the WQW potential, *i.e.* a smaller inter-layer bias (see Eq. 4.8 and previous ones), needed to adjust the same imbalance.

The comparable experiments at $\nu_{\mathrm{tot}} = 3$ and $\nu_{\mathrm{tot}} = 5$, displayed in Fig. 5.9, show an almost constant width of the transition regions consistent with the prediction that an increasing imbalance can never change the type of anisotropy if of the easy-plane type [71]. In contrast to the argument [68] that any pseudospin transition governed by easy-axis anisotropy is accompanied by hysteresis when sweeping the pseudospin field P, which is similar (but not identical) to a sweep of the total density at constant filling factor, no such observation is made in agreement with Muraki *et al.* [35], who also did not observe any hysteresis. Jungwirth *et al.* [68] argue that a too high temperature (of which 300 mK are regarded in this publication) can eliminate the hysteresis.

5.3.4 Experiments of others

Similar measurements were carried out by Muraki *et al.* [35] using a bilayer, which is confined in a 40 nm wide WQW (structure M1 of Tab. 3.1). Because of the much larger subband splitting of 78 K or 6.8 meV at a total density of 2.85$\times 10^{15}$ m^{-2}, the crossing points were found at much higher critical densities (magnetic fields) of about 3$\times 10^{15}$ m^{-2} (3.5 T). The crossing points were located at zero imbalance with a sweep of the total density as here, but the influence of an imbalance has not been investigated. Instead, thermal activation studies were performed and the energy gap E_{A} was evaluated in dependence of the theoretical pseudospin splitting (E_{PS} in Fig. 5.7). E_{PS} can be given explicitly, because it is a function of the subband splitting $\Delta\mathrm{SAS}$, the cyclotron energy, and the Zeeman energy according to the differences in the quantum numbers of the coinciding LLs. The number of pseudospin flips s per particle added or subtracted from the system (see Eq. 4.11) could be given by this analysis. Close to the crossing point, s tends to zero for $\nu_{\mathrm{tot}} = 3$, while its value is about 30 to 50 for $\nu_{\mathrm{tot}} = 4$. Both observations are consistent with the different types of anisotropy as already assigned here [68] (see also Fig. 4.8). Muraki *et al.* interpret the much larger number than unity found for s in the case of $\nu_{\mathrm{tot}} = 4$ [35] as an indication of the formation of spin Skyrmions, because the spin is involved at $\nu_{\mathrm{tot}} = 4$. See also the theoretical discussion in Sec. 4.2.

Muraki *et al.* also performed similar experiments using a DQW structure consisting of two 20 nm wide QWs separated by a 1 nm thick AlGaAs tunnel barrier with an Al content of 30% (structure M2 of Tab. 3.1) and found equivalent results [36] at a critical total density (magnetic field) of about 1.25$\times 10^{15}$ m^{-2} (1.3 T) (see also the related reference in [35]).

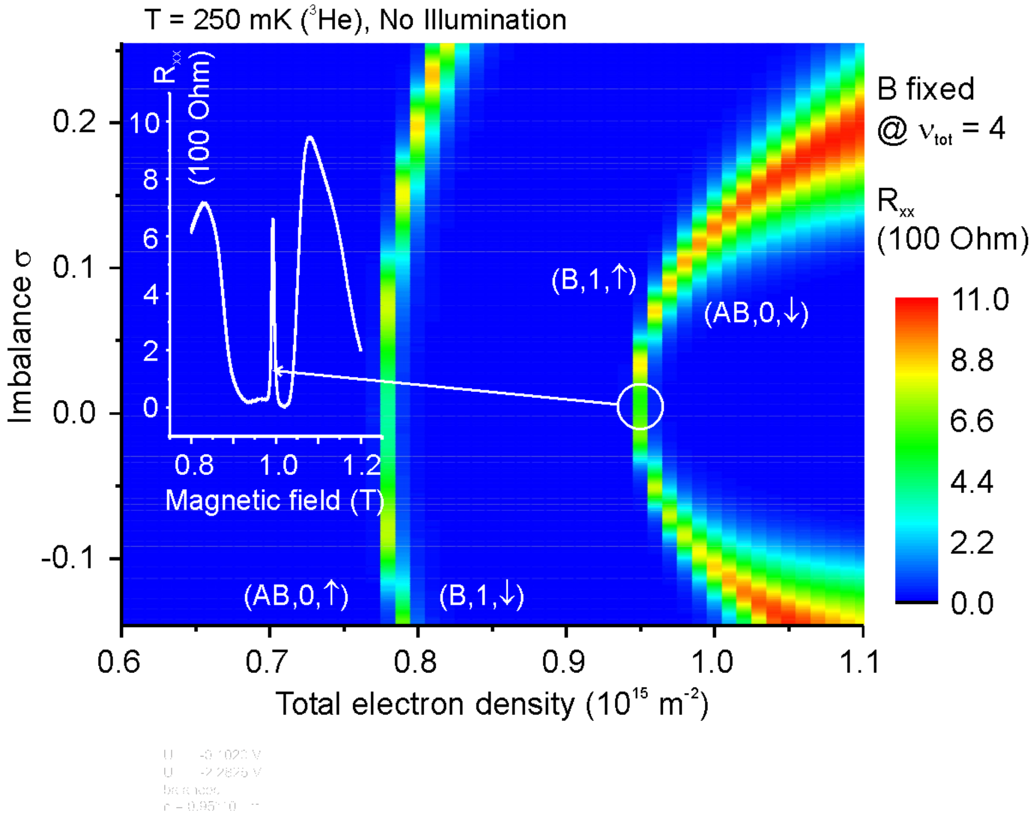

Figure 5.8: Magneto-transport measurement at constant total filling factor $\nu_{\rm tot} = 4$. The total density as well as the imbalance is varied. The two transition regions due to LL coincidences are indicated by a loss of the QHE (finite $R_{\rm xx}$). As expected, the transition regions are relocated to higher total densities with an approximately quadratic dependency on the imbalance and their width broadens. A sweep of the magnetic field across the plateau of $\nu_{\rm tot} = 4$ at the LL coincidence at a higher total density and $\sigma = 0$ reveals a narrow transition peak with a width of 8 mT (FWHM). The quantum numbers of the occupied LL next to the Fermi energy are given.

5.3.5 Quantitative analysis

The enhancement of the Zeeman splitting can be deduced, if the altogether four energetic relations valid at the four different crossing points are evaluated. These relations can be given analytically. Labeling the four crossing points involving the four total filling factors $\nu_{\rm tot} = 3$, $\nu_{\rm tot} = 5$, $\nu_{\rm tot} = 4$ at lower density and $\nu_{\rm tot} = 4$ at higher total density with the letters A, B, C, D, respectively, the relations

$$\begin{aligned}
\Delta\mathrm{SAS}^A - \tfrac{1}{2}C_{\rm Z}g^*\mu_{\rm B}B^A &= \hbar\omega_c^A - \tfrac{1}{2}C_{\rm Z}g^*\mu_{\rm B}B^A, \\
\Delta\mathrm{SAS}^B + \tfrac{1}{2}C_{\rm Z}g^*\mu_{\rm B}B^B &= \hbar\omega_c^B + \tfrac{1}{2}C_{\rm Z}g^*\mu_{\rm B}B^B, \\
\Delta\mathrm{SAS}^C - \tfrac{1}{2}C_{\rm Z}g^*\mu_{\rm B}B^C &= \hbar\omega_c^C + \tfrac{1}{2}C_{\rm Z}g^*\mu_{\rm B}B^C, \\
\Delta\mathrm{SAS}^D + \tfrac{1}{2}C_{\rm Z}g^*\mu_{\rm B}B^D &= \hbar\omega_c^D - \tfrac{1}{2}C_{\rm Z}g^*\mu_{\rm B}B^D,
\end{aligned} \qquad (5.3)$$

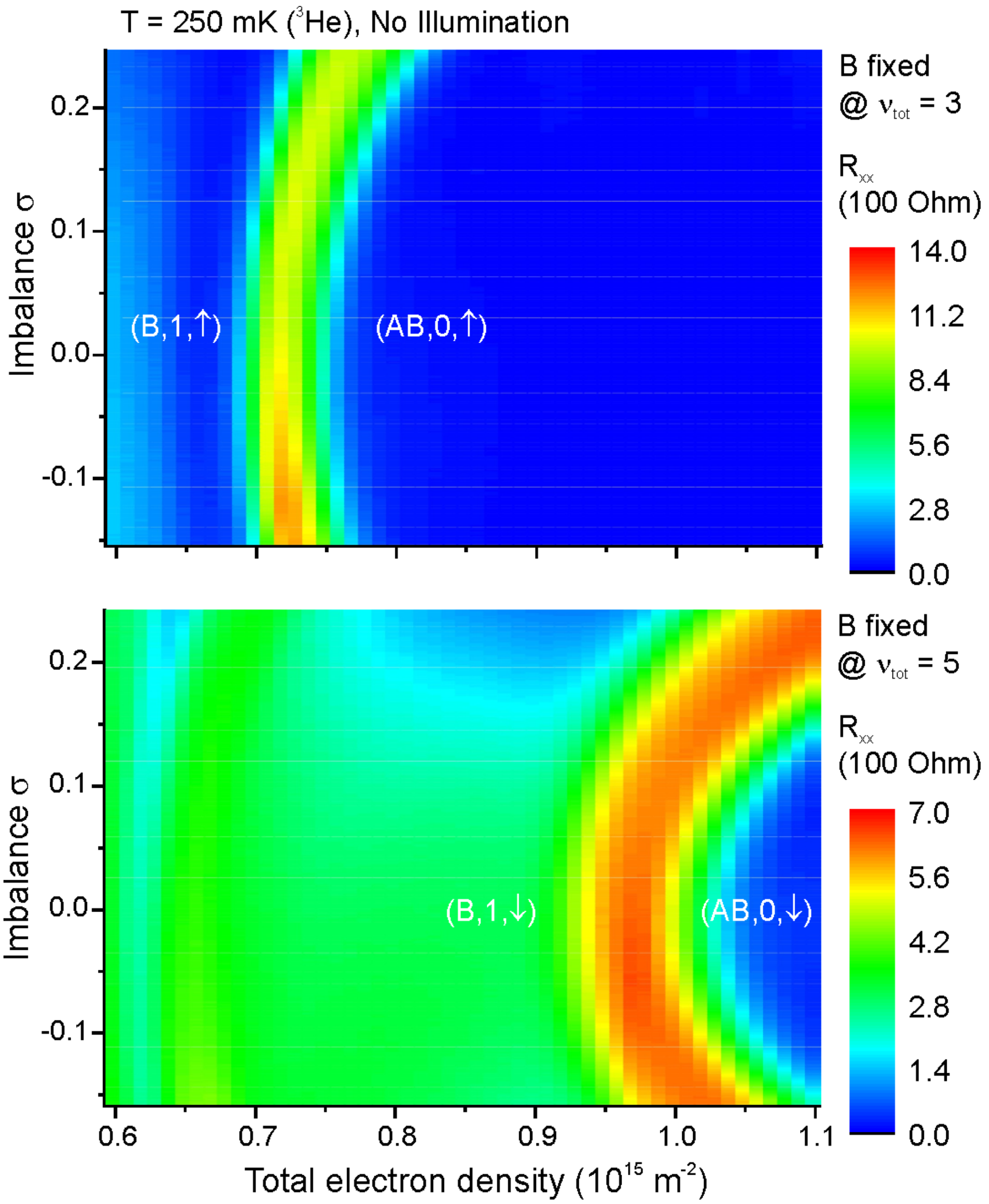

Figure 5.9: Same experiments as presented in Fig. 5.8 except at total filling factors $\nu_{\mathrm{tot}} = 3$ (upper panel) and $\nu_{\mathrm{tot}} = 5$ (lower panel). The width of the already broad transition regions remains with increasing imbalance.

are found, which simplify to[4]

$$\begin{aligned} \Delta\mathrm{SAS}^A &= \hbar\omega_c^A, \\ \Delta\mathrm{SAS}^B &= \hbar\omega_c^B, \\ \Delta\mathrm{SAS}^C &= \hbar\omega_c^C + C_Z g^* \mu_{\mathrm{B}} B^C, \\ \Delta\mathrm{SAS}^D &= \hbar\omega_c^D - C_Z g^* \mu_{\mathrm{B}} B^D, \end{aligned} \tag{5.4}$$

---

[4] The first to equations yield a relation of 1:1 between ΔSAS and $\hbar\omega_c$. Further crossings of LLs similar to the one at $\nu_{\mathrm{tot}} = 3, 4, 5$ can be found when the ratio between ΔSAS and $\hbar\omega_c$ reaches values of 1:2, 1:3, etc. The total filling factors concerned are then $\nu_{\mathrm{tot}} = 5, 6, 7$, $\nu_{\mathrm{tot}} = 7, 8, 9$, etc. Some of these additional LL coincidences are apparent in Fig. 5.6.

with the different subband splittings $\Delta\mathrm{SAS}^i$, cyclotron energies $\hbar\omega_c^i$, and magnetic fields B^i at the four crossing points i = A, B, C, D. C_Z denotes the enhancement of the Zeeman splitting.[5] The experiment reveals the following critical total densities and magnetic fields for the balanced case:

- $\nu_\mathrm{tot} = 3$: $n_\mathrm{tot}^A \cong 0.71 \times 10^{15}$ m^{-2}, $B^A \cong 0.98$ T,
- $\nu_\mathrm{tot} = 5$: $n_\mathrm{tot}^B \cong 0.965 \times 10^{15}$ m^{-2}, $B^B \cong 0.8$ T,
- $\nu_\mathrm{tot} = 4$: $n_\mathrm{tot}^C \cong 0.77 \times 10^{15}$ m^{-2}, $B^C \cong 0.8$ T,
- $\nu_\mathrm{tot} = 4$: $n_\mathrm{tot}^D \cong 0.945 \times 10^{15}$ m^{-2}, $B^D \cong 0.98$ T.

From the relations valid for $\nu_\mathrm{tot} = 3$ and $\nu_\mathrm{tot} = 5$ (A and B), the subband splittings can be immediately calculated, since $\hbar\omega_c^A$ and $\hbar\omega_c^B$ are entirely given by the magnetic field. Compared to the theoretical values, as derived from quantum mechanical calculations and displayed for a wide range of the total density in Fig. 4.4, it is again found that the quantum mechanical calculations underestimate the subband splitting by 30%. The values of $\Delta\mathrm{SAS}$ determined here can be used to estimate the subband splittings at the two crossing points involving $\nu_\mathrm{tot} = 4$ (C and D), which, in both cases, are characterized by not too different total densities (C corresponds to A, D to B).[6] Therefore, in the two relations valid at the crossing points C and D, only the Zeeman energy, or more precisely, its enhancement C_Z, remains to be specified. $C_\mathrm{Z} g^*$ can thus be calculated to be approximately -2.5, which yields a roughly 6-fold enhancement ($C_\mathrm{Z} \approx 6$) if compared to the bare value of the effective g factor $g^* =$ -0.44 of GaAs [96]. This enhancement is in agreement with other measurements [97] at comparable low densities.

5.4 QHE at total filling factor 1/2

5.4.1 Suitable wave function to describe a QHE at total filling factor 1/2

As discussed in Sec. 4.3, when two 2DES approach each other, the inter-layer Coulomb correlation energy E_d becomes important, in addition to the intra-layer Coulomb correlation energy E_C, of each layer. These energy scales are determined by the characteristic length scales, layer separation d and magnetic length l_B, respectively. Thus, altogether four energy scales are relevant with Zeeman energy E_Z, and subband splitting $\Delta\mathrm{SAS}$, being the other two. The Zeeman energy is neglected here. Only the intra-layer Coulomb correlation energy E_C depends on the externally applied magnetic field, while $\Delta\mathrm{SAS}$ and E_d are functions of certain boundary conditions of a considered double layer system (DLS). The latter two energy scales are at least

---

[5] This definition assumes that the enhancement is equal for all three different filling factors. This is justified as a first approximation [95].

[6] These almost coinciding critical magnetic fields appear by chance. In case of the structure M2 of Tab. 3.1 the values $B^A = 1.43$ T and $B^D = 1.52$ T were determined. The nevertheless similar values suggest an enhancement of the Zeeman splitting comparable to the value determined here, which is reasonable.

theoretically independent of each other and can be regarded as tunable quantities. It is therefore useful to normalize them to E_{C} and to define two dimensionless scales, which characterize the DLS. These are

$$\frac{d}{l_{\mathrm{B}}} = \frac{E_{\mathrm{C}}}{E_{\mathrm{d}}}, \tag{5.5}$$

and

$$\alpha = \frac{\Delta\mathrm{SAS}}{E_{\mathrm{C}}}, \tag{5.6}$$

where

$$E_{\mathrm{C}} = \frac{e^2}{4\pi\epsilon\epsilon_0 l_{\mathrm{B}}}, \tag{5.7}$$

and equivalently

$$E_{\mathrm{d}} = \frac{e^2}{4\pi\epsilon\epsilon_0 d}. \tag{5.8}$$

When the first scale is of the order of one, the formation of new collective states and the appearance of additional physical phenomena are expected. Some examples have already been given in Sec. 4.3. It has been pointed out by Chakraborty and Pietiläinen [98] that, due to the additional inter-layer Coulomb correlation energy, a collective state can be stabilized in a symmetric DLS at total filling factor $\nu_{\mathrm{tot}} = 1/2$ with an energy gap giving rise to a QHE. This suggests that a properly designed WQW might be a suitable candidate to exhibit a vanishing R_{xx} at $\nu_{\mathrm{tot}} = 1/2$ and a plateau in the Hall resistance pinned to $2h/e^2$.

Halperin [99] generalized Laughlin's wave function (see Sec. 2.2) to account for a DLS and included inter-layer correlation in the same manner as intra-layer correlation

$$\Psi_{m,m',m''} = \prod_{j,k}(\mathbf{z}_{j,1} - \mathbf{z}_{k,1})^{m} \prod_{j,k}(\mathbf{z}_{j,2} - \mathbf{z}_{k,2})^{m'} \prod_{j,k}(\mathbf{z}_{j,1} - \mathbf{z}_{k,2})^{m''} \prod_{j,k} e^{-\frac{|\mathbf{z}_{j,1}|^2}{4l_{\mathrm{B}}^2} - \frac{|\mathbf{z}_{j,2}|^2}{4l_{\mathrm{B}}^2}}. \tag{5.9}$$

The $\mathbf{z}$ denote the complex coordinates of the electrons with the first suffix the electron number and the second the layer number. The two leading products are due to intra-layer correlation in each of the two layers, while the third represents the inter-layer correlation. The exponents m and m' denote the number of flux quanta per electron in each layer, and m'' the number of flux quanta per quasi-hole in one layer shared with an electron in the other layer. Here, only the balanced case is of interest, implying $m = m'$. The exponents determine the properties of the wave function, as shown by MacDonald [87]. For simplicity, a state of a symmetric DLS represented by a wave function of the above given type is named (m, m, m'') according to its exponents. Such a state is associated with total filling factor $\nu_{\mathrm{tot}} = 2/(m + m'')$. Since the inter-layer correlation can never be larger than the intra-layer correlation,[7] it is essential that $m \geq m''$ and the existence of any inter-layer correlation requires $m'' > 0$. To ensure that the wave function describes an incompressible ground state giving rise to a QHE, m has to be odd [101]. Therefore, the only valid combination of exponents with respect to a QHE at total

---

[7] The requirement that the filling factor in each layer is positive, since the same magnetic field threads the layers, forces this relation [100].

filling factor $\nu_{\mathrm{tot}} = 1/2$ is $m = 3$ and $m'' = 1$. A descriptive picture of the (3,3,1) state [102] is given in Fig. 5.10.

However, the above wave function does not include any tunneling which means, that it is a valid description of an incompressible ground state of a DLS for a certain range of d/l_{B}, but only in the limit $\alpha = 0$, because no tunneling implies $\Delta\mathrm{SAS} = 0$. This neglect of tunneling is quite important, because tunneling cannot be avoided experimentally below a certain layer separation d and this is in particular true for the WQW. The finite charge carrier exchange between the two close electron layers of a bilayer might therefore be a limiting factor in realizing this (3,3,1) state.

Numerical calculations have been carried out by Scarola and Jain [103], showing that the (3,3,1) state is most certainly the incompressible ground state of a DLS within the range $d/l_{\mathrm{B}} = 1.5 \cdots 3.0$, when zero finite thickness is assumed for each electron layer, which would correspond to a realization in a DQW structure with very narrow QWs. Greiter *et al.* [104] calculate that $d/l_{\mathrm{B}} = 3 \cdots 10$ is a suitable range in the case of a WQW. The fact, that the ranges are different in both cases is mainly due to the additional inclusion of finite thickness in the case of the WQW. If correcting the DQW range by including the finite thickness into l_{B} (see the discussion in Subsec. 6.2.1), which reduces l_{B} by about a factor of 2.5, the two ranges almost coincide. How the ground state of a bilayer at $\nu_{\mathrm{tot}} = 1/2$ evolves in dependence of the two fundamental parameters d/l_{B} and α is discussed by Halperin [105] and depicted in a phase diagram shown in Fig. 5.11. At intermediate values of d/l_{B} the ground state gradually changes with increasing tunneling strength α [106, 107] from the (3,3,1) state to the Pfaffian state[8] [104, 108–111] in the strong tunneling or single layer limit [112]. In the vanishing tunneling limit the ground state evolves with an increasingly effective layer separation d/l_{B} from a one-component (1C), single layer-like, metallic and thus compressible (2,2,2) state exhibiting no QHE to a two-component (2C), double layer-like, metallic (4,4,0) state which again exhibiting no QHE and passes the incompressible (3,3,1) state which gives rise to a QHE.

---

[8] The Pfaffian state can be obtained from the (3,3,1) state by projecting out the layer index [108] (single layer regime). The name Pfaffian state arose in the literature from the prefactor to the corresponding wave function which involves the mathematical operation of a Pfaffian [109].

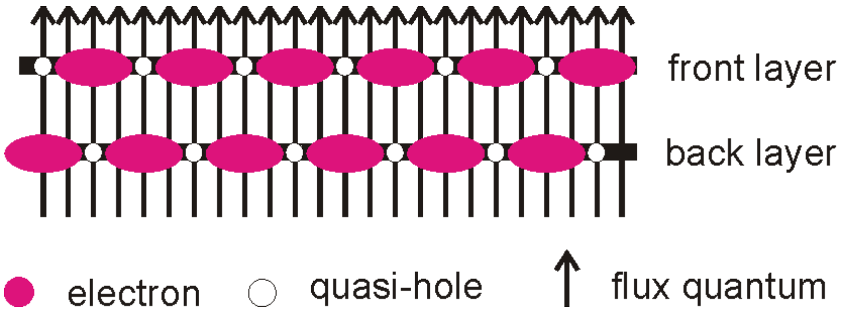

Figure 5.10: Descriptive picture of the (3,3,1) state. The Coulomb repulsive force repels electrons on the opposite layer and creates quasi-holes. The states of each layer are therefore locked (see [65]).

5.4.2 Locating a QHE at total filling factor 1/2

If the electron distribution of a WQW should stay balanced, than the only *in situ* tunable parameter that a WQW still provides is the total density. An increase of the total density reduces the subband splitting and thus α, whereas d/l_{B} is enlarged due to an increase of the layer separation and a decrease of the magnetic length. It is not therefore experimentally possible to tune both parameters (α and d/l_{B}) independently with the same WQW sample. Instead, a variation of the total density results in a move along a certain line within the given phase diagram. Only the width w of the used WQW determines the position of this tuning trace. A larger width shifts the trace towards the lower left corner of the phase diagram, while a smaller width displaces the trace towards the upper right corner [33]. In the case of a DQW the tuning trace is located at the left edge of the phase diagram and is very steep because $\Delta\mathrm{SAS}$ and hence α is much smaller compared to the WQW, and is only to a minor degree affected by a change of the total density. That a weakly tunnel coupled DQW structure has a tuning trace at all in that diagram, since the layer separation d is a constant, is due to the variation of l_{B} with the total density at fixed filling factor ($l_{\mathrm{B}} \propto 1/\sqrt{n_{\mathrm{tot}}}$). This kind of tuning has been used in experiments by the group of J. Eisenstein (Caltech) to move within the equivalent phase diagram of a bilayer at total filling factor $\nu_{\mathrm{tot}} = 1$, as discussed in Sec. 4.3. By tuning the total density of an appropriately wide WQW (or a certain DQW structure), it should be possible to intersect the theoretically predicted stable area of the (3,3,1) state in the given phase diagram, as displayed in Fig. 5.11, and thus realize a QHE at $\nu_{\mathrm{tot}} = 1/2$.

In the appropriate experiment using the WQW structure fabricated here the total density is increased stepwise while the electron distribution is kept balanced each time sweeps of the magnetic field are performed. The R_{xx}-pattern obtained is shown in Fig. 5.12. As can be seen, a QHE at $\nu_{\mathrm{tot}} = 1/2$ is found only within a small range of the total density. The QHE is most pronounced at a total density (magnetic field) of 1.4×10^{15} m^{-2} (11.6 T), which corresponds to $d/l_{\mathrm{B}} = 6.9$ and $\alpha = 0.07$. The optimal total density coincides with the total critical density of the one-component to two-component (1C-2C) phase transition[9] discussed in Sec. 4.3. This coincidence is not surprising, because the competing inter- and intra-layer Coulomb correlation energies, which stabilize the (3,3,1) state if approximately equal [98], are also comparable at the 1C-2C phase transition (see the further discussion in Chapter 7). Furthermore, in the data plot of Fig. 5.12 an unusual QH state at $\nu_{\mathrm{tot}} = 11/15$[10] appears towards higher total density as

---

[9] The 1C-2C phase transition is indicated in the plot of Fig. 5.12 by the change of several QH states towards higher total density than 1.4×10^{15} m^{-2}. The plateau width of $\nu_{\mathrm{tot}} = 1$ reduces because $\nu = 1/2$ in each layer separately does not give rise to a QHE and consequently this QHE gradually disappears. The FQHE at $\nu_{\mathrm{tot}} = 3/5$ disappears because it is a 1C state, while QHEs at $\nu_{\mathrm{tot}} = 4/5$ ($\nu = 2/5$ in each layer) and $\nu_{\mathrm{tot}} = 6/7$ ($\nu = 3/7$ in each layer) appear, which are 2C states.

[10] The ground state at $\nu_{\mathrm{tot}} = 11/15$ is a compound quantum Hall state as described in Sec. 4.3. The individual layer filling factors are 1/3 and 2/5 and the optimal imbalance is consequently $\pm 1/11$ according to Eq. 4.15. This is confirmed here by experiment. At a very high total density of 2.5×10^{15} m^{-2} and with the appropriate imbalance, an exactly quantized Hall plateau is achieved and the longitudinal resistance goes to zero already at a temperature of 250 mK. In the 2C regime several other minima in R_{xx} are observed with only one layer exhibiting a magic filling factor. As expected, the minima in the longitudinal resistance are not that deep in these cases. In particular,

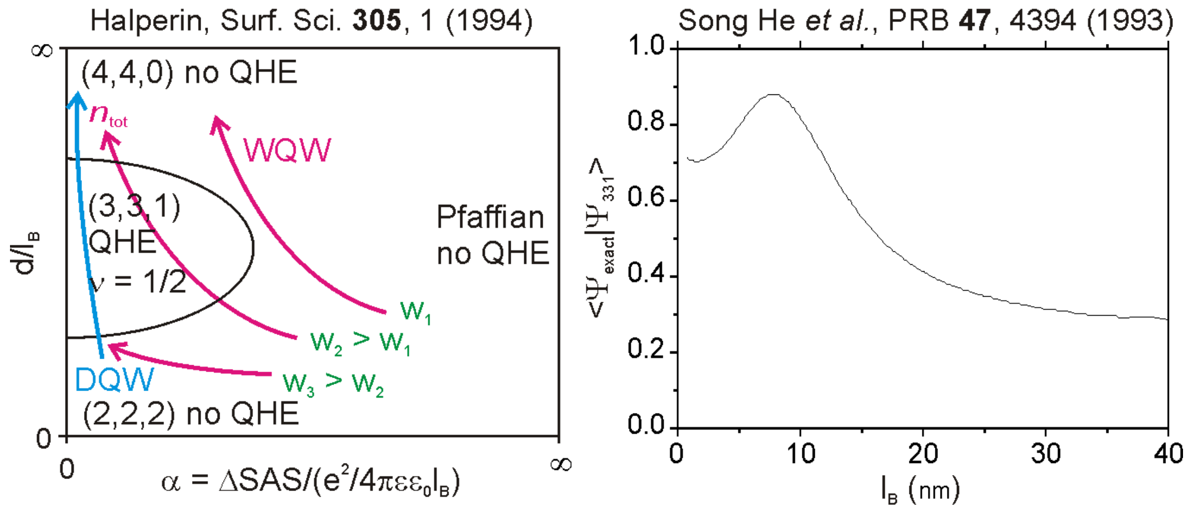

Figure 5.11: Left panel: Phase diagram of a double layer system (DLS) at total filling factor $\nu_{\mathrm{tot}} = 1/2$ in dependence of the tunneling strength α and the (normalized) inter-layer distance d/l_{B}. The different wave functions according to Eq. 5.9 are given. Towards vanishing tunneling and when d/l_{B} is of the order of one, the formation of the (3,3,1) state is expected exhibiting a QHE. The red lines indicate paths along which a balanced bilayer confined in a WQW of width w can be tuned by varying the total density. The blue line corresponds to a bilayer of a DQW structure. Right panel: Overlap between the exact ground state at $\nu_{\mathrm{tot}} = 1/2$ of a bilayer confined in 77 nm wide WQW with the (3,3,1) state in dependence of the magnetic length l_{B}, which represents the total density.

well as an insulating phase[11] (IP-WC).

The most striking difference to the comparable experiment of the group of M. Shayegan at Princeton University [32], which discovered the QHE at $\nu_{\mathrm{tot}} = 1/2$ using a nominal equally wide WQW, is the total density or magnetic field range within which this QHE is found to be stable. The Princeton group finds the QHE to be most pronounced around a total density (magnetic field) of $1.0{\times}10^{15}$ m^{-2} (8.5 T). The fact that the Princeton group observes the above mentioned 1C-2C phase transition also at a comparable lower total density [118], which coincides again with the optimal total density of the QHE at $\nu_{\mathrm{tot}} = 1/2$, suggests that the reason for this deviation is not intrinsic to this QHE, but of a more general origin, *i.e.* due to a difference in an external parameter, namely the width of the WQW. A variation of the critical total density or magnetic field of the 1C-2C phase transition by a change of the width of the WQW is possible [33], as mentioned in Sec. 4.3. Highly accurately calibrated RHEED oscillations [119] are

---

the compound quantum Hall state at $\nu_{\mathrm{tot}} = 11/15$ is extensively discussed in [15, 113].

[11] The insulating phase is according to [15] a bilayer stabilized Wigner crystal (WC). Theory predicts a bilayer stabilized WC towards a higher total density [114–117] which is in contrast to a single 2DES, where a higher density destroys the WC. The WC is destroyed with imbalance, *i.e.* its critical total density is shifted to higher values, as can be seen from Fig. 5.13. It has been found, that in this regime the longitudinal resistance increases exponentially towards lower temperatures, which supports the assignment to a WC. Equivalent results are observed using the DQW structure.

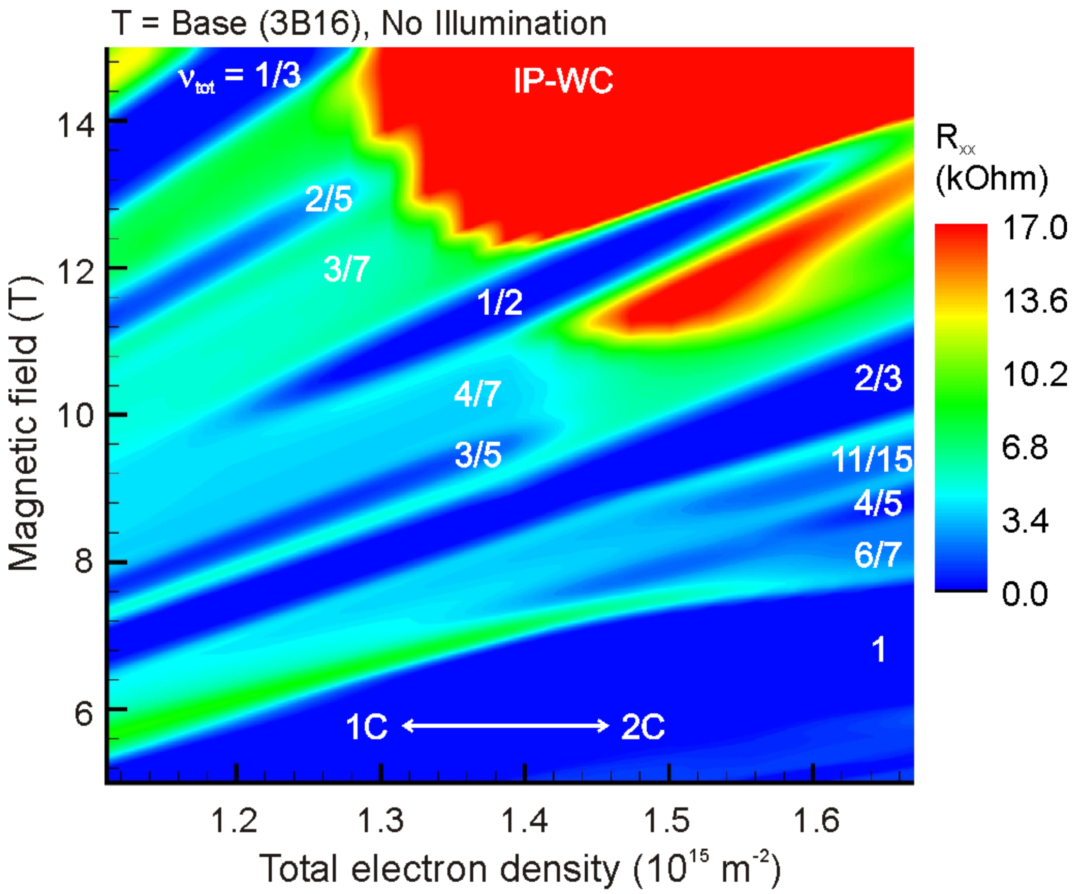

Figure 5.12: Magneto-transport measurement of the balanced bilayer confined to the 77 nm wide WQW structure. A QHE at $\nu_{\mathrm{tot}} = 1/2$ is observed only within a small range of the total density around $1.4{\times}10^{15}$ m^{-2}. This total density is also the phase boundary between the one component (1C) and two-component (2C) regimes (see Sec. 4.3). Towards higher total densities QHEs at total filling factors with odd nominator disappear (*e.g.* $\nu_{\mathrm{tot}} = 3/5$), whereas those with an even nominator are pronounced (*e.g.* $\nu_{\mathrm{tot}} = 4/5$ and $\nu_{\mathrm{tot}} = 6/7$). The case $\nu_{\mathrm{tot}} = 2/3$ is discussed in Chapter 7. The compound QH state at $\nu_{\mathrm{tot}} = 11/15$ is discussed in the text as well as the insulating phase (IP), which is attributed to the formation of a bilayer Wigner crystal (WC).

used here to determine the growth rate, present during the growth of the WQW structure under investigation and used also to adjust the growth time in order to achieve the intended WQW width. The nominal width of 77 nm is therefore reliable to within a few Å. REM images of the cross-section of the structure also confirm this statement. The Princeton group, however, deliberately grew its wafer without rotation in order to achieve a gradual change of the width of the WQW across it which enabled them to find the best suited WQW width. They then estimated the WQW width w by comparing values of the subband splitting ΔSAS determined experimentally with calculated values, which are a function of w for a specific total density. A comparison of the calculations of ΔSAS of a 77 nm wide WQW, based on equivalent methods and approximations as used by the Princeton group (see Sec. 4.1), with the experimental results given in Sec. 5.2, demonstrates that calculations underestimate $\Delta\mathrm{SAS}$, or conversely suggest a too narrow WQW width. The extent to which the Princeton group underestimated the width of their WQW can be roughly evaluated. The calculations carried out here reveal an increase of $\Delta\mathrm{SAS}$ by 1.5 K upon a reduction of the WQW width by 2 nm from 77 nm down to 75 nm at a constant total density of $1.0{\times}10^{15}$ m^{-2}, which is the critical total density to obtain a QHE at $\nu_{\mathrm{tot}} = 1/2$ with the WQW of the Princeton group. The calculated subband splitting (see Fig. 4.4) is about 5 K smaller than the experimentally determined value (see Sec. 5.2), which allows to estimate that the WQW width of the sample used by the Princeton group might be approximately 6.5 nm larger than nominally stated. This estimation is relevant for discussion of the relation between isospin transition and 1C-2C phase transition in Sec. 7.3.

Numerical calculations have been carried out by He *et al.* [120] addressing the QHE at $\nu_{\mathrm{tot}} = 1/2$ in a nominally 77 nm wide WQW. These calculations show that there is a strong overlap of the numerically found wave function, *i.e.* the exact ground state, and the proposed (3,3,1) state at $\nu_{\mathrm{tot}} = 1/2$. The overlap is found to be largest at a magnetic field value of 10.8 T (see the right panel of Fig. 5.11, where the overlap is plotted in dependence of the magnetic length), which is close to the value determined here (11.6 T), but quite different from the result obtained by the Princeton group (8.5 T). The overlap is found to be even larger [121] in the case of the DQW structure of Eisenstein *et al.* [34] mainly due to the reduced tunneling and lesser finite thickness.

A tilt of the WQW potential keeping the optimal total density for the QHE at $\nu_{\mathrm{tot}} = 1/2$ constant causes a gradual destruction of the incompressible ground state, as can be seen in Fig. 5.13. It indicates that this QH state is indeed a two-component (2C) state, because an imbalance discriminates 2C states and favors 1C states, as discussed in Sec. 4.3. The 2C nature is inherent in the wave function given in Eq. 5.9, because the intra-layer Coulomb correlation is independent for each layer and the inter-layer Coulomb correlation is superimposed, since all three different correlations are represented by individual products into which $\Psi_{m,m',m''}$ factorizes. Some other wave functions [42] proposed to describe the QHE at $\nu_{\mathrm{tot}} = 1/2$ are not of a 2C nature, and can be ruled out with this experiment. Temperature dependent measurements yield an activation energy of 0.43 K of the QH state at $\nu_{\mathrm{tot}} = 1/2$ for the balanced optimal total density. The Princeton group [33] found a value of 0.5 K.

5.4.3 The impact of an in-plane magnetic field

The experiments addressing the QHE at $\nu_{\mathrm{tot}} = 1/2$ are further extended to measurements with a variable in-plane magnetic field B_{ip} by tilting the sample *in situ*, because B_{ip} modifies the overlap between the two charge layers and therefore allows it to influence the tunneling strength [122, 123] between the layers, as will be explained in the following. An in-plane magnetic field B_{ip} distorts the shape of the Fermi circle of the bonding subband to that of a peanut shape and finally splits it into two elliptical contours offset along $k \perp B_{\mathrm{ip}}$. The actual subband splitting is increased, and reaches the in-plane cyclotron energy towards higher in-plane mag-

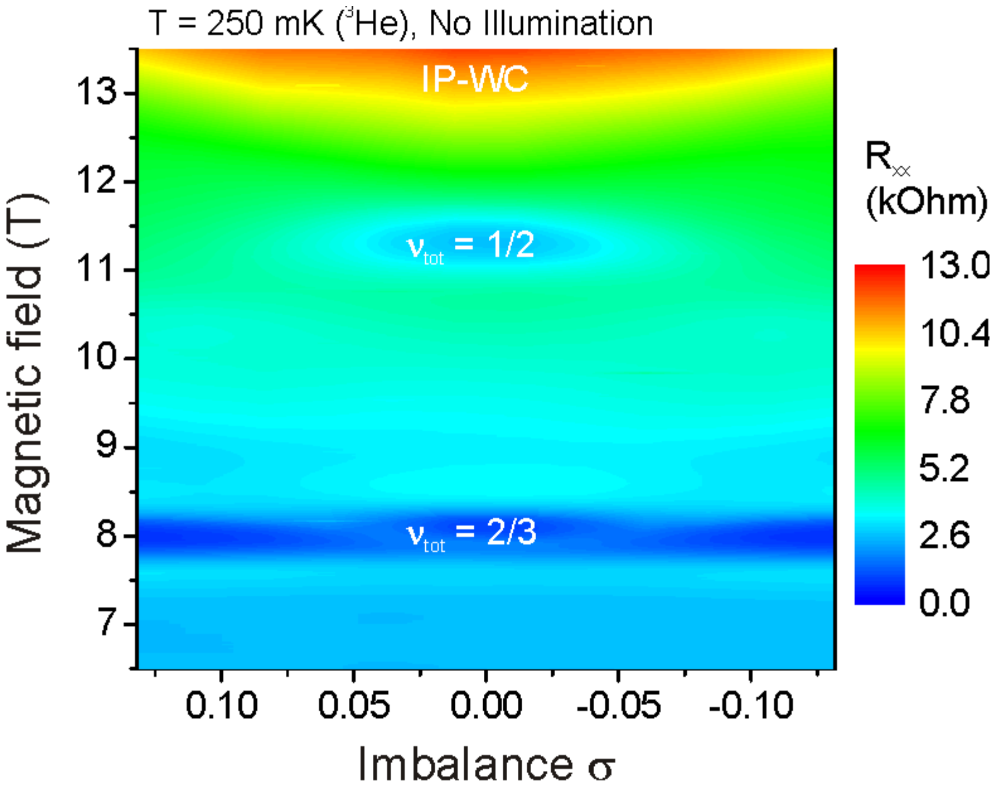

Figure 5.13: Magneto-transport measurement of the bilayer at constant total density 1.4×10^{15} m^{-2}, at which the QHE at $\nu_{\rm tot} = 1/2$ is most pronounced, and variable tilt (imbalance) of the WQW potential. The QHE at $\nu_{\rm tot} = 1/2$ is gradually destroyed with an increasing imbalance. Also the onset of the insulating phase (IP-WC) is transferred to a higher total density. This indicates (in both cases) the importance of the balanced Coulomb interaction between the two electron layers with respect to the stabilization of these effects.

netic fields [124], which causes a depopulation of the anti-bonding subband [125, 126]. This leads in total to a spatial redistribution of the electrons from the center of the WQW to its edges, as displayed in the left panel of Fig. 5.14. This is the intuitive reason for the now reduced tunneling strength which is no longer directly related to the actual subband splitting. Instead, both quantities develop contrarily. Therefore, the actual subband splitting is replaced by a purely tunneling-induced subband splitting to stay compatible with the phase diagram, which refers to the tunneling strength when using $\alpha = \Delta{\rm SAS}/E_{\rm C}$ on one axis. Accordingly, this effective ΔSAS continuously decreases with an increasing in-plane magnetic field, as shown in the right panel of Fig. 5.14. The change of the tunneling strength or effective ΔSAS with in-plane magnetic field is theoretically found to be proportional to $1/\exp[(B_{\rm ip}d/2B_\perp l_{\rm B})^2]$ [122, 127], where $B_\perp$ denotes the component of the applied magnetic field perpendicular to the bilayer. This analytic result is based on a tight-binding-approximation (TBA) model, which considers the electron distribution in each layer as Gaussian. Their guiding centers are relative to each other laterally displaced proportional to the strength of the in-plane magnetic field. Since only this change is taken into account, the derived dependence predicts the decrease of the effective subband splitting to be too rapid [123]. Therefore, a self-consistent local-density-functional-approximation (SCLDA) was used in [123], which cannot give an analytic relation for the dependency of $\Delta\mathrm{SAS}$ on B_{ip}, but the numerical result, shown in the right panel of Fig. 5.14, has been quantitatively confirmed by experiment [123]. Due to the in-plane magnetic field induced reduction of the tunneling strength α, it is expected that the QHE at $\nu_{\mathrm{tot}} = 1/2$ is even more pronounced as in the absence of an in-plane magnetic field, because tunneling is not necessary for the formation of the (3,3,1) state and even destroys it [128], as indicated in the phase diagram shown in Fig. 5.11.

The electron distribution is changed by an in-plane magnetic field, which in turn alters the detailed balance of the competing inter- and intra-layer Coulomb correlation energies responsible for the QHE at $\nu_{\mathrm{tot}} = 1/2$. Consequently, the experiment with a variable in-plane magnetic field is carried out for a larger range of the total electron density to account for any change in the critical total density of the QHE at $\nu_{\mathrm{tot}} = 1/2$. The data presented in Fig. 5.15 reveal that the QHE is slightly relocated to lower total densities with an increasing in-plane magnetic field, *i.e.*

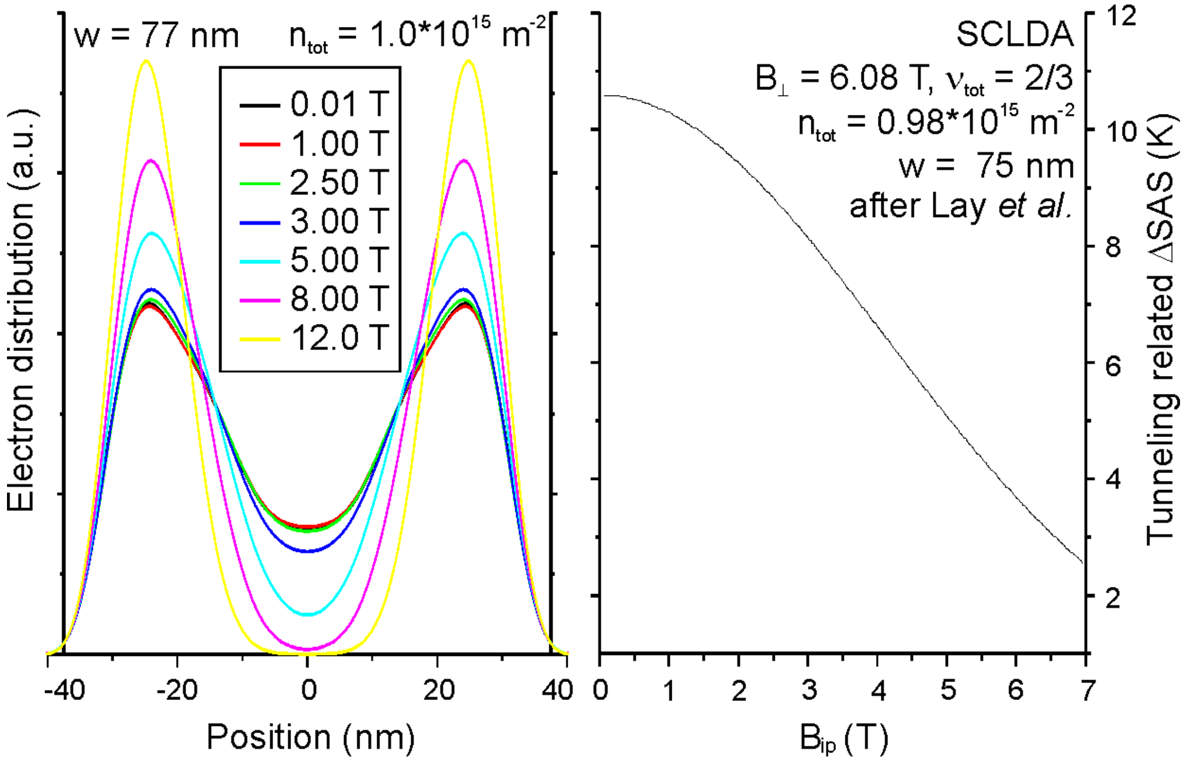

Figure 5.14: Calculated change of the balanced electron distribution in the WQW in dependence of the strength of an in-plane magnetic field B_{ip} (left panel). With increasing B_{ip} electrons are transferred from the center of the WQW towards the edges leading to an enhanced layer separation and a suppression of charge carrier exchange by virtue of quantum tunneling between the layers. The associated tunneling induced subband splitting after [123] is shown in the right panel.

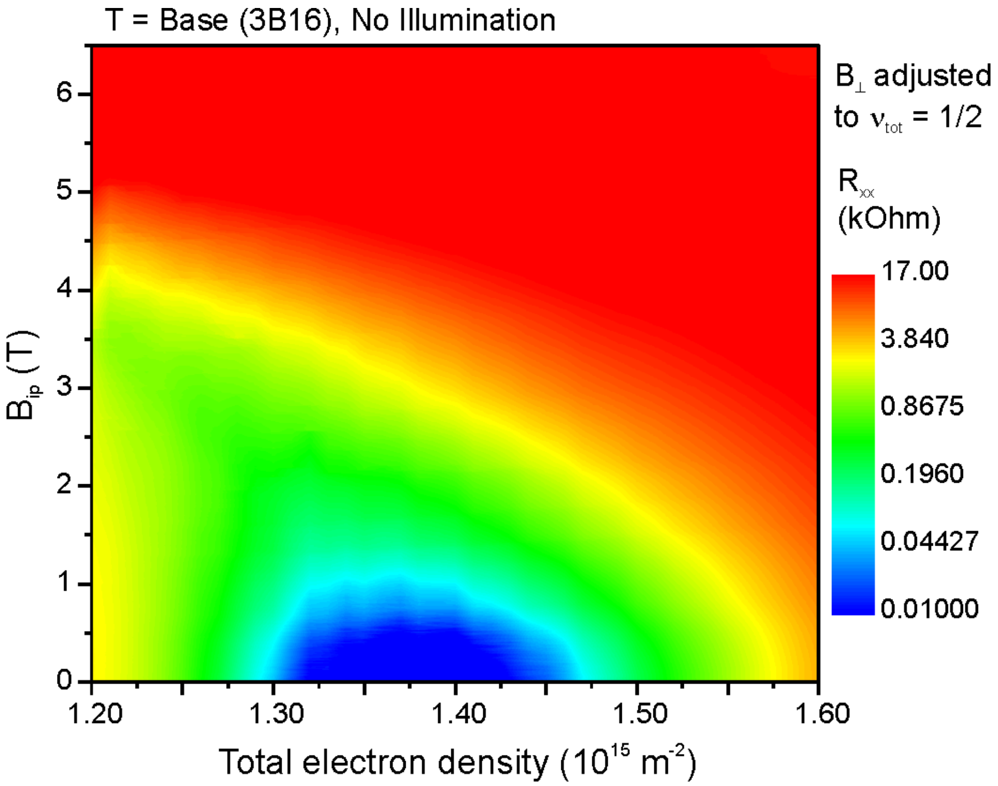

Figure 5.15: Magneto-transport measurement of the bilayer at constant total filling factor $\nu_{\rm tot} = 1/2$ in dependency of the balanced total density and an applied in-plane magnetic field $B_{\rm ip}$. The QHE present at $B_{\rm ip} = 0$ T and $n_{\rm tot} \approx 1.4\times10^{15}$ m^{-2} is successively destroyed with increasing $B_{\rm ip}$. A tendency of the resistance minimum towards lower total density is apparent, which is explained in the text.

reduced tunneling. This is not surprising, because the inter-layer Coulomb correlation is discriminated against the intra-layer Coulomb correlation energy with an increasing charge transfer from the center of the WQW to its edges, which can only be compensated for by a reduction of the total density, thus approaching the two layers again and reestablishing the critical relation between these two correlation energies. But despite the theoretical expectation, the QHE at $\nu_{\rm tot} = 1/2$ is always less pronounced for any in-plane magnetic field. Suen *et al.* [32] also found that the QHE at $\nu_{\rm tot} = 1/2$ is just suppressed by a rising in-plane magnetic field, but they restricted themselves to measurements at only a few tilt angles and in particular at only one total density, at which the QHE was most pronounced when $B_{\rm ip} = 0$. The gradual disappearance of the QHE suggests that the wave function of the actual ground state has an ever decreasing overlap with the (3,3,1) state towards larger $B_{\rm ip}$. The Laughlin-kind of a wave function, which gives rise to a QHE, is not fundamentally affected by an in-plane magnetic field [129], so that an in-plane magnetic field is basically not a limiting factor. But $B_{\rm ip}$ can change the effective g factor and the effective mass of the electrons (see references in [97]) and lead to LL mixing. Furthermore, $B_{\rm ip}$ enhances the intra-layer Coulomb correlation energy due to a squeezing of the electron distribution of each layer along the growth direction [130], which however should support the formation of the (3,3,1) state. Neither the literature nor the experiments here are able to resolve the contradiction between the descriptive theory presented above and the observations made. It should be noted that a similar result has been found in the case of the QHE at $\nu = 5/2$ using a single 2DES [131]. The ground state in this case has a strong overlap with the Pfaffian state [132–141], so the states at $\nu_{\text{tot}} = 1/2$ and $\nu = 5/2$ are regarded to be comparable.[12] The QHE at $\nu = 5/2$ also just disappears with an increasing in-plane magnetic field [142].

5.4.4 The DQW structure at total filling factor 1/2

The DQW structure produced here is intended to be as comparable as possible to the one used by Eisenstein *et al.* [34], exhibiting a QHE at $\nu_{\text{tot}} = 1/2$, in order to have a second, but different structure than the WQW, suitable to form this unique bilayer QH state. But the Al content of the AlGaAs material below and above the two QWs is here about 30% instead of 15% as in [34]. This might be the reason why the DQW structure fabricated here does not exhibit a QHE at $\nu_{\text{tot}} = 1/2$ regardless of the adjusted total density. However, the absolutely precise determination of the balanced condition is not possible, as in the case of the WQW structure, because of the noticeably different mobilities of the two QWs and the rather small subband splitting of about 1 K. The variation of the individual layer densities with gate bias, *i.e.* the parameters Δn_{FG} and Δn_{BG}, is also not precisely determinable, again due to the very small subband splitting, which makes it difficult to follow a certain filling factor over a sufficiently large density range, as utilized in Sec. 5.2. Altogether this makes an accurate statement about the actual charge distribution between the two QWs difficult. Because of the lack of a QHE at $\nu_{\text{tot}} = 1/2$ in the case of the DQW structure produced here, this structure is further used only for some experiments addressing the spin transition at filling factor $\nu = 2/3$, which are discussed in Sec. 6.7. The master structure of the DQW structure fabricated here, as presented in [34], had no gates at all but was prepared to exhibit a QHE at $\nu_{\text{tot}} = 1/2$ just after illumination. So neither the density nor the distribution could be tuned, which eliminated detailed investigations of the influences of such variations on the QHE at $\nu_{\text{tot}} = 1/2$. The only implemented variations were either higher total densities or a thicker barrier between the two QWs which was achieved with additionally grown DQW structures. Both variations resulted in a much weaker or even absent QHE at $\nu_{\text{tot}} = 1/2$ [34]. The optimal value for the ratio d/l_{B} was found to be 2.4, while above 3 the QHE disappeared, in agreement with the theory.

---

[12] Note the relation between the filling factors $5/2 = 2 + 1/2$. In first order, fully occupied LLs are often neglected.

Chapter 6

The spin transition at filling factor 2/3

This chapter discusses the crossing of two CF LLs at $\nu = 2/3$ accompanied by a change in the spin quantum number. Its various influencing parameters are studied using the WQW.

6.1 Origin of the spin transition

Proceeding from the IQHE to the fractional quantum Hall effect (FQHE) leads to the introduction of CF LLs and a functional replacement of the electron cyclotron energy $\hbar\omega_{\mathrm{c}}$ by the CF cyclotron energy $\hbar\omega_{\mathrm{c,CF}}$. The latter is governed by the Coulomb correlation energy E_{C}. The Zeeman energy E_{Z} as second decisive energy scale remains unaffected as has been already mentioned in Sec. 4.2. The dependencies of E_{C} and E_{Z} on the magnetic field or density are no longer equal as was the case in the IQHE. In fact, the Zeeman energy remains a linear function of the external magnetic field but the Coulomb correlation energy follows a square root dependence on the external magnetic field. These different dependencies imply that CF LLs with the same subband index (isospin) can exhibit a crossing by varying the magnetic field or density. This is in direct contrast to the IQHE regime, where crossings are only possible due to the occupation of two subbands which give rise to two intersecting LL fan-charts.[1] Therefore, in the FQHE regime, even if the subband index is effectively frozen out, *i.e.* in the single layer regime with only one CF LL fan-chart present, coincidences of CF LLs and thus ferromagnetic phase transitions can be studied. Fig. 6.1 depicts schematically the development of the lowest CF LLs with magnetic field or density when the filling factor is fixed to $\nu = 2/3$, which is in contrast to the penetrating LL fan-charts shown in Fig. 4.7 where the density was fixed. A crossing is apparent at a critical magnetic field B_{S} or density n_{S} involving filling factor $\nu_{\mathrm{CF}} = 2$ ($\nu = 2/3$). The energetically lowest CF LL is characterized by the quantum numbers (B,0,↑) and is always occupied. The two CF LLs involved in the crossing are characterized by the sets of quantum numbers (B,0,↓) and (B,1,↑), where the first set (pseudospin orientation) represents the ground state below the critical magnetic field and the second set represents the ground state above the

---

[1] Possibilities, how LL crossings can be achieved in the IQHE between LLs even of the same isospin are mentioned in Sec. 4.2.

critical magnetic field. Besides the orbital quantum number, the spin is also changed, and consequently the ferromagnetic phase transition is termed spin transition. Taking the spin of the two occupied CF LLs into account, the system experiences a transition from a spin unpolarized phase to a spin polarized phase with increasing magnetic field or density. The critical magnetic field or density is determined by the Zeeman and CF cyclotron energy, which are equal at the CF LL crossing point, because the two crossing CF LLs differ in the orbital quantum number by one unit and in the spin. Since the subband index is not affected, *i.e.* effectively frozen out, this ferromagnetic phase transition is present in every single 2DES. In order to explore it, a bilayer system can be tuned to a single layer system by depletion of one of the electron layers. Exploring this effect in a WQW allows for adjust of the shape of the single 2DES along the growth axis as determined by the tilt of the WQW potential, which can be controlled by the two gates. The shape of the electron layer sets the effective inter particle distance and hence effects the intra-layer Coulomb correlation energy, which can thus be tuned. In addition to this tunability tilted magnetic fields allow for the adjustment of the Zeeman energy, since the Zeeman energy follows the total magnetic field but the Coulomb correlation energy is only a function of the perpendicular component of the magnetic field intersecting the 2DES. Thus, the two competing energies can be independently tuned and used to study the spin transition as detailed in the following sections.

The spin transition at $\nu = 2/3$ was predicted by Chakraborty [85] and was experimentally verified by Eisenstein *et al.* [143] and Clark *et al.* [144, 145], who noticed a non monotonous dependence of the activation energy at $\nu = 2/3$ on density. Because of the different parameters

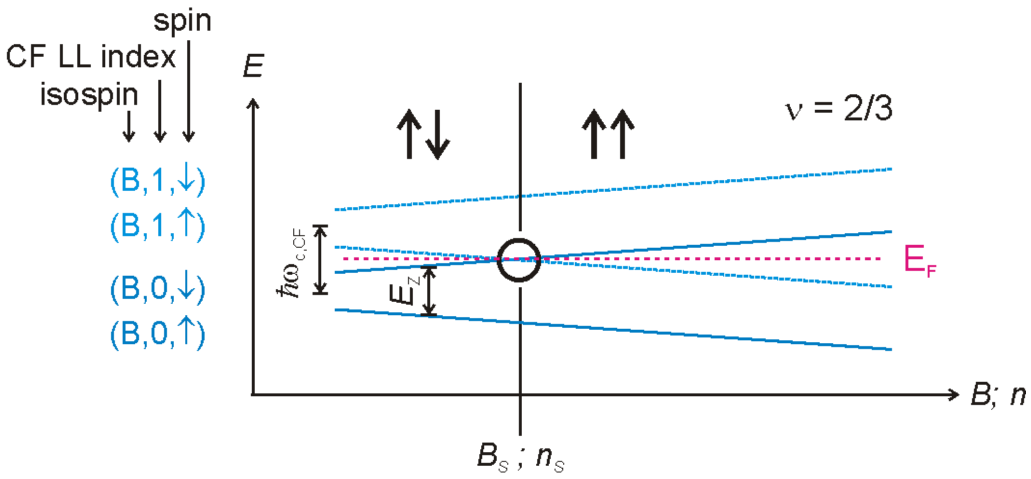

Figure 6.1: Qualitative variation of the energetically lowest CF LLs with magnetic field B or electron density n. Each pair of CF LLs separated by the CF cyclotron energy $\hbar\omega_{\mathrm{c,CF}}$ is further split by the Zeeman energy E_{Z}. Due to the different dependency of $\hbar\omega_{\mathrm{c,CF}}$ and E_{Z} on B or n, a Cf LL crossing occurs at a critical magnetic field B_{S} or density n_{S} involving filling factor $\nu_{\mathrm{CF}} = 2$ ($\nu = 2/3$). This leads *inter alia* to a change of the spin, wherefore the crossing point is termed spin transition. The spin configuration of the two occupied CF LLs below and above B_{S} or n_{S} is indicated by the pair of arrows.

that influence the competing energies, the spin transition can be formed in several ways:

- by tilting the sample [146] and thus increasing the Zeeman energy selectively against the Coulomb correlation energy,
- by applying hydrostatic pressure [147, 148] and thus increasing the effective g factor and even drive it through zero[2] which reduces the Zeeman energy,[3]
- or by sweeping the electron density at fixed filling factor $\nu = 2/3$ so utilizing the different dependencies of the two competing energies on magnetic field or density.

While the first two methods allow to force level crossings in the IQHE regime of a single 2DES, the latter cannot, because the different functional dependence of the two competing energy scales is restricted only to the FQHE regime.

Due to the CF LL coincidence and the thus reduced energy gap, the QHE at $\nu = 2/3$ is degraded. The usual minimum in the longitudinal resistance R_{xx} of a transport experiment is accompanied or even replaced by a resistance peak which is similar to that seen in the case of the LL crossings involving $\nu_{\mathrm{tot}} = 3, 4, 5$ (see Sec. 5.3). The actual shape and size of this peak can strongly vary from the hardly visible to the totally dominant.

It has been shown by Kraus *et al.* [150] that this spin transition also gives rise to the so-called huge longitudinal resistance (HLR), discovered by Kronmüller *et al.* [151, 152] close to $\nu = 2/3$. Originally the HLR was thought to be a different effect, but the HLR is nothing other than the resistance peak which is due to the spin transition. The shape of the HLR peak can vary according to different for different experimental conditions (temperature, current, magnetic field sweep rate, etc.) and even from sample to sample. Typically one speaks of the HLR when the peak is narrow and very tall or when it completely dominates the plateau region. It has been found, that the peak height both increases and widens in a non linear manner with the excitation current, and also widens with faster sweep rates of the magnetic field. It has been suggested, that the shape of the HLR peak is related to the morphology of domains in the electron system that have opposite spin and which can coexist at the transition point. It has also been shown, that the nuclear spin system is involved via the hyperfine interaction, which is thought to be the reason for the long timescales until the HLR settles [153]. Further details of the physics governing the HLR have been studied in the theses of S. Kraus [49] and O. Stern [154]. In Sec. 6.6 the influence of a current and its impact on the nuclear spin system is investigated in a way which is similar to the experiments shown in [49, 150, 154]. However, more details about the distinct influence of the nuclear spin system on the spin transition are presented in [154].

---

[2] Note, that the effective g factor is negative for bulk GaAs so that an increase leads at first to a decrease of its absolute value, which in turn determines the Zeeman splitting.

[3] This method has also been used to drive the comparable spin transition at $\nu = 2/5$ [149] and to explore the consequences of a vanishing effective g factor at $\nu = 1/3$ [84].

6.2 Influences on the competing energies

In various previous experiments by several groups [143, 146, 147, 151], the spin transition at $\nu = 2/3$ has been found at different critical magnetic fields or densities, which at first led to the assumption that the results of the different observations were not related to each other. The reason for the variability is due to the fact, that the actual critical magnetic field at the transition point is determined by the equality of the CF cyclotron energy $\hbar\omega_{\mathrm{c,CF}}$, which scales with the Coulomb correlation energy E_{C}, and the Zeeman energy E_{Z}. Both are not just functions of the magnetic field or density, but also depend on other significant parameters, the three most important of which are discussed below. The first parameter influences the Coulomb correlation energy and is the 2DES' finite thickness, which is often neglected but which can alter the Coulomb correlation energy substantially. The WQW structure with front and back gates offers the opportunity to arrange the charge distribution, which determines the finite thickness, and the electron density independently. This allows to drive the transition for different well defined electron distributions and to study systematically the influence of the finite thickness on the critical magnetic field. For narrow QWs ($w < 22$ nm) the finite thickness is determined by the physical confinement. The second parameter affects the Zeeman energy and is the effective g factor, which is, however, only subject to change in the case of narrow QWs ($w < 22$ nm) and is quantified in Subsec. 6.2.2. The third parameter is the additional magnetic field arising from the alignment of the nuclear spins and this also only affects the Zeeman energy. This nuclear magnetic field depends on the sample temperature and the external magnetic field but can be additionally altered as discussed in Sec. 6.6.

The dependence of the critical density or magnetic field of the spin transition can be modeled starting from the equality of CF cyclotron and Zeeman energy

$$\hbar\omega_{\mathrm{c,CF}} = E_{\mathrm{Z}}, \tag{6.1}$$

which holds at the transition point. The CF cyclotron energy reads (see Eqs. 2.20 and 2.21)

$$\hbar\omega_{\mathrm{c,CF}} = C_{\mathrm{C}} \frac{e^2}{4\pi\epsilon\epsilon_0 l_{\mathrm{B}}}, \tag{6.2}$$

where C_{C} acts as adjustment of the Coulomb correlation energy E_{C} to $\hbar\omega_{\mathrm{c,CF}}$. It is found numerically that C_{C} is of the order of 0.1 [155]. The Zeeman energy reads

$$E_{\mathrm{Z}} = C_{\mathrm{Z}} |g^*| \mu_B B, \tag{6.3}$$

where C_{Z} is introduced to account for a possibly enhanced Zeeman splitting [156]. All other variables are specified in Section 2.2.

6.2.1 Inclusion of finite thickness

The Coulomb correlation energy depends strongly on the average inter-particle distance between the electrons. The common length scale is the magnetic length l_{B}, which however does not account for the change of the average inter-particle distance due to a variable finite thickness of the 2DES. Therefore, an effective magnetic length $l_\mathrm{B}^\mathrm{eff}$ is defined. The collection of l_B and finite thickness to $l_\mathrm{B}^\mathrm{eff}$ is discussed in the following.

The Coulomb correlation energy can be calculated by taking into account the interaction between all electrons. The effective electron electron interaction potential of a quasi two-dimensional system can be written as [86]

$$V(|\vec{r_1}-\vec{r_2}|)=\frac{e^2}{4\pi\epsilon\epsilon_0}\int dz_1\int dz_2\frac{|\psi(z_1)|^2|\psi(z_2)|^2}{\sqrt{r^2+(z_1-z_2)^2}}, \tag{6.4}$$

where $\vec{r}=\vec{r_1}-\vec{r_2}$ is the vector within the plane of the 2DES between two electrons, $\psi(z)$ is the one-electron envelope wave function, which describes the distribution perpendicular to the plane, namely along the growth direction z, and $r^2=|\vec{r_1}-\vec{r_2}|^2$. The single layer regime, to which the WQW is tuned so that all electrons reside at one boundary of the WQW, is similar to the situation when a 2DES is formed at an interface of AlGaAs/GaAs. There, a roughly triangular confinement potential is present, which leads to an electron distribution that can be described by the Fang-Howard variational approximation [10]

$$\psi(z)=\left(\frac{b^3}{2}\right)^{1/2}ze^{-bz/2}, \tag{6.5}$$

where b represents its width. The total Coulomb correlation energy results from a sum over all of pairs of electrons, which interact with each other according to the above given potential. The spatial distribution within the plane is taken into account by using Laughlin's wave function (here for the FQHE at $\nu=1/3$)

$$\Psi=\prod_{j<k}(\mathbf{z}_j-\mathbf{z}_k)^3\exp\left(-\sum_j\frac{1}{4}\frac{|\mathbf{z}_j|^2}{l_\mathrm{B}^2}\right). \tag{6.6}$$

Usually, the numeric result is given in units of $e^2/(4\pi\epsilon\epsilon_0 l_\mathrm{B})$ per electron and strongly depends on the actual width b.

For simplification, *i.e.* easier inclusion of the finite thickness, it has been shown [86] that the effective interaction potential as well as the final Coulomb correlation energy (per electron), which is identical to the single particle excitation gap (activation energy E_A) of the FQH state, can be fairly well modeled by (see Fig. 6.2)

$$V(r)\propto\frac{1}{\sqrt{r^2+\Delta z^2}}, \tag{6.7}$$

and

$$E_\mathrm{C}(\Delta z)\propto\frac{1}{\sqrt{r_0^2+(\Delta z)^2}}, \tag{6.8}$$

where r_0 is the fixed mean intra-layer distance between two electrons, which is of the order of the magnetic length and depends on the filling factor as $1/\sqrt{\nu}$ [157]. From Fig. 2 of [86] it

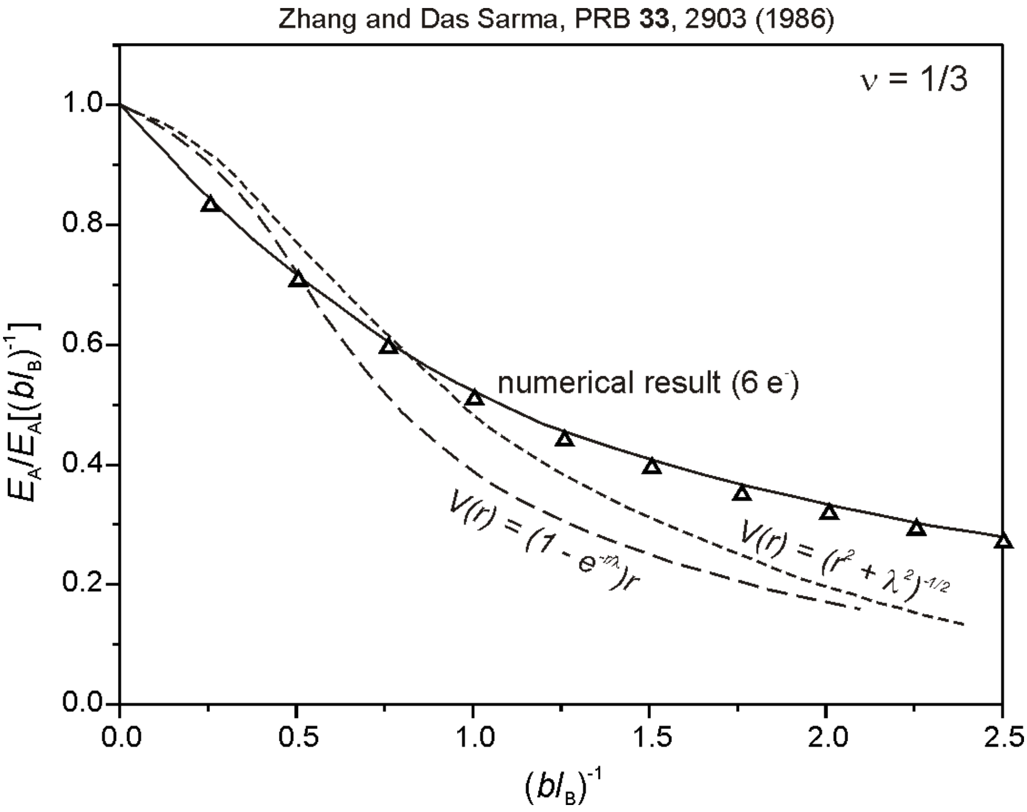
Zhang and Das Sarma, PRB **33**, 2903 (1986)

Figure 6.2: Variation of the activation energy E_A of $\nu = 1/3$ with increasing finite thickness (parameter b of Eq. 6.5) of a 2DES. The numerical result is compared to results for electron electron interaction potentials $V(r)$ with the finite thickness λ included in different ways.

can be deduced that $r_0 = \sqrt{3/8}l_\mathrm{B}$ at $\nu = 1/3$. Δz is the average separation between any two electrons in the direction perpendicular to the electron layer

$$(\Delta z)^2 = \langle \Psi | (z_1 - z_2)^2 | \Psi \rangle, \tag{6.9}$$

where Ψ is the wave function of the FQH state. A natural and easily deducible quantity that can be used to characterize the finite thickness of an electron layer is its FWHM λ. When the electron distribution follows the Fang-Howard variational approximation, the relation $\lambda = 2\Delta z$ holds[4] in good approximation [86]. Altogether, Eq. 6.8 can be rewritten as

$$E_\mathrm{C}(\lambda) \propto \frac{1}{\sqrt{l_\mathrm{B}^2 + \lambda^2}}, \tag{6.10}$$

for the case $\nu = 2/3$. The application of the particle hole symmetry, according to the relation $2/3 = 1 - 1/3$ between the filling factors, is used here, in order to pass over from the wave function at $\nu = 1/3$, for which the previous definitions are valid, to the here relevant wave

---

[4] In principle, one can also use the parameter b of Eq. 6.5 to account for the finite thickness, but the FWHM λ can be more easily quoted here.

function, which applies at $\nu = 2/3$. The effective magnetic length can thus be defined as

$$l_{\mathrm{B}}^{\mathrm{eff}} = \sqrt{l_{\mathrm{B}}^2 + \lambda^2}. \tag{6.11}$$

The finite thickness λ of the electron layer, as adjusted in the experiments using the WQW structure (see Subsec. 6.2.5), is extracted from simulations based on the self consistent solution of Poisson and Schrödinger equations using the program Poisson-Solver (see footnote on page 36.). The dimensions of the WQW structure as necessary input parameters to the program are slightly modified[5] compared to the nominal values, with the intention that every simulated configuration results in a density, which deviates from the experimentally found density by less than 3%. Configuration denotes here every pair of applied front and back gate voltages, which are the only variable input parameters to the program. In Subsec. 6.2.5 a wide range of gate voltage pairs is presented, for which the spin transition is observed with the WQW structure, and each pair defines such a configuration. The good agreement between experimentally determined and calculated density is important because it allows to deduce the correct finite thickness λ of the 2DES.

6.2.2 Confinement in QWs and influence on the effective g factor

To be able to account for the different critical magnetic fields of the spin transitions found for QW structures (results are presented below), the effect of the additional confinement has to be considered. A confinement not only influences the Coulomb correlation energy by means of the imposed finite thickness, but affects even more drastically the Zeeman energy, since the effective g factor is altered, as pointed out by Hashimoto *et al.* [159].

The finite thickness of a 2DES confined in a narrow (< 22 nm) QW is approximately given by half the QW width w plus about 8 to 10% ($\lambda \approx w/2 \times 1.1$) if the QW width is not too small, *i.e.* still larger than 14 nm as relevant here. This supplement of 8 to 10% is due to a finite penetration of the wave function into the barriers of the QW, since they are energetically not infinite in height. The given value is found with quantum mechanical calculations based on an analytical ansatz. The supplement further increases when w decreases.

The change of the effective g factor in the case of narrow QWs is mainly due to the confinement induced light-hole heavy-hole splitting in the valence band [160]. Consequently, this effect only exists for QWs, since in the case of an SHI only the electrons are confined. Furthermore, the confinement of a QW leads to an anisotropic effective g factor. Actually, the effective g factor is a tensor [161] and for QWs the three diagonal components are no longer equal. In the literature the two different principal components are labeled $g_{\parallel}^*$ and $g_{\perp}^*$ valid for a magnetic field applied parallel or perpendicular to the *growth* direction. The growth direction is here along the [001] axis of GaAs. The confinement induced change of the effective g factor

---

[5] For example, a thickness of 20.7 nm is used for the GaAs cap layer instead of the nominal value 20 nm. A comparable adjustment is applied to the thickness of the lower spacer. The Al contents are taken according to their nominal values. The doping densities are adjusted based on reasonably estimated values of the order of 10^{23} m^{-3} [158].

is more pronounced for $g^*_\perp$ than $g^*_\|$. Relevant here is $g^*_\|$, since the magnetic field is applied perpendicular to the 2DES, *i.e.* parallel to the growth direction. In some publications $g^*_\|$ is also labeled g_{zz} as in [162]. An experimental study of the different components in dependence of the QW width has been carried out by Hannak *et al.* [163] and also by Le Jeune *et al.* [164]. There, as in most other cases, $g^*_\|$ could not be directly measured, because the method used of spin quantum beats due to Kerr rotation [165] employs a magnetic field applied perpendicularly to the growth direction. The magnetic field component along the growth axis is then realized by a tilt of the sample with respect to the magnetic field axis. The tilt angle is usually taken between the plane of the 2DES and the magnetic field axis. The tilt angle relevant her of 90°, however, no longer provides the necessary magnetic field within the plane of the 2DES. The measured effective g factor is a tilt angle dependent combination of $g^*_\|$ and $g^*_\perp$ as given in [164]. A fit of the determined dependence on the tilt angle with the theoretically expected variation allows an extrapolation to tilt angle 90°, which yields $g^*_\|$. The calculated and experimentally refined variation of the two different components of the effective g factor with the QW width w is plotted in Fig. 6.3.

The component of the effective g factor relevant here steadily increases with ever stronger confinement and even changes its sign at a QW width of about 5.5 nm [163]. It should be again noted, that this strong variation of the effective g factor is due to a confinement induced light-hole heavy-hole splitting in the valence band of GaAs and not just due to an increased penetration of the electron wave function of the 2DES, confined to the QW, into the AlGaAs barrier. In fact, bulk AlGaAs has a markedly different effective g factor than bulk GaAs depending on the Al content. The inset to Fig. 6.3 shows the effective g factor for bulk AlGaAs as a function of the Al content according to [96]. At an Al content of about 13% the effective g factor changes its sign. Simulations using the quantum mechanical program of S.-J. Cheng (see Sec. 4.1) allow to determine the wave function's penetration into the barrier as a function of the QW width. Calculations of the effective g factor by weighting the relevant value of g^* (+0.4 in the AlGaAs barrier with an Al content of 30%, as valid here, while -0.44 in GaAs) with the electron distribution function, result in little change of the effective g factor even below QW widths of 5.5 nm. Therefore, merely accounting for the penetration is not sufficient. However, if the electron layer is increasingly squeezed towards one of the edges of the WQW, its penetration into the AlGaAs barrier is enlarged and the effective g factor of the total electron system slightly increases [162, 166]. This induced change of the effective g factor is only of the order of one percent, as indicated by calculations and experimental results [166].

Finally, it is important to consider the variation of the effective g factor with an applied magnetic field

$$\Delta g^* = 0.007 \times B[\mathrm{T}], \tag{6.12}$$

as determined with ESR measurements [167]. This dependence is due to the non-parabolicity [168] of the $E(\vec{k})$ dispersion relation of the various bands around the Γ-point of the conduction band [168] and to the larger $\vec{k}$ in GaAs.

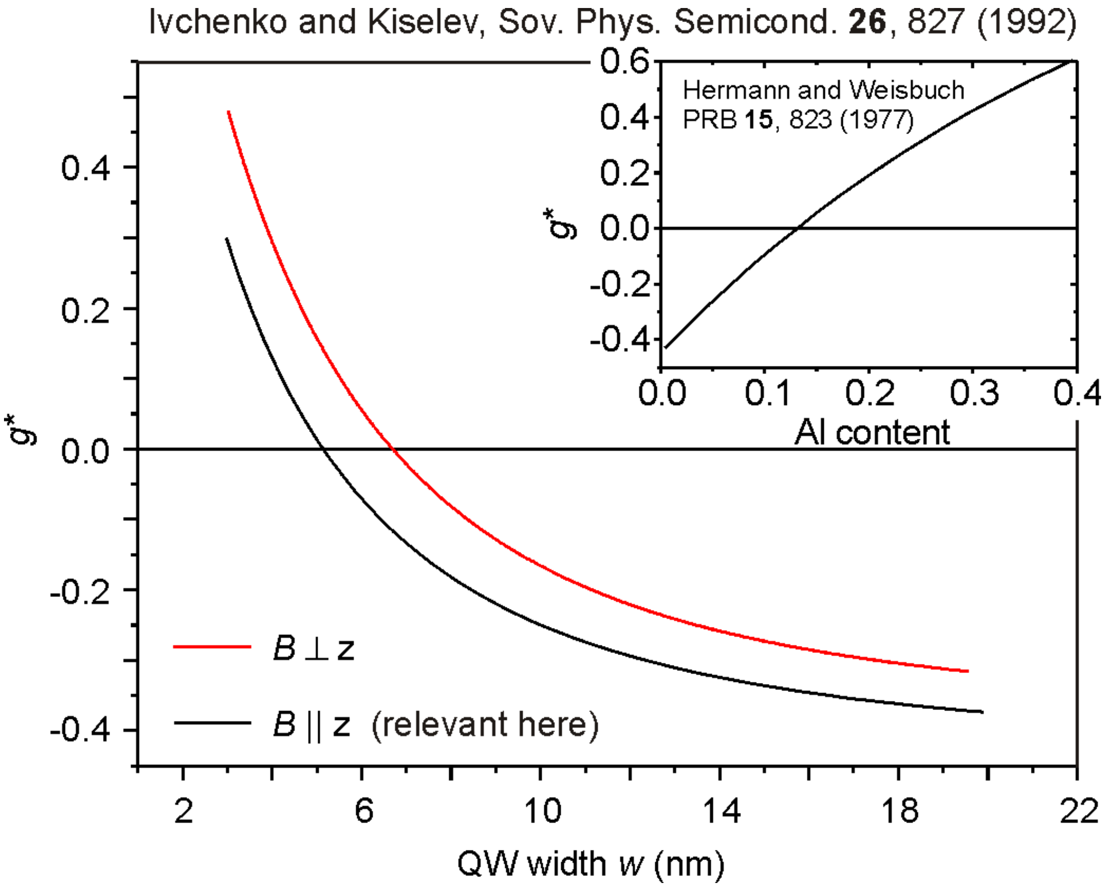

Figure 6.3: Variation of the effective g factor with the QW width w. Due to confinement effects, the effective g factor is anisotropic, *i.e.* is a function of the orientations of the external magnetic field B relative to the growth direction z, which is the normal axis to the plane of the QW. The inset depicts the effective g factor of bulk AlGaAs in dependence of the Al content.

6.2.3 Nuclear magnetic field

A nuclear magnetic field arises from a net nuclear spin polarization. The electrons can interact with the nuclei by means of the hyperfine interaction, whose Hamiltonian reads

$$H_{\mathrm{HF}} = \sum_{j,k} A\hat{\mathbf{I}}_j\hat{\mathbf{S}}_k, \tag{6.13}$$

where $\hat{\mathbf{I}}_j$ and $\hat{\mathbf{S}}_k$ are the nuclear and electron spin operators and

$$A = \frac{8}{3}\pi g^* \mu_B g_{\mathrm{N}} \mu_{\mathrm{N}} |\psi(0)|^2 \langle \mathrm{I} \rangle, \tag{6.14}$$

is the hyperfine coupling constant with g_{N} and μ_{N} the nuclear effective g factor and nuclear magnetic moment. $\langle \mathrm{I} \rangle$ is the average nuclear spin polarization. The hyperfine interaction ($\mathrm{I} \cdot \mathrm{S}$ coupling) depends on the probability $|\psi(0)|^2$ to find an electron at the site of a nucleus. For that reason this coupling is also known as Fermi contact interaction. The mentioned probability is largest for s-type electrons as present at the conduction band edge of GaAs. Holes at the valence band edge, however, are of p-type, consequently the hyperfine interaction in their case is much weaker. A two-dimensional hole gas (2DHS) is discussed in Subsec. 6.8.4. There are two mechanisms that can induce nuclear spin polarization. One is a sufficiently low temperature together with the presence of an external magnetic field. The other is a dynamically induced nuclear spin polarization due to electron-nucleus spin flip-flop processes, because the Hamiltonian of Eq. 6.13 can be rewritten as

$$H_{\mathrm{HF}} = \sum_{\mathrm{electrons,nuclei}} A[1/2(\hat{I}_{+}\hat{S}_{-} + \hat{I}_{-}\hat{S}_{+}) + \hat{I}_{\mathrm{z}}\hat{S}_{\mathrm{z}}], \tag{6.15}$$

where the plus and minus indexed variables are the spin flip-flop operators. It is therefore possible to induce a nuclear spin polarization or change it by means of spin flips in the electron system. Such spin flips can be achieved *e.g.* by means of interacting edge channels [169–172] or optical orientation (see [173–175] and references therein).

The actual nuclear magnetic field depends on the average nuclear spin polarization $\langle \mathrm{I} \rangle$, which is in the absence of any intentionally altering influence a function of the temperature T_{c} of the crystal, which hosts the electron system, and the external magnetic field B. The average nuclear spin polarization of the individual isotopes i present in GaAs[6] $i = {}^{69}$Ga, ^{71}Ga, ^{75}As is determined by Boltzmann statistic (paramagnetic ordering) and can be calculated with the Brillouin function $B_J(X)$

$$\langle \mathrm{I} \rangle_i = B_{J_i}(J_i \gamma_i h B / k_{\mathrm{B}} T_{\mathrm{c}}), \tag{6.16}$$

where γ_i is the gyromagnetic ratio ($\gamma \propto g_{\mathrm{N}}\mu_{\mathrm{N}}$ for each nucleus), J_i is the total nuclear spin of the isotope i, and k_{B} is Boltzmann's constant. Typically, the values for γ_i are given in units of MHz/T and are of the order of 100 MHz at 10 T. The Brillouin function is defined as

$$B_J(X) = \frac{2J+1}{2J} \coth\left(\frac{(2J+1)X}{2J}\right) - \frac{1}{2J}\coth\left(\frac{X}{2J}\right), \tag{6.17}$$

where $X = J_i \gamma_i h B / k_{\mathrm{B}} T_{\mathrm{c}}$. The total nuclear field is then

$$B_{\mathrm{N}} = -\sum_i A_i J_i \langle \mathrm{I} \rangle_i. \tag{6.18}$$

The individual hyperfine coupling constants A_i have to be determined experimentally as has been done by Paget *et al.* [176]. The last equation can be simplified to

$$B_{\mathrm{N}} = A \langle \mathrm{I} \rangle, \tag{6.19}$$

where A is a unified hyperfine coupling constant and

$$\langle \mathrm{I} \rangle = \sum_i \frac{1}{2} a_i J_i \langle \mathrm{I} \rangle_i, \tag{6.20}$$

---

[6] The contribution of the Al nuclei, which are incorporated exclusively in the barriers, is negligible, because the electron layer resides almost entirely in GaAs independent of the certain structure, *i.e.* SHI, WQW, or QW.

where a_i represents the abundance of the individual isotope on the lattice site, and the factor 1/2 is due to the two different lattice sites in GaAs. In the following, the relevant material parameters are listed:

- $i = {}^{69}\mathrm{Ga}$, $J_i = 3/2$, $a_i =$ 60.4%, $\gamma_i = 10.219$ MHz/T, $A_i = -0.91$,
- $i = {}^{71}\mathrm{Ga}$, $J_i = 3/2$, $a_i =$ 39.6%, $\gamma_i = 12.984$ MHz/T, $A_i = -0.78$,
- $i = {}^{75}\mathrm{As}$, $J_i = 3/2$, $a_i =$ 100%, $\gamma_i = 7.2919$ MHz/T, $A_i = -1.84$.

The total nuclear spin of all isotopes is $J_i = 3/2$ and is from here on referred to as J. The sum of the A_i yields the unified hyperfine coupling constant $A = -3.53$. A measurement found $A = -3.7$ [177]. Using the material parameters, the nuclear magnetic field can be explicitly calculated, where the crystal temperature T_c and the externally applied magnetic field B are the only input parameters

$$\begin{aligned} B_\mathrm{N} = -J \times [&0.91 \times B_J(J\gamma({}^{69}\mathrm{Ga})hB/k_\mathrm{B}T_\mathrm{c}) \\ &+ 0.78 \times B_J(J\gamma({}^{71}\mathrm{Ga})hB/k_\mathrm{B}T_\mathrm{c}) + 1.84 \times B_J(J\gamma({}^{75}\mathrm{As})hB/k_\mathrm{B}T_\mathrm{c})]. \end{aligned} \tag{6.21}$$

A plot of the result is given in Fig. 6.4 for the relevant range of the external magnetic field and crystal temperature. As can be seen, the typical values of B_N expected in the experiments here are lower than -0.4 T which is confirmed in experiment (see Sec. 6.5). When the crystal temperature approaches zero ($T_\mathrm{c} \to 0$ K), the Brillouin function tends to unity and the nuclear magnetic field reaches $B_\mathrm{N} = -J \times (0.91 + 0.78 + 1.84) = -J \times 3.53 = -5.29$ T [156].

Because of the absence of spin-orbit interaction in the conduction band of GaAs [178], neither the cyclotron energy nor the Coulomb correlation energy are affected by B_N, regardless of the magnitude or sign of B_N. Instead, the nuclear magnetic field contributes solely to the Zeeman energy ($E_\mathrm{Z} = g^*\mu_B(B + B_\mathrm{N})$) and since it points in the opposite direction[7] to the external magnetic field, the Zeeman energy is reduced [169].

6.2.4 How the critical magnetic field of the spin transition is altered

The variation of the decisive energy scales $\hbar\omega_\mathrm{c,CF}$ and E_Z with magnetic field or density are schematically plotted in Fig. 6.5 together with the influence of the different parameters, which affect these energies. The critical magnetic field B_S or density n_S at the spin transition is given by the equality of both energies. A reduced finite thickness λ enhances the Coulomb correlation energy and thus $\hbar\omega_\mathrm{c,CF}$ which rises B_S and n_S. A smaller absolute value of the effective g factor reduces the Zeeman energy which causes a shift of B_S and n_S to higher values. The finite thickness is determined by the actual confinement potential of the 2DES and can be adjusted in the case of the WQW structure. With respect to the variability of g^*, the WQW structure can be regarded as an SHI because of its large width. For a narrow ($w < 22$ nm) QW, the

---

[7] The opposite direction of the nuclear magnetic field is accounted for by a negative sign of B_N. But B_N can be intentionally altered as previously mentioned so that even positive values are possible, see *e.g.* [174].

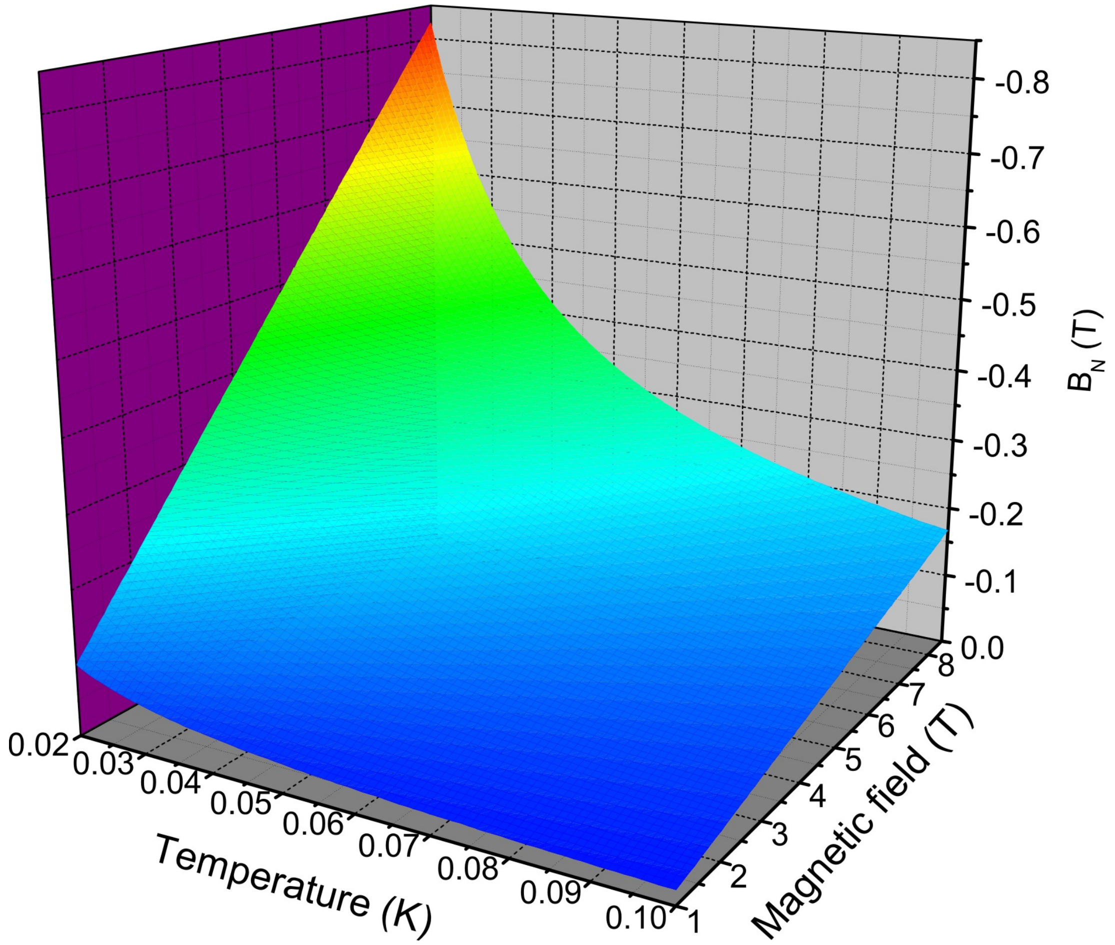

Figure 6.4: Calculated nuclear magnetic field B_N for the here relevant ranges of the crystal temperature T_c and the external magnetic field B.

finite thickness is governed by the width w of the QW. The effective g factor is altered due to the confinement in the valence band as only provided by a QW structure [179]. Therefore, the characteristic B_S or n_S value of a certain narrow QW is larger when compared to an SHI structure that provides the same finite thickness λ. A stronger negative nuclear magnetic field B_N increases B_S and n_S. The detailed relation between B_N and the additional shift of the critical magnetic field is discussed in Sec. 6.5. At first glance, B_N leads to a further increase of B_S by about $1.5 \times B_\mathrm{N}$; the actual ratio $\Delta B_\mathrm{S}/\Delta B_\mathrm{N}$ is discussed in Sec. 6.5.

6.2.5 Measurements, fit and discussion

A series of measurements is carried out to determine the variation of the critical magnetic field or density of the spin transition in dependence of the 2DES' finite thickness using the WQW structure. The back gate voltage is fixed to a certain value in the range from -3.7 V to +0.6 V. The range of the back gate voltage allows a redistribution of the quasi 2DES from a squeezed electron layer at the lower interface ($U_\mathrm{BG} = +0.6$ V) to a loosely confined sheet at the upper

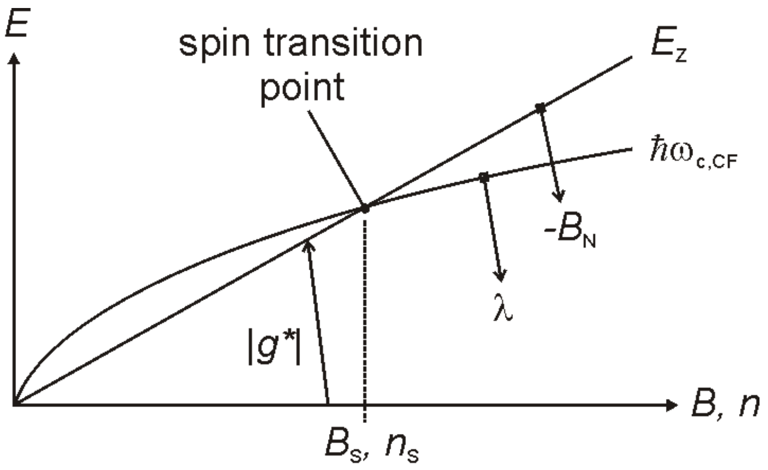

Figure 6.5: Schematic picture of the dependencies of the CF cyclotron $\hbar\omega_{\mathrm{c,CF}}$ and Zeeman energy E_{Z} competing for the spin transition. $\hbar\omega_{\mathrm{c,CF}}$ scales with the square root of the external magnetic field B or density n, whereas the Zeeman energy is a linear function of B or n at fixed filling factor $\nu = 2/3$. The slope of E_{Z} is given by the absolute value of the effective g factor. E_{Z} is further altered by the nuclear magnetic field B_{N}. A larger width λ of the electron wave function lowers $\hbar\omega_{\mathrm{c,CF}}$. Changes of the different decisive parameters leads to a relocation of the spin transition point to another value of B_{S} or n_{S}.

interface ($U_{\mathrm{BG}} = -3.7$ V). The limit to higher back gate voltage is the onset of parallel conductivity, the limit to lower back gate voltage is the increasing leakage current. The spin transition is located by a sweep of the density with the front gate alone which is equivalent to step along the abscissa of the plot in Fig. 6.5. At each density step the magnetic field is swept around $\nu = 2/3$ and R_{xx} recorded. Scans of the density and magnetic field across the spin transition are given in Fig. 6.6 for two very different values of the back gate voltage together with the simulated electron distribution.

Equivalent scans are taken at about 20 different back gate voltages. The critical magnetic field B_{S} or density n_{S} is deduced from each scan using the resistance peak, which cuts through the plateau region of $\nu = 2/3$, as indicator (see Sec. 4.2). B_{S} or n_{S} is assigned when the peak is located at filling factor $\nu = 2/3$, *i.e.* close to the center of the plateau region. All determined values of n_{S} are plotted versus the used back gate voltage in Fig. 6.7 together with the necessary front gate voltage at the spin transition point. According to Subsec. 6.2.4, the lowest value of n_{S} is expected when the wave function is broadest, *i.e.* when the WQW is balanced or its potential untilted, because this situation provides the weakest confinement potential. The spin transition can be located for any back gate voltage except for a small range (± 0.3 V) around $U_{\mathrm{BG}} = -3.2$ V. There, the spin transition cannot be induced because n_{S} turns out to be too low and consequently the FQHE at $\nu = 2/3$ is destroyed by disorder. To even lower as well as higher back gate bias, n_{S} can be determined and increases symmetrically around $U_{\mathrm{BG}} = -3.2$ V when the back gate voltage is tuned further away from this value. This suggests that at $U_{\mathrm{BG}} = -3.2$ V the balanced case is reached leading to the largest width of the 2DES

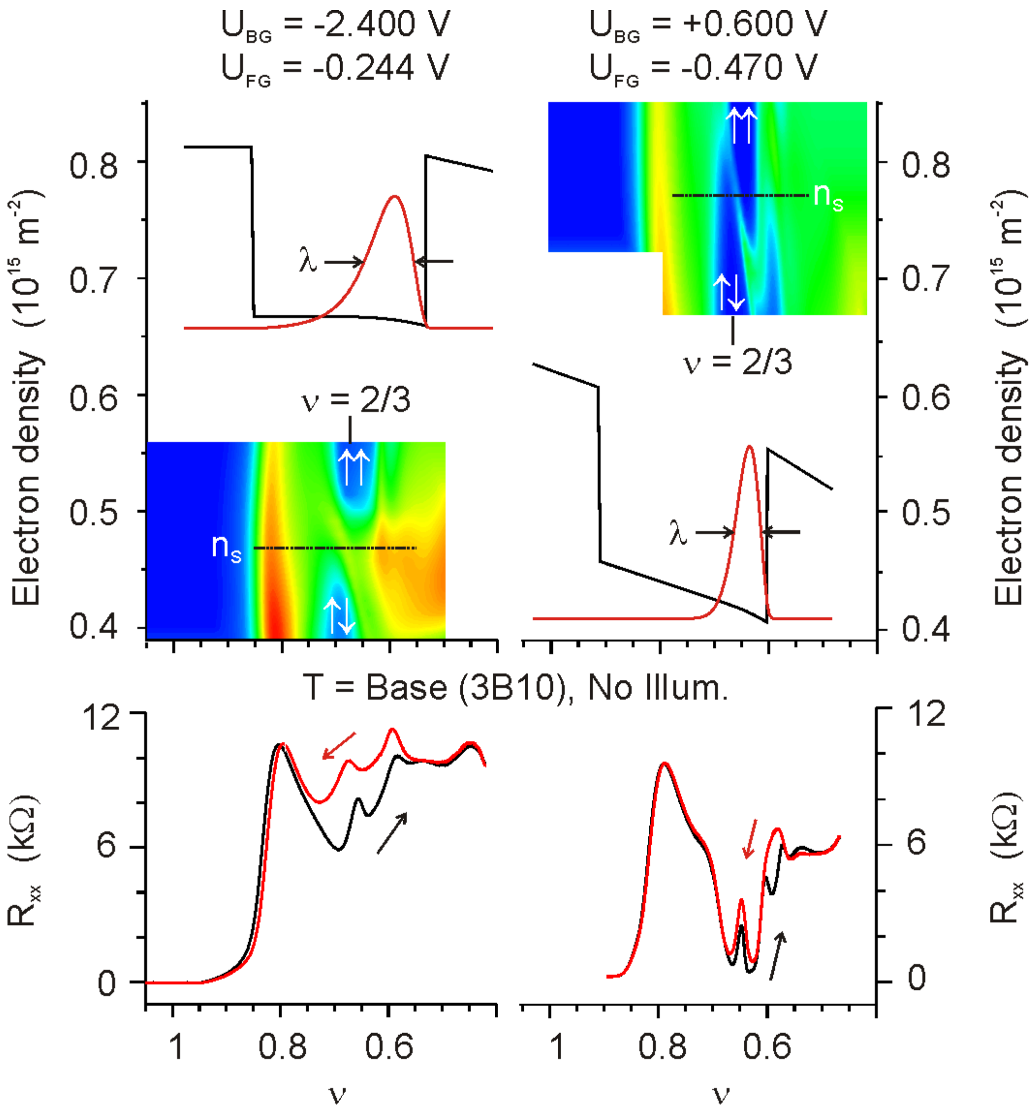

Figure 6.6: Color plots of $R_{\rm xx}$ measurements obtained by scans of the density and magnetic field across the spin transition for two different electron distributions in the WQW as shown (the growth direction z is to the left). The transition is indicated by the resistance peak, which cuts through the plateau region of $\nu = 2/3$. A broad wave function results in a low critical density $n_{\rm S}$ of the spin transition, whereas a narrower electron layer exhibits a higher $n_{\rm S}$ value. In the lower panel, traces of the longitudinal resistance $R_{\rm xx}$ at $n_{\rm S}$ are given, which display the transition peak in the center of the plateau region of $\nu = 2/3$ accompanied by hysteresis.

and the smallest Coulomb correlation energy. In Fig. 6.8 the different critical magnetic fields $B_{\rm S}$ and densities $n_{\rm S}$ are plotted versus the finite thickness λ of the electron layer as deduced for each pair of gate voltages from the simulations mentioned in Subsec. 6.2.1.

The reduction of $B_{\rm S}$ with the increasing width of the wave function is similar to the dependence of the excitation gap of FQH states on the finite thickness of a 2DES as calculated by several authors [86, 155, 180, 181]. The close relationship between a larger finite thickness and

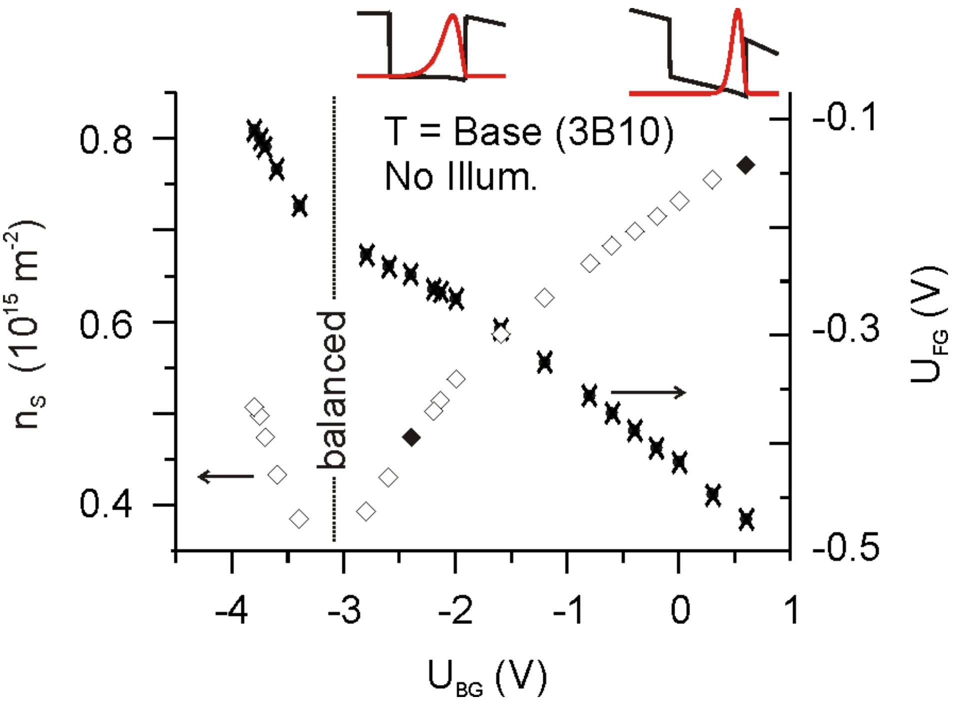

Figure 6.7: Variation of the experimentally determined critical densities n_S of the spin transition with back gate voltage applied to the WQW structure. A minimum in n_S is found around $U_{BG} = -3.2$ V representing the balanced case. The two filled diamonds correspond to the two depicted charge distributions. Also plotted is the corresponding critical front gate voltage at the spin transition point.

a reduced critical magnetic field allows to state, that a small critical magnetic field as in [143] (3.3 T), where an SHI structure was used, indicates a broad wave function. The width of the wave function is determined by the present confinement potential. In the case of an SHI structure, the confinement is influenced by several parameters such as the spacer thickness and the doping density. In particular, the type and magnitude of the background doping is important, because it determines the conduction band profile away from the AlGaAs/GaAs interface deeper into the structure. Usually, the background doping is p-type and reduces the mobility when its density is larger. A larger background doping density leads to a faster rise of the conduction band profile away from the interface (towards smaller z, see Fig. 2.1b). This faster rise in turn causes a stronger confinement. It is therefore expected, that SHI structures with a higher quality, *i.e.* lower background doping, will exhibit a smaller critical magnetic field, although otherwise identical. Two almost equal SHI structures of different quality exhibit critical magnetic field of $B_S = 4.9$ T [182] and $B_S = 3.3$ T [143]. The mobilities of both samples are 600 m^2/Vs but in the first case at a density of 2.0×10^{15} m^{-2} while at 0.7×10^{15} m^{-2} in the second case; the mobility scales as $n^{0.7}$ [183] so that the quality of the second SHI structure can be regarded as superior compared to the first one. In conclusion, the critical magnetic field of the spin transition is in the case of SHI structures a measure of the quality of the structure with respect to the background doping density.[8] This noticeable influence of the background doping on the critical magnetic field is almost absent in the case of QW structures (including the WQW).

The variable parameters that influence the Zeeman energy, apart from the external magnetic field, are the effective g factor and the nuclear magnetic field. The effective g factor is a function of the QW width w. Since the finite thickness λ is also a function of the QW width, g^* can be expressed as a function of λ. In the case of an SHI g^* is roughly constant. Additionally, the external magnetic field changes g^*. The nuclear magnetic field is at a constant temperature a function of the external magnetic field. The variable parameters that influence the CF cyclotron energy are the magnetic length, which is given by the external magnetic field, and the finite thickness λ. So all parameters that influence either the Zeeman or the CF cyclotron energy can be expressed in dependence of the external magnetic field B and the finite thickness λ. From this it follows that the equality of $\hbar\omega_{\mathrm{c,CF}}$ and E_{Z}, valid at the spin transition point according to Eq. 6.1, can be solved for B. It results in an implicit equation for the critical magnetic field B_{S} depending on λ and can be numerically fitted to the experimentally found data for B_{S} as a function of λ with $C_{\mathrm{C}}/C_{\mathrm{Z}}$ as the only fit parameter. The least square root fit to the data shown in Fig. 6.8 yields $C_{\mathrm{C}}/C_{\mathrm{Z}}$ = 0.0174 if the nuclear magnetic field is neglected. Including a variable nuclear magnetic field according to the experimentally found increase (see Sec. 6.5) of B_{S} by about 0.4 T to 4.5 T caused by a cool down from 250 mK to base temperature ($\approx$ 40 mK)[9], the fit results in $C_{\mathrm{C}}/C_{\mathrm{Z}} = 0.0167$. The theoretical value of $C_{\mathrm{C}} \approx 0.092$ [184] leads to the suggestion that the Zeeman splitting is enhanced by $C_{\mathrm{Z}} \approx 5.4$. A quite similar value has been found by Tutuc *et al.* [97] for such a dilute electron gas. Furthermore, this enhancement is surprisingly equal to the one found in Sec. 5.3 by the analytic analysis of the LL coincidences at $\nu_{\mathrm{tot}} = 3, 4, 5$. But this correspondence is not necessarily significant, since the enhancement is a function of the filling factor [95]. However, the experiments in [184] show, that $C_{\mathrm{C}} \approx 0.092$ is usually an upper limit, which leads to the conclusion that the found enhancement is also an upper limit. Freytag *et al.* found an enhancement of 1.54 at $\nu = 2/3$ [185] but at twice as high magnetic field values.

Even if the wave function is strongly squeezed to one interface, its penetration into the barrier material remains low. But nevertheless, the absolute value of the effective g factor is slightly reduced and as is also, therefore the Zeeman splitting, which in turn leads to a higher critical magnetic field. The resultant increase of the critical magnetic field can be estimated from [166] to be in maximum 2.5% for the range of the confinement investigated here with the WQW. Therefore, this influence is neglected.

In addition to the WQW structure three different QW structures are used of width 22 nm, 15 nm, and 18 nm. The latter is actually the DQW structure fabricated here, as described in

---

[8] In the case of n-type background doping the critical magnetic field will be hardly affected by the actual background doping density, because the variation of the confinement potential with the density of dopants is in this case small.

[9] In this thesis the term "base temperature" denotes the lowest temperature of the dilution refrigerator cryostat used for the measurement. A brief description of the different cryogenic systems is given in Appendix A.2. Every cryogenic system has a slightly different base temperature but all are of the same order.

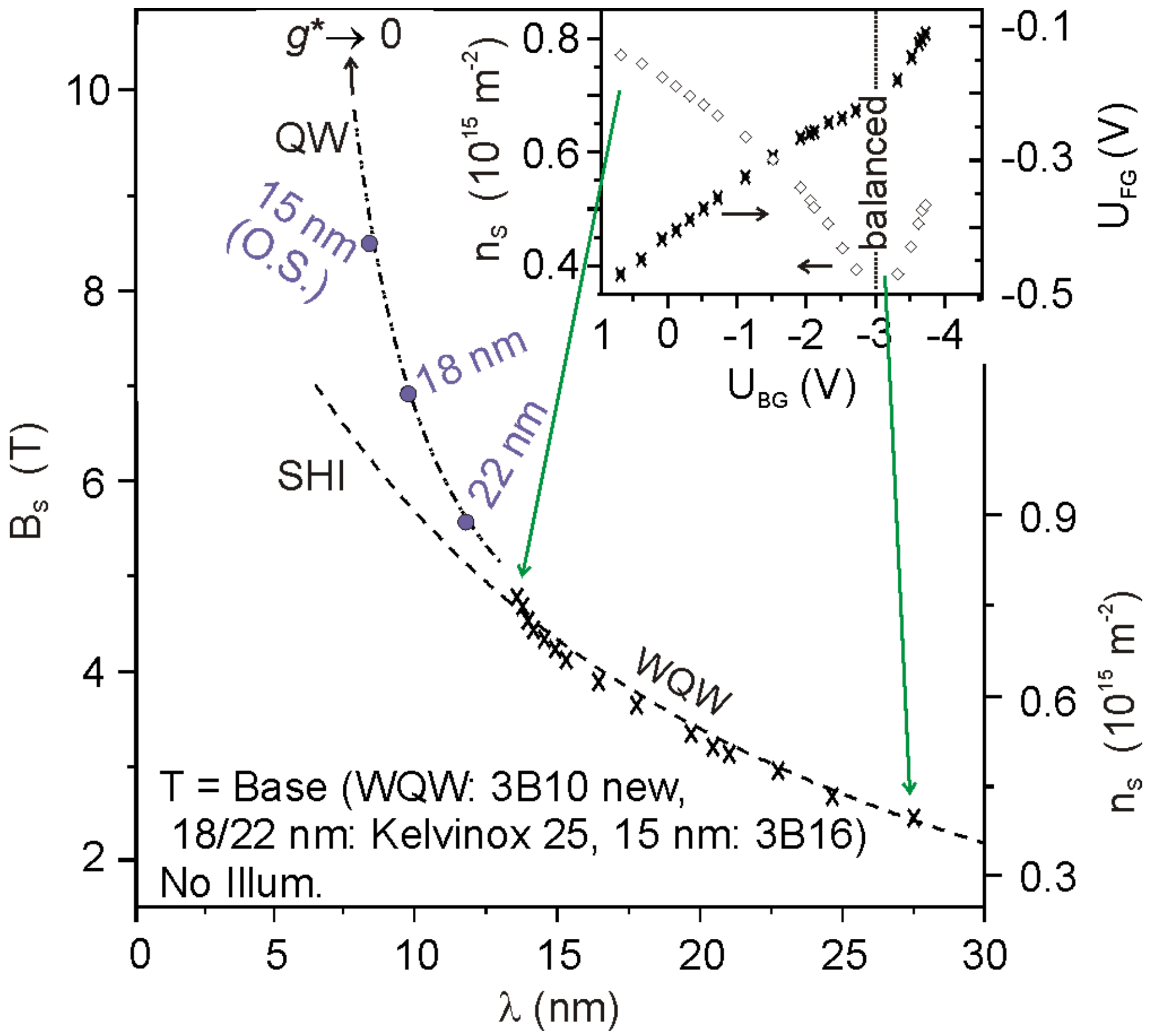

Figure 6.8: Plot of the experimentally determined critical magnetic fields B_C or densities n_S of the spin transition versus the finite thickness λ of the electron layer, as deduced from corresponding simulations, and measured as FWHM. The dashed line is a fit of Eq. 6.1 to the data obtained with the WQW structure and is extrapolated to narrower wave functions. The increase of B_C towards smaller λ is different for SHI and QW structures due to the additional change of the effective g factor in the case of QW structures. This effect is included in the dash-dotted line and the data points for three different QW structures are shown. B_S diverges when the effective g factor changes its sign.

Sec. 3.1. Hence, it should be kept in mind that in this case the electrons are confined on one side by a small barrier of AlAs. In the experiments, which are further discussed in Sec. 6.7, one of the two QWs is depleted with the front or back gate while the other gate is used to sweep the density in the second QW. The data concerning the 15 nm QW are either supplied by O. Stern (O.S.) [154] or S. Kraus (S.K.) [49]. The sample of S.K. is a DQW structure without tunnel coupling because of a 20 nm thick AlGaAs barrier between the two 15 nm wide QWs. The

22 nm wide QW is designed according to the dependence of the critical magnetic field on λ, as found with the help of the WQW structure and the other two QW structures. The spin transition points derived at a temperature of 250 mK are: 4.8 T (22 nm), 6.6 T (18 nm), 9.4 T (S.K.). The critical magnetic field of the sample of O.S. has not been determined at this temperature. The spin transition points derived at base temperature ($T \approx$ 40 mK, but the measurements were carried out using different cryogenic systems) are: 5.4 T (22 nm), 7.2 T (18 nm), 8.3 T (O.S., $T = 22$ mK) and $\approx$ 10.5 T (S.K., average value, because although nominal identical, the results differ for the two QWs, see the discussion below). Kumada *et al.* [186] explored a DQW structure with an AlGaAs barrier of 3.1 nm between the two 20 nm wide QWs (structure M3 of Tab. 3.1). They observe in the monolayer limit, *i.e.* one QW is depleted, and at a temperature of 50 mK the spin transition at a density of 0.95$\times 10^{15}$ m^{-2} and magnetic field of 5.9 T, which is in good agreement with the expectations for such a structure according to the measurements here. They deduced at only one critical magnetic field (5.9 T) the relation $C_\mathrm{C}/C_\mathrm{Z} = 0.026$ which is far off the one here. One reason for this is that they neglect finite thickness and a further reason is that they used a magnetic length defined on the basis of the effective magnetic field (see Eq. 2.18).

The theory noted above and validated with the WQW data can also very well account for the critical magnetic fields found for the different QWs if the change of the effective g factor due to the additional confinement in the valence band is further included. It is thus possible to predict the critical magnetic field of a certain QW structure which is even applied here. The 22 nm wide single QW is fabricated accordingly with the aim of achieving a critical field slightly above 5 T at base temperature. This is achieved, which demonstrates, how well the location of the spin transition can be predicted with the help of the detailed finite width study carried out here. In Fig. 6.8 it is also shown, how the critical magnetic field develops towards stronger squeezed electron layers. Below a finite thickness λ of the electron layer of about 13 nm, the type of confinement has to be considered. If squeezed by a further steeper triangular potential of an SHI structure, the effective g factor is only slightly affected, as discussed above, and the critical magnetic field increases steadily but will approach a finite value towards zero finite thickness. If the confinement is provided by a QW structure, which is experimentally the only possibility available to reach much stronger confinements, the effective g factor is heavily altered and dominates the variation of the critical magnetic field. Since the effective g factor changes its sign at a critical QW width of about 5.5 nm, the critical magnetic field is expected to diverge there, but towards even narrower QW structures B_S will be finite again.

The distinct sensitivity of B_C with respect to the actual finite thickness is most apparent in the case of the DQW structure of S.K. [49]. The critical magnetic fields of the two nominally identical 15 nm wide QWs differ by more than 1 T at base temperature (and are also quite different from the critical magnetic field found for the single QW structure of O.S. having the same nominal width). The spin transition in the lower QW is located slightly above 11 T while a value of 10 T is found for the upper QW at base temperature. The most probable reason is a noticeable difference in the width of the two QWs which leads to different Coulomb correlation energies but more importantly to different effective g factors. According to the above found dependence, a reduction of the QW width from 15 nm down to 14.5 nm already causes an increase of the critical magnetic field by almost 1 T. This demonstrates the significant influence of already slight variations in the QW width once they are very narrow. If the potential of a QW (wider than 5.5 nm) is tilted, the absolute value of the effective g factor is further decreased, which leads to an additional increase of the critical magnetic field of the spin transition. However, this effect is less pronounced on a relative basis if the QW is very narrow [162]. Nevertheless, the existence of this effect implies that the variation of the critical magnetic field with λ as suggested here in the case of QW structures (see the dash-dotted line in Fig. 6.8), which refers to a symmetric QW potential, is in general a lower limit. Simulating the gradient of the conduction band profile of the DQW structure of S.K. as present at the spin transition, reveals a potential drop of approximately 17 mV across the QW, which corresponds to an electric field of about 1 mV/nm. This induces according to [162] a change of the effective g factor by less than 2%. Consequently, this effect is ruled out to be responsible for the large discrepancy between the two critical fields, particularly since the tilt of the QW potential is almost the same although opposite for the two QWs. But different morphologies of the two interfaces of a QW [187] can be a source for different energetic properties. If MBE growth is partly inhomogeneous, slight fluctuations of the QW width are expected and these should become apparent in a broad transition region. But no such evidence has been found [49]. It should be noted that proper MBE growth allows to achieve QWs with atomically smooth interfaces over macroscopic distances [188].

As can be seen from Fig. 6.6, a sweep of the magnetic field close to the transition point is accompanied by hysteresis. Smet *et al.* [182] argue that this is in accordance with the formation of an Ising ferromagnet governed by easy-axis anisotropy. Jungwirth *et al.* argued that in the case of easy-axis anisotropy, the ferromagnetic system (here the electron system at $\nu = 2/3$) should exhibit hysteresis. But since there is some influence on the electron system by the nuclear spin system, with those long timescales that equilibrium is not achieved within the timescale of data recording, a contribution from it to the hysteresis is expected. This contribution is discussed below.

6.3 In-plane magnetic field

So far, only the Coulomb correlation energy and hence $\hbar\omega_{\mathrm{c,CF}}$ has been tuned here *in situ* by adjusting a specific width of the wave function using the WQW structure. Also the second energy that competes with it, the Zeeman energy, can be selectively tuned *in situ* with an additional in-plane magnetic field.

An in-plane magnetic field B_{ip} is realized by tilting the sample. The specific tilt angle θ is measured between the sample's normal axis and the magnetic field axis. B_{ip} is related to the externally applied magnetic field B as

$$B_{\mathrm{ip}} = B\sin(\theta), \tag{6.22}$$

and the magnetic field component which is perpendicular to the plane of the 2DES as

$$B_\perp = B\cos(\theta). \tag{6.23}$$

The Zeeman energy E_Z is determined by the externally applied magnetic field B while the competing CF cyclotron energy $\hbar\omega_\mathrm{c,CF}$ depends only on $B_\perp$ [178]. Thus, with an increasing tilt angle E_Z is favored against $\hbar\omega_\mathrm{c,CF}$. Assuming that the spin transition point is adjusted at zero tilt angle, the tilt angle induced preference of E_Z must be balanced in order to reestablish the CF LL coincidence. This can be accomplished by a reduction of the density, because it causes a stronger decrease of E_Z than $\hbar\omega_\mathrm{c,CF}$ due to the different dependencies on the density (see Fig. 6.5). Consequently, a reduction of the critical perpendicular magnetic field with increasing tilt angle is expected. Experimentally, a certain tilt angle is adjusted and the spin transition is located each time with scans of the density and magnetic field. The back gate voltage is set to $U_\mathrm{BG} = 0$ V and any change of the density is realized exclusively with the front gate. The actual tilt angle is determined from the $\cos(\theta)$ shift of the SdH oscillations to a precision of approximately $\pm 0.5°$. The found variation of the critical magnetic field B_S (which refers to the externally applied magnetic field) is shown in Fig. 6.9. The largest tilt angle is determined by the lowest density, at which the spin transition can be observed before the FQHE is destroyed by disorder.

In order to describe the variation of the critical magnetic field with the tilt angle, the following analytical model is used, starting from the definitions of the Zeeman energy

$$E_\mathrm{Z} = C_\mathrm{Z}|g^*|\mu_\mathrm{B}B, \tag{6.24}$$

and the CF cyclotron energy

$$\hbar\omega_\mathrm{c,CF} = C_\mathrm{C}\frac{e^2}{4\pi\epsilon\epsilon_0 l_\mathrm{B}^\mathrm{eff}}, \tag{6.25}$$

with

$$l_\mathrm{B}^\mathrm{eff} = \sqrt{l_\mathrm{B}^2 + \lambda^2}, l_\mathrm{B} = \sqrt{\frac{\hbar}{eB_\perp}}. \tag{6.26}$$

The critical magnetic field follows from the equality $E_\mathrm{Z} = \hbar\omega_\mathrm{c,CF}$ and can be written after a mathematical evaluation as

$$B_\mathrm{S} = -\frac{u}{\cos(\theta)} + \sqrt{\left(\frac{u}{\cos(\theta)}\right)^2 + v\left(\frac{C_\mathrm{C}}{C_\mathrm{Z}g^*}\right)^2}, \tag{6.27}$$

where u and v contain all the constants including the finite thickness λ of the 2DES. This relation is again an implicit equation for the critical magnetic field B_S due to the known dependence of the effective g factor g^* on the magnetic field (see Eq. 6.12). The variation of λ is deduced from simulations of the WQW potential profile for every configuration defined by the front gate voltage at the spin transition and $U_\mathrm{BG} = 0$ V. The program Poisson-Solver is used as has been already mentioned in Subsec. 6.2.1. The finite thickness is found to increase from 13 nm to 14 nm over the range of decreasing density. Furthermore, a nuclear magnetic field is included

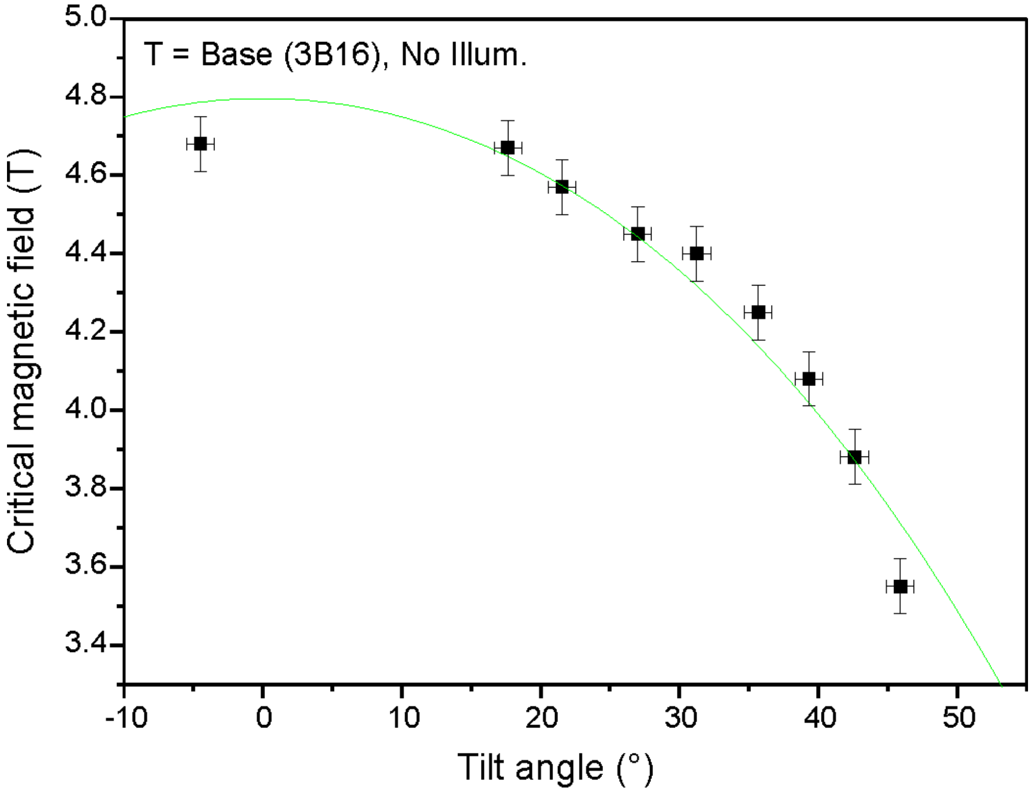

Figure 6.9: Plot of the experimentally determined critical magnetic fields B_S of the spin transition for different tilt angles θ of the samples normal axis with respect to the magnetic field. The line is the result of a fit of Eq. 6.27 to the data.

in the same way as in Subsec. 6.2.5. The fit of the data with the theoretical model of Eq. 6.27 yields $C_\mathrm{C}/C_\mathrm{Z} = 0.0169$ in agreement with the value found above for a fit with respect to λ. The fit fails if finite thickness is neglected, which again confirms the importance of its consideration.

6.4 The reset procedure

6.4.1 Variation of the spin flip-flop rate with filling factor

As already mentioned in Subsec. 6.2.3 the nuclear magnetic field, arising from a net nuclear spin polarization, influences the Zeeman energy and alters the critical magnetic field of the spin transition. The strength of the interaction between the nuclear spin system and the electron spin system is usually suppressed due to a violation of the energy conservation law accompanying a spin flip-flop process according to the Hamiltonian given in Eq. 6.15. The reason for the energy mismatch is the huge difference between the magnetic moments of the nucleus and the electron. The reduced interaction strength between the nuclear spin system and the environment can result in a very long equilibration time of the order of hours [170].

If the system would exhibit sufficiently low energetic excitations, which could account for the energy mismatch, the interaction strength, *i.e.* the spin flip-flop rate, would increase. Indeed, gapless excitations exist in the electronic system if Skyrmions are formed. Skyrmions are spin textures [72, 74, 82, 189, 190] formed slightly away from filling factor $\nu = 1$ (other integer filling factors do not seem to give rise to Skyrmion physics [191]), because the creation of quasi holes towards a lower filling factor or the population of the second LL towards a higher filling factor introduces spins with an opposite orientation compared to all other electron spins. Due to exchange interaction, the system prefers a gradual change of the spin orientation of spatially adjacent spins rather than adjacent spins with opposite orientation. This leads to the formation of spin textures known as Skyrmions. The number of gradually reoriented spins and thus the size of a Skyrmion is determined by the competition between the Zeeman and the Coulomb energies [7]. Since a Skyrmion carries a single unit of charge, the Coulomb interaction extends the size of a Skyrmion over an area as large as possible and causes therefore many reoriented spins. The Zeeman energy tries to minimize the number of reoriented spins. The classical energy of a Skyrmion is invariant for translation in real space consequently Skyrmions can order regularly due to Coulomb interaction. A Skyrme crystal [78] can thus forme, which gives rise to Goldstone modes with low energy excitations all the way down to zero frequency, similar to phonons of a conventional crystal. The interaction strength between electron and nuclear spin system will be large if such excitations are available. The interaction strength depends on the filling factor and is found to be largest at $\nu \approx 0.9$ and $\nu \approx 1.1$ [159].

6.4.2 Implementation of the reset procedure

The possibility of varying the interaction strength between the electron and the nuclear spin system by adjusting the filling factor is used here to influence the nuclear spin polarization, *i.e.* the nuclear magnetic field, on a reasonable short timescale of the order of seconds. This is important when studying the spin transition, because the degree of nuclear spin polarization affects the critical magnetic field or density of the spin transition. Furthermore, due to the variability of the nuclear magnetic field, the critical magnetic field of the spin transition is time dependent and reflects how the sample has been treated previously. In order to avoid this unsatisfactory state but instead ensure the always same starting point for an experiment, the nuclear spin polarization needs to be controlled. The procedure for this purpose, called reset, is as follows. Prior to data acquisition, the filling factor is appropriately set at a fixed magnetic field only by changing the density with the gate, so that the interaction strength between the electron and the nuclear spin system is large. During the subsequent period of time t_{reset}, increased spin flip-flop processes alter the nuclear magnetic field. The chosen filling factor ν_{reset} needs to persist for a sufficiently long time t_{reset} and the same experimental conditions always need to be provided so that the achievement of a constantly equal nuclear spin polarization is guaranteed. Then the gate voltage is set to a value that ensures the desired filling factor ν_{count} at which data are intended to be taken. Data recording starts after an additional idle time t_{count} typically determined by the settling time of the lock-in amplifier, used to detect the signal.[10] After the data recording at ν_{count} the desired tune parameter is changed, a reset performed again, and the next series of data acquisition follows. The overall procedure is schematically displayed in Fig. 6.10. With this technique certain parameter ranges are scanned and the results are discussed below. The necessary change of the gate bias is performed instantaneously. This implies that the front gate is used exclusively since the back gate voltage cannot be changed in such large and sudden steps as required (see Sec. 3.3). The time constant of the low-pass filter (RC-element) at the front gate is reduced to 1 ms instead of 1 s (see Appendix A.2). The time constant of the lock-in amplifier is chosen to be 300 ms.

In order to determine the critical density of the spin transition, a scan of R_{xx} over a sufficiently large density range at fixed filling factor $\nu = 2/3$ is required. This is equivalent to a move along the abscissa of the diagram in Fig. 6.1. The density region close to the crossing point is indicated by a loss of the FQHE, *i.e.* finite R_{xx} values form a transition peak around the critical density or magnetic field. The longitudinal resistance R_{xx} at fixed $\nu = 2/3$ can already

---

[10] Note that t_{count} should be as short as possible, because the different condition, *i.e.* filling factor, already changes the nuclear magnetic field in an undesired fashion. This change is measured in dependence of time. Results are presented below.

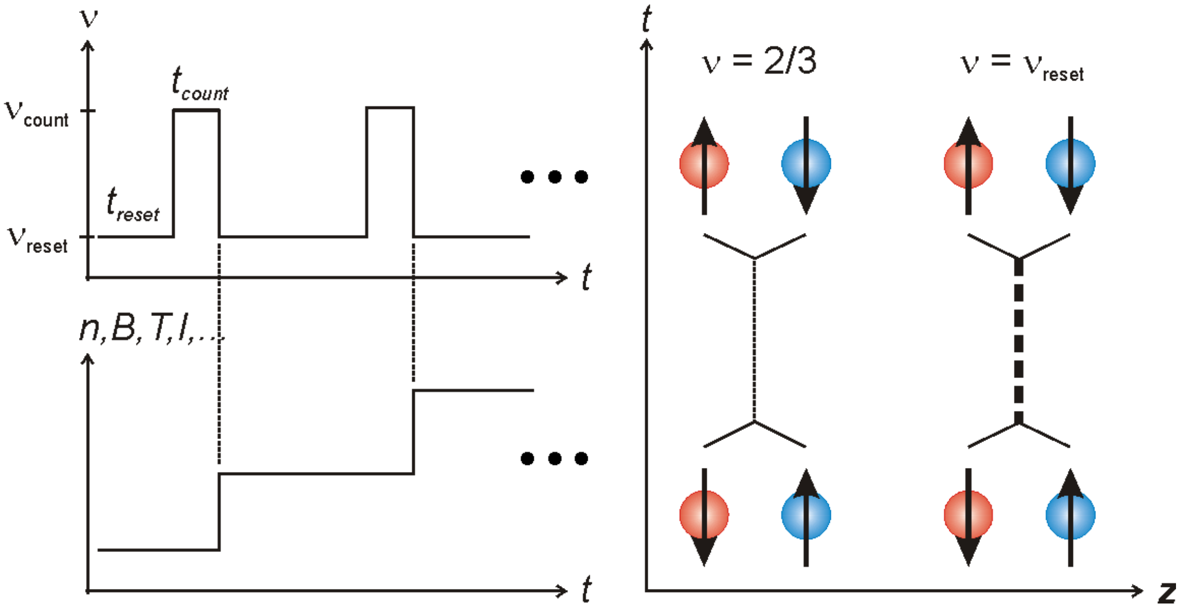

Figure 6.10: Left panel: Time scheme for a reset experiment. Exclusively with the front gate, the filling factor is switched from ν_{reset}, at which the reset takes place, to ν_{count}, at which data are subsequently recorded. After that, the particular parameter of interest *e.g.* the magnetic field, the density, the temperature, the current etc. is varied and the procedure repeated. Right panel: Feynman diagram of a spin flip-flop process involving an electron (red) and a nucleus (blue). The transition probability indicated by the thickness of the dashed line depends on the filling factor.

exhibit a temporal variation due to a relocation of the transition peak with time, provided that the relocation is large enough to involve the density point chosen for the detection. Such an observation is desirable because it provides information about the change of the nuclear spin polarization. The detection point is chosen therefore as being already close[11] to the critical density of the spin transition as determined by sweeps of the magnetic field for a larger range of the density. R_{xx} will saturate after a sufficiently long time when the equilibrium between the electron and the nuclear spin systems is reached terminating the relocation of the transition peak.

6.4.3 Impact of the reset procedure

To ensure the best working conditions for the reset, a suitable reset filling and reset time need to be determined. The appropriate procedure, as put forward by Hashimoto *et al.* [159, 192], is described in the following. The magnetic field is set close to the critical value of the spin transition and the density is tuned to $\nu_{\mathrm{count}} = 2/3$. The longitudinal resistance R_{xx} is monitored with time. When R_{xx} is about to settle, which is the case typically after some 10 minutes, a reset is performed using a certain reset filling factor ν_{reset}. A recording is then made of the change of the longitudinal resistance ΔR_{xx} after the reset time t_{reset}. Such a measurement is shown in the left panel of Fig. 6.11. The variation of ΔR_{xx} in dependence of the reset time is fitted exponentially. The characteristic time constant is a measure of T_1, which is the equilibration time for the nuclear spin system under the specific conditions. The data obtained at $\nu_{\mathrm{reset}} = 0.5$ (5.5 T) using the 22 nm wide single QW structure (see Subsec. 6.2.5) are displayed in the right panel of Fig. 6.11. T_1 is determined to about 75 s. Hashimoto *et al.* [159] found about 110 s for an SHI structure at 5.8 T. For any other reset filling factor noticeably away from $\nu_{\mathrm{reset}} = 0.5$ (and ν_{count}) ΔR_{xx} settles for already that short reset times (< 3 s) that an exponential dependence can no longer be stated. Hashimoto *et al.* [159] find $T_1 \approx 2.2$ s at $\nu_{\mathrm{reset}} \approx 0.9$ and $\nu_{\mathrm{reset}} \approx 1.1$ while a several orders of magnitude larger (not further specified) value at $\nu_{\mathrm{reset}} = 1$ in good agreement with the expected variation of the Skyrmion density, which is thought to be largest at $|\nu - 1| \approx 0.1$ [75] and zero at $\nu = 1$. Here, however, no significant variation of T_1 within the range $0.9 < \nu_{\mathrm{reset}} < 1.1$ is found. This observation suggests that Skyrmions are not solely responsible for the low energy excitations, which account for the energy mismatch between electron and nuclear spin flips. This indication is supported by the fact that Skyrmions only form when the Zeeman energy E_{Z} is sufficiently low compared to the Coulomb correlation energy E_{C}. Kukushkin *et al.* [174] found that above a ratio of $E_{\mathrm{Z}}/E_{\mathrm{C}} = 0.011$, which increases with the external magnetic field, Skyrmions are quenched. At a critical magnetic field of about 4.4 T as valid here, this ratio appears to be approximately 0.0125, so that it would appear to be most probable that Skyrmions are quenched. The same conclusion is drawn by Stern *et al.* [193], who observe a similar reset behavior as discussed here using a 15 nm wide QW structure with a critical magnetic field of about 8.5 T at base temperature (55 mK). However, if a sufficiently large nuclear spin polarization and thus a nuclear magnetic field can be induced, the

---

[11] As is shown below, the relocation of the transition peak is very small, making this approach essential.

Zeeman energy is preferentially reduced, since the nuclear magnetic field is oriented opposite to the external magnetic field. This reduction allows for the existence of Skyrmions even at high magnetic fields, as confirmed by Barret *et al.* [74] at about 7 T.

The observation of a small T_1 at $\nu \approx 1$ also holds for the WQW structure.[12] $T_1 < 3$ s is even obtained at $\nu_{\mathrm{reset}} = 0.5$. In conclusion, almost any reset filling factor sufficiently far away from 2/3 and any reset time well above a few seconds can be used to achieve an always equal nuclear magnetic field. This observation is in strong contrast to the results obtained in a sample realized on an *in situ* cleaved edge by overgrowth (CEO) [194]. Measurements show that the specific values of the reset filling factor and the reset time are very important. The reason for this very different observation compared to the findings for the different structures here is not yet understood. Since the 2DES of this CEO sample spreads effectively within the (110) plane of GaAs, an investigation of a sample grown on GaAs(110) substrate is carried out (see Subsec. 6.8.3).

The right panel of Fig. 6.12 displays measurements of R_{xx} at $\nu_{\mathrm{count}} = 2/3$ for a larger range of the magnetic field (or density equivalently). The cases with and without application of the reset procedure prior to every data point are compared. In contrast to the case without the reset procedure (sweep rate of the magnetic field $\Delta B = 0.1$ T/min.), the usage of the reset (parameters are given in the figure) leads to almost identical traces for up and down sweep, as expected when the influence of a prior treatment of the sample is eliminated. This indicates

---

[12] Exclusively the situation with all electrons residing on the inverted interface using $U_{\mathrm{BG}} = 0.0$ V is investigated.

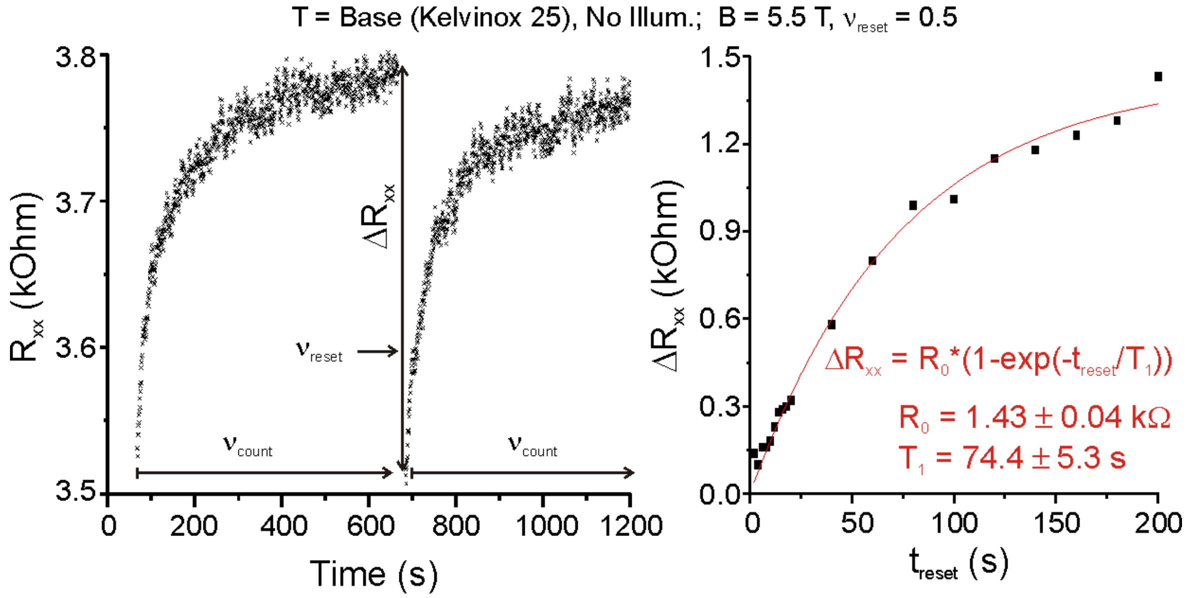

Figure 6.11: Left panel: Temporal variation of R_{xx} at $\nu = 2/3$ and a magnetic field close to the transition point of a 22 nm wide QW structure at base temperature. When R_{xx} almost settled, a reset is performed leading to the change ΔR_{xx}. Right panel: Variation of ΔR_{xx} with reset time for reset filling factor $\nu_{\mathrm{reset}} = 0.5$. An exponential fit yields T_1.

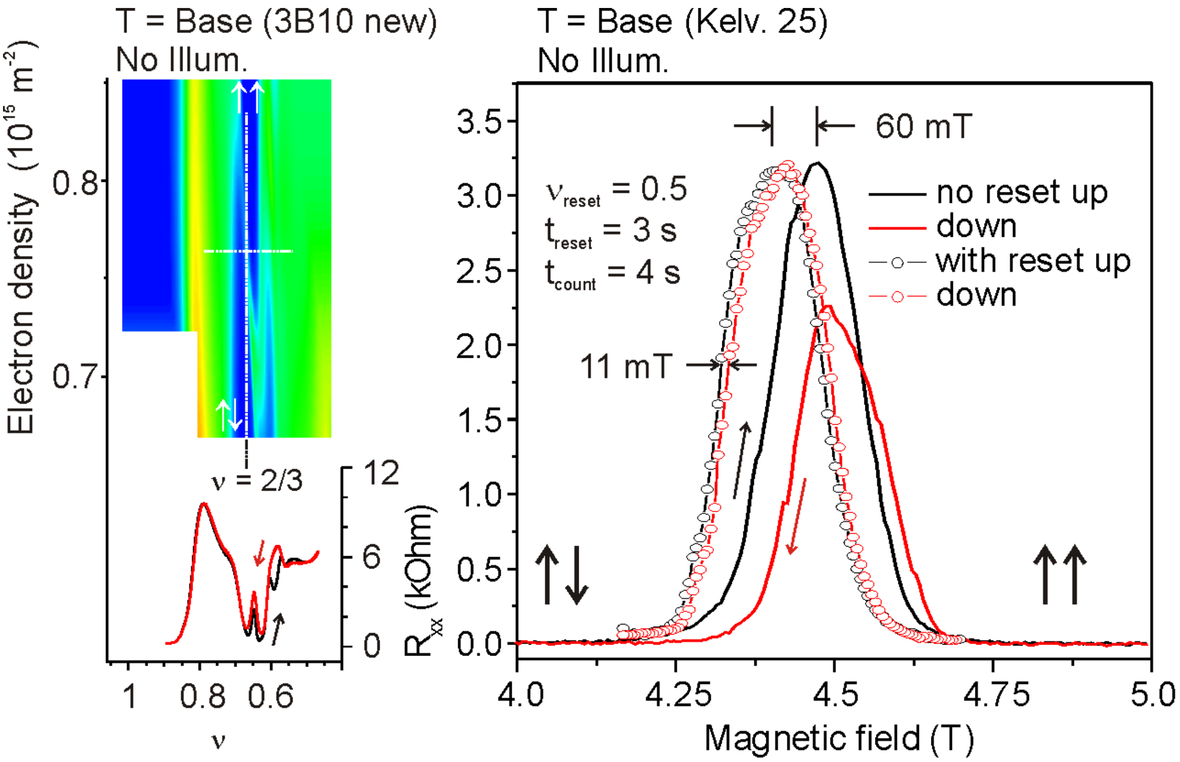

Figure 6.12: Left panel: Magnetic field sweeps across the spin transition at base temperature using the WQW structure with $U_{\mathrm{BG}} = 0$ V. The trace in the lower left diagram corresponds to the white horizontal line in the color plot. Right panel: Density sweeps at fixed filling factor $\nu = 2/3$ across the spin transition. This trace corresponds to the white vertical line in the color plot. The transition is indicated by the peak in R_{xx}. Compared are traces with and without the application of the reset procedure (the reset parameters are indicated). With the help of the reset procedure, the hysteresis between up and down sweep is strongly reduced.

that the reset procedure does provide an always equal B_{N}.[13] A small displacement of 11 mT between the traces for the two different sweep directions remains independent of the specific reset parameters. Its origin could be *e.g.* the inherent hysteresis of a ferromagnetic phase transition, as theoretically expected [68] in the case of easy-axis anisotropy, which applies here. The overall influence of the reset procedure, *i.e.* the variation of the critical magnetic field of the spin transition, is however small for the WQW structure (and all other structures presented in this chapter, which allow to access the spin transition), if compared to the CEO sample. Using $\nu_{\mathrm{reset}} = 0.5$ a maximal reduction of the critical magnetic field of about 60 mT compared to the no reset case is achieved for the WQW structure, while for $\nu_{\mathrm{reset}} = 0.9$ an increase of about 60 mT is found. In the case of the CEO sample the critical magnetic field can also be either increased or decreased but by several Tesla, depending on the specific reset filling factor and reset time [195]. Furthermore, for the two reset filling factors mentioned above the sign of the

---

[13] Note that this state may be denoted equilibrium, but depends on the specific conditions, *i.e.* the state will be different for different reset (and other) parameters.

change of the nuclear magnetic field during reset is opposite compared to the impact in the case of the CEO sample. T_1 varies [194] with the expected dependence of the Skyrmion density on the filling factor for the CEO sample (critical magnetic field without reset procedure about 6 T). The large and strongly variable nuclear magnetic field might be the reason for this incident, since a large nuclear magnetic field supports the formation of Skyrmions. The observation of a very limited variability of the nuclear magnetic field with the reset procedure is consistent with the expected influence of the short equilibration time T_1 determined here.

6.4.4 Temporal variation of the longitudinal resistance

In order to explore the temporal variation of R_{xx} close to the spin transition the magnetic field together with the density is varied stepwise at constant $\nu = 2/3$ using the WQW structure. At each density point a reset with the parameters $\nu_{\mathrm{reset}} = 0.9$ and $t_{\mathrm{reset}} = 90$ s is performed to ensure the always same starting point for the subsequent measurement. To avoid a noticeable influence[14] of the probing AC-current a small amplitude of 0.6 nA is used and the longitudinal resistance is monitored for 300 s at each density point. The result is shown in Fig. 6.13. The critical magnetic field of the spin transition shifts towards a lower value with time, which is not surprising, because the reset leads to equilibration between electron and nuclear spin systems under the specific conditions provided by the reset parameters; since the conditions at ν_{count} are different, B_{N} is subject to change again. The overall relocation is just about 10 mT and corresponds to a reduction[15] of the absolute value of the nuclear magnetic field of about 7 mT within 300 s. The temporal developments of both flanks of the transition peak are noticeably different. According to the definition given in the beginning of this chapter, the spin polarized phase (↑↑) is present towards higher magnetic field or density, while towards lower magnetic field or density the spin unpolarized phase (↑↓) is found. The transition region, represented by the width of the transition peak, is most likely characterized by the formation of electron spin domains due to easy-axis anisotropy and disorder (see Sec. 4.2). Consequently, a mixture of domains of both spin orientations may exist at each flank. The spin orientation of the majority of the domains is determined by the nature of the nearest phase. When the majority phase is spin polarized, the variation of R_{xx} in time is monotonous and uniformly continuous, while a predominantly spin unpolarized state gives rise to a discontinuous and even fluctuating temporal development of R_{xx}. This observation suggests that the equilibration between the electron and nuclear spin system happens differently depending on the type of spin polarization of the majority phase if the influence of the AC-current is regarded as small. The nuclear magnetic field can change even without the support by spin flip-flop processes, *i.e.* in the absence of electrons [159]. For this case a rather uniform development of B_{N} with time is expected if the environment provides steady conditions. However, the presence of electrons opens an additional relaxation channel for the nuclear spin polarization via spin flip-flop processes, which require low energy excitations that account for the energy mismatch, as discussed above. It seems as if the contribution

---

[14] The influence of a current is discussed in Sec. 6.6.

[15] That indeed a reduction of the net nuclear spin polarization applies is demonstrated in Sec. 6.5.

of the electron system to the equilibration of electron and nuclear spin system is only noticeable in the spin unpolarized phase. Two implications of the spin unpolarized electron system are conceivable compared to the spin polarized one: it leads either to much more low energy excitations or to an enhanced electron spin flip rate, which in turn enhances the spin flip-flop rate. Both require a kind of CF LL mixing, which however is most likely due to the small magnetic field. It has been estimated [196] that only a minor part of the electrons but most of the nuclei are involved in spin flip-flop processes, so the spin flip rate is most probably not the limiting factor. Consequently, the provision of much more low energy excitations by the spin unpolarized phase seems to be a reasonable argument for the significant different temporal development of R_{xx} at both flanks of the transition peak.

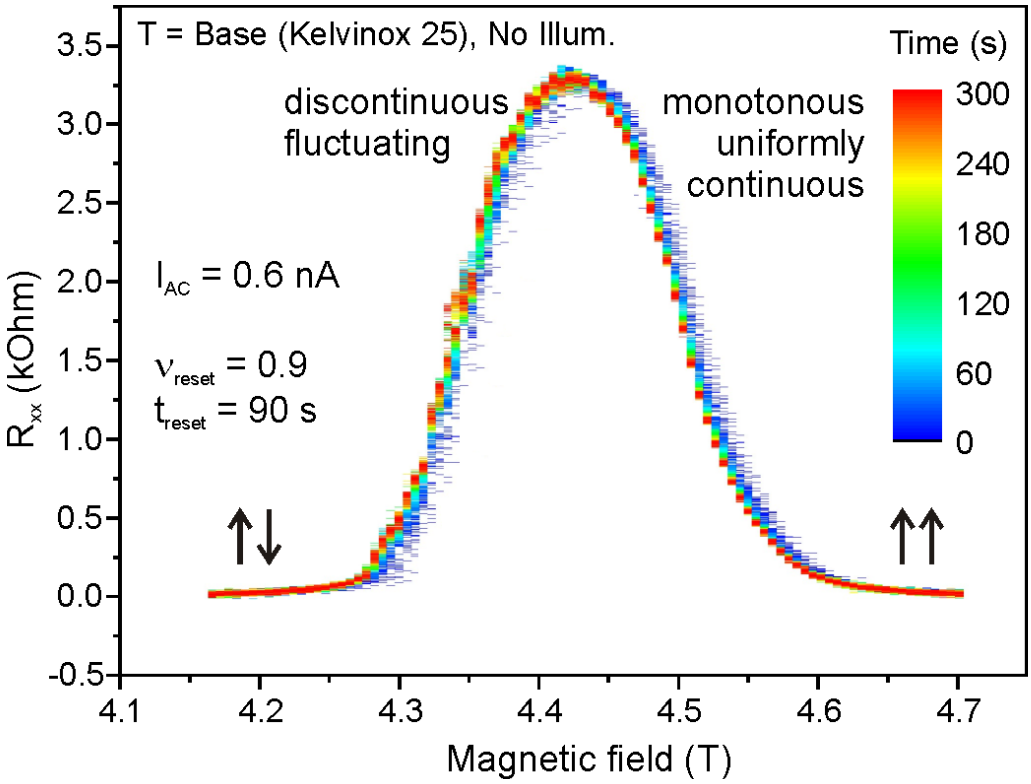

Figure 6.13: Temporal variation of R_{xx} at $\nu = 2/3$ for a larger range of the magnetic field covering the spin transition at base temperature. The WQW structure with $U_{\mathrm{BG}} = 0$ V is used. At each magnetic field value a reset is performed prior to the data acquisition. The reset parameters are indicated. An AC-current with amplitude 0.6 nA is used to probe R_{xx}. The change of R_{xx} with time is different for the both flanks of the transition peak and leads to a shift of the transition peak to smaller magnetic fields by about 10 mT.

6.5 Temperature dependent measurement

The spin transition is studied for a wide range of temperatures, since the temperature dependence of the critical magnetic field can reveal the magnitude of the nuclear magnetic field. For this study the WQW structure is tuned to the single layer regime with all the electrons residing on the inverted interface using $U_{\mathrm{BG}} = 0.0$ V and the density is tuned exclusively with the front gate. Measurements of R_{xx} are performed at $\nu = 2/3$ for a sufficiently large density range to cover the spin transition. The temperature is varied from base temperature to 250 mK in non equidistant steps. Prior to every data point, a reset is performed according to Sec. 6.4 using $t_{\mathrm{reset}} = 90$ s at $\nu_{\mathrm{reset}} = 0.9$. The data point is recorded after $t_{\mathrm{count}} = 3$ s after the density settled at $\nu_{\mathrm{count}} = 2/3$ when U_{FG} is set. The result is shown in Fig. 6.14. As can be seen the critical magnetic field reduces with increasing temperature indicating an increase of the Zeeman energy due to a change of the nuclear magnetic field. As demonstrated in Subsec. 6.2.3 a higher temperature leads to a lower absolute nuclear magnetic field B_{N}. Therefore, the sign of B_{N} must be negative. The variation of the critical magnetic field is about 0.4 T over the entire temperature range. A change of B_{N} results in an always larger change ΔB_{S} of the critical magnetic field B_{S}. According to the implicit equation for the critical magnetic field including B_{N}, as discussed in Subsec. 6.2.5, $\Delta B_{\mathrm{S}} \approx 1.3 B_{\mathrm{N}}$ at small external magnetic fields $B \approx 4$ T, while $\Delta B_{\mathrm{S}} \approx 1.8 B_{\mathrm{N}}$ at $B \approx 10$ T. It can thus be estimated that $B_{\mathrm{N}} \approx -0.3$ T, which corresponds to a net nuclear spin polarization of $\langle \mathrm{I} \rangle \approx 0.085$ (see Eq. 6.19). With the external magnetic field 4.5 T, as determined for the spin transition at base temperature, and the estimated nuclear magnetic field, the actual crystal temperature T_{c} of the sample can be estimated with Eq. 6.21 to about 30 mK. This is a reasonable value, because the base temperature of the used cryogenic system (see Appendix A.2) is nominally 21 mK at the mixing chamber, to which the sample is attached via copper wires.

The resistance peak accompanying the spin transition increases with temperature. Its height reaches a maximum at about 170 mK and then decreases again. This specific temperature is regarded as the Curie temperature of the quantum Hall ferromagnet [200] and induces a changeover to the paramagnetic phase towards higher temperatures. A similar behavior has been observed by Muraki *et al.* for the resistance spikes at the LL coincidences involving $\nu_{\mathrm{tot}} = 3, 4, 5$ [36] and the Curie temperature has been determined to about 1.5 K.

The FQHE to lower densities (spin unpolarized phase $(\uparrow\downarrow)$) is lost more rapidly with increasing temperature, which indicates a smaller energy gap than for the FQHE at higher densities (spin polarized phase $(\uparrow\downarrow)$) in agreement with an activation study of Eisenstein *et al.* [143]. At base temperature the height of the resistance peak is lowered by a factor of just two compared to its maximum value at 170 mK. The extraction of an activation energy on the basis of an Arrhenius plot is therefore not possible. A similar behavior has been observed at $\nu = 3$ for a 15 nm wide AlAs QW structure subject to a specific in-plane magnetic field [201]. There, the height of the resistance spike at its peak reduces continuously but slowly towards lower temperature as it does here. From this De Poortere *et al.* [201] conclude that no activation behavior is present. For the 15 nm wide QW structure of O.S. with a critical magnetic field of 8.3 T at base

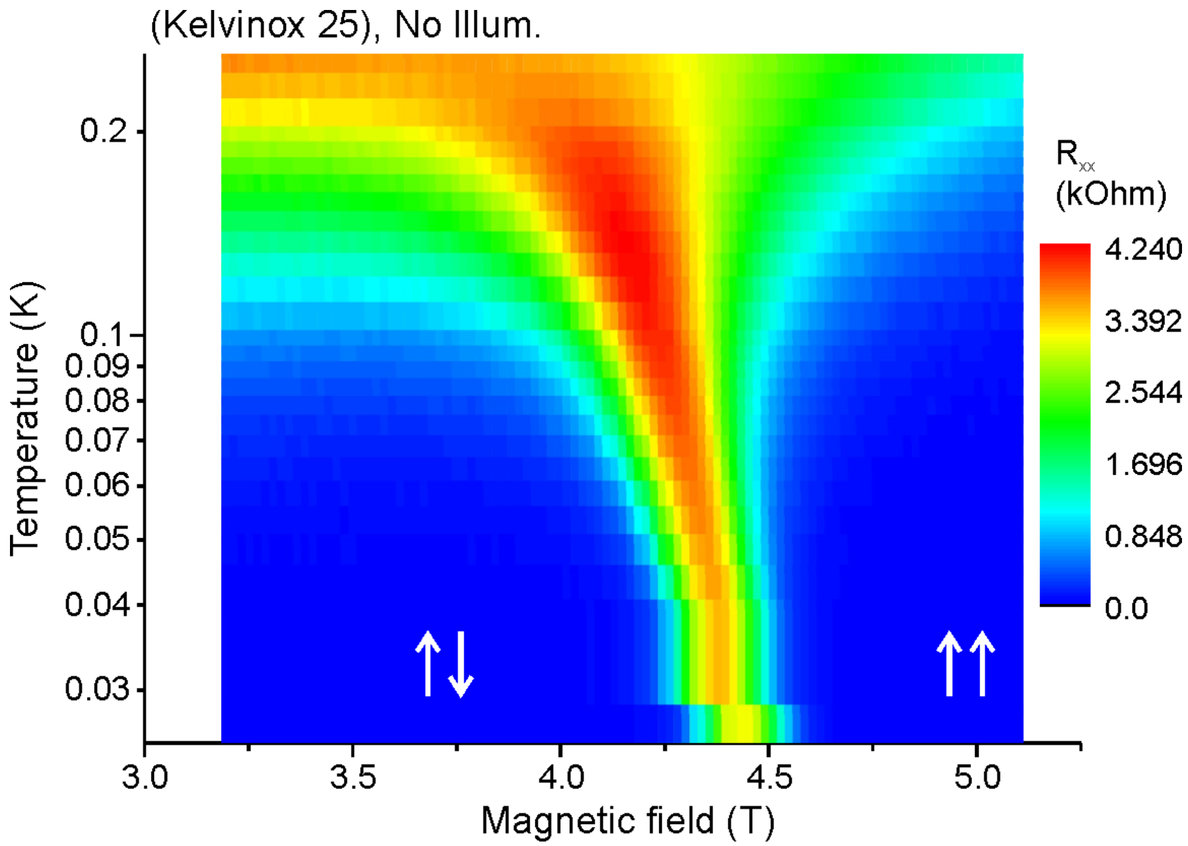

Figure 6.14: Development of R_{xx} at $\nu = 2/3$ with temperature for a larger range of the magnetic field covering the spin transition region using the WQW structure with $U_{\mathrm{BG}} = 0$ V. The critical magnetic field is reduced with increasing temperature due to a smaller net nuclear spin polarization. The Curie temperature separating ferromagnetic and paramagnetic phase is indicated by the maximal peak height reached at 170 mK.

temperature (22 mK), as mentioned in Subsec. 6.2.5, an activation energy of 320 mK has been determined and the resistance peak of the spin transition almost vanishes at the lowest temperature [154]. Most of the so far published resistance spikes, associated with phase transitions in quantum Hall ferromagnets, are summarized in Tab. 6.1 with an emphasis on their temperature dependence.

6.6 Influence of a current

6.6.1 AC-current

It was found that the current amplitude used to probe the HLR (see the beginning of this chapter) strongly influences the result [153] with respect to the shape and height of this resistance peak. A relation between the HLR and the spin transition was proven by Kraus *et al.* [150]. Kraus *et al.* compared the results of sweeps of the magnetic field and the density across the spin

Sample	Tune parameter	ν	Quantum numbers of coinciding LLs	Hyst.	Development of transition peak towards lower temperature	Ref.
2DES SHI	density	2/3	(0,↓)(1,↑)	yes	non vanishing but decreasing towards base temperature	This thesis
electron bilayer 77 nm WQW	density	2/3	(B,1,↑)(A,0,↑)	no	vanishing (see Sec. 7.3)	This thesis
2DES SHI	density	2/3	(0,↓)(1,↑)	yes	non vanishing	[182]
electron bilayer 40 nm WQW	density	3	(A,0,↑)(B,1,↑)	no	vanishing	[35]
electron bilayer 40 nm WQW	density	4	(A,0,↑)(B,1,↓) (A,0,↓)(B,1,↑)	no	vanishing	[35]
2DHS SHI	tilt angle	3 4 5	(ν,↓)(ν+1,↑)	no	non vanishing down to $T = 280$ mK	[197]
2DES SHI	tilt angle	2/3 3/5	2/3:(0,↓)(1,↑)	no	non vanishing	[146]
electron bilayer 35 nm WQW	tilt angle	4 6 8	(2,0,↑)(1,2,↓)	no	vanishing and non vanishing, anisotropy	[61]
2DES AlAs QW	tilt angle	3 5 7	(0,↓)(2,↑) (1,↓)(3,↑) (2,↓)(4,↑)	yes and no	3: vanishing, others not	[198]
electron bilayer 60 nm WQW	density	2 4	(L,0,↓)(R,0,↑) (L,1,↓)(R,0,↑) [R,L: left, right layer]	yes	non vanishing down to $T = 330$ mK	[199]
2DES 25 nm QW	pressure	2/5 3/7 4/7 4/3	not assigned	yes	non vanishing	[147]

Table 6.1: Summary of the properties of most of the so far observed ferromagnetic phase transitions.

transition obtained with two different (1 nA, 50 nA) AC-current amplitudes and found that the large amplitude heavily increases the spin transition peak as typical for the HLR regime, but no relocation of the transition point was found. However, a systematic variation of the amplitude of the probing AC-current was not carried out. The possibility[16] that HLR and spin transition are related triggered the measurement here. The WQW structure is tuned to the single layer regime with all the electrons residing at the lower inverted interface using $U_{\mathrm{BG}} = 0$ V. The density is adjusted with the front gate to a value (0.75×10^{15} m^{-2}) so that the transition peak is found in the center of the plateau region of $\nu = 2/3$ for the lowest AC-current amplitude used. The magnetic field is swept around $\nu = 2/3$ and the amplitude of the probing AC-current of frequency 5.8 Hz is varied from 5 nA to 50 nA in steps of 3 nA. The result is shown in Fig. 6.15. At the lowest current amplitude just a small and narrow transition peak is found. The height of this transition peak increases nonlinearly with the increasing AC-current amplitude. Furthermore, the hysteresis between up and down sweeps of the magnetic field is gradually enhanced, leading to a larger separation of the peaks on the magnetic field axis for up and down sweep. Even the filling factor range around $\nu = 3/5$ is strongly affected in a way similar to the observation of Smet *et al.* [182]. For the largest AC-current amplitudes a huge bump is present fully dominating the plateau region. This is the typical indication for the HLR regime at an intermediate sweep rate of the magnetic field of $\Delta B = 0.1$ T/min. Kraus *et al.* [150] speculate, that electron spin domains, which are thought to exist close to the transition point, are forced to ever smaller sizes by an increasing AC-current so that the number of scatterers, represented by the domain walls, is increased. Kraus *et al.* assume, that a larger number of scatterers results in a larger longitudinal resistance. But an explanation of the HLR regime based on experimental evidence is still lacking. As in [150] no clear indication for a shift of the critical magnetic field or density of the spin transition is found.

6.6.2 DC-current

It was shown by Smet *et al.* [194] that a current can alter the degree of nuclear spin polarization via spin flip-flop processes. However, because of the long response time of the hyperfine interaction, the influence of a current on the nuclear spin polarization is only present, when the frequency of the current is lower than the inverse timescale T_1. In the case of the CEO sample in [194], the cutoff frequency was found to be approximately 10 mHz. In other words, a DC-current is best suited to achieve a current induced change of the nuclear spin polarization. Based on this observation, the experiments are extended for measurements with a DC-current.

A modification of the net nuclear spin polarization causes a change of the (local) nuclear magnetic field and thus a change of the Zeeman energy, which in turn leads to a change of the critical magnetic field of the spin transition. In order to detect any induced variation of the critical magnetic field or density correctly, a scan of the density at constant $\nu = 2/3$ is carried out for each different DC-current amplitude in the same way as has already been done for the

---

[16] The measurements here were carried out earlier than the experiments of Kraus published in [150], *i.e.* prior to the proof that HLR and spin transition are related.

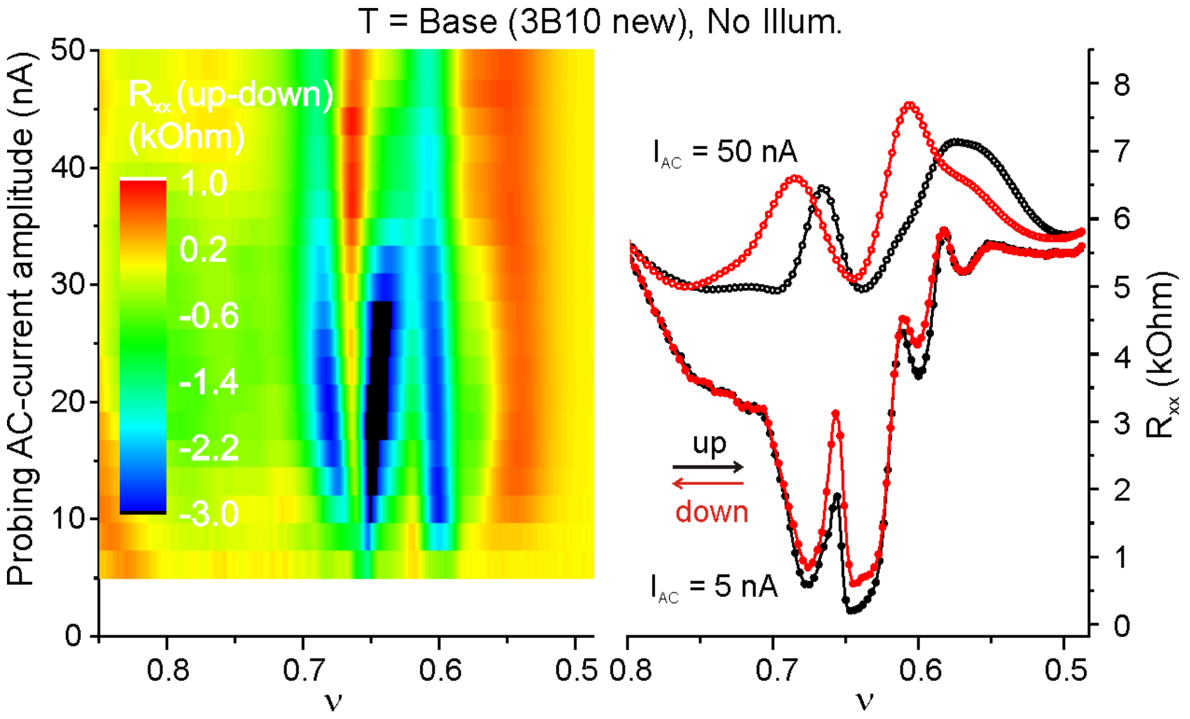

Figure 6.15: Right panel: Magnetic field sweeps at a density (0.75×10^{15} m^{-2}) close to the spin transition point using the WQW structure with $U_{\mathrm{BG}} = 0$ V at base temperature. The results strongly depend on the amplitude of the probing AC-current of frequency 5.8 Hz. Left panel: Difference between R_{xx} values of up and down sweep at a sweep rate of 0.1 T/min. and increasing AC-current amplitude.

reset experiments in Sec. 6.4. The measurement of the longitudinal resistance is accomplished by using a low noise lock-in technique, which requires a probing AC-current superimposed on the DC-current.

The DC-current is provided by a DC-voltage that drops across a 100 MΩ resistance in series with the sample (WQW structure with $U_{\mathrm{FG}} = 0.0$ V at base temperature), which is grounded at one current contact (see Fig. 2.1a). The experiment covers the range from 0 nA up to 60 nA for the DC-current amplitude. Prior to every data point a reset is performed using $\nu_{\mathrm{reset}} = 0.9$ and $t_{\mathrm{reset}} = 30$ s. The data acquisition at $\nu = 2/3$ happens $t_{\mathrm{count}} = 20$ s after the density is set with the front gate. The inherent variation of R_{xx} during this time can be neglected according to the results of Sec. 6.4. It can be seen from Fig. 6.16 that the transition peak becomes larger with an increasing DC-current amplitude and that the boundary of the peak to the spin unpolarized phase ($\uparrow\downarrow$) successively extends to lower densities, while the boundary to the spin polarized phase ($\uparrow\uparrow$) is almost unaffected by the DC-current. The transition peak is found to shift to smaller magnetic fields or densities with the increasing DC-current amplitude, which indicates according to the determined sign and influence of the nuclear magnetic field (see Sec. 6.5) that the net nuclear spin polarization is reduced. Comparing the measured temperature dependence of the transition peak (Fig. 6.14) with the influence of a variable DC-current (Fig. 6.16), it seems unlikely that the

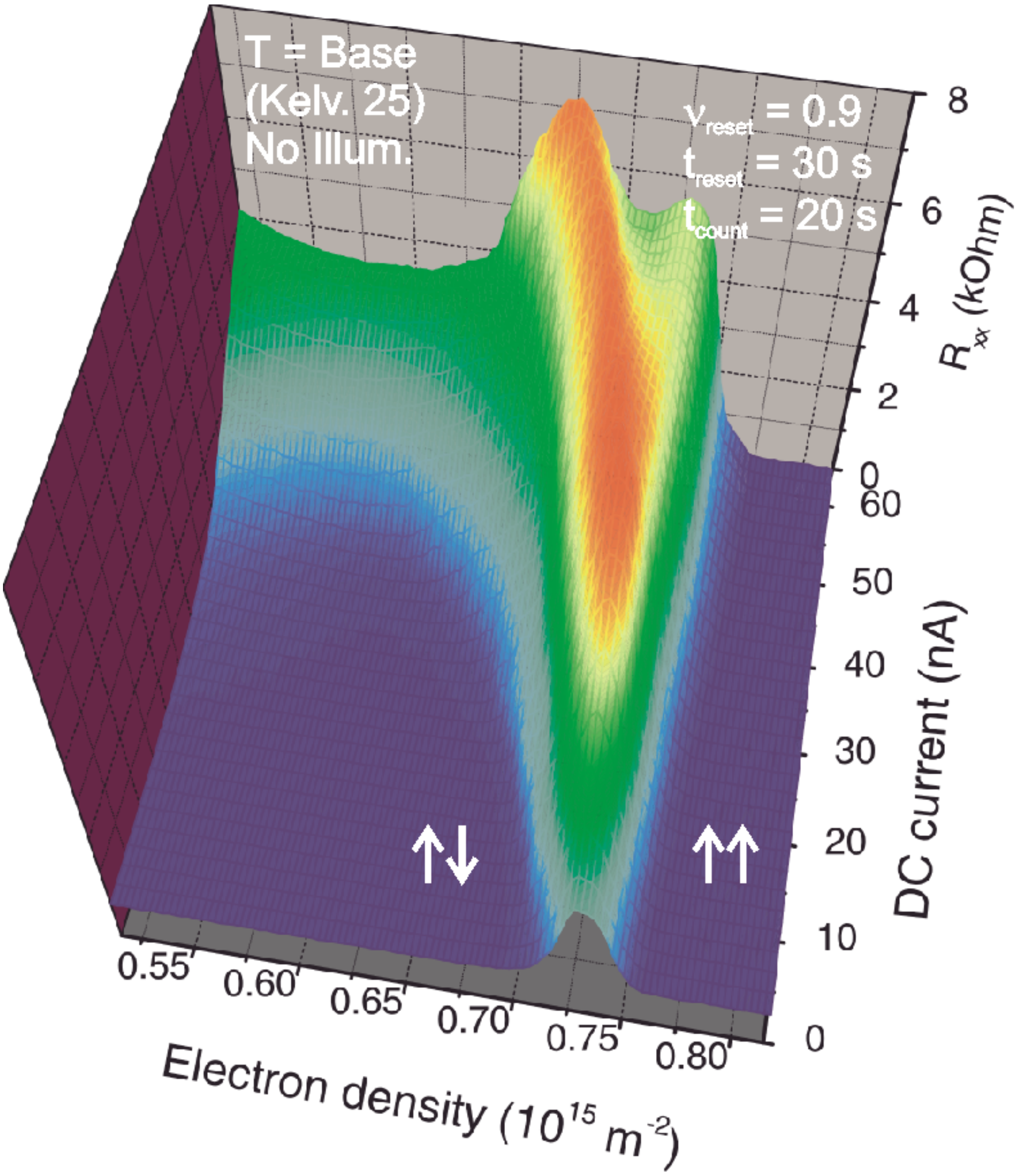

Figure 6.16: DC-current induced variation of R_{xx} at $\nu = 2/3$ for a larger range of the density covering the spin transition at base temperature. The WQW structure with $U_{\mathrm{BG}} = 0$ V is used. Prior to each data point a reset is performed using the parameters as indicated. The boundary to the spin polarized phase (↑↑) is almost unaffected, while the spin unpolarized phase (↑↓) boundary shifts to smaller densities with increasing DC-current amplitude. The peak position also shifts to lower densities.

DC-current alters the nuclear spin polarization exclusively by means of heating. This is because the boundary of the transition peak to the spin polarized phase is almost unaffected by the DC-current, while a shift towards lower density would be expected in the case of heating. However, due to a *e.g.* disorder induced spatially nonuniform DC electric field a spatially inhomogeneous DC-current distribution has to be taken into account. An inhomogeneous current distribution will lead to a spatially different change of the nuclear spin polarization and consequently to a broadening of the transition region. Since the boundary to the spin unpolarized phase extends with an increasing DC-current amplitude while the boundary to the spin polarized phase remains almost unaffected and the maximum of the transition peak is slightly shifted to lower densities, an inhomogeneous current distribution is highly probable. Apparently, the spin unpolarized phase is much more affected by the DC-current so that an enhanced current induced hyperfine interaction may apply there which is similar to the observation of a pronounced discontinuous time dependence of R_{xx} towards the spin unpolarized phase (see Fig. 6.13). A negative DC-current, not shown here, produces almost the same result. This is in contrast to the observation of Smet *et al.* [194] using the CEO sample. Either an increase or a decrease of the nuclear magnetic field is found depending on the sign of the DC-current. It should be noted, however, that the usage of DC-current amplitudes smaller than 3 nA yields here only slight differences in the rate and amplitude of the temporal change of the longitudinal resistance. But the sign of the change of the nuclear spin polarization is nevertheless independent of the sign of the DC-current. For very large DC-currents the transition peak is found to split into two peaks. This observation cannot as yet be explained, but since such a splitting is absent in the case of a rising temperature, it supports the argument that a DC-current affects only to a minor degree the nuclear spin polarization by means of heating.

6.7 The spin transition in the DQW structure

A double quantum well (DQW) structure provides the alternative approach to the WQW structure in order to establish a bilayer. Based on the literature [34] a DQW structure is created consisting of two 18 nm wide QWs separated by a 3.1 nm thick AlAs barrier. Although this structure is intended as an option to the WQW structure with respect to a QHE at $\nu_{\mathrm{tot}} = 1/2$, no indication for this effect is observed (see Sec. 5.4). Therefore, the DQW structure is exclusively used to investigate the spin transition at $\nu = 2/3$. It is found, that the longitudinal resistance at the spin transition is accompanied by sudden jumps upon a very slow change of the applied magnetic field.

6.7.1 General characterization of the DQW structure

The layer sequence of the DQW structure is displayed in Fig. 3.1. The general characterization of the DQW structure is done similar as for the WQW structure (see Sec. 5.2). Measurements of the longitudinal resistance R_{xx} with magnetic field at temperatures of 1.5 K and 250 mK are shown in Fig. 6.17 with zero bias applied to both gates. The untypical SdH oscillations indicate the bilayer nature of the electron system. At a total density of 2.0×10^{15} m^{-2} the mobility is 235 m^2/Vs, which is noticeably lower compared to the WQW structure.

The determination of the as-grown electron distribution between the two QWs is achieved with transport measurements at small (< 0.5 T) magnetic fields for a larger imbalance range keeping the total density constant. Due to the identical design of the DQW structure compared

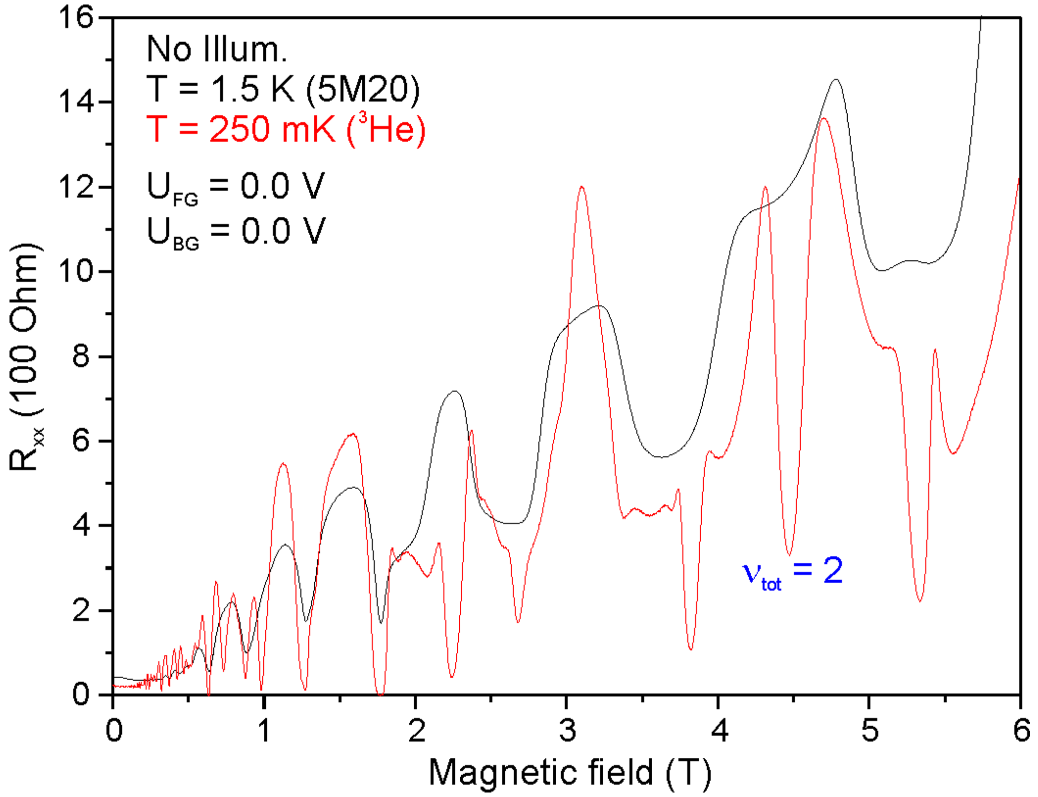

Figure 6.17: Magneto-transport measurement of a processed DQW sample at 1.5 K and 250 mK with both gates held at zero bias.

to the WQW structure (apart from the active region), the relation $\Delta n_{\mathrm{FG}}/\Delta n_{\mathrm{BG}}$ is assumed to be the same as for the WQW structure, namely 11.37 (see Sec. 5.2). The pattern of SdH oscillations is shown in Fig. 6.18. The balanced case is indicated by the line of constant front gate (and back gate) voltages (white dashed line in Fig. 6.18) relative to which the resistance data of the individual magnetic field sweeps are roughly mirror images to each other. With the known total density adjusted with the front and back gate voltages for the balanced case, the as-grown electron distribution can be estimated. The as-grown densities in the upper (front) and lower (back) QW are $n_{\mathrm{f},0} = 0.9 \times 10^{15}$ m^{-2} and $n_{\mathrm{b},0} = 1.1 \times 10^{15}$ m^{-2}, respectively. Their ratio is similar to that found for the as-grown WQW structure, as expected. Although the SdH oscillations are approximately mirror images with respect to the balanced case, they differ in the resistance values (away from any magic filling factor) quite noticeably, which indicates a difference in the quality of the two QWs. The resistance values are considerably larger when the majority of the electrons resides in the lower QW. The subband splitting $\Delta\mathrm{SAS}$ cannot be determined from a Fourier analysis of the SdH oscillations at low magnetic fields because the occupation difference between the two lowest subbands is too small to be resolved. This is already indicated by the many dot like features in the pattern of SdH oscillations (see Fig. 6.18), which is according to Ezawa [67] typical for a bilayer with a subband splitting as small as 1 K. A much smaller subband splitting than that which manifests for the WQW structure can be anticipated due to the additional AlAs barrier between the two electron layers.

6.7.2 Locating the spin transition in the DQW structure

As mentioned in Sec. 4.2, the spin transition at $\nu = 2/3$ is a phenomenon present in every single 2DES. To explore this the DQW structure is tuned to the single layer regime, *i.e.* one of the two QWs is depleted. Keeping $U_{\text{BG}} = 0$ V fixed and sweeping the front gate voltage, the upper QW is depleted and the density of the lower QW is tuned to the critical density of the spin transition. The same can be done with the upper QW when using $U_{\text{FG}} = 0$ V and sweeping the back gate voltage. Two measurements of R_{xx} are shown in Fig. 6.19 for almost the same density but each time located in a different QW. In both cases, a narrow and tall peak in R_{xx} appears instead of a deep minimum as expected due to the FQHE at $\nu = 2/3$. The assumption that this

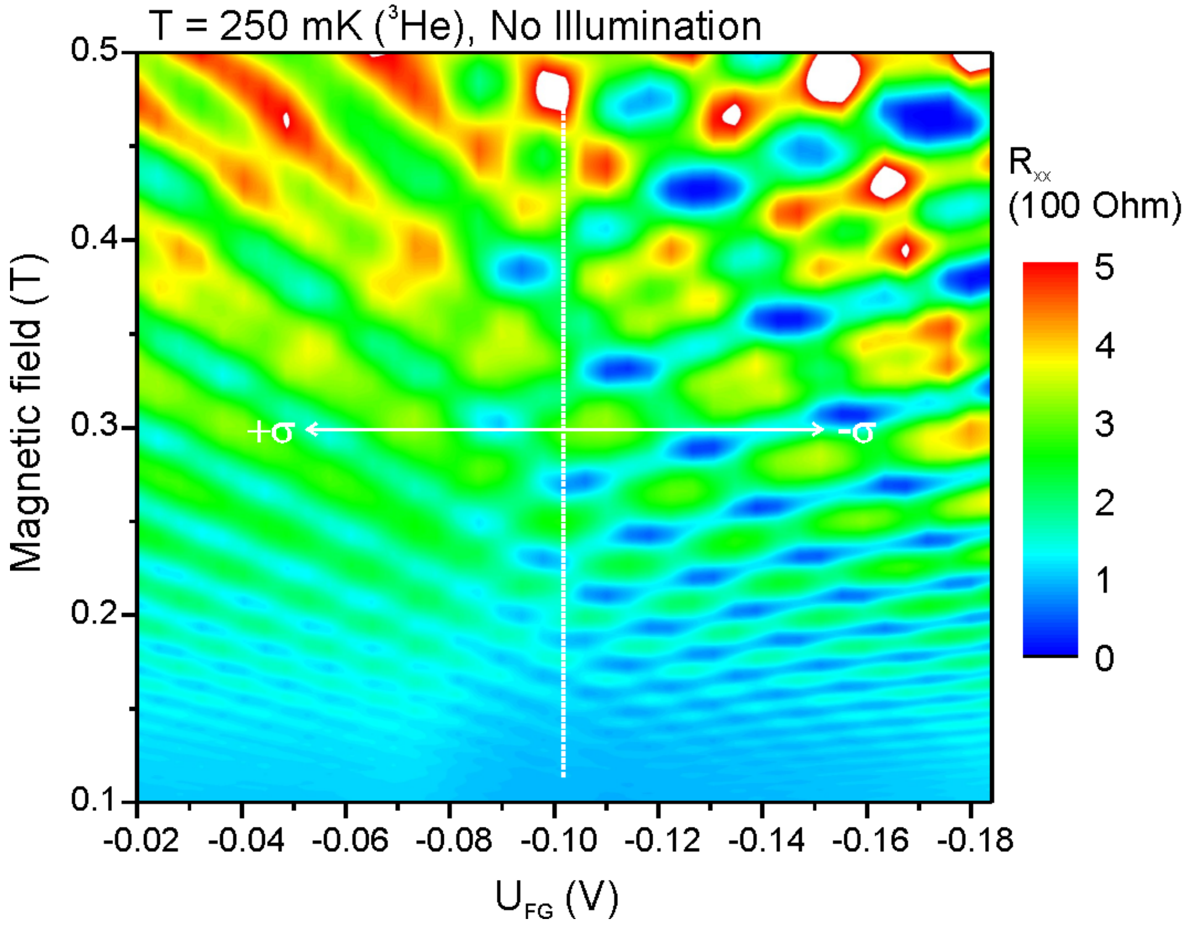

Figure 6.18: Magneto-transport measurements of the DQW structure with a variation of the imbalance at an almost fixed total density of about $1.2{\times}10^{15}$ m^{-2}. The balanced case is found at roughly $U_{\text{FG}} = -0.1$ V. The front gate voltage is displayed since the actual imbalance cannot be given sufficiently accurate. It is estimated that the boundaries of the color plot correspond to $\sigma \approx \pm 0.5$.

resistance peak is due to the spin transition is justified by several reasons. One reason is that a resistance peak can indicate a level coincidence. Another reason is that the sample is in the single layer regime with no other coincidence of CF LLs involving $\nu = 2/3$ possible than the one corresponding to the spin transition. Finally, the critical magnetic field (6.6 T) is consistent with the value expected for the spin transition in a QW of the given width at a temperature of 250 mK. The critical magnetic field of the spin transition is found to be almost equal for the two QWs. Since the width of a QW has a distinct influence on the critical magnetic field, it can be stated that both QWs investigated here have the same width in contrast to the DQW structure of S.K. (see Subsec. 6.2.5).

Magneto-transport measurements at base temperature of a dilution refrigerator are shown in Fig. 6.20. The back gate voltage is used exclusively to tune the density, while $U_{\mathrm{FG}} = 0$ V. The up and down sweeps of the magnetic field (sweep rate $\Delta B = 0.05$ T/min.) are displayed separately so that the hysteresis reveals the spin transition.[17] As expected, the critical magnetic field is shifted to a higher value (≈ 7.1 T) compared to the value found at 250 mK (6.6 T). The reason for this is the increasing nuclear spin polarization towards lower temperature, which

---

[17] At a temperature of 250 mK only a tiny hysteresis can be observed at the spin transition.

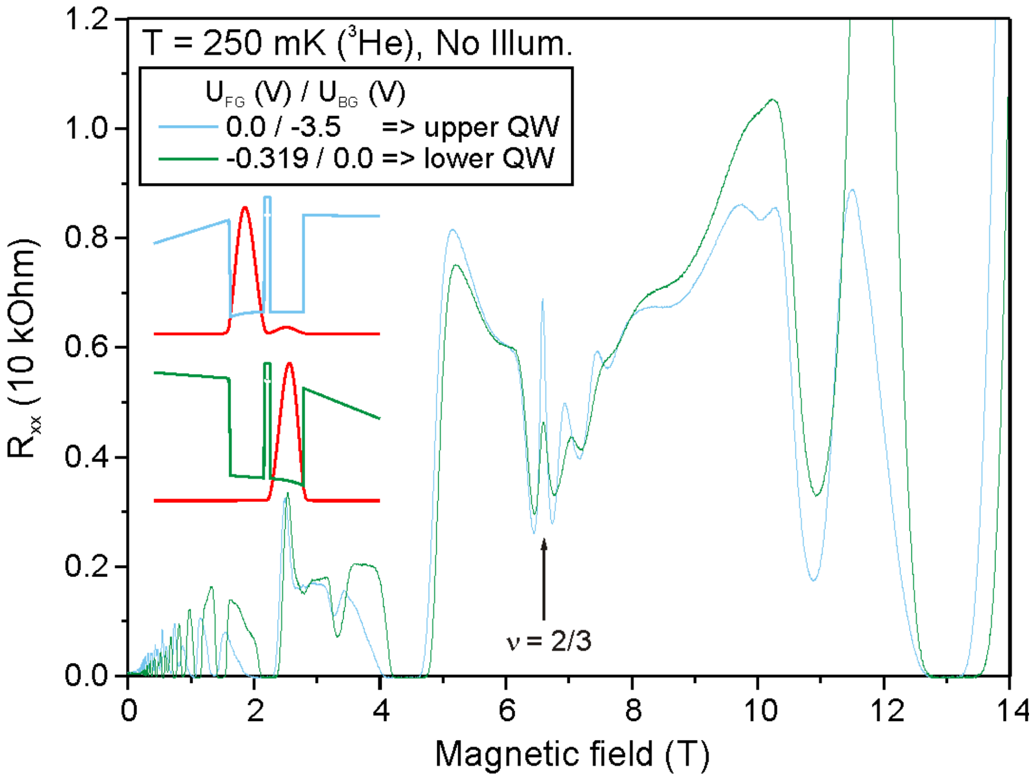

Figure 6.19: Magneto-transport measurements at 250 mK. The density is adjusted to the critical density of the spin transition, indicated by the peak at $\nu = 2/3$, in the upper and lower QW of the DQW structure individually. The insets are simulations of the profile of the conduction band edge and the electron distribution function for both cases calculated with the Poisson-Solver.

leads to a reduction of the Zeeman splitting. A back gate voltage of $U_{\mathrm{BG}} = -3.5$ V appears to be the boundary above which the lower QW starts to be filled with electrons (see the dashed horizontal line in Fig. 6.20). This onset is indicated by the change in the variation of the position of some features (resistance minima) with back gate voltage. The spin transition (indicated by the difference in the resistance data between up and down sweep of the magnetic field, as displayed in Fig. 6.20) is located when a back gate voltage is applied slightly above this boundary. Also the equivalent experiment, *i.e.* using $U_{\mathrm{BG}} = 0$ V and a variable front gate voltage in order to locate the spin transition at base temperature in the lower QW, brings about that the other (upper) QW is occupied by a minor part of the charges.

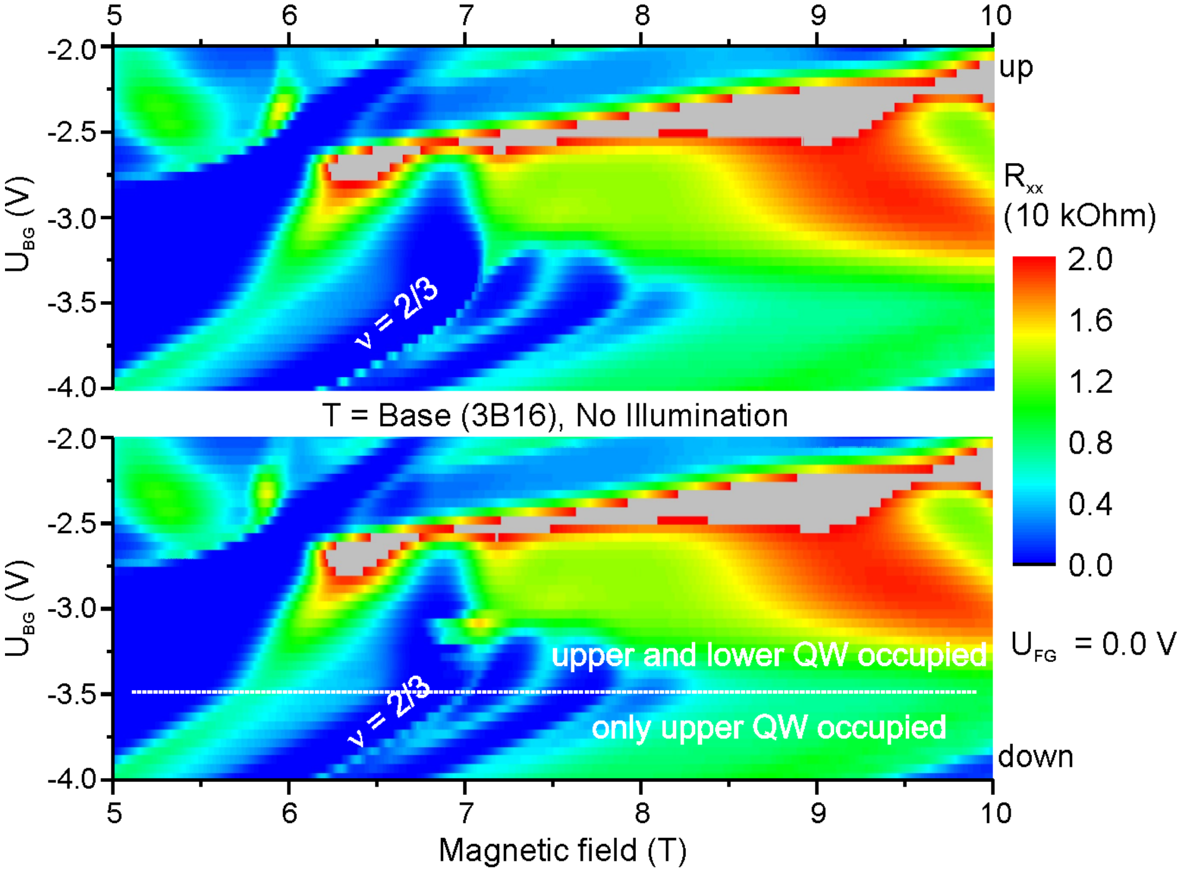

Figure 6.20: Magneto-transport measurement of the DQW structure at base temperature. The density is varied using only the back gate. Starting from low back gate voltages, where the lower QW is completely depopulated, the onset of the occupation of the lower QW becomes apparent at about $U_{\mathrm{BG}} = -3.5$ V. The difference in resistance between up and down sweeps at about 7 T and $U_{\mathrm{BG}} = -3.2$ V indicates the spin transition at $\nu = 2/3$. The magnetic field sweep rate is $\Delta B = 0.05$ T/min.

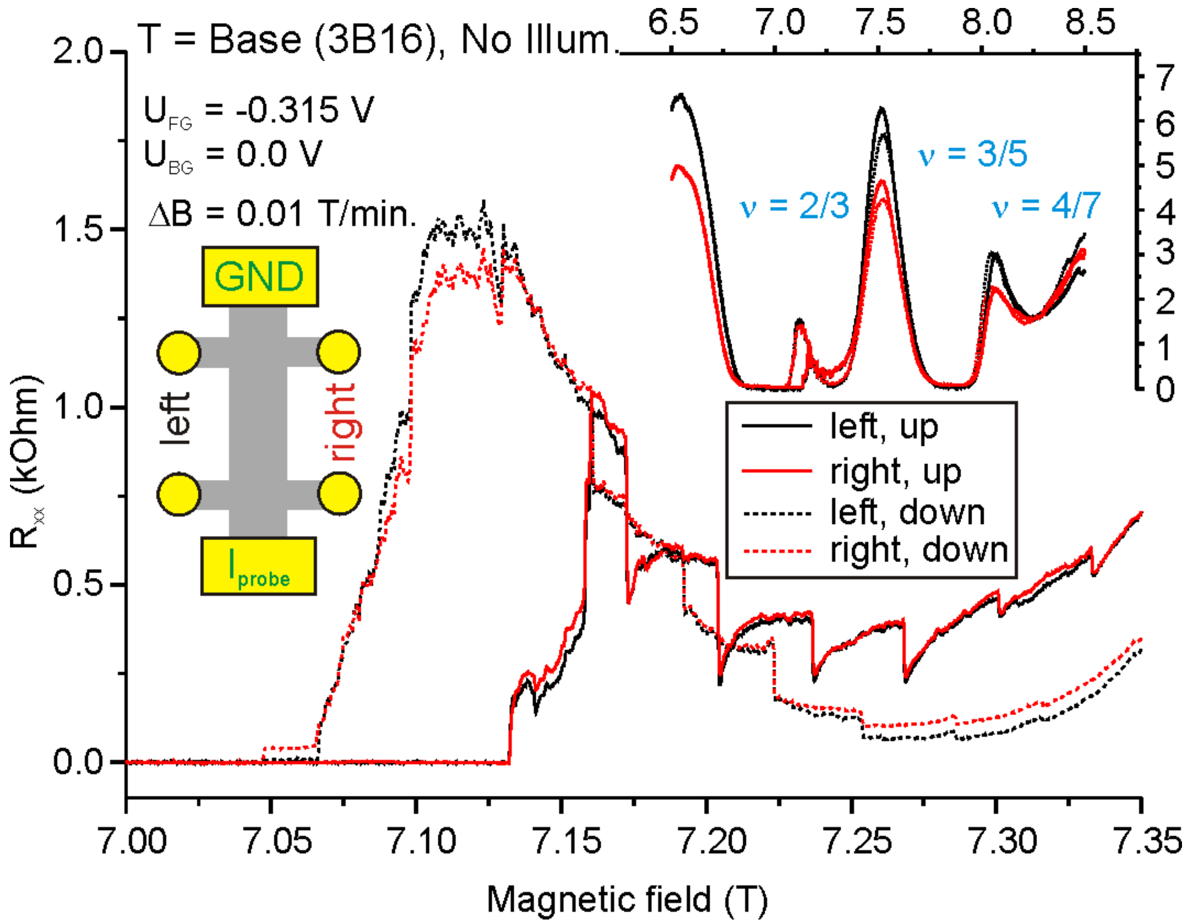

Figure 6.21: Magneto-transport measurements in the lower QW of the DQW structure at base temperature and at a sweep rate of the magnetic field of $\Delta B = 0.01$ T/min. The magnification visualizes the jumps in the longitudinal resistance. The traces are almost equal if detected either at the left or at the right mesa edge of the Hall bar. The plateau region is dominated by hysteresis.

6.7.3 Resistance jumps at the spin transition in the DQW structure

The transition peak is accompanied by additional jumps in the longitudinal resistance if the sweep rate of the magnetic field is reduced below $\Delta B = 0.1$ T/min. The number of jumps increases towards lower ΔB. A sweep at a density of 1.14×10^{15} m^{-2} close to the spin transition in the lower QW, where the number of jumps is particularly large, is shown in Fig. 6.21 for a sweep rate of $\Delta B = 0.01$ T/min. The magnification reveals a large number of sudden jumps in the longitudinal resistance superimposed on a wide bump. The transition peak is strongly hysteretic, *i.e.* different in size and shape, and is shifted along the magnetic field axis for up and down sweeps. This is also true for the jumps, but it seems as if most of them could be related to each other. For repeated sweeps of the magnetic field the jumps differ in their positions, in their height, and their number. The number of jumps as well as their height reduces towards smaller AC-current amplitudes used to probe the DQW structure. Below 1.5 nA only one very tiny jump remains. Above an AC-current amplitude of about 20 nA the jumps also disappear because they are overwhelmed by a huge resistance bump that dominates the plateau region due to the changeover to the HLR regime. If not otherwise stated, an AC-current amplitude of 10 nA is used for all measurements here. Most jumps occur apparently quasi periodically with a period of 30 mT. The entire transition peak as well as the jumps are reproduced almost perfectly if detected at opposite mesa edges of a Hall bar (L =300 μm, W =100 μm). But these two properties are found to be valid for only one specific sample. Other samples showed noticeable differences in the traces when $R_{\rm xx}$ is measured at opposite mesa edges of the Hall bar. Also the distinct periodicity is not reproduced. So the characteristics of the jumps appear to be sample specific.

Measurements of $R_{\rm xx}$ in the lower QW with time are performed, in part similar to reset experiments. For this a temperature of 250 mK is first chosen and the magnetic field is fixed to 6.55 T, which is the critical value for the spin transition. The filling factor is set close to $\nu = 2/3$ with the front gate only and $R_{\rm xx}$ is monitored for 600 s. As can be seen from the inset in Fig. 6.22, the change of $R_{\rm xx}$ with time is entirely smooth and continuous with a time constant of almost three minutes. For the equivalent measurement at base temperature the magnetic field is set to -7.09 T.[18] The density is then tuned instantaneously with the front gate to match $\nu = 2/3$ and the resistance recorded with time. A fluctuating *i.e.* unreproducible development of $R_{\rm xx}$ with time is observed, as can be seen in Fig. 6.22. The underlying and increasing bump is accompanied by small jumps towards higher as well as lower resistance. These fluctuations remain present even after several hours. Similar jump like features were observed by Smet *et al.* [182] for the CEO sample, but the jump direction was uniform. Hashimoto *et al.* [159] did not observe any jumps in an equivalent experiment using an SHI structure ($B_{\rm S} = 5.8$ T) at a temperature of 140 mK.

These resistance jumps bear some resemblance to Barkhausen jumps (BJs) which are jumps in the magnetization of a ferromagnetic material. A ferromagnetic material is characterized by the existence of many local energetic minima and maxima depending on the morphology of spin domains. A BJ reflects a change of the spin domain morphology due to domain wall movement and occurs in order to lower the total energy of the system by reaching another local energy minimum. BJs are typically observed when tuning an externally applied magnetic field, which changes the potential landscape. But they can also be observed with time, since BJs can be induced by thermal fluctuations as well. Since BJs resemble a change of the spin domain morphology *e.g.* with magnetic field, the resistance jumps here may be regarded as changes of the morphology of the electron spin domains, which most likely exist at the spin transition. But this remains a speculation, because the relation between the morphology of electron spin domains and the longitudinal resistance is not yet known. Nevertheless, assuming for a moment that such a relation exists, it is at least feasible to assume further that the large resistance jumps may reflect larger changes of the morphology of electron spin domains. How then should one account for the significant discontinuous movement of the domain walls in case of the DQW

---

[18] The negative sign does not matter.

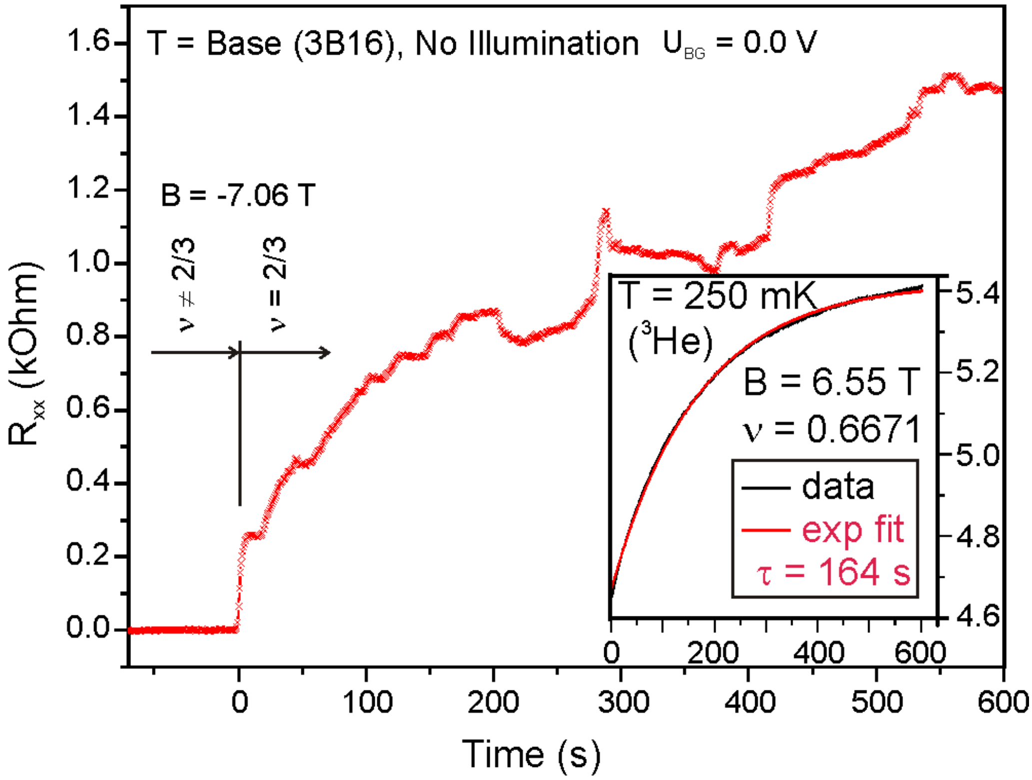

Figure 6.22: Temporal development of the longitudinal resistance close to the spin transition for two different temperatures. At a temperature of 250 mK (see the inset) R_{xx} develops entirely smoothly and uniformly with time and a time constant of 164 s can be deduced. At base temperature a nonuniform time dependence of R_{xx} is apparent and is characterized by bidirectional jumps.

structure? Considering the DQW structure's layer sequence, one reason might be the interface GaAs/AlAs, which is known to exhibit a much larger roughness than the GaAs/AlGaAs interface [187] due to enhanced segregation of Ga. The resulting potential fluctuations could play the role of pinning centers and thus amplify the discontinuous movement of the domain walls. Referring to the CEO sample [182], one can think of a similar mechanism provided by the superlattice close to the 2DES and furthermore, the 2DES in the CEO sample is confined on one side by a GaAs/AlAs interface just as here (DQW structure). It can be speculated [202] that the hysteresis at $\nu = 2/3$ might be enhanced by a material with a higher Al content in the vicinity of the electron layer. This assumption is in accord with the observation that the amplitude of the hysteresis loop obtained in a magnetic field sweep at 250 mK is significantly increased, when the single 2DES of the lower QW is pushed towards the AlAs barrier with the gates.

Another reason for the pronounced resistance jumps in the DQW structure could be the critical density of the spin transition of almost 1.2×10^{15} m^{-2}, which is slightly larger than the density that naturally resides in the lower QW (1.1×10^{15} m^{-2}; the same is equivalently true for the upper QW). The minor density in the second QW might lead to localized puddles and to the formation of a nonuniformly conducting layer parallel to the 2DES under investigation. The spatially inhomogeneous distribution of these charges can be supported by potential fluctuations as possibly caused by the AlAs material. There have been observations showing that a slight parallel conductivity induced by a gate can lead to unusual spikes in R_{xx} [203]. The existence of charge puddles would also conform with the observation of the current dependence of the number and height of the jumps, because the actual R_{xx} value can depend on the area of the electron system probed with a current. If changes of the potential landscape cannot be reached by a small current because these areas are off the current path, possible contributions of these areas to R_{xx} (such as resistance jumps) are absent. At larger currents tunneling through potential barriers can occur leading to a contribution of additional sample areas to R_{xx}. In particular, if spatially separated charge puddles exist, current induced tunneling becomes relevant, *i.e.* a pronounced dependence on the current amplitude is expected.

It should be noted that sharp resistance spikes can be observed, if a steady change of the nuclear spin polarization exists. If such a process would lead to a continuous decrease of the nuclear spin polarization, *i.e.* of the nuclear magnetic field, then the crossing point of the two CF LLs, leading to the spin transition at $\nu = 2/3$, would shift to lower values of the external magnetic field with time. If simultaneously sweeping up the external magnetic field then the crossing point would be passed more rapidly than it would upon a down sweep of the external magnetic field. It has been shown by Dobers *et al.* [156] that such contrarily changing magnetic fields can lead to spike-like features in R_{xx}, while a broad bump in R_{xx} results if both magnetic fields develop unidirectionally. Since the $R_{\mathrm{xx}}(B)$ traces (see Fig. 6.21) for up and down sweep of the external magnetic field B are rudimentarily shaped as just described, it is possible that a steady reduction of the nuclear magnetic field by the AC-current may exist. In addition, the jumps are larger upon an up sweep than upon a down sweep of the external magnetic field, as would be expected for contrarily developing magnetic fields. The current dependence of the jump heights may then be partly attributed to the efficiency of the dynamic nuclear spin polarization by the AC-current. However, the influence of the AC-current should be small according to the relation between $1/T_1$ and the frequency of the AC-current. But the AC-current can have an influence on the nuclear spin system [204, 205], as shown in Fig. 6.15. However, according to the picture outlined above the number of resistance jumps would correspond to the number of CF LL crossing points. Since this number increases with the AC-current amplitude, an increasing inhomogeneity of the sample with increasing AC-current would be required, leading to spatially dependent conditions for the crossing point. AC-current induced inhomogeneity is conceivable, as proposed by Kraus *et al.* [150].

So far the only observation of resistance jumps equivalent to those here has been made on a bilayer of holes [206, 207] at a temperature of about 30 mK. A slightly imbalanced hole bilayer exhibits hysteresis in R_{xx} when sweeping the magnetic field at values of B where either the majority or minority layer is at Landau level filling factor one. Subsequent measurements of R_{xx} with time at a fixed magnetic field in the hysteretic regions are characterized by jumps followed by an exponential recovery much the same as is apparent in Fig. 6.21. The time constant for the recovery is found to be about 5 s directly after the jump and 90 s on a longer timescale. Jumps either up or down in resistance occur. Even after days no settlement appears.

It has been suggested that fluctuations of the charge distribution between the two hole layers may be responsible for the jumps. It is worth mentioning that the barrier material between the two hole layers consists of AlAs.

6.8 Additional experiments and perspectives

6.8.1 Anisotropy

A coincidence of LLs with opposite spin involving $\nu = 4$ has been induced with an in-plane magnetic field (tilt angle about 70° at a total magnetic field of about 23 T) in a Si/SiGe heterostructure [208]. The transport properties were found to be strongly anisotropic at the coincidence for temperatures below 1 K, depending on the direction of the current with respect to the in-plane magnetic field axis. Comparable experiments on structures with a QW out of AlAs [209] also exhibit anisotropy. Pan *et al.* [61] observed large anisotropy effects, *i.e.* different transport properties along the two different principal crystal axes, at crossing points of LLs with different subband index (isospin), orbital quantum number, and spin involving the total filling factors $\nu_{\mathrm{tot}} = 4, 6, 8$. They used a 35 nm wide GaAs QW hosting a total density of 4.2$\times 10^{15}$ m^{-2}, which gives rise to the formation of a bilayer. LL coincidences are induced with an in-plane magnetic field and the anisotropy is visible only below temperatures of 400 mK. Furthermore, some theoretical work concerning anisotropy at LL coincidences in GaAs has been carried out. One theoretical treatment calculates that even random surface roughness [210] can induce anisotropy. Another predicts the onset of anisotropy above a critical in-plane magnetic field in a bilayer [211]. It was these results that led directly to the present study. Because of a possible connection between an in-plane magnetic field and anisotropy, the tilted field measurements discussed in Sec. 6.3 are also used to seek for anisotropy. The experiments are carried out on a sample in Van der Pauw geometry, *i.e.* a square of 300$\times$300 μm^2, processed from the WQW structure with one ohmic contact at each corner, because anisotropy effects are most pronounced for this type of geometry [212] if any exist. The edges of the Van der Pauw square are oriented along the two principal and orthogonal crystal axes within the (001) plane of GaAs namely the [110] and [$1\bar{1}0$] directions. The probing AC-current is sent from one ohmic contact to an adjacent one. The longitudinal resistance then is determined by the voltage drop between the two ohmic contacts on the opposite side of the sample. In order to unveil anisotropy, two probing AC-currents are applied; one sent along each principal crystal axis. The two AC-currents have different frequencies of 6.8 Hz and 14.4 Hz.

The orientation of oval defects allows to determine the crystal axes of a piece of GaAs(001). Oval defects always spread along the [110] direction [213–215]. Already at 1.5 K the two crystal axes differ in their mobilities at zero magnetic field by about 20% where the measurements reveal the [$1\bar{1}0$] axis to be the hard direction for transport. This observation holds for all samples investigated in this thesis.

Besides this difference in the longitudinal resistance, which further increases to about a factor of three at high magnetic fields in the regime of the FQHE, no anisotropy is found at base temperature independent of the tilt angle. Contingently, the sample quality is not sufficient. The mobility of the Si/SiGe sample of Zeitler *et al.* [208] is 20 m^2/Vs at 7×10^{15} m^{-2}, which is much less than here, so mobility alone might not be the decisive factor. According to [212], anisotropy effects depend exponentially on the size of the Van der Pauw square. So it might be the case that the size used here is too small. But the quality of the wafer with the WQW structure does not allow to process much larger samples due to a high defect density and its impact on the back gate's leakage current, as discussed in Sec. 3.3.

6.8.2 Modulated samples

Modulation means the periodic variation of the confinement potential of a 2DES along its plane. The reason for using modulated samples is to introduce potential fluctuations artificially and in a controlled way. Spin domains, which most likely form throughout a sample at the spin transition point, might be influenced in their size and pinned by these potential fluctuations. The expectation is an enhancement of the hysteresis if the spin domains could be pinned.

Wire modulation is imposed on a Hall bar with an active area of $L\times W = 100\times100$ μm^2 using a regular SHI structure. The period of the lines is 400 nm with a duty cycle of 50%. The lines are defined with electron beam lithography and transferred 40 nm deep into the sample by a dry etch process using SiCl$_4$. Such a pattern has exhibited excellent modulation properties (modulation strength 84 μeV or 0.9% of the electron Fermi energy) in previous experiments [216]. The samples have to be illuminated; the implementation of this is described in Appendix A.2. It is assumed that the critical magnetic field of the spin transition is approximately the same as in the case of an unpatterned sample, for which it is found to be about 5 T at base temperature [182]. Two samples are investigated. The *in situ* grown back gate[19] is used to tune the carrier density. In one case, although the unpatterned sample has a mobility above 600 m^2/Vs, the mobility is so strongly reduced by the modulation process, that the FQHE at $\nu = 2/3$ just vanishes towards lower densities but never reappears as would be typical when passing the spin transition point. In the second case, the *in situ* grown back gate freezes out at low temperatures, most probably due to an insufficient doping density of the GaAs layer intended as back gate. This behavior is possible, since the underlying wafer had not been rotated during the growth process of the structure leading to a distinct non-uniformity of the actual layer thickness and material composition across the wafer.

A third sample is investigated with a period of the lines of 700 nm. The sample comprises no *in situ* grown back gate and since it is further decided not to evaporate a metallic front gate, which is known to noticeable reduce the quality of modulated samples [217], the metallic layer on the back side of the sample is used as back gate. This procedure requires high voltages of the order of 100 V due to the large distance of approximately 450 μm between the back gate and the 2DES. The density at zero back gate bias is 1.7×10^{15} m^{-2} and since it is again assumed, that the critical density is approximately the same as in the case of the unpatterned sample, *i.e.*

---

[19] This is one of the seldom structures with an *in situ* grown back gate and a still sufficiently low leakage current between back gate and 2DES after illumination.

around 0.85×10^{15} m^{-2}, exclusively negative back gate biases are used. But this method to tune the density turns out to be insufficient, because strong hysteresis and time dependencies in $R_{\rm xx}$ are present when sweeping the back gate voltage. Towards desirable low back gate voltages no reasonable measurement of $R_{\rm xx}$ is possible anymore. The reason is most probably the number and kind of defects and impurities of the substrate, which resides between the 2DES and the back gate. A low substrate quality can lead to unreproducible charging effects (see Sec. 3.3), which can result in a very inhomogeneous charge distribution.

6.8.3 Sample on GaAs(110)

The idea of exploring the spin transition with samples grown on GaAs(110) substrate arises from the fact, that the conducting channel of a sample [182, 194], which exhibits extremely pronounced hysteretic effects close to the spin transition, resides on a cleaved edge (CEO) equivalent to the GaAs(110) surface. In order to test whether or not this distinct orientation has an influence on the peculiarities at the spin transition *e.g.* the strength of the hysteresis, a regular SHI structure is grown on GaAs(110) substrate. The delta-doping is set back from the 2DES, which resides 230 nm below the surface, by an 80 nm thick spacer.

The parameters, which influence the Zeeman energy and the Coulomb correlation energy, *i.e.* the effective g factor and the finite thickness of the 2DES, determine the critical magnetic field of the spin transition in the same way as in the case of a structure on GaAs(001). In the case of GaAs(110), the effective g factor is anisotropic. The absolute values of the three diagonal components of the effective g tensor are found to be 0.0184 if the magnetic field is oriented along the [001] axis, 0.0376 if oriented along the [$\bar{1}10$] axis, and 0.1415 if oriented parallel to the [110] axis. These absolute values are valid for a 7.5 nm wide QW [218] at 135 K. Towards 5 K, the absolute value of the effective g factor for an orientation of the magnetic field along the [110] axis, which is relevant here, increases[20] to 0.16 and its sign is determined to be negative [218]. In the case of GaAs(001) the effective g factor is lifted from -0.44 for bulk material to -0.16 for a 7.5 nm wide QW (see the discussion in Subsec. 6.2.2). Because of the similarity of the effective g factors of these two differently oriented QW structures, it might be that the effective g factors of GaAs(001) and GaAs(110) are identical even for wider QW and SHI structures. Just this speculation can be given, since so far no data for the effective g factor exist referring to structures on GaAs(110) substrate other than the 7.5 nm wide QW structure. The assumption of a similar confinement potential as for an SHI structure on GaAs(001) together with the estimated effective g factor leads to the expectation of a critical magnetic field for an SHI structure on GaAs(110) which is comparable to an SHI structure on GaAs(001).

An SHI structure on GaAs(110) (07-08-02.1) is supplied by the Walter Schottky Institute. Strong illumination is necessary, because the doping efficiency is reduced by almost 50% compared to GaAs(001) [222, 223]. The necessity for strong illumination excludes the usage of a buried back gate, as discussed in Sec. 3.3. However, in order to be able to locate the spin

---

[20] The experimentally determined variation of the effective g factor of GaAs with temperature [219, 220] is in contradiction to theory and so far not understood [221].

transition point, a tunability of the electron density is necessary. For that purpose, a 8.5 nm thin and thus still sufficiently transparent metallic front gate consisting of AuPd with a Pd content of 40% (see Sec. 3.4) is evaporated on top of a processed Hall bar. All the processing steps are the same as for the samples of the WQW or DQW structure.

The evaporation of the thin metallic front gate renormalizes the surface potential by about 1 eV. This value is determined by the observation that a front gate voltage of about +1 V is required to establish the same carrier density as is available in an ungated and comparably illuminated sample. This completely different behavior compared to GaAs(001), where the metallic front gate affects the surface potential just by a few mV (see Sec. 3.4), is due to the different atomic configurations of the surfaces of GaAs(110) and GaAs(001). The (110) surface consists of an equal number of Ga and As atoms and is thus nonpolar in contrast to the (001) surface, which is realized exclusively by As atoms. It turns out, that the illumination is best done at a front gate bias of +0.5 V, which reflects the onset of charge accumulation for the particular device design used here. The mobility of a gated sample is 230 m^2/Vs at a density of 1.5×10^{15} m^{-2} after illumination.

Magnetic field sweeps around $\nu = 2/3$ are performed at base temperature throughout the whole of the accessible density range. The upper limit in the electron density of about 1.65×10^{15} m^{-2} is given by the leakage current of the front gate, which increases dramatically above $U_{\rm FG} \approx +1.1$ V. Towards lower densities, the resistance minimum corresponding to the FQHE at $\nu = 2/3$ successively vanishes but does not reappear, which however would be a necessary indication for that the spin transition point is passed. The fact, that the spin transition cannot be located within the magnetic field range from 3 T to 10 T suggests that the critical magnetic field lies below 3 T. The assumption that the effective g factor of GaAs(110) is the same as in the case of GaAs(001) implies, that $\hbar\omega_{\rm c,CF}$ is small, which suggests a weak confinement potential. As already mentioned in the discussion in Subsec. 6.2.5, the confinement potential in the case of an SHI structure is significantly influenced by the background doping. The reduced doping efficiency in the case of GaAs(110) compared to GaAs(001) results from the fact that a noticeable amount of the dopants (Si atoms) form acceptors [223] and thus partly compensate the donors. It is conceivable therefore that the impurities, responsible for the background doping, are also incorporated differently on GaAs(110), which would lead to a different conduction band profile and confinement potential as in the case of GaAs(001).

A useful experiment would be to use a QW structure on GaAs(110), which would allow to make a constructive statement about the finite thickness, because the influence of the background doping on the confinement potential is much less. The experimentally determined critical magnetic field of the spin transition could be compared to the result of an equivalent sample on GaAs(001) and would allow *e.g.* an estimation of the effective g factor.

6.8.4 Hole gas sample

The investigation of a two-dimensional hole gas (2DHS) is based on the possibility, that in this case the Fermi contact interaction (see Subsec. 6.2.3) is strongly reduced due to the p-type

Bloch functions, which compose the valence band edge. Consequently, the hyperfine interaction between the electron and nuclear spins, which contributes to the hysteresis at the spin transition, is suppressed. This would allow to identify the contribution of the nuclear spin system to the hysteresis at the spin transition.[21]

An SHI structure was grown on GaAs(311)A substrate by K. Muraki (NTT Basic Research Laboratories, Japan). Due to the surface orientation of the substrate, the mobility is strongly anisotropic where the $[\bar{2}33]$ axis provides the highest mobility. The Hall bars were oriented accordingly. The mobility is 60 m^2/Vs. An evaporated 8.5 nm thin AuPd front gate with an Pd content of 40% is used to tune the hole density.

The effective g factor for holes in GaAs(311)A is about a factor of two larger than for electrons in bulk GaAs(001) [224, 225]. The assumption that the confinement potential and hence the finite thickness of the 2DHS is comparable to that of a regular SHI structure based on GaAs(001), leads to the expectation of a noticeable reduced critical magnetic field of the spin transition compared to an equivalent SHI structure based on GaAs(001) hosting a 2DES. That the critical magnetic field is most probably very low is supported by a study of the reentrant QHE at $\nu = 4/3$ by Muraki *et al.* [226]. The crossing of CF LLs, which is responsible for the latter effect, occurs at a much lower magnetic field in the case of a 2DHS than in the case of the equivalent 2DES, which is mostly due to the larger effective g factor for the holes in GaAs(311)A. The minimum of the longitudinal resistance due to the FQHE at $\nu = 2/3$ can be resolved up to a magnetic field value as low as 3 T at base temperature. The $R_{\rm xx}$ minimum successively vanishes but never reappears when the hole density is continuously decreased with the help of the front gate. Consequently, the spin transition point cannot be located. It is however worth mentioning that no hysteresis at all around $\nu = 2/3$ is found even at the lowest density of 0.5×10^{15} m^{-2}. But since the spin transition point is not identified, this observation cannot be interpreted as indication that the hyperfine coupling is predominantly responsible for the hysteresis observed in 2DES devices.

A useful approach to study the spin transition in a 2DHS would be to realize a 2DHS in a narrow QW. The confinement would result in a larger critical magnetic field due to the enhanced Coulomb correlation energy. This implication should allow access to the spin transition point. The confinement induced change of the effective g factor for holes in GaAs(311)A is similar to the impact of the confinement effect on the effective g factor for electrons in GaAs(001) [224], *i.e.* the Zeeman splitting will be reduced, which would support the aim of increasing the critical magnetic field of the spin transition in a 2DHS.

---

[21] Jungwirth *et al.* [68] argue that a quantum Hall ferromagnet that undergoes a phase transition governed by easy-axis anisotropy (valid at $\nu = 2/3$ [182]) should also exhibit an intrinsic hysteresis. However, the calculations of Jungwirth *et al.* refer only to the IQHE regime.

Chapter 7

The isospin transition at total filling factor 2/3

This chapter discusses the second ferromagnetic phase transition at total filling factor $\nu_{\mathrm{tot}} = 2/3$. In contrast to the spin transition this phase transition is only present in a bilayer, because it is due to a crossing of CF LLs with different subband index, *i.e.* the isospin, as introduced in Sec. 4.2, is changed. Due to the presence of a bilayer, the term total filling factor is used here referring to both charge layers altogether. The relationship between the isospin transition and the changeover of the bilayer from a one-component (1C) to a two-component (2C) regime, as discussed in Sec. 4.3, is discussed.

7.1 Theory of the isospin transition at total filling factor 2/3

The extension of the schematic development of the CF LLs with magnetic field or density at $\nu_{\mathrm{CF}} = 2$ given in Fig. 6.1 to CF LLs emanating also from the anti-bonding subband energy, leads to the expectation of another crossing of CF LLs at a higher density than the spin transition, as can be seen from Fig. 7.1. The CF LLs (B,1,↑) (AB,0,↑) with different subband index or isospin but the same spin orientation are concerned. This additional crossing of CF LLs is mostly due to the reduction of the subband splitting $\Delta\mathrm{SAS}$ towards higher total density (see Fig. 4.4). Continuing the nomenclature of Sec. 4.2 and taking the isospin of both occupied CF LLs into account, the system undergoes a changeover from the isospin polarized (B,B) to the isospin unpolarized (B,AB) phase with an increasing total density.

Since the subband splitting is a relevant quantity and a bilayer-like electron distribution is established, the imbalance is important. First the case of a balanced electron distribution will be discussed. The impact of an imbalance on the isospin transition is the subject of Sec. 7.4. In addition to the crossing of CF LLs with different isospin, the layer separation increases towards higher total electron density, as shown in Fig. 4.4, so that the intra-layer Coulomb correlation energy in each layer finally wins over the inter-layer Coulomb correlation energy, as discussed in Sec. 4.3. Then, correlated states like FQHEs develop independently in each layer and the

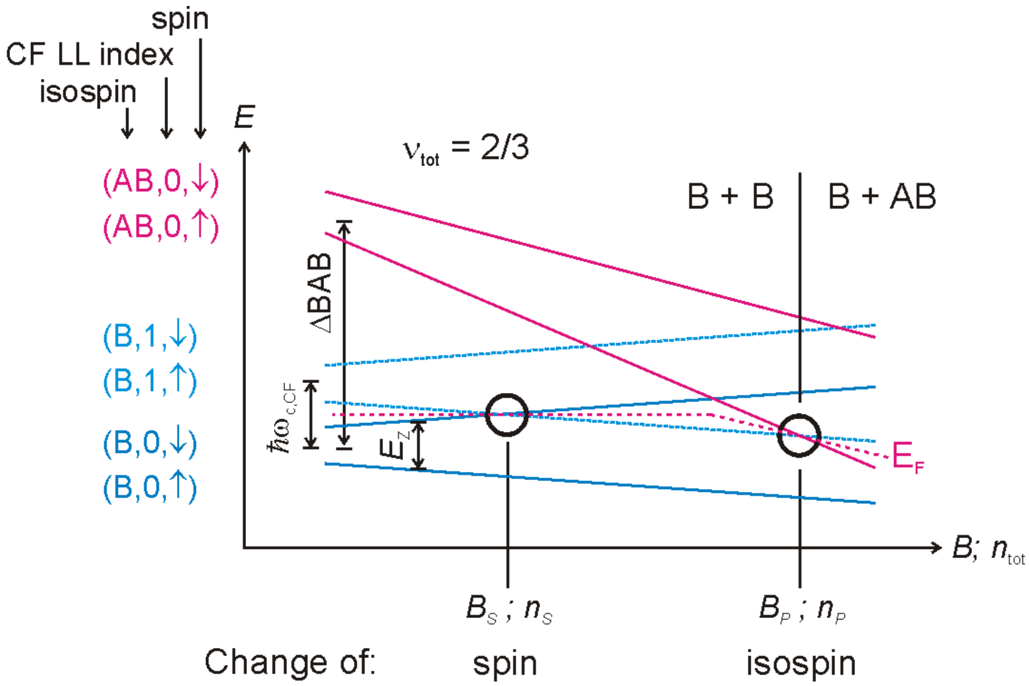

Figure 7.1: Schematic variation of the energetically lowest CF LLs in a bilayer with magnetic field or balanced total density when ν_{tot} is fixed to 2/3 . Besides the CF LL coincidence producing the spin transition at lower density, there occurs another CF LL coincidence at higher total density due to the drop of the subband splitting ΔSAS. This crossing causes a change of the isospin configuration.

bilayer is in the two-component (2C) regime. Below the critical total density in the so-called one-component (1C) regime, correlation effects originate from the Coulomb interaction among all electrons confined in the WQW, even though they are spread over two layers. The bilayer behaves as a single 2DES. Since the reason for the 1C-2C phase transition is at first glance associated with an increase of the layer separation, this transition is expected to apply to all total filling factors and at approximately the same density.[1] This consequence proves to be the case, as can be seen for some FQHEs in Fig. 5.12. Due to the fact that fractional quantum Hall states occur at filling factors with odd denominators only (except $\nu = 5/2$ [131] and $\nu = 7/2$ [227]), all FQHEs at a fractional total filling factor with odd nominators are lost above that critical total density. This is clearly seen for instance for $\nu_{\text{tot}} = 3/5$ at a total density of about 1.4×10^{15} m^{-2}. The same holds for quantum Hall states at odd integer filling factors. In Fig. 5.12 only the implication on the quantum Hall state at $\nu_{\text{tot}} = 1$ can be seen, namely a strong reduction of the plateau width above a total density of about 1.4×10^{15} m^{-2}. The impact on other quantum Hall states is not shown but has been reported in the literature for equivalent bilayer systems [87, 88]. It is not surprising that the critical total density coincides well with

---

[1] As discussed in Sec. 4.3, the decisive relation between intra- and inter-layer Coulomb correlation energy depends not only on the layer separation d, but also on the magnetic length. Therefore, the critical total density is slightly different for every total filling factor.

the total density at which the QHE with $\nu_{\mathrm{tot}} = 1/2$ is most pronounced, because this state is stabilized by comparable inter- and intra-layer Coulomb correlation energies, as discussed in Sec. 5.4.

According to Fig. 7.1, the two coinciding CF LLs involved in the isospin transition differ by the isospin, equivalent to the energy difference ΔSAS, and by one unit in the orbital quantum number, equivalent to the energy difference $\hbar\omega_{\mathrm{c,CF}}$. The subband splitting is related (but not equal) to the inter-layer Coulomb correlation energy and the CF cyclotron energy is related (but not equal) to the intra-layer Coulomb correlation energy. So at the crossing point the suggestion of comparable inter- and intra-layer Coulomb correlation energies should hold. This similarity is elaborated quantitatively in Sec. 7.3. More importantly, due to this correspondence and its relation to the 1C-2C phase transition, a promising density range to find the isospin transition seems to occur around 1.4$\times 10^{15}$ m^{-2}.

The isospin transition involves the redistribution of half of the charge carriers since one CF LL with the isospin B is depopulated and the charges are transferred to a CF LL with the isospin AB and the two isospin orientations (B,AB) represent a different charge distribution with respect to the center of the WQW. This difference implies, that in real space charges are transferred from the center of the WQW towards the edges while preserving the balanced

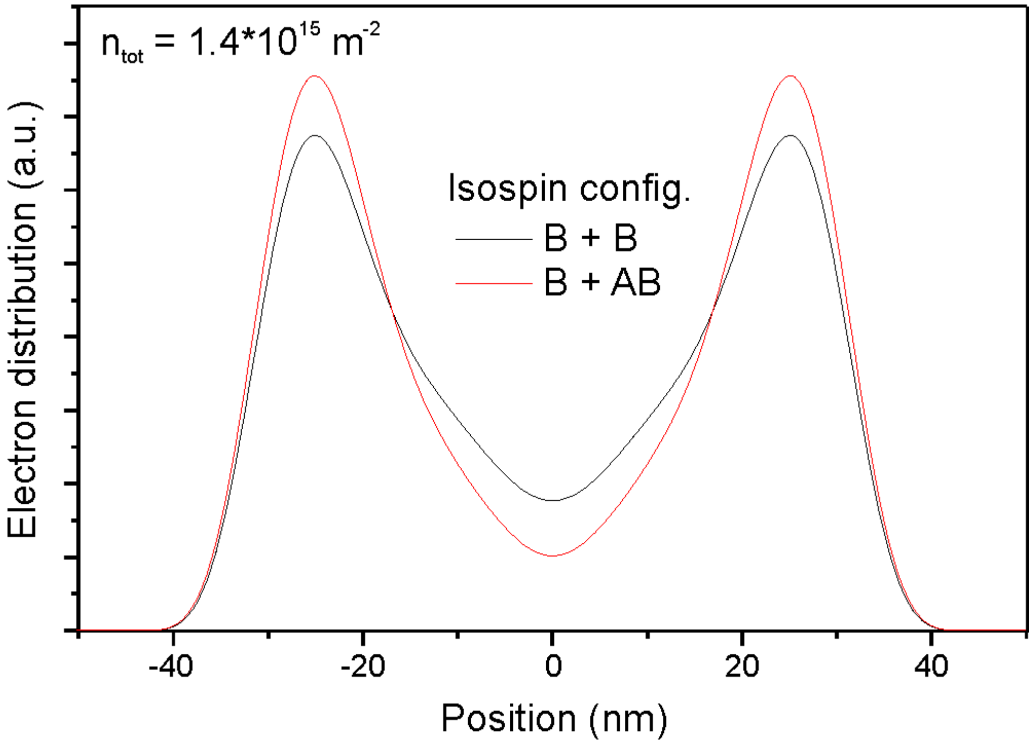

Figure 7.2: Calculated charge distributions at the isospin transition due to the transfer of half of the electrons residing on a CF LL with isospin B to a CF LL with isospin AB. This transfer enhances the layer separation. The critical total density is taken to be 1.4$\times 10^{15}$ m^{-2} as found by experiment.

condition and also supports the argument for layer decoupling with increasing total density and the formation of correlated states in each layer separately. A calculation using the quantum mechanical program of S.-J. Cheng (see Sec. 4.1) reveals the change of the charge distribution within the WQW when passing the coincidence. The result is shown in Fig. 7.2 for an assumed critical total density of 1.4$\times 10^{15}$ m^{-2}. In the following, the connection between the isospin transition and the 1C-2C phase transition is discussed.

7.2 Location of the isospin transition

It can be clearly seen from Fig. 5.12 that something happens with the FQHE at $\nu_{\mathrm{tot}} = 2/3$ at a balanced total density of 1.4$\times 10^{15}$ m^{-2} at which the 1C-2C phase transition of other FQHEs occurs and the QHE at $\nu_{\mathrm{tot}} = 1/2$ is most stable. Above that total density, the plateau width of $\nu_{\mathrm{tot}} = 2/3$ significantly increases towards a higher total density, while below the plateau width is almost independent of the total density (for the range of the total density relevant in this plot). Sweeps of the magnetic field and the total density with a higher resolution than in Fig. 5.12 around this critical total density are shown in Fig. 7.3 for the balanced case at base temperature. A resistance peak although small (less than 10 $\Omega/\Box$) is cutting through the plateau region of $\nu_{\mathrm{tot}} = 2/3$, indicating a strongly reduced energy gap near the Fermi energy.[2] Due to the lack of a further resistance spike at another total density and since the found total critical density is quite reasonable, it can be concluded that the found resistance spike at a total density of about 1.4$\times 10^{15}$ m^{-2} is associated with the isospin transition at $\nu_{\mathrm{tot}} = 2/3$.

7.3 Activation study at total filling factor 2/3

7.3.1 Implementation of the activation study

For the activation study, the temperature is set and each time a scan of the total density between 1.3$\times 10^{15}$ m^{-2} and 1.8$\times 10^{15}$ m^{-2} is performed for fixed filling factor $\nu_{\mathrm{tot}} = 2/3$ within a small imbalance range $\sigma = \pm 0.05$. Around the important total density 1.4$\times 10^{15}$ m^{-2} the total density steps are reduced from 0.01$\times 10^{15}$ m^{-2} to the lowest possible value 0.002$\times 10^{15}$ m^{-2} limited by the resolution of the voltage source (minimum increment 0.3 mV) used to control the gates. The logarithm of the measured resistance along the balanced line is plotted versus the inverse temperature (Arrhenius plot). The slope of a fitted straight line yields a half value of the activation energy. Activated behavior is found for all total densities and even directly at the isospin transition point, which is characterized by a strongly temperature dependent resistance spike.[3] The extracted values of the energy gap are plotted versus the scanned total density

---

[2] The variation of the magnetic field position of the resistance peak with total density is almost negligible in contrast to the related observation at the spin transition.

[3] The properties of resistance spikes of identical origin as well as for different types of transitions reported in the literature are listed in Tab. 6.1 including their temperature dependencies.

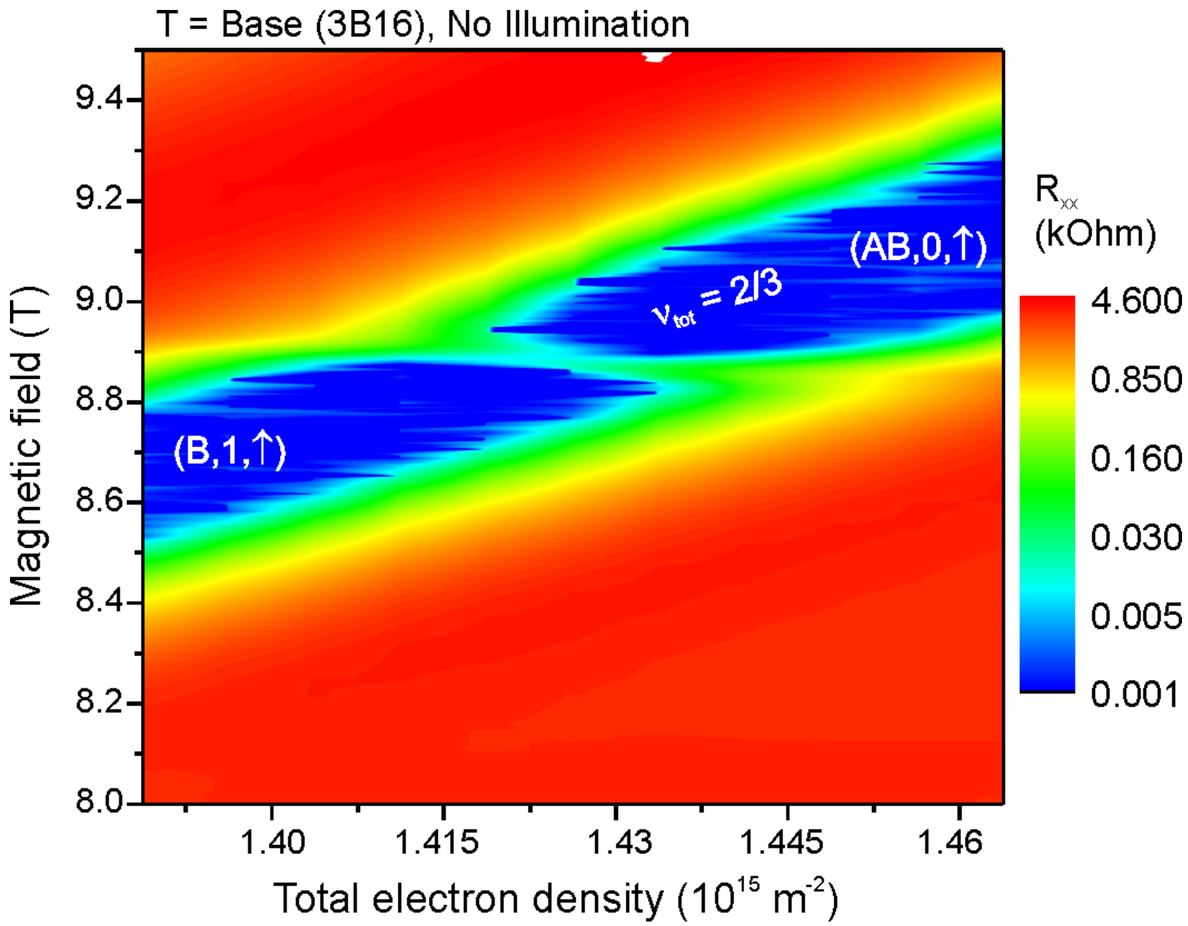

Figure 7.3: Magneto-transport measurements across the isospin transition at base temperature for a balanced electron distribution. The collapse of the FQHE indicates the phase transition. Note the logarithmic color scale.

range in Fig. 7.4. It is found that the activation energy with a minimum of about 0.5 K remains finite at the transition point $n_{\mathrm{tot}} \approx 1.4{\times}10^{15}$ m^{-2} in agreement with Suen *et al.* [118] and Lay *et al.* [123]. The experiment presented in [123] is discussed in the next subsection. Suen *et al.* [118] carried out a thermal activation study at $\nu_{\mathrm{tot}} = 2/3$ (which is presented again in [123]) for a wide range of the total density and fixed balanced distribution. They used a WQW with a nominal width of 77 nm, which however has been underestimated most probably by 5 to 10%, as already elucidated in Sec. 5.4. Due to that, the minimum in the activation energy is found at a total density of $1.0{\times}10^{15}$ m^{-2} noticeably below the value determined here.

7.3.2 Unification of the isospin and the 1C-2C phase transition

A phase diagram of a balanced bilayer at $\nu_{\mathrm{tot}} = 2/3$ has been given by McDonald and Haldane [228]. They calculated the different topological orders as a function of the subband splitting $\Delta\mathrm{SAS}$ and the layer separation d. Theoretically, both quantities can be handled independently.

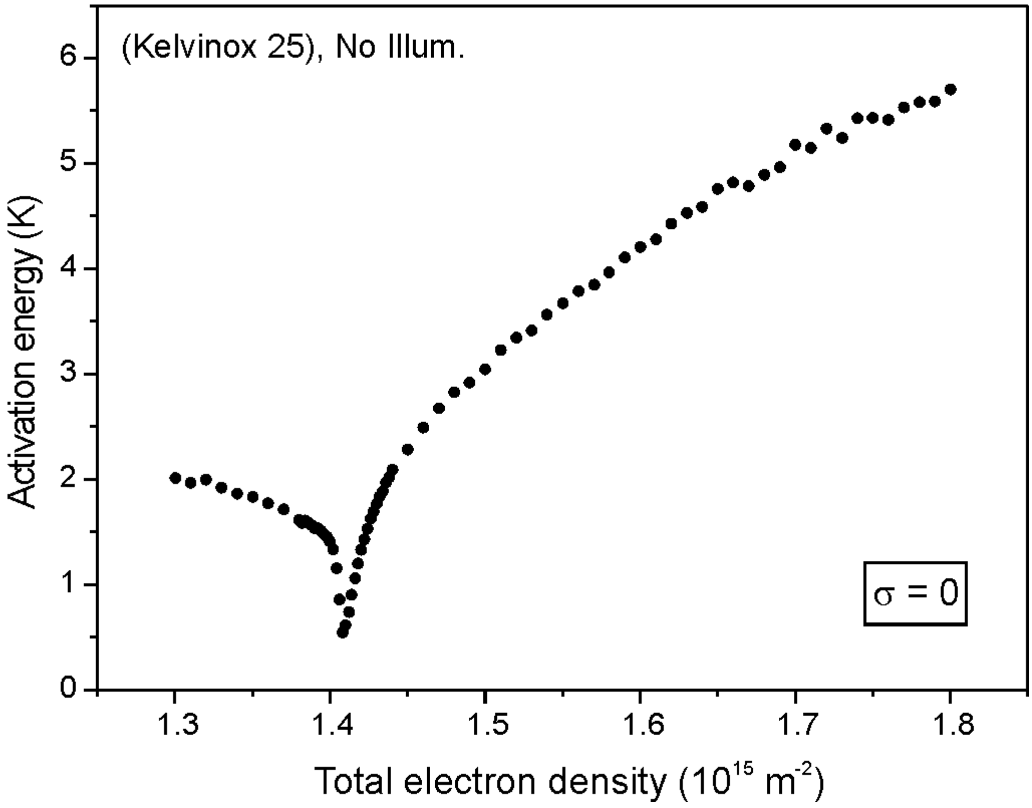

Figure 7.4: Plot of the activation energy at $\nu_{\text{tot}} = 2/3$ versus the total electron density for the balanced case. The minimum at a total density of about 1.4×10^{15} m^{-2} is due to a CF LL coincidence giving rise to the isospin transition.

Finite thickness has been neglected. At large layer separation, which corresponds for a WQW to a large total density, McDonald and Haldane find the ground state to be a (3,3,0) state. Referring to Eq. 5.9, the formation of this state requires the 2C regime. For small layer separation and non-zero subband splitting, which applies for a WQW at low total density, McDonald and Haldane predict the 1C regime.

An increasing in-plane magnetic field enhances the separation of the two electron layers as shown in Fig. 5.14, and leads to a 1C-2C phase transition. It has been pointed out by Lay *et al.* [123] that the activation energy at $\nu_{\text{tot}} = 2/3$ for a nominal 75 nm wide WQW sample and a balanced total density of 1.0×10^{15} m^{-2} has a minimum at a specific value of an additionally applied in-plane magnetic field. Lay *et al.* [123] argue that they have observed a 1C-2C phase transition, because an in-plane magnetic field enhances the layer separation (see Fig. 5.14). In order to observe this transition when applying an in-plane magnetic field the total density has to be small enough to ensure that at zero in-plane magnetic field the 1C regime is present. In [123] the reduction of the tunneling induced subband splitting ΔSAS with an in-plane magnetic field is calculated as well as the variation of the subband splitting ΔSAS with density for the balanced case and without any in-plane magnetic field. The tunneling induced subband splitting at the critical value of the in-plane magnetic field leading to the 1C-2C phase transition is found to be equivalent to a subband splitting naturally present at a balanced total density of 1.35$\times 10^{15}$ m^{-2}. Because of the very similar structure in that work (75 nm wide WQW) compared to the structure here (77 nm wide WQW), this result together with the also very similar critical total density of about 1.4$\times 10^{15}$ m^{-2} for the isospin transition suggests that the 1C-2C transition driven by an in-plane magnetic field is the same as the isospin transition driven here by a sweep of the total density.

The possibility of layer decoupling as induced by an in-plane magnetic field obviously does not provide a reason for a minimum in the activation energy. However, a minimum in the activation energy with respect to a density sweep is expected when passing the isospin transition. Since an in-plane magnetic field not only separates the layers but also reduces the tunneling induced subband splitting, which is also a direct function of the total density, it is clear that by applying an in-plane magnetic field, the CF LL coincidence associated with the change of the isospin at $\nu_{\rm tot} = 2/3$ can be shifted along the magnetic field axis or total density axis of the diagram in Fig. 7.1. Consequently, the isospin transition can be driven with an in-plane magnetic field as well as by sweeping the total density. The isospin transition observed here is thus identical to the one seen by Lay *et al.* [123]. In conclusion, the 1C-2C phase transition of $\nu_{\rm tot} = 2/3$ may also be viewed as originating from a level crossing of CF LLs with different subband index.

7.3.3 Modeling the pseudospin field at the isospin transition

The particular variation of the activation energy with the pseudospin field P in the vicinity of a coincidence of (CF) LLs provides useful information about the type of anisotropy governing the pseudospin reorientation [35, 68] and reveals the number of pseudospin flips per particle added to or subtracted from the system [72, 73, 80], as discussed in Sec. 4.2 and illustrated in Fig. 4.8. The underlying analysis requires that the activation energy $E_{\rm A}$ is plotted versus the theoretical pseudospin splitting $E_{\rm PS}$, *i.e.* the energy difference between the two relevant CF LLs close to the Fermi energy with the quantum numbers (B,1,↑) and (AB,0,↑):

$$E_{\rm PS} = E({\rm B}, 1, \uparrow) - E({\rm AB}, 0, \uparrow), \tag{7.1}$$

where

$$\begin{array}{rcl} E({\rm B}, 1, \uparrow) & = & 0 \times \Delta{\rm SAS} + \frac{3}{2} \times \hbar\omega_{\rm c,CF} + \frac{1}{2} \times E_{\rm Z}, \\ E({\rm AB}, 0, \uparrow) & = & 1 \times \Delta{\rm SAS} + \frac{1}{2} \times \hbar\omega_{\rm c,CF} + \frac{1}{2} \times E_{\rm Z}, \end{array} \tag{7.2}$$

so that the energy difference between these CF LLs can be calculated

$$E_{\rm PS} = \hbar\omega_{\rm c,CF} - \Delta{\rm SAS}. \tag{7.3}$$

This splitting vanishes at the transition point so that

$$\Delta{\rm SAS} = \hbar\omega_{\rm c,CF}. \tag{7.4}$$

The known subband splitting $\Delta{\rm SAS} = 12.4$ K at the critical total density of about 1.4$\times 10^{15}$ m^{-2} allows to calculate the CF cyclotron energy $\hbar\omega_{\rm c,CF}$ at this total density. However, of further interest is the variation of the CF cyclotron energy with the total density which raises the question, of how to express the CF cyclotron energy as a function of the total density. One approximation is to model the CF cyclotron energy as sum of the appropriately scaled intra-layer (E_C) and inter-layer (E_d) Coulomb correlation energies, as suggested by Suen *et al.* [33]

$$\hbar\omega_\mathrm{c,CF} = E_\mathrm{intra} + E_\mathrm{inter} = C_\mathrm{C}E_\mathrm{C} + C_\mathrm{d}E_\mathrm{d} = C_\mathrm{C}\frac{e^2}{4\pi\epsilon\epsilon_0\sqrt{l_\mathrm{B}^2+\lambda^2}} + C_\mathrm{d}\frac{e^2}{4\pi\epsilon\epsilon_0 d}. \qquad (7.5)$$

The prefactor C_C is the same as already found in Subsec. 6.2.5, because the same physics is involved. The value of the prefactor C_d is not necessarily equal to the value of C_C, because the many particle interaction giving rise to the inter-layer Coulomb correlation happens not within a plane but between two close planes. Due to this difference the Coulomb correlation can contribute differently to the CF cyclotron energy. But based on the knowledge of E_intra in good approximation since $C_\mathrm{C} \approx 0.1$ [155, 184] and $\lambda \approx 17.9$ nm (deduced from the calculations presented in Fig. 4.3), the intra-layer Coulomb correlation energy can be calculated at the critical magnetic field of about 8.8 T, which determines l_B. It results that $E_\mathrm{intra} \approx 0.5$ meV which implies that $E_\mathrm{inter} \approx E_\mathrm{intra}$ (with an error of less than 10%) because of the known subband splitting $\Delta\mathrm{SAS} \approx 1$ meV (see Sec. 5.2). This is not surprising, since the theory expects this "equality" in the vicinity of the appearance of the QHE at $\nu_\mathrm{tot} = 1/2$ which is what happens at precisely this total density. Furthermore, the "equality" is the condition for the 1C-2C phase transition. It should be noted, that although it is stated above, that the subband splitting corresponds to the inter-layer Coulomb correlation energy, they are not the same but just scale equivalently. According to the rough equality of E_intra and E_inter it follows for the second prefactor $C_\mathrm{d} \approx 2.8C_\mathrm{C} \approx 0.28$ when employing the layer separation $d = 52$ nm (see d as a function of the total density in Fig. 4.4).[4] It should be noted, that Eq. 7.5 is only an attempt to approximate the CF cyclotron energy in an analytical form based on intuitive arguments. A more accurate description would require a numerical treatment. But the given approximation of the CF cyclotron energy is sufficient to account for the qualitative dependence on the total density.

The parameters λ, d, and l_B vary with the total carrier density. The dependence of the magnetic length l_B on the total density can be easily calculated. The variation of the finite thickness λ is deduced from the calculations shown in Fig. 4.3. It is found to be linear in a reasonably good approximation over the total density range relevant here: $\Delta\lambda$ = -4.9 nm/(1×10^{15} m^{-2}).[5] The variation of d with total density is also known from calculations with the quantum mechanical program of S.-J. Cheng (see Fig. 4.4) and found to be 3.5 nm/(1×10^{15} m^{-2}) for the relevant total density range here. The variation of $\Delta\mathrm{SAS}$ with density along the balanced line

---

[4] Experimentally, an optimal value of 2.2 for d/l_B was found by Eisenstein *et al.* [34] to establish a QHE at $\nu_\mathrm{tot} = 1/2$ using a tunnel coupled DQW. For the determination of this ratio, l_B was not corrected for finite thickness. If so, the ratio reduces to about 1.5. Comparing E_C and E_d with E_intra and E_inter, the experimentally found optimal value for d/l_B reflects $C_\mathrm{d}/C_\mathrm{C}$ when multiplied with the finite thickness correction factor. This leads to $C_\mathrm{d}/C_\mathrm{C} = 3.4$, which is not too far from the value of 2.8 found here.

[5] In Sec. 4.1 it was stated that the finite thickness of each electron layer in the case of a bilayer scales approximately inversely with the total density. Since the change of the total density is only small here, the variation of λ with n_tot can be regarded as linear.

is known from Fig. 4.4. Having this, the experimentally determined activation energy E_A of Fig. 7.4 can be plotted versus the theoretical pseudospin splitting E_PS between the adjacent CF LLs involved in the isospin transition. The plot is shown in Fig. 7.5.

7.3.4 Analysis of the activation data

The slope s of the activation energy E_A plotted as a function of the theoretical pseudospin gap E_PS, as defined in Eq. 4.11, is shown in Fig. 7.6 and found to be unity away from the transition as expected. This shows that the lowest energy excitation within the system is one pseudospin flip. However, in the vicinity of the isospin transition, the slope becomes steeper and hence the number of pseudospin flips per unit of charge added to or subtracted from the system is larger than one. In fact, values of up to eight are reached. This feature was not observable by Suen *et al.* [118] and Lay *et al.* [123], because they changed the transition driving parameter, *i.e.* the

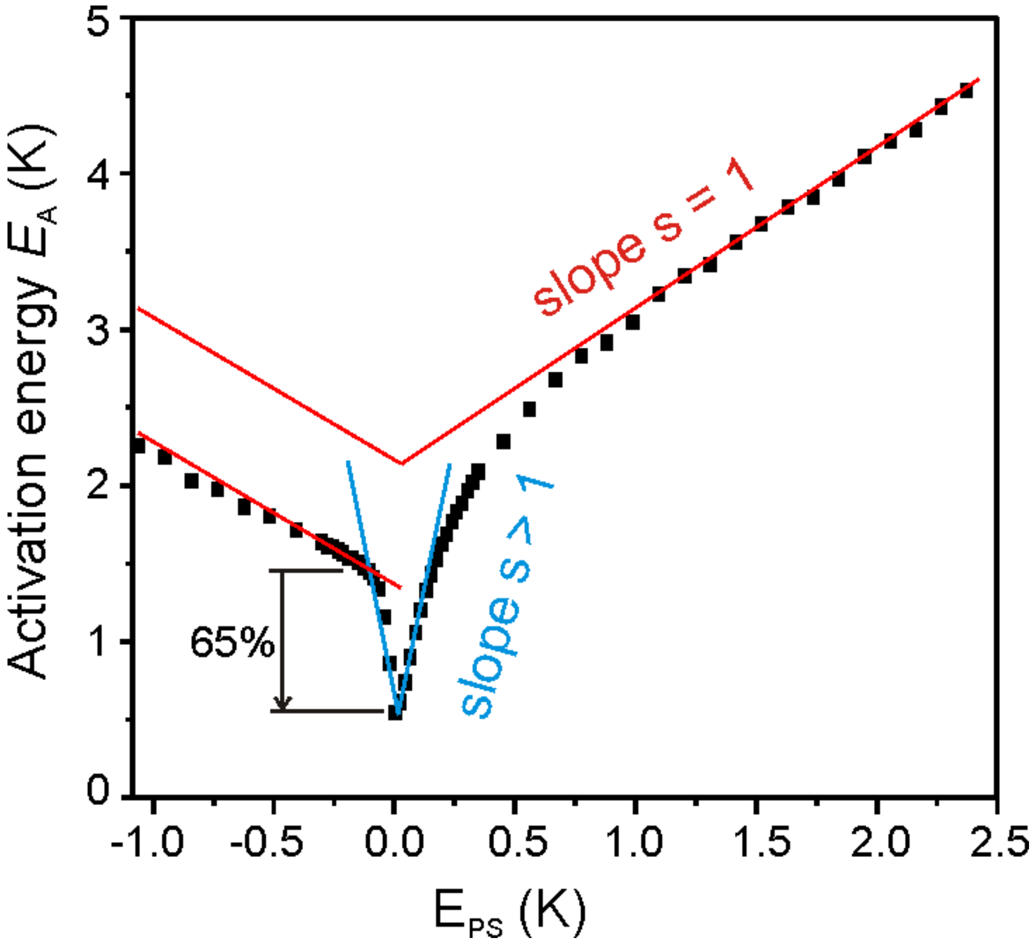

Figure 7.5: Plot of the activation energy of $\nu_\mathrm{tot} = 2/3$ versus the pseudospin gap. The reduced activation energy at negative values of the pseudpsin splitting, *i.e.* at total densities below the isospin transition point, is due to the fact, that the nature of the QH state is different for both sides of the transition point (see Sec. 7.4).

total density or the in-plane magnetic field, on too coarse a scale.

The shape of the trace obtained from the plot of the activation energy E_A versus the pseudospin field E_PS suggests two things (see the discussion in Sec. 4.2), which are discussed separately in this and the next paragraph. The absence of a region where E_A is independent of E_PS (see Fig. 4.8e) suggests that the isospin transition is governed by easy-axis but not by easy-plane anisotropy. Since the isospin and orbital quantum numbers change but the spin does not, the situation seems to be similar to the LL coincidences associated with the integer total filling factors $\nu_\mathrm{tot} = 3$ and $\nu_\mathrm{tot} = 5$, which exhibit easy-plane anisotropy. Instead, the isospin transition is similar to the spin transitions at $\nu_\mathrm{tot} = 4$ with respect to the type of anisotropy. Provided that the pseudospin anisotropy classification of Jungwirth and MacDonald [71], put forward for the IQHE regime, is still qualitatively valid in the FQHE regime, easy-axis anisotropy is in principle possible for the isospin transition but would require that the layer separation d were below a critical value d^*. Hysteresis at the isospin transition would provide additional support for easy-axis anisotropy. But it is absent just as for the transitions at $\nu_\mathrm{tot} = 4$, where a hysteresis is expected but not observed in experiment. The theory shows that the type of anisotropy can change to easy-plane with increasing imbalance. One indication could be a broadening of the transition region, as discussed in Sec. 5.3 with respect to the LL coincidences at $\nu_\mathrm{tot} = 4$. Just

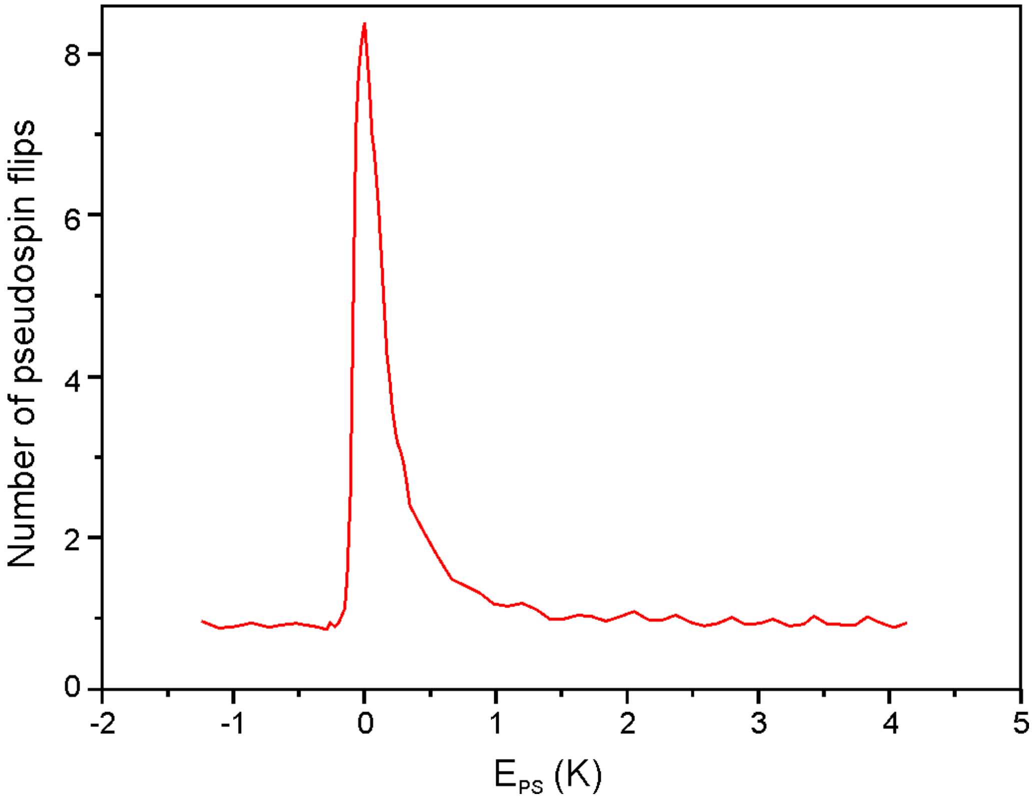

Figure 7.6: Slope s of the experimentally determined activation energy along the balanced line of $\nu_\mathrm{tot} = 2/3$ plotted versus the pseudospin splitting. The slope is equivalent to the number of pseudospin flips per particle added to or subtracted from the system.

such a broadening with imbalance is found and the experiment is discussed in more detail in Sec. 7.4. For easy-axis anisotropy the sample is likely to break up into domains of different pseudospin orientations for instance as a result of potential fluctuations [70]. The domains differ also in their isospin, which is associated with the number of nodes of the wave function. This suggests that the charge distribution along the growth axis of the WQW varies throughout the lateral extent of the sample close to the transition point. Both possible charge distributions displayed in Fig. 7.2 are symmetric relative to the center of the WQW and give rise to the same total density. So, only the distribution with respect to the center of the WQW is a function of the lateral coordinate.

A slope s larger than unity indicates that the system exhibits charged excitations lower in energy than a single pseudospin flip excitation. This requires the formation of a certain pseudospin texture that allows the existence of low energy excitations. In analogy to spin Skyrmions formed *e.g.* at the spin transitions involving $\nu_{\rm tot} = 4$ [35] or other LL coincidences [73, 229], it might be conceivable to speculate that here isospin Skyrmions are formed. They have been suggested by Sondhi *et al.* [82] and theoretically modeled by Ezawa [60, 77]. Skyrmion theory suggests a reduction of the energy gap by 50% at the center of the transition region. Here, a reduction of about 65% is seen (Fig. 7.5). A similar value has been reported by Muraki *et al.* [35] in the cases of the spin transitions at $\nu_{\rm tot} = 4$. See also the discussion in Sec. 4.2 of potential reasons leading to a finite energy gap.

The transition peak is quite sharp as expected for easy-axis anisotropy (see Fig. 7.7). Very similar to the dependence of the resistance spikes at $\nu_{\rm tot} = 3, 4, 5$ observed by Muraki *et al.* [35], the spike here increases with temperature. Above a certain temperature the height of the spike is expected to reduce again due to a changeover from the ferromagnetic to the paramagnetic phase of the bilayer. The critical temperature is known as the Curie temperature. For $\nu_{\rm tot} = 4$ the Curie temperature has been determined to be about 1.5 K [230]. Here, no culmination of the resistance spike height is observed up to the highest temperature of about 1 K used for the activation study.

The resistance spike vanishes towards lower temperatures equivalent to the resistance spikes at $\nu_{\rm tot} = 3, 4, 5$. The observation in the latter cases is attributed to a reduction of the size of domains towards lower temperatures [70] so that the overlap between domain wall loops, giving rise to scattering, will be smaller (see Sec. 4.2). Thus, the resistance spike should become smaller and finally disappear towards lower temperatures. According to the same theory [71] put forward for the IQHE regime, the size of domains also scales with the magnetic length, so that a higher magnetic field has the same impact as a lower temperature. Speculating that a qualitatively similar behavior is present in the FQHE regime, the critical magnetic field of the isospin transition here appears to be large enough and the base temperature low enough to result in small domains with almost no overlapping domain wall loops.[6]

---

[6] Note that the resistance spike, which indicates the spin transition at $\nu = 2/3$, does not vanish here (see Sec. 6.5) at base temperature. However, this activation study exhibits no indication for a saturation of the peak height towards lower temperatures. In fact, measurements using a 15 nm wide single QW structure with a critical magnetic field of 8.3 T show that this resistance spike can vanish [154, 231]. This clearly demonstrates the

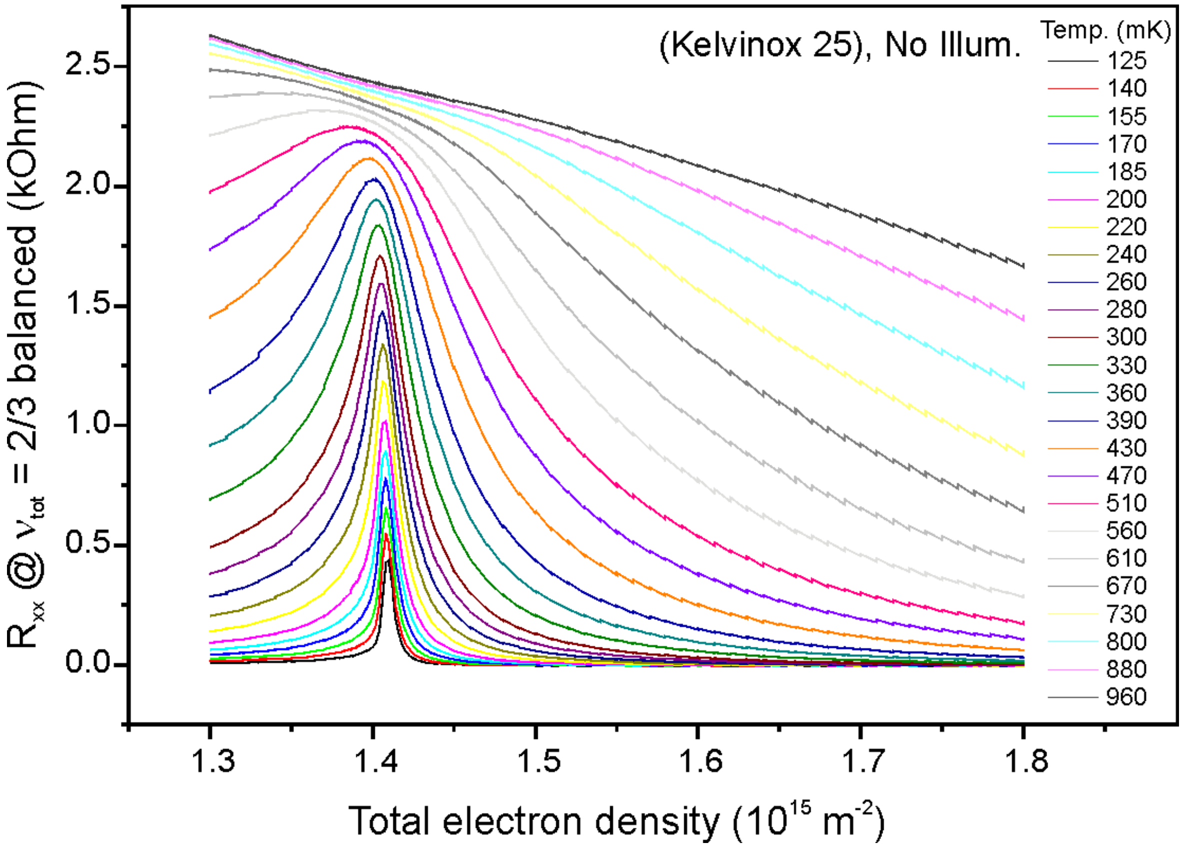

Figure 7.7: Temperature dependence of the longitudinal resistance at $\nu_{\rm tot} = 2/3$ along the balanced line over a wide range of the total density including the critical total density for the isospin transition. Towards lower temperatures the transition peak drops. A very small shift of the transition peak to lower densities can be seen with an increasing temperature.

As can be seen from Fig. 7.7 the resistance spike associated with the isospin transition shifts slightly towards lower total densities with increasing temperature. This suggests a change either of one or of both of the decisive energies $\hbar\omega_{\rm c,CF}$ and $\Delta{\rm SAS}$ with temperature. A variation of $\Delta{\rm SAS}$ due to temperature induced changes of parameters, which affect $\Delta{\rm SAS}$ *e.g.* the conduction band offset, the band gap of GaAs, the effective mass of the electrons, the lattice constant, the dielectric constant etc., are according to the literature (Landolt-Börnstein) far too small to produce this shift. A change of $\hbar\omega_{\rm c,CF}$ with temperature cannot be given. The asymmetric line shape of the peak with total density is due to the different ferromagnetic and topological orders of the bilayer on both sides of the peak, which results in very different activation energies. Also this asymmetry affects the actual peak position.

---

importance of the temperature and the magnetic field with respect to the actual height of the transition peak.

7.4 Measurement in the total density-imbalance-plane

Since the imbalance σ increases the subband splitting, σ also alters the critical total density of the isospin transition and favors the 1C phase over the 2C regime. It is therefore interesting to extend the study of the isospin transition in the presence of an imbalance. For that purpose, the filling factor is kept fixed at $\nu_{\rm tot} = 2/3$ as accurately as possible, while the total density is increased from 1.3×10^{15} $\rm m^{-2}$ to 2.0×10^{15} $\rm m^{-2}$ in steps of 0.01×10^{15} $\rm m^{-2}$. For every step the imbalance is tuned from $\sigma = -0.4$ to $\sigma = +1$ (and back again). The longitudinal and the Hall resistances are measured. The limit $\sigma = +1$ is natural, while the other limit $\sigma = -0.4$ is imposed by strong leakage currents and parallel conductivity for back gate voltages above $U_{\rm BG} = +0.6$ V.

The data are plotted in Fig. 7.8. Slightly away from the balanced line, the isospin transition shifts to higher total densities. The critical total density increases very well quadratically with

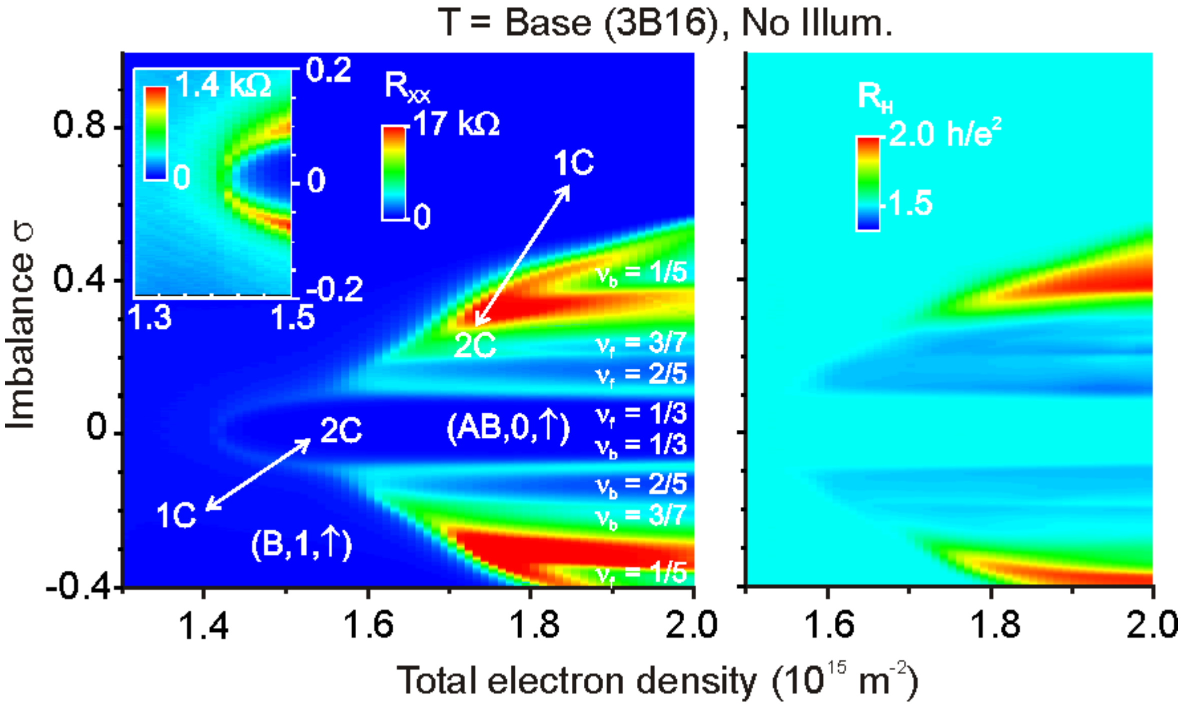

Figure 7.8: Measurement of the longitudinal and Hall resistances at fixed filling factor $\nu_{\rm tot} = 2/3$ over a wide total density and imbalance range at base temperature. At a total density of about 1.4×10^{15} $\rm m^{-2}$ and with a balanced electron distribution the isospin transition is indicated by a finite longitudinal resistance. With increasing imbalance, this critical total density is shifted in a quadratic manner to higher values and the transition region broadens. The phase boundary to a larger imbalance separates the 1C from the 2C regime. In the 2C regime, the Hall resistance is found to deviate noticeably from its expected value $\frac{3}{2}h/e^2$ for certain imbalance values whenever the longitudinal resistance exhibits a minimum. These minima are due to incompressible states, which form in one of the layers individually. The specific magic filling factors are given.

imbalance for $|\sigma| < 0.1$ analog to the increase of the subband splitting $\Delta\mathrm{BAB}$ with the square of σ, as displayed in Fig. 4.5. Due to that, a most likely imbalance induced change of the associated CF cyclotron energy, which competes with $\Delta\mathrm{BAB}$ for the critical total density since the two coinciding CF LLs also differ by one unit in the orbital quantum number, seems to be small compared to the variation of $\Delta\mathrm{BAB}$ with σ at these small imbalance values. It is further evident from the inset in Fig. 7.8 that the transition region widens with increasing imbalance. As previously mentioned in Sec. 5.3, this widening could be an indication of a gradual changeover from easy-axis to easy-plane anisotropy.

The uniformly colored area in the total density-imbalance-plane below the critical total density of about $1.4{\times}10^{15}$ m^{-2} for zero imbalance and also towards higher total densities for larger imbalance values corresponds to the 1C phase. The FQHE with $\nu_{\mathrm{tot}} = 2/3$ arises from the whole bilayer, since it behaves like a single 2DES. This is confirmed by the fact, that an FQHE is present for any imbalance value because an imbalance favors the 1C regime, as discussed in Sec. 4.3. The evaluation of the data of the activation study in Sec. 7.3 at $\sigma \neq 0$ shows, that the activation energy E_{A} increases in the 1C regime with an increasing imbalance. Suen *et al.* [118] found the same result and Sawada *et al.* [232] suggested this behavior, based on the increase of the plateau width towards larger imbalance values. The rise of E_{A} is due to an imbalance induced reduction of the effective thickness of the bilayer. It enhances the Coulomb correlation energy, which is responsible for the formation of the energy gap that stabilizes the FQHE.

Along the balanced line and above the critical total density of about $1.4{\times}10^{15}$ m^{-2}, the vanishing longitudinal resistance is due to an FQHE with filling factor $\nu = 1/3$ in each layer separately. Because of its 2C nature a good description for this bilayer state should be the wave function as given by Eq. 5.9 for the (3,3,0) state[7] proposed by McDonald and Haldane [228]. Furthermore, the FQHE breaks down for small imbalances which confirms the 2C nature, since an imbalance destroys the 2C regime. Consequently, the activation energy strongly reduces with increasing imbalance as is apparent from the evaluation of the data of the activation study (see Sec. 7.3) at $\sigma \neq 0$. The same behavior has been verified in [118, 232]. The imbalance range within which the FQHE at $\nu_{\mathrm{tot}} = 1/3 + 1/3$ in the 2C regime is stable reflects the plateau width of the FQHE at $\nu = 1/3$ for a single layer. Therefore, this range will most probably depend on the quality of the sample. It is almost independent of the total density, since the imbalance is a quantity normalized to the total density and since the plateau width is also a function of the (total) density; note the increase of the plateau width towards larger total density in this regime, as is apparent from Fig. 5.12.

According to the picture of crossing CF LLs, as given in Fig. 7.1, an increasingly larger imbalance is required towards larger total densities in order to force the CF LL crossing and thus to reestablish the 1C regime (FQHE at $\nu_{\mathrm{tot}} = 2/3$). So, once the necessary imbalance exceeds the value, the FQHE of the 2C regime ($\nu = 1/3$ in each layer separately) can withstand to disappear ($|\sigma| \approx 0.1$), it is expected that a large area in the total density-imbalance-plane emerges where the FQHE vanishes. This area is characterized by the appearance of minima

---

[7] However, the quantum mechanical overlap between the actual ground state and the (3,3,0) state will not be exact because of a *e.g.* still finite charge carrier exchange between the layers.

in R_{xx} at certain imbalance values accompanied by deviations of R_{H} from $\frac{3}{2}h/e^2$. In the 2C regime the appearance or the disappearance of an FQHE is not governed simply by the CF LL crossing but also by the requirement for a specific charge distribution between the layers. This is because the formation of an incompressible state is a matter of correlation in each layer individually. With this argument in mind, it is conceivable that several minima in R_{xx} can emerge due to an FQHE either in one or both layers separately (see Sec. 4.3). The formation of a fractional quantum Hall state in just one of the layers should be sufficient to produce a minimum in R_{xx} since the other layer is shortened by the vanishing longitudinal resistance of the incompressible layer.

The relation between the imbalance and the individual layer filling factors is given in Eq. 4.15. Simplified to the special case here $\nu_{\mathrm{tot}} = 2/3$, one finds for the front layer filling factor $\nu_{\mathrm{f}} = 1/3(1+\sigma)$ and for the back layer filling factor $\nu_{\mathrm{b}} = 1/3(1-\sigma)$. These two filling factors add up to 2/3. In particular, for $\sigma = 0$ one obtains $\nu_{\mathrm{b}} = \nu_{\mathrm{f}} = 1/3$. According to the Jain series of FQHEs towards higher and lower filling factors than $\nu = 1/3$ the following individual layer filling factors are expected with increasing positive imbalance before the 2C regime is destroyed, when taking only those magic numbers into account, which are associated with the most pronounced FQHEs: $\nu_{\mathrm{b}} = 2/7$ at $\sigma \approx 0.143$, $\nu_{\mathrm{f}} = 2/5$ at $\sigma = 0.20$, $\nu_{\mathrm{f}} = 3/7$ at $\sigma \approx 0.286$, $\nu_{\mathrm{b}} = 1/5$ at $\sigma = 0.4$. And, as anticipated, the experiment does reveal minima in the longitudinal resistance. They appear in the plot of Fig. 7.8 as small strips parallel to the balanced line at a specific constant imbalance value. Altogether three imbalance values (0.14, 0.21, 0.4) are apparent at which the longitudinal resistance drops. These minima may thus be attributed to the magic filling factors $\nu_{\mathrm{b}} = 2/7$, $\nu_{\mathrm{f}} = 2/5$, and $\nu_{\mathrm{f}} = 1/5$ in the order of their appearance when moving away from $\sigma = 0$ towards positive[8] imbalance values. The associated front/back layer filling factor of the second layer is in each case not a magic number but that does not, as previously mentioned, impede the appearance of an R_{xx} minimum. However, the strength of the R_{xx} minima, as suggested by their widths, is contradictory to expectations. The minimum assigned to $\nu_{\mathrm{b}} = 2/7$ is much more pronounced than that at $\nu_{\mathrm{f}} = 2/5$. This is unusual. In addition, at an imbalance value of $\sigma = 0.286$ no R_{xx} minimum is present, although one obtains $\nu_{\mathrm{f}} = 3/7$ for this imbalance value. It seems probable then that the given assignment might be not correct. The imbalance used as one axis for the plot of Fig. 7.8 is calculated based on the assumption that the density change with gate voltage is constant for both layers. This assumption also may not be entirely correct, because a slight change of the distance between the individual electron layer and its corresponding gate exists in dependence of the total density (see Fig. 4.4) and the imbalance (see Fig. 4.6). Consequently, some uncertainty in determining the imbalance is unavoidable. Furthermore, it is assumed for the sake of simplicity that the border between the front and the back layer is at the center of the WQW. Due to these issues the assignment of the different R_{xx} minima with individual layer filling factors is taken as displayed in Fig. 7.8 in correspondence with the usual strength of FQH states.

In order to support this assignment of the minima the longitudinal resistance R_{xx} is mea-

---

[8] The same sequence of filling factors is found for negative imbalance values, only the indexes for the front and back layer are exchanged.

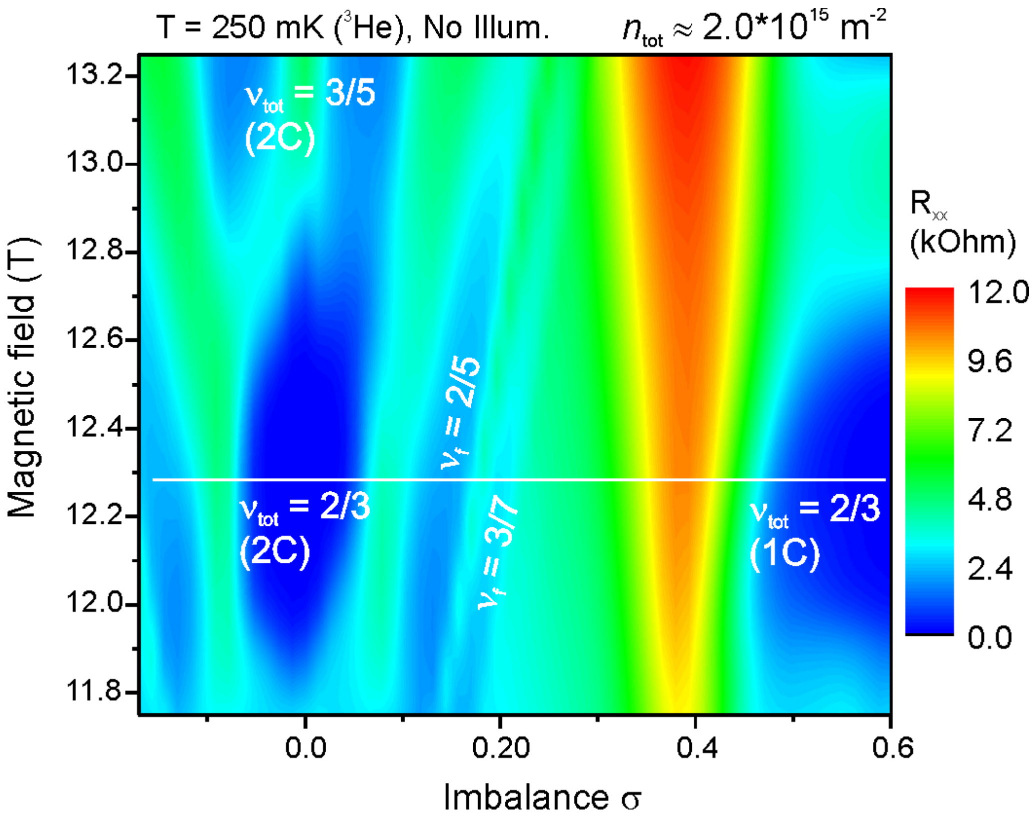

Figure 7.9: Measurement of $R_{\rm xx}$ with magnetic field and imbalance at $T = 250$ mK and a constant total density of about 2.0×10^{15} m^{-2}. The white horizontal line marks $\nu_{\rm tot} = 2/3$ and corresponds to the right edge of the plot given in the left panel of Fig. 7.8. It can be seen that the two minima in $R_{\rm xx}$ that appear parallel to the balanced line at finite imbalance values in the 2C regime of Fig. 7.8 are most pronounced at slightly smaller total fillings than 2/3 and imbalance values.

sured for a total density of about 2.0×10^{15} m^{-2} as a function of the magnetic field around $\nu_{\rm tot} = 2/3$ with imbalance as an additional parameter. The result for a temperature of 250 mK is shown in Fig. 7.9 and for base temperature in Fig. 7.10. In particular, the experiment carried out at 250 mK shows that the two $R_{\rm xx}$ minima, which appear away from, but closest to, the balanced line, are not most pronounced at $\nu_{\rm tot} = 2/3$ (the white horizontal line) but appear to be strongest at a slightly higher total filling factor or smaller magnetic field and at an equivalently slightly lower imbalance. For $\nu_{\rm f} = 2/5$ this is not surprising, because a total filling factor enlarged from 2/3 to ≈ 0.686 and an imbalance comparably reduced from 0.14 would in addition allow the energetically favored FQH state $\nu_{\rm b} = 2/7$ for the bottom layer. The formation of this incompressible state would theoretically require a reduction of the magnetic field by about 2.86%. This reduced optimal magnetic field is confirmed by the experiment since the $R_{\rm xx}$ minimum appears there most pronounced. Equivalently, for $\nu_{\rm f} = 3/7$ a reduction of the magnetic field and imbalance from their values present at the white horizontal line by about 7.14% would again allow the formation of an FQH state with $\nu_{\rm b} = 2/7$. The necessary reduction of B and σ

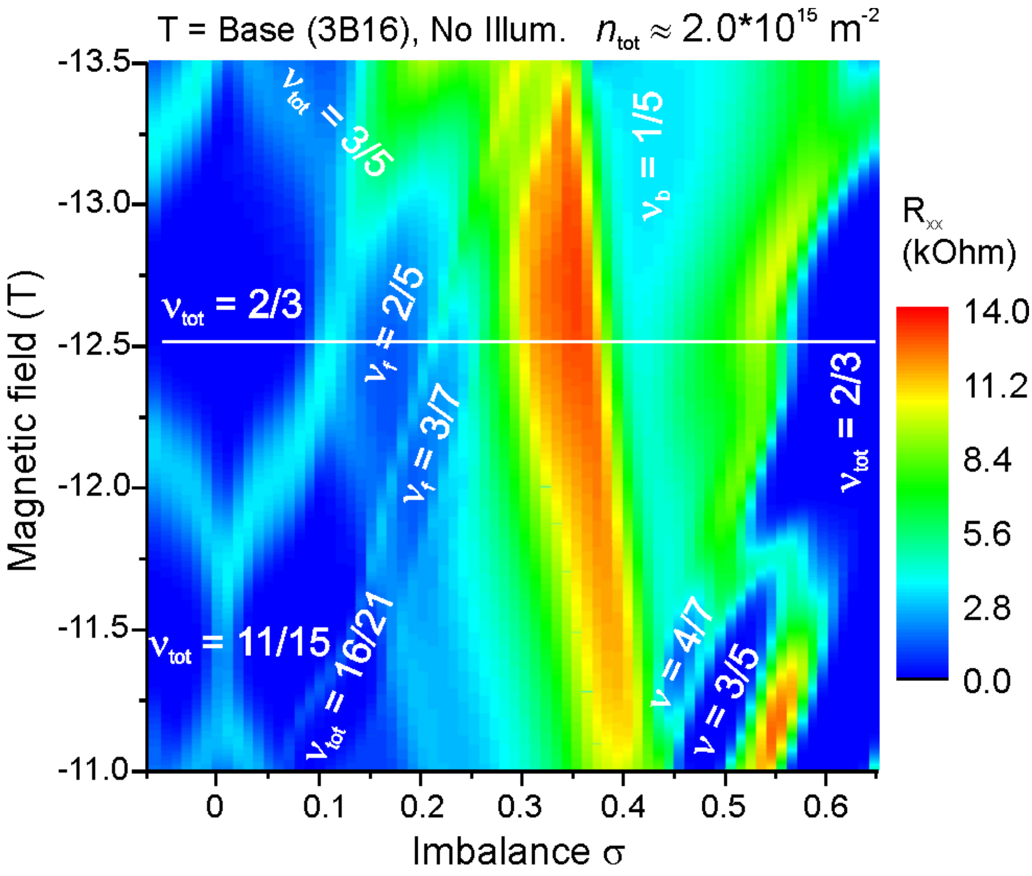

Figure 7.10: Measurement of $R_{\rm xx}$ with magnetic field and imbalance at base temperature and a constant total density of about $2.0{\times}10^{15}$ m^{-2}. The white horizontal line marks $\nu_{\rm tot} = 2/3$ and corresponds to the right edge of the plot given in the left panel of Fig. 7.8. In addition to the two $R_{\rm xx}$ minima away from balanced already visible in Fig. 7.9 a third minimum in Fig. 7.8 at $|\sigma| \approx 0.4$ is resolved and more pronounced at much larger magnetic fields than that magnetic field necessary to obtain $\nu_{\rm tot} = 2/3$. The measurement also discloses two further compound quantum Hall states at $\nu_{\rm tot} = 11/15$ with $\nu_{\rm b} = 1/3$ and $\nu_{\rm f} = 2/5$ and $\nu_{\rm tot} = 16/21$ with $\nu_{\rm f} = 1/3$ and $\nu_{\rm b} = 3/7$.

is confirmed by the experiment carried out at base temperature. The assignment of the individual layer filling factors $\nu_{\rm f} = 3/7$ and $\nu_{\rm b} = 2/7$, which sum up to $\nu_{\rm tot} = 5/7$, is supported by the observation of the Hall resistance quantized to $\frac{7}{5}h/e^2$ at the reduced B and σ values. At the two imbalance values at which the $R_{\rm xx}$ minima, discussed above, are observed for $\nu_{\rm tot} = 2/3$, a drop in the Hall resistances by about 1.5% from its expected value $\frac{3}{2}h/e^2$ is observed (see the right panel of Fig. 7.8). This reduction is most probably due to the onset of an incompressible state in the second layer (the first layer already being in an incompressible state) which starts to force the Hall resistance towards a quantized value slightly below $\frac{3}{2}h/e^2$, since the magic filling factors of both layers do not add up to 2/3.

The observation (see Fig. 7.8) of an $R_{\rm xx}$ minimum at $\sigma = +0.4\,(-0.4)$ leads to $\nu_{\rm b} = 1/5$ and

$\nu_\text{f} \approx 0.47$ ($\nu_\text{f} = 1/5$ and $\nu_\text{f} \approx 0.47$). The agreement of the expected and the measured optimal imbalance for this FQHE in one of the layers indicates that the calculation of the imbalance is accompanied by only minor uncertainties. As can be seen in Fig. 7.10, this R_xx minimum is more pronounced towards smaller total filling factors. Remarkably, this R_xx minimum is at $\nu_\text{tot} = 2/3$ accompanied by a Hall resistance (see Fig. 7.8) very close to $2h/e^2$, but the formation of a plateau is not found as for the other two R_xx minima at their optimal ν_tot and σ values. No explanation for this strong deviation from $\frac{3}{2}h/e^2$ can as yet be given. However, such deviations of the Hall resistance from its normal value do occur more frequently in bilayers. For instance a drop of the Hall resistance in the WQW close to the insulating phase (IP, see Fig. 5.12) can be observed. In the case of the DQW structure fabricated here a strong increase of the Hall resistance by about a factor of two from its normal value is present above magnetic fields of about 7 T and at imbalance values close to zero and around 0.6 in combination with total densities of $1.0{\times}10^{15}$ m^{-2} and $1.2{\times}10^{15}$ m^{-2} (no data are shown here). Some mechanisms that can lead to deviations of the Hall resistance are discussed in [233–237]. For a single 2DES an overshoot in the Hall resistance is explained as a magnetic field driven decoupling of the two edge states associated with the topmost spin split LLs. This decoupling occurs because of the enhanced spin splitting due to electron-electron interaction [237]. In the case of a bilayer it has been suggested that the exchange interaction between the two layers, which is a function of occupied CF LLs with different subband index, leads to an overshoot in the Hall resistance [235]. It should be noted that when the filling factor of one layer is 1/5 and consequently the other layer reaches a filling factor of ≈ 0.47, it might be that a major part of the current is carried by the layer with the larger filling factor. Because 1/5 is already a very low filling factor close to an insulating phase [238]. An inhomogeneous current distribution can lead to a Hall resistance that tends to $\frac{1}{0.47}h/e^2$, *i.e.* $\approx 2h/e^2$.

The experiment at base temperature (see Fig. 7.10) further reveals two compound quantum Hall states [113]. They are $\nu_\text{tot} = 11/15$ with $\nu_\text{b} = 1/3$ and $\nu_\text{f} = 2/5$ and $\nu_\text{tot} = 16/21$ with $\nu_\text{f} = 1/3$ and $\nu_\text{b} = 3/7$. This assignment can be given due to the imbalance values at which they are most pronounced, the optimal magnetic field values, and the quantized Hall resistances. The state at $\nu_\text{tot} = 11/15$ is also discussed in Sec. 5.4 (see Fig. 5.12).

7.5 Phase diagram of filling factor 2/3 for a bilayer at finite temperature

The variations of the CF LL energies upon changes of the (total) electron density and its distribution within the WQW can be estimated qualitatively and could be even partly quantified here by tracking spin and isospin transition at $\nu_\text{CF} = 2$ in dependence of the shape of the WQW potential. This combination of theoretical and experimental results allows to draw a phase diagram of the ferromagnetic (and topological) order at $\nu_\text{CF} = 2$ as a function of the (total) density and the electron distribution independent of the regime (single layer or bilayer). One axis is the (total) density but the other axis can neither be the imbalance σ, which by definition is only valid in the bilayer regime, nor the finite thickness λ, which cannot describe a distribution in the bilayer regime. A useful parametrization of the electron distribution in the WQW regardless of the actual regime (tilt of the WQW potential) is the normalized mean electron position of all charges $\bar{z}$ with respect to the center of the WQW

$$\bar{z} = \frac{1}{w/2} \frac{\int z\rho(z)dz}{\int \rho(z)dz}. \tag{7.6}$$

Here, z is the position coordinate along the growth direction measured from the middle of the WQW, w is the width of the WQW, and $\rho(z)$ is the electron distribution function. $\bar{z}$ is similar to the imbalance σ as long as both layers are noticeably occupied, *i.e.* the imbalance is not too close to ± 1. An imbalance of $\sigma = \pm 1$ represents the boundary to the single layer regime and corresponds to approximately $\bar{z} = \pm 0.6$ for the WQW here. $\bar{z} = \pm 1$ corresponds to the hypothetical case where charges are entirely pushed to one of the heterointerfaces of the WQW. For the single layer regime, the finite thickness λ is closely related to the mean electron position; for instance, λ is maximal for $\bar{z} = 0$ and reaches zero for $\bar{z} = \pm 1$. Hence, the parameters λ and σ can be unambiguously mapped onto the single parameter $\bar{z}$ so that the phase diagram can be drawn. This is shown in Fig. 7.11. The variations of the different critical (total) densities of the different transitions with $\bar{z}$ is qualitatively similar to their dependence on λ or σ, since both parameters have a monotonous relation to $\bar{z}$. It is important to note, that this phase diagram is drawn for a non-zero temperature. It is not clear what actually happens *e.g.* with the width of the transition regions or with the finite R_{xx} values when the temperature approaches zero.

A similar phase diagram of the different topological orders at $\nu_{\text{tot}} = 2/3$ has been suggested by Kumada *et al.* [37] based on plausibility arguments with respect to the increase of the critical (total) density of the spin and isospin transition with imbalance. A phase diagram of a balanced bilayer at $\nu_{\text{tot}} = 2/3$ has been given by McDonald and Haldane [228]. They calculated the different topological orders as a function of the subband splitting ΔSAS and the layer separation d. Theoretically, both quantities can be handled independently. Finite thickness has been neglected. For large layer separation, which corresponds in the case of a WQW to a large total density, they find the ground state to be a (3,3,0) state as is also suggested here. For small layer separation and non-zero subband splitting, this regime is entered in the case of a WQW at low total density, they find the 1C phase as observed here.

In the case of a WQW structure at $\nu_{\text{CF}} = 2$ the isospin transition is found at a higher (total) density than the spin transition independent of the tilt of the WQW potential, because the bilayer regime already sets in before the CF LL with AB subband index becomes occupied. This is even true independently of the width w of the WQW, because the subband splitting and the critical density above which a bilayer is formed are similar functions of w. The marginal case where both transitions coincide can be reached for the DQW structure. From Fig. 7.1 it is apparent that by lowering the subband splitting, exclusively the isospin transition can theoretically be shifted to smaller total densities. Once the critical density dropped below the critical density of the spin transition, only one CF LL crossing would exist throughout the entire density range at $\nu_{\text{CF}} = 2$. This remaining ferromagnetic phase transition would combine both the

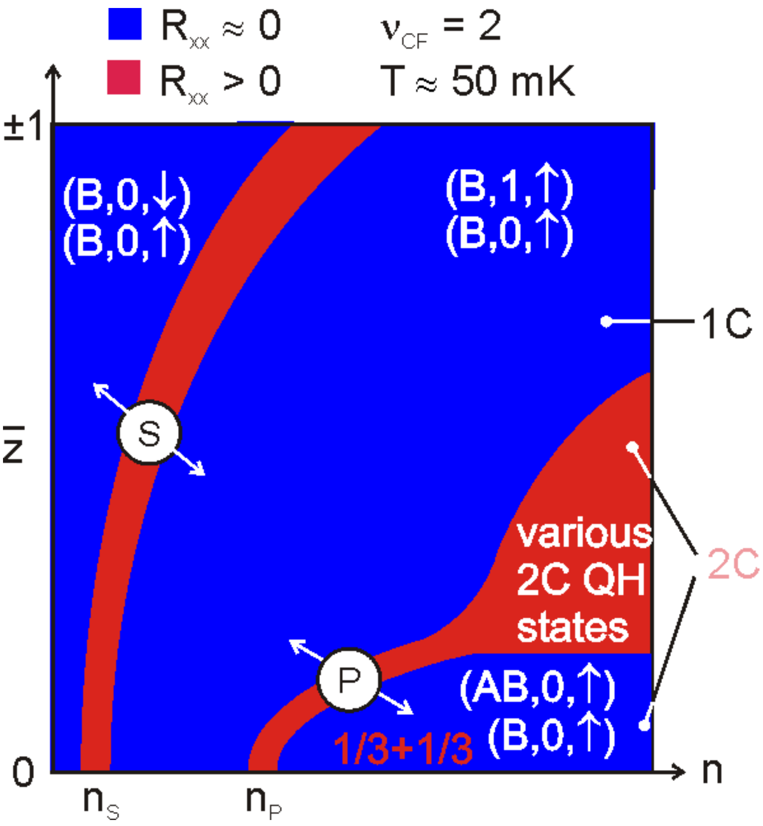

Figure 7.11: Phase diagram of an electron system confined to a WQW at $\nu_{\mathrm{CF}} = 2$ and finite temperature. At a lower density the spin transition (S) is found with its critical density n_{S} increasing when $\bar{z}$ is displaced from the center ($\bar{z} = 0$) of the WQW corresponding to a reduced finite thickness of the electron layer. At a higher total density n_{P} the isospin transition (P) occurs which then shifts to an even higher total density due to the increase of the subband splitting when the electron distribution is forced into asymmetry. In the 2C regime incompressible states (FQHEs) are formed in each layer separately even for an intermediate asymmetry of the WQW potential. The different quantum numbers of the CF LLs involved are marked.

change of the isospin (subband index) and the spin while at the same time the orbital quantum number would be preserved. It would be interesting to address this phase transition. If the pseudospin anisotropy classification (see Fig. 4.9) is still qualitatively valid in the FQHE regime, the changed quantum numbers would allow for only easy-plane anisotropy at a non-zero imbalance and no anisotropy at all for the balanced case. In a DQW structure the subband splitting can be adjusted independently of the total density by means of an appropriate barrier between the QWs hosting the two electron layers. It should be thus possible to realize a $\Delta\mathrm{SAS}$ small enough for both spin and isospin transitions to coincide.

Chapter 8

Summary

The main subject of this thesis are ferromagnetic phase transitions (FPTs) in single layer and bilayer electron systems. An FPT denotes the change of the ground state of a low-dimensional electron system under quantum Hall conditions. Bilayers, *i.e.* double layer two-dimensional electron systems (2DESs) that exhibit charge carrier exchange, are used to study FPTs by means of magneto-transport. Bilayers are realized in a remotely doped 77 nm wide GaAs quantum well (WQW) and in a double quantum well (DQW) consisting of two 18 nm wide GaAs QWs separated by 3.1 nm AlAs. These structures are fabricated with molecular beam epitaxy (MBE) on GaAs with (001) surface orientation. An *in situ* grown back gate and an evaporated front gate allow for the independent control of the individual layer electron densities. A thicker than 5 nm Ni wetting layer underneath the ohmic contacts of the bilayer and specifically annealed low-temperature (LT) grown GaAs, covering the back gate, are found to be necessary for a sufficient reduction of the leakage current from the back gate to the bilayer. The as-grown total electron density (sum of the individual layer densities) is about 2.1×10^{15} m^{-2} and the mobilities are 530 m^2/Vs (WQW) and 280 m^2/Vs (DQW). Most of the experiments are carried out on the WQW structure, so all results summarized below refer to this structure if not otherwise stated.

The charge carrier exchange induces a hybridization of the energy levels leading to the formation of two subbands for each level labeled bonding and anti-bonding. The two lowest subbands, which are exclusively occupied, are offset by the subband splitting $\Delta\mathrm{BAB}$. Quantum mechanical calculations are carried out in order to quantify those parameters, which govern FPTs. The calculations show that $\Delta\mathrm{BAB}$ increases approximately as the square of the imbalance σ, which is defined as the normalized electron density difference between the front and the back layer densities. $\Delta\mathrm{BAB}$ is found to scale approximately inversely with the total density. A value of about 0.8 meV is calculated at a total density of 1.0×10^{15} m^{-2}. Furthermore, when the total density (for the symmetric case $\sigma = 0$) is increased from 1.0×10^{15} m^{-2} to 2.0×10^{15} m^{-2} the peak to peak distance d between the electron layers rises from 50 nm to 54 nm.

A magnetic field B applied perpendicularly to the bilayer leads to the condensation of all states of the occupied subbands into two fan-charts of Landau levels (LLs). Each state is, besides its charge (electron or quasi-hole), characterized by several quantum numbers: orbital quantum number (0,1,2,...) associated with the electron cyclotron energy $\hbar\omega_\mathrm{c}$, spin ($\uparrow$,$\downarrow$) associated with the Zeeman energy E_{Z}, and subband index (bonding, anti-bonding) related to $\Delta \mathrm{BAB}$. Since only the two lowest subbands are relevant, the subband index is treated like an isospin. The quantum numbers (of each states) are bundled into an artificial single particle pseudospin. Ideally, when the ratio of electrons and magnetic flux quanta per unit area (filling factor) adopts a magic number (integer value at first), all pseudospins of each LL become aligned. Analogous to conventional ferromagnetism, this alignment is regarded as ferromagnetic order and designated by the term quantum Hall ferromagnetism (QHF). A ferromagnetic phase transition (FPT) is induced when two LLs of different ferromagnetic order are tuned through their energetic resonance, *i.e.* a crossing of two LLs occurs.

A generalized theoretical description of an FPT is introduced. The global pseudospin of a LL is defined as the collection of the single particle pseudospins of each LL. The two crossing LLs are assigned to have global pseudospin orientation up and down. The energy difference between the two LLs under consideration, termed pseudospin splitting E_{PS}, is defined to scale linearly with the pseudomagnetic field P. According to theory the process of the reorientation of the global pseudospin by passing the crossing point is governed by the anisotropy energy between the two different pseudospin orientations. Either an always pseudospin polarized state (easy-axis anisotropy) or a coherent superposition of both pseudospin orientations (easy-plane anisotropy) is preferred throughout the transition region, *i.e.* region of P around the LL coincidence point. The derivative of the activation energy E_{A}, which is a direct measure of the actual pseudospin splitting, with respect to the theoretical pseudospin splitting E_{PS} yields the number of pseudospin flips s upon a charged excitation of the system. s is always expected to be unity except when close to the transition point. For easy-plane anisotropy s tends to zero, while for easy-axis anisotropy s remains unity or can become even larger. The latter is only possible when the system allows energetically lower excitations than one pseudospin flip, which can be the case *e.g.* when Skyrmions form.

The two LL fan-charts are offset by $\Delta \mathrm{BAB}$ so that they intersect as a function of B, which leads to FPTs. In experiment, the crossing point of two LLs is tuned to the Fermi energy. The disappearance of the QHE, *i.e.* the appearance of a finite longitudinal resistance R_{xx}, due to the quenching of the energy gap between the concerned LLs at the crossing point, is taken as indication of an FPT. For ideally aligned single particle pseudospins the global pseudospin of each LL simplifies to a set of three single particle quantum numbers. The change of the global pseudospin orientation is therefore equivalent to a change of quantum numbers, and so the ground state is changed. According to the pseudospin anisotropy classification (PAC) given in the literature, the type of anisotropy is determined by the changed quantum numbers. In the regime of the integer QHE (IQHE) the isospin and the orbital quantum number are always changed. In the case of an even total filling factor (the sum of the individual subband filling factors) the spin is also flipped.

Measurements of R_{xx} at low B, *i.e.* Shubnikov-de Haas (SdH) oscillations, exhibit two beating frequencies due to the two different subband densities, which are extracted from a Fourier analysis. Their difference is used to quantify $\Delta \mathrm{BAB}$. In comparison with experiment, the calculations underestimate $\Delta \mathrm{BAB}$ by about 30%. At a temperature of 250 mK four FPTs are investigated in detail. The coincidences are passed by varying the total density, which is similar to a sweep of P, while a balanced distribution ($\sigma = 0$) is maintained. Two FPTs involving $\nu_{\mathrm{tot}} = 4$ are indicated by very narrow transition regions, *i.e.* ranges of the total density within which the QHE is lost. The other two FPTs involving $\nu_{\mathrm{tot}} = 3$ and $\nu_{\mathrm{tot}} = 5$ exhibit much broader transition regions. The critical total densities are approximately 0.85×10^{15} m^{-2} each time. The PAC predicts easy-axis anisotropy for the FPTs at $\nu_{\mathrm{tot}} = 4$ consistent with the narrow transition regions. For the FPTs at $\nu_{\mathrm{tot}} = 3$ and $\nu_{\mathrm{tot}} = 5$ the PAC cannot state which type of anisotropy applies. But based on the two broad transition regions in contrast to the small ones, these two FPTs are considered to be governed by easy-plane anisotropy. With an increasing imbalance σ the critical total densities are found to shift to higher values with a quadratic dependence on σ due to the equivalent rise of $\Delta\mathrm{BAB}$. For the FPTs at $\nu_{\mathrm{tot}} = 4$ the transition regions widen and this is attributed to a gradual change towards easy-plane anisotropy, as expected theoretically. For $\nu_{\mathrm{tot}} = 3$ and $\nu_{\mathrm{tot}} = 5$ the width of the transition regions remains constant, which is again consistent with expectation. A quantitative theoretical analysis of E_{PS} for all four FPTs reveals an approximately 6-fold enhancement of the Zeeman splitting due to exchange interaction.

The regime of the fractional QHE (FQHE) is traced back to the IQHE regime by considering two fan-charts of LLs occupied with composite Fermions (CFs) instead of electrons. The same quantum numbers of electron LLs are assigned to CF LLs and the pseudospin description is applied as well. One exception to this is the new definition of the energy, which is now associated with the orbital quantum number. This is termed CF cyclotron energy $\hbar\omega_{\mathrm{c,CF}}$ and reckoned to be governed by the Coulomb correlation energy E_{C}. E_{C} arises entirely from the Coulomb interaction among the electrons and is a function of the average distance between them. The magnetic length $l_{\mathrm{B}} = \sqrt{\hbar/eB}$ is used as a scale for the average inter-electron distance within the plane of the 2DES.

The CF filling factor of interest is exclusively $\nu_{\mathrm{CF}} = 2$ (corresponding to $\nu = 2/3$), which signals two fully occupied CF LLs. Two FPTs involving $\nu_{\mathrm{CF}} = 2$ are investigated. The FPTs occur due to the crossing of the second and third lowest CF LLs in dependence of the magnetic field. These two CF LLs belong either to the same CF LL fan-chart (first FPT) or to two different CF LL fan-charts (second FPT). For the first FPT the second CF LL fan-chart is irrelevant, *i.e.* the isospin is effectively frozen out, so this FPT is observable only in the single layer regime. The orbital quantum number and the spin are changed. Due to the latter incident this FPT is termed spin transition. The CF cyclotron energy $\hbar\omega_{\mathrm{c,CF}}$ and the Zeeman energy E_{Z}, which are both a function of B, compete for the critical magnetic field B_{S}. The CF cyclotron energy is quantified as $\hbar\omega_{\mathrm{c,CF}} = C_{\mathrm{C}}E_{\mathrm{C}}$, where $E_{\mathrm{C}} = e^2/4\pi\epsilon\epsilon_0 l_{\mathrm{B}}^{\mathrm{eff}}$ and C_{C} is the scaling prefactor. According to numerical calculations in the literature $C_{\mathrm{C}} \approx 0.1$. The effective magnetic length $l_{\mathrm{B}}^{\mathrm{eff}}$ is used to include the additional electron separation that is due to the finite thickness λ of the 2DES. The value λ is taken from self-consistent simulations as FWHM of the extent of the electron layer perpendicular to its plane. The bare magnetic length l_{B} together with λ defines the effective magnetic length $l_{\mathrm{B}}^{\mathrm{eff}} = \sqrt{l_{\mathrm{B}}^2 + \lambda^2}$. It is shown that this rule applies for $\nu = 2/3$. The Zeeman energy $E_{\mathrm{Z}} = C_{\mathrm{Z}}|g^*|\mu_{\mathrm{B}}B$ depends on the effective Landé-factor g^*, which is -0.44

for bulk GaAs (the WQW can be regarded as such). The prefactor C_Z is introduced to account for any enhanced Zeeman splitting.

The two gates of the WQW structure allow to deplete one electron layer (single layer regime) and to position the remaining single quasi 2DES almost arbitrarily within the WQW. This opportunity is used to adjust the 2DES' distribution function perpendicular to its plane and to tune thus $\hbar\omega_\mathrm{c,CF}$ preferentially via λ. In order to locate the spin transition point for a specifically adjusted λ the density of the single 2DES is varied stepwise and the filling factor is kept constant at $\nu = 2/3$ by sweeping the magnetic field accordingly. This procedure is equivalent to a tuning of P. The critical density or the critical magnetic field B_S is, as in the IQHE regime, indicated by the loss of the FQHE, *i.e.* a peak in R_xx. At base temperature of a dilution refrigerator (electron temperature about 40 mK) B_S is found to drop continuously from 4.5 T to 2.5 T following a change of the electron distribution from being squeezed at one of the WQW edges to being very broad when almost centered in the WQW. A larger B_S, *i.e.* a stronger squeeze of the 2DES, is limited by the leakage current of the back gate. The sample quality limits the determination of B_S towards lower magnetic fields. About 20 different values of λ are adjusted and the ever different B_S value is determined. The equality $\hbar\omega_\mathrm{c,CF}(\lambda, B) = E_\mathrm{Z}(B)$, valid at the spin transition point, is solved for B, which yields B_S as a function of λ. $B_\mathrm{S}(\lambda)$ is fitted to the determined B_S values in dependence of λ, where C_Z is the fit parameter. The fit suggests $C_\mathrm{Z} \approx 6$. The extension of the relation between B_S and λ onto narrow ($w \leq$ 22 nm) QWs requires the consideration of the additional confinement in the valence band. It induces, in particular, a splitting between the heavy- and the light-hole bands, which leads to an increase of g^*. For 15 nm wide QW $g^* \approx$ -0.3 and E_Z is accordingly reduced. This leads to an additional increase of B_S besides the increase caused by the reduced finite thickness λ. It is shown that λ as well as g^* are an unambiguous function of the QW width w. Experimentally determined B_S values for 15 nm (8.3 T), 18 nm (7.2 T), and 22 nm (5.5 T) wide QWs match very well with the expectations according to $B_\mathrm{S}(\lambda(w), g^*(w))$.

Sweeps of the magnetic field close to the spin transition point are accompanied by hysteresis. One reason for is the nuclear magnetic field B_N, which changes *e.g.* due to spin flip-flop processes combining spins of the electron (the spin orientation of the electrons can be easily manipulated) and the nuclear systems by means of the hyperfine coupling. B_N results from a net nuclear spin polarization, which is also due to paramagnetic order of the nuclear spins induced by an increasing external magnetic field B and by a decreasing crystal temperature T_c. B_N only affects the Zeeman energy. For λ such adjusted in the WQW that $B_\mathrm{S} =$ 4.5 T at base temperature, it is found that B_S reduces by about 0.4 T when reaching 250 mK. The decrease of B_S with an increasing temperature indicates that B_N is oriented opposite to B. B_N is estimated to be approximately -0.3 T at base temperature ($T_\mathrm{c} \approx$ 30 mK) which is in agreement with the spin statistics. Furthermore, it is found that with rising temperatures the height of the resistance peak indicating the spin transition increases. But the height decreases again above 170 mK. This behavior is due to a changeover from the ferromagnetic to the paramagnetic phase of the electron system separated by the Curie temperature.

The huge energy mismatch between the electron and the nuclear spin splittings in magnetic field leads to a strongly suppressed spin flip-flop rate and causes slow and long lasting changes of B_N. In experiment the strength of the hyperfine coupling and thus the variation rate of B_N and B_S is controlled by short excursions to a filling factor other than 2/3 at fixed magnetic field. This control is possible, because the density of Skyrmions, which provide low energy excitations that can account for this energy mismatch, depends on the filling factor. The adjustment of the specific filling factor ν_reset for a certain time t_reset is labelled the reset procedure. The change of B_S in dependence of t_reset yields the equilibration time T_1 of the nuclear spin system under the conditions present at ν_reset. T_1 is determined to about 75 s for $\nu_\mathrm{reset} = 0.5$. It is found to drop to less than 3 s for $\nu_\mathrm{reset} = 0.9$ in agreement with the expected filling factor dependent Skyrmion density. However, T_1 remains low for $\nu_\mathrm{reset} = 1$, where ideally no Skyrmions are formed. This observation is considered as an indication that Skyrmions are not the only source of low energy excitations. The variation of B_S due to the manipulation of B_N by means of the reset procedure is about 60 mT. This is almost two orders of magnitude smaller than was reported for a sample grown on a cleaved edge by overgrowth (CEO), but matches with the rather short T_1 times. The reasons for the widely differing behaviors of different structures as as yet unknown.

According to the spin configuration of the two occupied CF LLs, the spin polarized phase is present towards higher B, while the spin unpolarized phase is present towards lower B. Measurements of the spin transition peak over time at base temperature using an AC-current amplitude of 0.6 nA and an AC-current frequency of 5.8 Hz show a uniformly continuous temporal development of the upper flank of the peak towards the spin polarized phase and a nonuniform and fluctuating behavior of the lower flank towards the spin unpolarized phase. No explanation for this behavior can as yet be given. It is known from the literature that a current alters the nuclear spin polarization due to a transfer of spin angular momentum from the electrons to the nuclei. But this effect is expected to be noticeable only if frequency of the current is smaller than $1/T_1$. Consequently therefore, a DC-current of up to 60 nA is used. With an increasing DC-current the transition peak increases and shifts only slightly towards lower densities. Its upper flank is not affected while the lower one is continuously extended into the spin unpolarized phase. This impact is not entirely due to heating, because the overall shape of the transition peak develops differently than it would in the case of a rising temperature. The overall change of B_S signals a reduction of the net nuclear spin polarization by the DC-current. This result is found to be almost independent of the sign of the DC-current in contrast to the observation reported for the CEO sample. The rather short T_1 times are again considered to be responsible for this.

For a bilayer formed in the WQW, the increase of the layer separation d towards larger total densities leads to the loss of correlation between the two layers. Above the critical total density the electron layers behave almost independently with respect to correlation effects like FQHEs. This phenomenon is known as the one-component (1C) to two-component (2C) phase transition. One experimental indication is the loss of FQHEs at $\nu_\mathrm{tot} = p/q$, where p is an odd number. If p is an even number, the topological order changes. Since the decisive issue is the layer separation, the 1C-2C phase transition concerns every filling factor at approximately the same total density. This is confirmed by experiment to happen around 1.4×10^{15} m^{-2} for the balanced case. The 1C-2C phase transition is identified as the second FPT involving $\nu_{\mathrm{CF}} = 2$ ($\nu_{\mathrm{tot}} = 2/3$) on the basis of thermal activation studies. Using the picture of crossing CF LLs, this FPT occurs due to the intersection of the two CF LL fan-charts. This incident is caused by the reduction of $\Delta\mathrm{BAB}$ towards larger total densities. The relevant CF LL crossing involves a change of the isospin (subband index), consequently this FPT is termed isospin transition and requires the bilayer regime. In addition the orbital quantum number is changed while the spin is conserved. The CF cyclotron energy $\hbar\omega_{\mathrm{c,CF}}$ and the subband splitting $\Delta\mathrm{BAB}$ compete for the critical total density (or critical magnetic field B_{P}), because both energies are a function of the total density (or the magnetic field). The isospin transition is found for the balanced case at a total density of about 1.4×10^{15} m^{-2} ($B_{\mathrm{P}} \approx$ 8.75 T). The analysis of thermal activation measurements reveals that the isospin transition is governed by easy-axis anisotropy and is accompanied by $s \approx 8$ pseudospin flips per particle added to or subtracted from the system close to the transition point. The large number of pseudospin flips is attributed to the existence of isospin Skyrmions, which are predicted for $\nu_{\mathrm{tot}} = 2/M$, where M is an odd integer. The change of the isospin causes a redistribution of a minor part of the charges from the center of the WQW symmetrically towards its edges. This is because the isospin determines the number of nodes in the wave function. As a result a spatially dependent shape of the symmetric charge distribution function throughout the lateral extend of the sample is predicted for the case that domains of different pseudospin and thus isospin coexist as possible close to the transition point *e.g.* due to disorder.

B_{P} is found to increase with a quadratic dependence on σ at small (< 0.1) imbalance values due to the equivalently and dominating increase of the subband splitting $\Delta\mathrm{BAB}$ with σ. Furthermore, the transition region, *i.e.* total density range characterized by a loss of the QHE, broadens, equivalent to the observation at $\nu_{\mathrm{tot}} = 4$. It is found that below B_{P} the activation energy increases, while it decreases rapidly with imbalance above B_{P}. Since an imbalance discriminates against the 2C regime and favors the 1C regime, this proves, that below B_{P} the 1C regime is present, while above the 2C regime applies. In the 1C regime the FQHE with $\nu_{\mathrm{tot}} = 2/3$ is established due to a correlated state to which all electrons contribute, despite being located in different layers. In the 2C regime an FQHE with $\nu = 1/3$ in each layer separately develops at $\sigma \approx 0$. In accord with the picture of crossing CF LLs it is found that an increasingly larger imbalance is required towards higher total densities in order to reestablish the 1C regime of the FQHE. Since the FQHE of the 2C regime is already lost for slight imbalance values, an area opens above B_{P}, which is characterized by several R_{xx} minima at certain imbalance values $\sigma \neq 0$. The reason for this is that the charge distribution between the layers is decisive in the 2C regime with respect to the formation of FQHEs. The R_{xx} minima represent FQH states with different filling factors ν_{f} and ν_{b} for the front and back electron layer. Experimentally R_{xx} minima are found at the following individual filling factors: $\nu_{\mathrm{f}} = 2/5$ (for $\sigma \approx 0.14$), $\nu_{\mathrm{f}} = 3/7$ (for $\sigma \approx 0.2$), and $\nu_{\mathrm{b}} = 1/5$ (for $\sigma \approx 0.4$). The filling factor of the other electron layer is not a magic number each time, but it is for the first two cases $\nu_{\mathrm{b}} \approx 2/7$, so these two R_{xx} minima are more pronounced. For the third R_{xx} minimum, which is much more weakly pronounced, the Hall resistance increases by about 30% when compared to its expected value $\frac{3}{2}h/e^2$. This phenomenon cannot as yet be explained.

Based on the investigations of the spin and isospin transition a phase diagram of the ferromagnetic and topological order at $\nu_{\mathrm{CF}} = 2$ is drawn, which is valid for any (total) density and charge distribution in a WQW at a finite temperature below the Curie temperature. The normalized mean electron position with respect to the center of the WQW $\bar{z}$ is used as a unified description of any arbitrary charge distribution.

One important feature of the results is the fact that the established relation between B_{S} and λ for the spin transition offers the opportunity to draw a conclusion about the actual shape of the confinement potential in particular in the case of single heterointerfaces (SHIs). This shape is strongly influenced by the background doping depending on the particular MBE machine so very different values of B_{S} were found for otherwise identical structures. B_{S} thus represents a direct quantitative measure of the background doping. Since scaling parameters in calculations addressing many body correlation effects are often idealized the WQW structure can be used as a model system to quantify the impact of λ on many body correlation effects. The scaling parameters can thus be adjusted to reality.

Chapter 9

Zusammenfassung

Hauptaspekt der vorliegenden Arbeit sind ferromagnetische Phasenübergänge (FPTs) in elektronischen Einzel- und Doppelschichtsystemen. Ein FPT bezeichnet die Änderung des Grundzustandes eines niedrigdimensionalen Elektronsystems unter Quanten-Hall-Bedingungen. Doppelschichtsysteme, d.h. zwei nahe und parallel zueinander liegende zweidimensionale Elektronensysteme (2DESs) die Ladungsaustausch aufweisen, werden genutzt um FPTs mittels Magnetotransport zu studieren. Doppelschichtsysteme werden in einem modulationsdotierten 77 nm breiten Quantentopf (WQW) aus GaAs und in einem Doppelquantentopf (DQW), bestehend aus zwei 18 nm breiten Quantentöpfen (QWs) aus GaAs getrennt durch 3.1 nm AlAs, realisiert. Die Strukturen wurden mittels Molekularstrahlepitaxi (MBE) auf GaAs mit Oberflächenorientierung (001) hergestellt. Ein *in situ* gewachsenes Gate unterhalb und parallel zu den Quantentöpfen sowie ein auf der Oberseite aufgedampftes Gate erlauben eine unabhängige Kontrolle der Ladungsträgerdichten der einzelnen Schichten. Eine wenigstens 5 nm dicke Benetzungsschicht aus Ni unterhalb der ohmschen Kontakte der Doppelschicht sowie spezifisch ausgeheiltes GaAs, das bei niedrigen Temperaturen (LT) gewachsen wurde und sich zwischen dem unteren Gate und den Quantentöpfen befindet, stellen sich als notwendig heraus, um eine ausreichende Unterdrückung des Leckstroms von dem unteren Gate zur Doppelschicht zu erreichen. Die intrinsische Gesamtelektronendichte (Summe der Ladungsdichten der einzelnen Schichten) beträgt ungefähr 2.1×10^{15} m^{-2} und die Beweglichkeiten sind 530 m^2/Vs (WQW) bzw. 280 m^2/Vs (DQW). Die meisten Experimente wurden an der WQW Struktur durchgeführt, weshalb sich alle im folgenden zusammengefaßten Ergebnisse auf diese Struktur beziehen, falls nicht anders erwähnt.

Der Ladungsaustausch zwischen den Schichten bewirkt eine Aufspaltung der Energieniveaus, was zur Ausbildung von zwei Subbändern pro Energieniveau führt, die als bindend und antibindend bezeichnet werden. Nur die zwei niederenergetischsten Subbänder sind besetzt und durch die Subbandaufspaltung $\Delta\mathrm{BAB}$ voneinander getrennt. Zur Quantifizierung derjenigen Parameter, die FPTs beeinflussen, wurden quantenmechanische Rechnungen durchgeführt. Die Rechnungen zeigen, daß $\Delta\mathrm{BAB}$ ungefähr mit dem Quadrat der Asymmetrie der Ladungsverteilung σ, die definiert ist als die normierte Differenz zwischen den Elektronendichten der oberen und der unteren Schicht, ansteigt. Zudem zeigt sich, daß $\Delta\mathrm{BAB}$ ungefähr invers mit der Gesamtdichte skaliert. Bei einer Gesamtdichte von 1.0×10^{15} m^{-2} berechnet sich ein Wert von etwa 0.8 meV. Desweiteren zeigt sich, daß der Abstand d zwischen den Elektronenschichten von 50 nm auf 54 nm ansteigt, wenn die Gesamtdichte (bei symmetrischer Verteilung $\sigma = 0$) von 1.0×10^{15} m^{-2} auf 2.0×10^{15} m^{-2} erhöht wird.

Ein magnetisches Feld B, das senkrecht zur Doppelschicht angelegt wird, führt zur Kondensation aller Zustände der besetzten Subbänder auf zwei Fächer von Landau-Niveaus (LLs). Jeder Zustand ist, abgesehen von seiner Ladung (Elektron oder Loch), durch mehrere Quantenzahlen charakterisiert: orbitale Quantenzahl (0,1,2,...), verbunden mit der Zyklotronenergie $\hbar\omega_\mathrm{c}$ der Elektronen, Spin ($\uparrow$,$\downarrow$), verbunden mit der Zeemanenergie E_Z, und Subbandindex (bindend, antibindend), verknüpft mit $\Delta\mathrm{BAB}$. Da nur die zwei niederenergetischsten Subbänder relevant sind, wird der Subbandindex wie ein Isospin behandelt. Die Quantenzahlen (eines jeden Zustandes) werden zu einem künstlichen Einteilchen-Pseudospin zusammengefaßt. Wenn das Verhältnis von Elektronen und magnetischen Flußquanten pro Flächeneinheit (Füllfaktor) eine magische Zahl (zunächst ein ganzzahliger Wert) annimmt, so sind idealerweise alle Pseudospins eines jeden LLs ausgerichtet. In Analogie zum herkömmlichen Ferromagnetismus kann man diese Ausrichtung als ferromagnetische Ordnung ansehen und der Begriff Quanten-Hall-Ferromagnetismus (QHF) hat sich hierfür etabliert. Ein ferromagnetischer Phasenübergang wird induziert, wenn zwei LLs verschiedener ferromagnetischer Ordnung durch ihre energetische Resonanz hindurch gestimmt werden, d.h. wenn eine Kreuzung von LLs auftritt.

Um FPTs zu charakterisieren wird eine verallgemeinerte theoretische Beschreibung einer Kreuzung von LLs eingeführt. Alle Einteilchen-Pseudospins eines jeden LL werden zu einem globalen Pseudospin eines LL zusammengefaßt. Den beiden kreuzenden LLs werden die globalen Pseudospinorientierungen auf (up) und ab (down) zugeordnet. Die Energiedifferenz zwischen den beiden betroffenen LLs, genannt Pseudospinaufspaltung E_PS, wird so definiert, daß sie linear mit einem Pseudomagnetfeld P skaliert. Theoretisch bestimmt die Anisotropieenergie zwischen den beiden unterschiedlichen Pseudospinorientierungen den Prozeß der Umorientierung des globalen Pseudospins, wenn man den Kreuzungspunkt passiert. Im Übergangsbereich (d.h. nahe am Kreuzungspunkt) bevorzugt das System entweder einen stets pseudospinpolarisierten Zustand (easy-axis Anisotropie) oder eine kohärente Überlagerung beider Pseudospinorientierungen (easy-plane Anisotropie). Die Ableitung der Aktivierungsenergie E_A, die ein direktes Maß für die eigentliche Pseudospinaufspaltung darstellt, nach der theoretischen Pseudospinaufspaltung E_PS liefert die Zahl der Pseudospinflips s bei einer geladenen Anregung des Systems. Man erwartet, daß s stets eins ist außer im Übergangsbereich. Im Falle von easy-plane Anisotropie tendiert s nach Null, während im Falle von easy-axis Anisotropie s eins bleibt oder sogar einen größeren Wert annehmen kann. Letzteres ist nur möglich, wenn das System niederenergetischere Anregungen als einen Pseudospinflip zuläßt, was der Fall sein kann, wenn sich z.B. Skyrmionen ausbilden.

Die beiden Fächer von LLs sind energetisch versetzt um $\Delta\mathrm{BAB}$, weswegen sich LLs als Funktion von B kreuzen, was zu FPTs führt. Experimentell wird ein Kreuzungspunkt von zwei LLs an die Fermienergie gebracht und das Verschwinden des QHE, d.h. das Auftreten eines endlichen Längswiderstandes R_xx, wird als Indiz genommen, weil die Energielücke zwischen den betroffenen LLs am Kreuzungspunkt verschwindet. Im Falle von ideal ausgerichteten Einteilchen-Pseudospins vereinfacht sich der globale Pseudospin eines jeden LL zu einem Satz von drei Einteilchen-Quantenzahlen. Die Änderung der Orientierung des globalen Pseudospins ist daher äquivalent zu einer Änderung von Quantenzahlen, wodurch sich der Grundzustand ändert. Gemäß der Klassifikation der Anisotropie nach dem Pseudospin (PAC), wie sie in der Literatur gegeben ist, hängt die Art der Anisotropie von den sich ändernden Quantenzahlen ab. Im Bereich des ganzzahligen QHE (IQHE) ändert sich an jedem FPT der Isospin and die orbitale Quantenzahl. Im Falle eines geradzahligen Gesamtfüllfaktor (Summe der Füllfaktoren der einzelnen Subbänder) ändert sich zusätzlich der Spin.

Die Shubnikov-de Haas (SdH) Oszillationen aus Messungen von R_{xx} bei kleinem B zeigen zwei überlagerte Frequenzen, die den beiden unterschiedlichen Subbanddichten entsprechen und mit einer Fourieranalyse extrahiert werden. Mit deren Unterschied läßt sich $\Delta\mathrm{BAB}$ quantifizieren. Im Vergleich zeigt sich, daß die Rechnungen $\Delta\mathrm{BAB}$ um etwa 30% unterschätzen. Bei einer Temperatur von 250 mK werden vier FPTs im Detail untersucht. Die betroffenen LL Koinzidenzen werden durch eine Variation der Gesamtdichte unter Aufrechterhaltung einer symmetrischen Ladungsverteilung ($\sigma = 0$) durchlaufen, was einem Durchfahren von P ähnelt. Zwei FPTs bei $\nu_{\mathrm{tot}} = 4$ zeigen sehr schmale Übergangsgebiete, d.h. Bereiche der Gesamtdichte innerhalb derer der QHE verloren geht. Die anderen beiden FPTs bei $\nu_{\mathrm{tot}} = 3$ und $\nu_{\mathrm{tot}} = 5$ zeigen wesentlich breitere Übergangsgebiete. Die kritische Gesamtdichte ist in allen Fällen ungefähr 0.85×10^{15} m^{-2}. Die PAC sagt im Einklang mit den schmalen Übergangsgebieten easy-axis Anisotropie für die FPTs bei $\nu_{\mathrm{tot}} = 4$ voraus. Für die FPTs bei $\nu_{\mathrm{tot}} = 3$ und $\nu_{\mathrm{tot}} = 5$ kann man auf der Basis der PAC nicht angeben, welche Art Anisotropie zutrifft, aber wegen der Beobachtung zweier breiter Übergangsregionen im Unterschied zu schmalen bei $\nu_{\mathrm{tot}} = 4$, werden diese FPTs als von easy-plane Anisotropie geprägt angesehen. Mit einer zunehmenden Asymmetrie der Ladungsverteilung σ steigen die kritischen Gesamtdichten und zwar mit einer quadratischen Abhängigkeit von σ, was durch den ebensolchen Anstieg von $\Delta\mathrm{BAB}$ mit σ bedingt ist. Die Übergangsgebiete der FPTs bei $\nu_{\mathrm{tot}} = 4$ weiten sich, was einem graduellen Übergang zu easy-plane Anisotropie zugeschrieben wird, wie man es theoretisch erwartet. Die Breite der Übergangsgebiete der FPTs bei $\nu_{\mathrm{tot}} = 3$ und $\nu_{\mathrm{tot}} = 5$ bleibt konstant, ebenfalls im Einklang mit der theoretischen Erwartung. Eine quantitative Analyse von E_{PS} an allen vier FPTs ergibt eine ungefähr sechsfache Überhöhung der Zeemanaufspaltung durch die Austauschwechselwirkung.

Der Bereich des fraktionalen QHE (FQHE) wird durch Betrachtung von zwei Fächer von LLs, die mit Composite Fermions (CFs) anstatt Elektronen besetzt sind, auf den Bereich des IQHE zurückgeführt. Den CF LLs werden die gleichen Quantenzahlen wie den elektronischen LLs zugeordnet; ebenso wird die Beschreibung mittels Pseudospins angewandt. Lediglich die Energie, die nun mit der orbitalen Quantenzahl verbunden ist, wird neu definiert. Sie wird CF Zyklotronenergie $\hbar\omega_{\mathrm{c,CF}}$ genannt und als von der Coulomb Korrelationsenergie E_{C} bestimmt aufgefaßt. E_{C} entspringt vollständig der Coulombwechselwirkung zwischen allen Elektronen und ist somit eine Funktion des mittleren Abstandes der Elektronen. Als Maß für den mittleren Abstand der Elektronen entlang der Ebene des 2DES wird die magnetische Länge $l_{\mathrm{B}} = \sqrt{\hbar/eB}$

verwendet.

Ausschließlich der CF Füllfaktor $\nu_{\rm CF} = 2$ (entspricht $\nu = 2/3$) ist von Interesse, der zwei voll besetzte CF LLs anzeigt. Zwei FPTs bei $\nu_{\rm CF} = 2$ werden untersucht, die durch vom Magnetfeld getriebene Kreuzungen der zweit- und drittniedrigsten CF LLs auftreten. Im Falle des ersten FPT gehören die zwei betroffenen CF LLs zum selben CF LL Fächer, hingegen zu zwei unterschiedlichen CF LL Fächer im Falle des zweiten FPT. Im Falle des ersten FPT ist der zweite CF LL Fächer irrelevant, d.h. der Isospin ist effektiv ausgefroren, weshalb dieser FPT nur dann auftritt, wenn ein einzelnes 2DES präsent ist. Die orbitale Quantenzahl und der Spin ändern sich. Wegen letzterer Eigenschaft wird dieser FPT Spinübergang genannt. Die CF Zyklotronenergie $\hbar\omega_{\rm c,CF}$ und die Zeemanenergie $E_{\rm Z}$, die beide eine Funktion von B sind, konkurrieren um das kritische Magnetfeld $B_{\rm S}$. Die CF Zyklotronenergie wird quantifiziert als $\hbar\omega_{\rm c,CF} = C_{\rm C}E_{\rm C}$, worin $E_{\rm C} = e^2/4\pi\epsilon\epsilon_0 l_{\rm B}^{\rm eff}$ ist und $C_{\rm C}$ einen skalierenden Vorfaktor darstellt. Gemäß numerischer Rechnungen in der Literatur ist $C_{\rm C} \approx 0.1$. Eine effektive magnetische Länge $l_{\rm B}^{\rm eff}$ wird verwendet, um den zusätzlichen Abstand der Elektronen untereinander, auf Grund der endlichen Dicke λ des 2DES, mit einbeziehen zu können. Der Wert λ, gemessen als volle Breite der Elektronenverteilungsfunktion senkrecht zur Ebene des 2DES bei halber Höhe (FWHM), wird mittels selbstkonsistenter Simulationen der Ladungsverteilung quantifiziert. Die ursprüngliche magnetische Länge $l_{\rm B}$ zusammen mit λ definieren die effektive magnetische Länge $l_{\rm B}^{\rm eff} = \sqrt{l_{\rm B}^2 + \lambda^2}$. Die Gültigkeit dieser Summenregel für $\nu = 2/3$ wird gezeigt. Die Zeemanenergie $E_{\rm Z} = C_{\rm Z}|g^*|\mu_{\rm B}B$ hängt von dem effektiven Landéfaktor g^* ab, der für GaAs Volumenmaterial (als solches kann man den WQW ansehen) -0.44 ist. Der Vorfaktor $C_{\rm Z}$ wird eingeführt, um eine durch Austauschwechselwirkung eventuell überhöhte Zeemanaufspaltung berücksichtigen zu können.

Die zwei Gates der WQW Struktur ermöglichen es, eine Elektronenschicht zu verarmen (d.h. der Zustand einer Einzelschicht wird erreicht) und das verbleibende quasi 2DES nahezu beliebig innerhalb des WQW zu positionieren. Diese Möglichkeit wird genutzt, um die Verteilungsfunktion des 2DES senkrecht zu seiner Ebene zu verändern und somit vorzugsweise $\hbar\omega_{\rm c,CF}$ über λ zu beeinflussen. Um den Spinübergang bei einem spezifisch eingestellten λ zu lokalisieren, wird die Dichte des einzelnen 2DES schrittweise variiert und der Füllfaktor durch entsprechendes anpassen des Magnetfeldes konstant bei $\nu = 2/3$ gehalten. Diese Prozedur ist vergleichbar mit einer Veränderung von P. Die kritische Dichte oder das kritische Magnetfeld $B_{\rm S}$ werden wie im IQHE Bereich durch einen Verlust des FQHE d.h. durch ein $R_{\rm xx}$ Maximum angezeigt. Bei Basistemperatur eines Entmischungscryostaten (Elektronentemperatur etwa 40 mK) ergibt sich eine kontinuierliche Absenkung von $B_{\rm S}$ von 4.5 T auf 2.5 T, wenn man die Elektronenverteilung von an einem der Ränder des WQW zusammengedrückt bis zu sehr breit weil annähernd im WQW zentriert ändert. Die Erzielung eines größeren $B_{\rm S}$, d.h. ein stärkeres Zusammendrücken des 2DES, ist durch den Leckstrom des unteren Gates limitiert. Die Bestimmung von $B_{\rm S}$ hin zu niedrigeren Magnetfeldern ist durch die Probenqualität begrenzt. Etwa 20 verschiedene Werte für λ werden eingestellt und der jeweils spezifische Wert für $B_{\rm S}$ wird bestimmt. Löst man die Gleichung $\hbar\omega_{\rm c,CF}(\lambda, B) = E_{\rm Z}(B)$, die am Punkt des Spinübergangs gültig ist, nach B auf, so liefert dies $B_{\rm S}$ als Funktion von λ. $B_{\rm S}(\lambda)$ wird an die gemessenen

Werte für B_S in Abhängigkeit von λ angefittet, wobei C_Z der Fitparameter ist. Der Fit ergibt $C_\mathrm{Z} \approx 6$. Die Übertragung der gefundenen Beziehung zwischen B_S und λ auf enge ($w \leq$ 22 nm) QWs erfordert die Berücksichtigung der durch den Einschluß der Löcher bedingten zusätzlichen Quantisierung im Valenzband. Dies bewirkt insbesondere eine Aufspaltung zwischen den Bändern der schweren und leichten Löcher, was zu einem Anstieg von g^* führt. Für einen 15 nm breiten QW ist $g^* \approx$ -0.3 und E_Z ist entsprechend abgesenkt. Dies führt zu einem weiteren Anstieg von B_S zusätzlich zu dem Anstieg, der durch die reduzierte Breite λ verursacht ist. Es wird gezeigt, daß λ und g^* Funktionen von der QW Breite w sind. Experimentell bestimmte Werte für B_S für 15 nm (8.3 T), 18 nm (7.2 T) und 22 nm (5.5 T) breite QWs stimmen sehr gut mit den Erwartungen gemäß $B_\mathrm{S}(\lambda(w), g^*(w))$ überein.

Eine Messung von R_xx als Funktion des Magnetfeldes nahe des Spinübergangs zeigt Hysterese. Ein Grund ist das Kernmagnetfeld B_N, welches variabel ist, bedingt etwa durch Spin-Flipflop-Prozesse, die über die Hyperfinewechselwirkung die Spins von Elektronen (die Spinorientierung der Elektronen kann einfach manipuliert werden) und Kernen kombinieren. B_N folgt aus einer netto Kernspinpolarisation, die sich auch aus der paramagnetischen Ordnung der Kernspins ergibt und von einem steigenden externen Magnetfeld B sowie einer sinkenden Kristalltemperatur T_c induziert wird. B_N wirkt sich ausschließlich auf die Zeemanenergie aus. Für ein derart eingestelltes λ, so daß sich für den WQW bei Basistemperatur $B_\mathrm{S} = 4.5$ T ergibt, beobachtet man bei einem Anstieg der Temperatur auf 250 mK eine Reduktion von B_S um etwa 0.4 T. Die Reduktion von B_S mit steigender Temperatur zeigt, daß B_N entgegengesetzt zu B orientiert ist. B_N lässt sich zu ungefähr -0.3 T bei Basistemperatur ($T_\mathrm{c} \approx$ 30 mK) abschätzen in Übereinstimmung mit der Spinstatistik. Desweiteren zeigt sich, daß die Höhe des Widerstandsmaximums, der den Spinübergang markiert, mit zunehmender Temperatur steigt aber oberhalb von 170 mK wieder fällt. Dieses Verhalten ist bedingt durch den Übergang des Elektronensystems von der ferromagnetischen zur paramagnetischen Phase, wobei die Curie-Temperatur die Grenze markiert.

Die riesige Energiediskrepanz zwischen der Elektronen- und der Kernspinaufspaltung im Magnetfeld führt zu einer stark unterdrückten Rate von Spin-Flipflop-Prozessen, weshalb es zu langsamen und langanhaltenden Veränderungen von B_N kommt. Im Experiment kann die Stärke der Hyperfinewechselwirkung und somit die Änderungsrate von B_N und B_S durch kurze Variation des Füllfaktors hin zu Werten verschieden von 2/3 bei festem Magnetfeld kontrolliert werden. Diese Steuerung ist möglich, weil die Dichte von Skyrmionen, die niederenergetische Anregungen zur Verfügung stellen und somit die Energiediskrepanz kompensieren können, vom Füllfaktor abhängt. Die Einstellung eines spezifischen Füllfaktors ν_reset für eine bestimmte Zeit t_reset wird als Resetprozedur bezeichnet. Die Änderung von B_S in Abhängigkeit von t_reset liefert die Zeit T_1, innerhalb derer das Kernspinsystem sein Gleichgewicht unter Bedingungen, wie sie bei ν_reset gegeben sind, findet. Bei $\nu_\mathrm{reset} = 0.5$ ist T_1 etwa 75 s. Bei $\nu_\mathrm{reset} = 0.9$ fällt T_1 auf weniger als 3 s in Einklang mit der erwarteten Abhängigkeit der Skyrmionendichte vom Füllfaktor. Allerdings bleibt T_1 auch bei $\nu_\mathrm{reset} = 1$, wo sich idealerweise keine Skyrmionen ausbilden, niedrig. Diese Beobachtung wird als Anzeichen dafür gewertet, daß Skyrmionen nicht die einzige Quelle niederenergetischer Anregungen sind. Die Veränderbarkeit von B_S durch die Manipulation von B_{N} mittels der Resetprozedur beträgt etwa 60 mT. Dies ist nahezu zwei Größenordnungen weniger als für eine Probe berichtet wurde, die durch Überwachsen auf einer Spaltkante (CEO) hergestellt wurde, paßt aber ins Bild von tendenziell kurzen T_1 Zeiten. Das enorm unterschiedliche Verhalten zwischen verschiedenen Strukuturen bleibt jedoch eine offene Frage.

Gemäß der Spinkonfiguration der zwei besetzten CF LLs existiert die spinpolarisierte Phase zu höherem B, während die spinunpolarisierte Phase zu kleinerem B vorgefunden wird. Zeitabhängige Messungen des Widerstandsmaximums, der den Spinübergang markiert, unter Benutzung einer AC-Stromamplitude von 0.6 nA und einer AC-Stromfrequenz von 5.8 Hz zeigen bei Basistemperatur eine gleichförmig stetige zeitliche Entwicklung der oberen Flanke des R_{xx} Maximums hin zur spinpolarisierten Phase und ein unstetiges und fluktuierendes Verhalten der unteren Flanke hin zur spinunpolarisierten Phase. Dieses Verhalten kann nicht erklärt werden. Aus der Literatur ist bekannt, daß ein Strom die Kernspinpolarisation durch Transfer von Spinmoment von den Elektronen auf die Kerne ändern kann. Es wird aber erwartet, daß dieser Effekt nur nennenswert ist, wenn die Frequenz des Stromes klein ist im Vergleich zu $1/T_1$. Im weiteren wurde daher ein DC-Strom bis 60 nA verwendet. Mit zunehmender DC-Stromamplitude steigt das Widerstandsmaximum and schiebt geringfügig zu kleineren Dichten. Seine obere Flanke bleibt unbeeinflußt während die untere Flanke sich kontinuierlich in die spinunpolarisierte Phase hinein ausdehnt. Diese Auswirkung ist zumindest nicht vollständig auf Heizung zurückzuführen, denn die gesamte Form des R_{xx} Maximums entwickelt sich anders als im Falle einer steigenden Temperatur. Die Änderung von B_{S} deutet eine Verminderung der netto Kernspinpolarisation durch den DC-Strom an. Dieses Ergebnis ergibt sich nahezu unabhängig von dem Vorzeichen des DC-Stroms, im Gegensatz zur für die CEO Probe berichteten Beobachtung. Als Grund werden erneut die kurzen T_1 Zeiten angesehen.

Für den Fall, daß sich ein Doppelschichtsystem im WQW ausbildet, führt die zunehmende Trennung der Schichten d hin zu höheren Gesamtdichten zu einem Verlust der Korrelation zwischen den zwei Schichten. Oberhalb der kritischen Gesamtdichte verhalten sich die Elektronenschichten in Bezug auf Korrelationseffekte wie FQHEs nahezu unabhängig voneinander. Dieses Phänomen ist als einkomponenten (1C) zu zweikomponenten (2C) Phasenübergang bekannt. Ein experimenteller Hinweis ist der Verlust von FQHEs bei $\nu_{\mathrm{tot}} = p/q$ wenn p eine ungerade Zahl ist. Ist p eine gerade Zahl, so ändert sich die topologische Ordnung. Da der ausschlaggebende Punkt der Abstand der Schichten ist, betrifft der 1C-2C Phasenübergang jeden Füllfaktor bei ungefähr der gleichen Gesamtdichte. Dies wird im Experiment bestätigt und die kritische Gesamtdichte ergibt sich für den Fall einer symmetrischen Ladungsverteilung zu etwa 1.4×10^{15} m^{-2}. Auf der Basis von thermischen Aktivierungsmessungen wird der 1C-2C Phasenübergang als der zweite FPT bei $\nu_{\mathrm{CF}} = 2$ ($\nu_{\mathrm{tot}} = 2/3$) identifiziert. Im Bild sich kreuzender CF LLs tritt dieser FPT durch die Überschneidung der zwei CF LL Fächer auf, verursacht durch die Reduktion von $\Delta\mathrm{BAB}$ hin zu größeren Gesamtdichten. Die relevante CF LL Kreuzung hat eine Änderung des Isospins (Subbandindex) zur Folge, weshalb dieser FPT Isospinübergang genannt wird und es zu dessen Untersuchung eines Doppelschichtsystems bedarf. Zudem ändert sich die orbitale Quantenzahl, während der Spin unverändert bleibt. Um die kritische Gesamtdichte (bzw. das kritische Magnetfeld B_P) konkurrieren die CF Zyklotronenergie $\hbar\omega_\mathrm{c,CF}$ und die Subbandaufspaltung $\Delta\mathrm{BAB}$, denn beide Energien sind eine Funktion der Gesamtdichte (bzw. des Magnetfeldes). Für den Fall einer symmetrischen Ladungsverteilung tritt der Isospinübergang bei einer Gesamtdichte von etwa 1.4×10^{15} m^{-2} ($B_\mathrm{P}\approx 8.75$ T) auf. Die Analyse von thermischen Aktivierungsmessungen offenbart, daß der Isospinübergang durch easy-axis Anisotropie geprägt ist und daß eine geladene Anregung nahe dem Übergangspunkt bis zu $s\approx 8$ Pseudospinflips bewirkt. Die große Zahl von Pseudospinflips wird der Ausbildung von Isospin-Skyrmionen zugeschrieben, die für $\nu_\mathrm{tot}=2/M$, worin M eine ungerade ganze Zahl ist, vorhergesagt ist. Die Änderung des Isospins verursacht eine Umverteilung eines kleinen Teils der Ladungen von der Mitte des WQW symmetrisch zu dessen Rändern, denn der Isospin bestimmt die Zahl der Knoten in der Wellenfunktion. Eine ortsabhängige Form der symmetrischen Ladungsverteilung über die laterale Ausdehnung der Probe hinweg wird daher für den Fall, daß Domänen mit unterschiedlichem Pseudospin und somit Isospin koexistieren, vorausgesagt, wie dies nahe am Punkt des Phasenübergangs beispielsweise auf Grund von Unordnung möglich ist.

Mit zunehmend asymmetrischer Ladungsverteilung ergibt sich, daß B_P mit einer quadratischen Abhängigkeit von σ zunimmt, sofern σ klein ist (< 0.1). Der Grund liegt in dem gleichermaßen und dominierenden Anstieg der Subbandaufspaltung $\Delta\mathrm{BAB}$ mit σ. Außerdem verbreitert sich das Übergangsgebiet, d.h. der Bereich der Geamtdichte, der durch einen Verlust des QHE gekennzeichnet ist, äquivalent zu der Beobachtung bei $\nu_\mathrm{tot}=4$. Es zeigt sich, daß die Aktivierungsenergie unterhalb von B_P mit σ ansteigt, während sie oberhalb von B_P rapide abnimmt. Da eine asymmetrische Ladungsverteilung die 2C Phase benachteiligt und die 1C Phase bevorzugt, beweist dies, daß unterhalb von B_P die 1C Phase existiert, während sich oberhalb die 2C Phase einstellt. In der 1C Phase bildet sich der FQHE bei $\nu_\mathrm{tot}=2/3$ in Form eines korrelierten Zustandes aus, zu dem alle Elektronen beitragen, auch wenn sie in unterschiedlichen Schichten lokalisiert sind. In der 2C Phase entwickelt sich ein FQHE mit $\nu=1/3$ für jede Schicht separat, sofern $\sigma\approx 0$. Gemäß dem Bild sich kreuzender CF LLs findet sich, daß mit zunehmender Gesamtdichte eine stetig asymmetrischere Ladungsverteilung zwischen den Schichten nötig ist, um die 1C Phase des FQHE wieder herzustellen. Doch da der FQHE in der 2C Phase schon bei kleinem σ verloren geht, eröffnet sich oberhalb von B_P ein Bereich, der von mehreren R_xx Minima bei bestimmten Werten von $\sigma\neq 0$ gekennzeichnet ist. Der Grund ist, daß mit Blick auf die Ausbildung von FQHEs die Ladungsverteilung zwischen den Schichten in der 2C Phase entscheidend ist. Die R_xx Minima repräsentieren FQH Zustände mit unterschiedlichen Füllfaktoren ν_f und ν_b für die vordere und die hintere Elektronenschicht. Experimentell finden sich R_xx Minima bei folgenden individuellen Füllfaktoren (für bestimmtes σ): $\nu_\mathrm{f}=2/5$ (bei $\sigma\approx 0.14$), $\nu_\mathrm{f}=3/7$ (bei $\sigma\approx 0.2$) und $\nu_\mathrm{b}=1/5$ (bei $\sigma\approx 0.4$). Der Füllfaktor der jeweils anderen Elektronenschicht ist jedesmal keine magische Zahl, aber in den ersten beiden Fällen findet sich, daß $\nu_\mathrm{b}\approx 2/7$, weshalb diese beiden R_xx Minima deutlich ausgeprägt sind. Im Falle des dritten R_xx Minimums, welches wesentlich schwächer ausgeprägt ist, steigt der Hall-Widerstand verglichen mit dem erwarteten Wert $\frac{3}{2}h/e^2$ um etwa 30% an. Dieses Phänomen kann nicht erklärt werden.

Basierend auf der Untersuchung von Spin- und Isospinübergang wird ein Phasendiagramm der ferromagnetischen und topologischen Ordnung von $\nu_{\mathrm{CF}} = 2$ angegeben, welches für jede (Gesamt)dichte und Ladungsverteilung in einem WQW bei endlicher Temperatur unterhalb der Curie-Temperatur gültig ist. Die vereinheitlichte Beschreibung einer beliebigen Ladungsverteilung geschieht hierbei durch den Erwartungswert der Position eines Elektrons normiert auf die Mitte des WQW $\bar{z}$.

Die Tragweite der Ergebnisse liegt beispielsweise darin, daß die etablierte Beziehung zwischen B_{S} und λ am Spinübergang insbesondere im Falle von Heterostrukturen mit einer Grenzfläche (SHIs) die Möglichkeit eröffnet, Schlußfolgerungen hinsichtlich der eigentlichen Form des Einschlußpotentials zu ziehen. Dessen Form hängt stark von der für jede MBE-Anlage spezifische Hintergrundsdotierung ab, weshalb sehr unterschiedliche Werte für B_{S} für ansonsten identische Strukturen gefunden werden. B_{S} stellt daher ein direktes quantitatives Maß für die Hintergrundsdotierung dar. Häufig sind Skalierungsparameter in Rechnungen zu Korrelationseffekten von Vielteilchensystemen idealisiert. Die WQW Struktur stellt ein Modellsystem dar, den Einfluß von λ auf Korrelationseffekte von Vielteilchensystemen quantitativ erfassen kann. Die Skalierungsparameter können somit an die Realität angepaßt werden.

Appendix A

Technical aspects

A.1 Processing of samples

In the following, the procedure is discussed how to process samples either of the WQW or DQW structure (see also [239]). First, small pieces are cleaved from the source material (wafer). The size of each piece is 4.3×4.3 mm^2, which is the largest size that can be placed into the cavity (carrier) available for the different cryogenic systems. The pieces are chosen as large as possible since a maximum number of samples (*e.g.* Hall bars) per piece is desired. The reason is that just one or two of about 20 Hall bars, which fit on one piece, are of sufficient quality, *i.e.* free of defects within the mesa region. This is, however, not due to a low yield of the individual process steps, but due to the high defect density of the source material, *inter alia* caused by the necessary incorporation of LT-GaAs.

The cleaved pieces are cleaned in a standard cleaning process. They are immersed in acetone, subject to ultrasound, for several minutes. Finally, the pieces are rinsed in propanol, to remove any residual acetone, and dried by blowing with nitrogen gas.

Sample patterns are defined lithographically. For this purpose two different resists are used labeled S1805 and AZ5214E. The latter is used for an image reversal process, which applies in general when the evaporation of material(s) after the lithography is intended except in the case of the evaporation of the materials for the ohmic contacts to the back gate. The reason for this exception is that in this case a wet chemical etch step is required prior to the evaporation. This etch step, however, leads to an unfavorable large undercut when the resist AZ5214E is used, because this resist does not stick very firmly on the semiconductor surface. The reason for the usage of image reversal processes at all arises from the fact, that the lithography mask represents in this case a positive image of the pattern, wherefore an easier alignment of the lithography mask is feasible. The resist is spun on the pieces, which rotate at a speed 4500/6000 rpm (S1805/AZ5214E) for 30 s. The resist is dried on a hotplate at 90°C for 2/7 min., and exposed to the UV-light of a Hg-lamp for 7/6.7 s with the lithography mask in place. When using the resist AZ5214E, a post exposure bake on a hotplate at 121°C for 60 s is necessary. It ensures that an undercut is formed after the development. The temperature is very crucial. A variation of only a few °C already leads to an insufficient or even to no undercut. And the intended lift-off process after the evaporation of the desired material will not work. The post exposure bake is followed by a flood illumination with UV-light for 70 s without any lithography mask in place. The exposed resist is developed by immersing the pieces in undiluted developer (AZ726MIF) for 60/35 s. Immediately afterwards the pieces are extensively rinsed in deionized(DI)-water. After the definition of the desired pattern in the resist, a visual inspection under the microscope, with the red filter applied to the light source, is performed. If the lithography process is properly completed, the actual process step follows. If done so, the resist is stripped (lift-off) in acetone with the help of ultrasound. Only a reduced ultrasound power is applied after the evaporation of a thin metallic (AuPd) front gate to avoid any damage. Finally, the pieces are rinsed in propanol and dried by blowing with nitrogen gas.

The different process steps are:

- Etching of the mesa.
  The pattern is defined lithographically using the resist S1805. The Hall bars (or other sample geometries) are oriented along the cleaved edges of the pieces, which represent the two principal crystal axes within the (001) plane of GaAs. The best choice for the current path is the [110] direction, because it provides the highest mobility. It can be identified by the orientation of oval defects (see Subsec. 6.8.1). The transfer of the pattern into the semiconductor is realized by a wet chemical etch process using a solution consisting of sulfuric acid (H_2SO_4), hydrogen peroxide (H_2O_2), and DI-water (volume ratios 1:8:1000). The etch time is determined by the desired height of the mesa. A sufficient etch depth is usually assured when the doped region between the surface and the active region is removed. The etch rate of that solution is about 40 nm/min. for GaAs and 20% larger for AlGaAs with an Al content of about 30%. The pieces are immersed in the solution, which is stirred slowly during the etch process. Subsequently, the pieces are extensively rinsed in DI-water.

- Evaporation of materials for ohmic contacts to the bilayer.
  The pattern is defined lithographically using the resist AZ5214E. In addition, the pieces are treated in oxygen plasma for 30 s to remove any residual resist from the contact areas. Subsequently, the pieces are immersed in Semicoclean for 2 min., in DI-water for 5 s, in HCl (31%) for 5 s, in DI-water for several seconds, and finally dried by blowing with nitrogen gas. This procedure removes the native surface oxide, which can hamper the diffusion process of the materials for the ohmic contacts during alloying. The pieces are then immediately loaded into the evaporator. At a pressure below 10^{-5} mbar, the materials for the ohmic contacts are evaporated, consisting of the sequence Ni/Ge/Au/Ni with typical thicknesses 10/110/220/36 nm (see the discussion of the different thicknesses in Sec. 3.3).

- Evaporation of materials for ohmic contacts to the back gate.
  The pattern is defined lithographically using the resist S1805. Since the back gate is

several microns below the surface, it is necessary to fabricate contact holes prior to the evaporation. The contact holes are transferred into the semiconductor with a wet chemical etch step using a solution consisting of sulfuric acid, hydrogen peroxide, and DI-water (volume ratios 1:8:400). The etch time is determined by the desired depth of the contact holes. The etch depth is determined by the goal to remove the LT-GaAs layer, which covers the back gate, but not to remove the back gate underneath. The material removed already during the mesa etch process step must be considered. The etch rate of that solution is about 100 nm/min. for GaAs and 20% larger for AlGaAs with an Al content of about 30%. The pieces are immersed in the solution, which is stirred slowly during the etch process. Subsequently, the pieces are extensively rinsed in DI-water. Otherwise the etch process might continue due to residual acid, which can be trapped in the contact holes. Finally, the pieces are dried by blowing with nitrogen gas and immediately loaded into the evaporator. At a pressure below 10^{-5} mbar, the material for the ohmic contacts are evaporated, consisting of the sequence Ni/Ge/Au/Ni with typical thicknesses 5/110/220/36 nm.

- Alloying of ohmic contact materials.
  The pieces are put into an oven (AZ450) where the temperature is controlled by a hotplate. The atmosphere in the oven is forming gas consisting of 20% hydrogen and 80% nitrogen at a pressure 300 mbar. The following temperatures are adjusted in succession: 300°C for 60 s, 440°C for 30 s, cool down to RT.

- Evaporation of materials for bond pads.
  The pattern is defined lithographically using the resist AZ5214E. The pieces are immediately loaded into the evaporator and either Ti/Au or Cr/Au with typical thicknesses of 20/100 nm are evaporated.

- Evaporation of a thin metal layer acting as front gate.
  The pattern is defined lithographically using the resist AZ5214E. The pieces are immediately loaded into the evaporator. AuPd with a Pd content of 40% is evaporated with a thickness of 8.5 nm at a very low rate of 0.05 nm/s. If an additional Hall probe can be used to contact the front gate (see Sec. 3.4), the evaporation happens perpendicular to the surface of the pieces. Otherwise (*e.g.* in the case of hole gas samples presented in Subsec. 6.8.4), the front gate is evaporated under a certain angle of typically 45° and the pieces are rotated around their normal axis at a rate of about 1 Hz during the evaporation.

The processed samples are glued into a carrier using PMMA with the lowest dilution ratio. The PMMA is hardened in an oven at 160°C for 6 minutes. One sample (*e.g.* Hall bar) is selected by visual inspection. It is electrically connected to the carrier by bonds of Au wires. If no bond pads are available, as in some cases for the front gate (see Sec. 3.4), a two-component epoxy silver paint is used to fix the Au wire.

A.2 Measurement techniques

All samples investigated here are Hall bars with two current contacts (see Fig. 2.1a). For a measurement, one current contact is grounded while a probing AC-current is applied to the other one. In the case of the square sample (Van der Pauw geometry) discussed in Sec. 6.3 and Subsec. 6.8.1, one of the four equivalent contacts to the bilayer is grounded. An AC-current is used to benefit from the usage of the lock-in technique. Either the oscillator of one lock-in amplifier or an external signal generator is used as source. The latter method applies when a variation of the amplitude of the probing AC-current is desired. The provided AC-voltage of the oscillator or signal generator is applied via a series resistance of 100 MΩ to the sample. The series resistance defines the probing AC-current to 10 nA when an AC-voltage amplitude of 1 V is used as usually the case here. Typical frequencies are 13.4 Hz at 1.5 K and 5.8 Hz at lower temperatures. The principal of measuring the longitudinal resistance R_{xx} and the Hall resistance R_{H} is discussed in Sec. 2.2. The gate bias is controlled with a voltage source with a minimum step size 0.3 mV. The bias is applied to the gates via a low-pass filter consisting of an RC-circuit with a typical time constant 0.1 s (cut-off frequency 10 Hz). For the reset experiments in Sec. 6.4, the time constant of the low-pass filter attached to the front gate is reduced to 1 ms. The integration time of the lock-in amplifiers, which record the signals, is adjusted to 1 s and lowered to 300 ms only for the reset experiments. This basic setup is modified if necessary (see Sec. 6.6) and is accordingly described in the text.

The measurements are carried out in different cryogenic systems which are listed in the following. The legend for each data plot in this thesis indicates *inter alia* which cryogenic system is used for the underlying measurement. This determines in particular what the temperature declaration "T = Base" means, which is usually given when a dilution refrigerator is used.

- ^{4}He 5M20/5M22, regular cryostat:
  The sample resides in liquid ^{4}He, which is pumped to about 1 mbar. This results in a sample[1] temperature of about 1.5 K.

- ^{3}He 5D8, Heliox:
  This is an insert[2] with a closed volume of ^{3}He. The ^{3}He is condensed into the ^{3}He pot and subsequently pumped by a sorption pump. Therefore, only single shot operation is possible. After about 72 hours, the ^{3}He has to be recondensed, which involves a warm up of the sample to about 1.8 K. But the sample does not suffer any changes by that procedure. The sample is mounted to the outside of the ^{3}He pot and resides in vacuum. The minimum sample temperature achievable is about 250 mK.

- 3B16, dilution refrigerator:
  This top-loading dilution refrigerator provides the lowest base[3] and sample[4] temperature

---

[1] The temperature of the electron system is meant here.

[2] Insert means that the hole system has to be placed into a bath of ^{4}He to be operated.

[3] The temperature of the mixing chamber is meant here.

[4] The fact, that the sample temperature is also the lowest, is indicated by a virtually vanishing resistance peak at

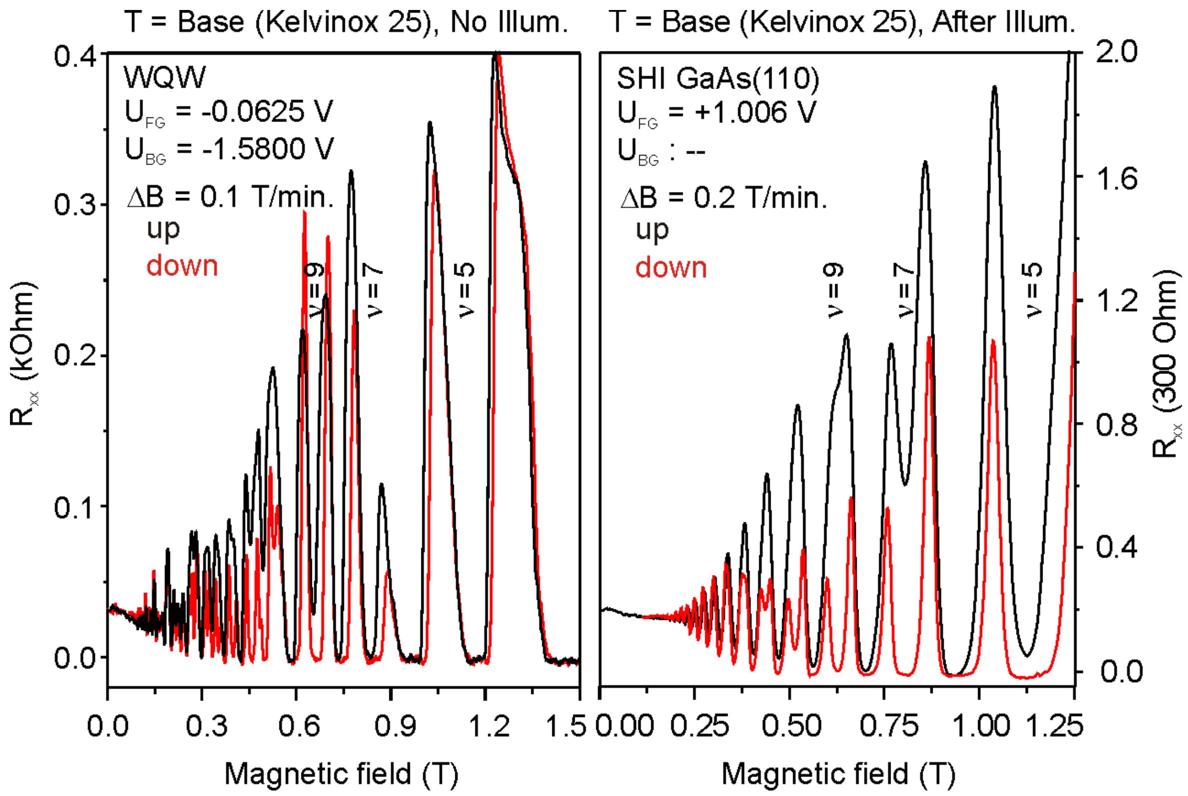

Figure A.1: Comparison of R_{xx} traces obtained during up and down sweeps of the magnetic field using the Kelvinox 25 dilution refrigerator insert. A significantly lower sample temperature for a down sweep of the magnetic field is indicated by the much better resolved quantum Hall states (R_{xx} minima) at odd filling factors, which are due to spin split LLs. This effect is even pronounced for a higher sweep rate (ΔB) of the magnetic field. An influence of the sweep direction or rate is absent above a magnetic field of about 2 T.

of all used dilution refrigerators. The nominal base temperature is well below 20 mK. The sample resides within a mixture of ^{3}He/^{4}He. The cooling power originates from a continuous dilution of ^{3}He in ^{4}He in the mixing chamber (see [240]). The sample temperature is estimated to about 40 mK.

- 3B10 new, dilution refrigerator:

  This top-loading dilution refrigerator is comparable to the previous one but the sample temperature is found to be a few mK higher at base temperature. Most probably this is due to less extensive filtering of the cables, which feed into the cryostat to the sample.

- 3B10 old, dilution refrigerator:

  The base temperature of this top-loading dilution refrigerator is a few mK higher than that of the latter system , because the cooling power is less.

---

the isospin transition (see Sec. 7.3 and Fig. 7.7), since its height is very sensitive to the actual sample temperature.

- Kelvinox 25, dilution refrigerator:
  This is a dilution refrigerator insert with a base temperature at the mixing chamber of 21 mK. The sample is attached to the outside of the mixing chamber via a silver rod and is cooled by copper wires which are thermally anchored at the silver rod. Due to that the sample temperature is slightly higher than the temperature of the mixing chamber at base temperature, *i.e.* about 40 mK. The crystal temperature T_{c} is estimated to be 30 mK (see Sec. 6.5). A sweep of the magnetic field alters the sample temperature noticeable in the magnetic field range up to 2 T depending on the sweep direction. A comparison of R_{xx} traces obtained during up and down sweeps of the magnetic field is given in Fig. A.1. Probably the nuclear demagnetization of the copper wires leads to a significantly lower sample temperature when the magnetic field is swept downwards. Due to this effect, data are recorded in the most cases during the down sweep of the magnetic field. This effect is absent above a magnetic field of about 2 T.

If illumination of a sample is necessary, a regular red LED is used, which is placed in the vicinity to the sample's surface, *i.e.* a few millimeters above it. Illumination is performed at a sample temperature of 1.5 K. The illumination strength is controlled by the current which is sent through the LED. The current can range from well below 1 μA to several mA depending on the sample and the actual distance between sample and LED. The duration of the illumination can range from a few seconds to several minutes also depending on the sample and the illumination strength. After illumination, the sample needs a few minutes until the carrier density, which is altered by the illumination, settles. During illumination, the front and back gates are held at zero bias except in the case of the sample realized on GaAs(110) substrate (see Subsec. 6.8.3).

Bibliography

[1] I. B. SPIELMAN, J. P. EISENSTEIN, L. N. PFEIFFER, and K. W. WEST, *Observation of a linearly dispersing collective mode in a quantum Hall ferromagnet,* Phys. Rev. Lett. **87**, 036803 (2001).

[2] S. K. LYO and J. A SIMMONS, *Nonequilibrium DC and photon-assisted interlayer tunneling in a bilayer tunneling structure,* Physica B **314**, 417 (2002).

[3] M. M. KHODIER, C. G. CHRISTODOULOU, and J. A. SIMMONS, *Equivalent circuit model for a THz detector based on the double-electron layer tunneling transistor (DELTT),* IEEE Trans. Electron. Dev. **49**, 1701 (2002).

[4] X. G. PERALTA, S. J. ALLEN, M. C. WANKE, N. E. HARFF, J. A. SIMMONS, M. P. LILLY, J. L. RENO, P. J. BURKE, and J. P. EISENSTEIN, *Terahertz photoconductivity and plasmon modes in double-quantum-well field-effect transistors,* Appl. Phys. Lett. **81**, 1627 (2002).

[5] V. V. POPOV, O. V. POLISCHUK, T. V. TEPERIK, X. G. PERALTA, S. J. ALLEN, N. J. M. HORING, and M. C. WANKE, *Absorption of terahrtz radiation by plasmon modes in a grid-gated double-quantum-well field-effect transistor,* J. Appl. Phys. **94**, 3556 (2003).

[6] V. W. SCAROLA, K. PARK, and S. DAS SARMA, *Pseudospin quantum computation in semiconductor nanostructures,* Phys. Rev. Lett. **91**, 167903 (2003).

[7] S. M. GIRVIN, *Spin and Isospin: Exotic order in quantum Hall ferromagnets,* Physics Today **June 2000**, 39 (2000).

[8] K. V. KLITZING, G. DORDA, and M. PEPPER, *New method for high–accuracy determination of the fine–structure constant based on quantized Hall resistance,* Phys. Rev. Lett. **45**, 494 (1980).

[9] L. PFEIFFER, E. F. SCHUBERT, K. W. WEST, and C. W. MAGEE, *Si dopant migration and the AlGaAs/GaAs inverted interface,* Appl. Phys. Lett. **58**, 2258 (1991).

[10] F. F. FANG and W. E. HOWARD, *Negative field–effect mobility on (100) Si surfaces,* Phys. Rev. Lett. **16**, 797 (1966).

[11] J. SINGH, *Physics of semiconductors and their heterostructures*, McGraw-Hill, New York (1993).

[12] L. J. VAN DER PAUW, *A method of measuring specific resistivity and Hall effect of discs of arbitrary shape,* Philips Res. Repts. **13**, 1 (1958).

[13] B. JECKELMANN and B. JEANNERET, *The quantum Hall effect as an electrical resistance standard,* Rep. Prog. Phys. **64**, 1603Ű1655 (2001).

[14] D. YOSHIOKA, B. I. HALPERIN, and P. A. LEE, *Ground state of two–dimensional electrons in strong magnetic fields and* $\frac{1}{3}$ *quantized Hall effect,* Phys. Rev. Lett. **50**, 1219 (1983).

[15] H. C. MANOHARAN, *New particles and phases in reduced–dimensional systems*, Ph.D. thesis, Princeton University (1998).

[16] R. B. LAUGHLIN, *Anomalous quantum Hall effect: An incompressible quantum fluid with fractionally charged excitation,* Phys. Rev. Lett. **50**, 1395 (1983).

[17] D. C. TSUI, H. L. STORMER, and A. C. GOSSARD, *Two–dimensional magnetotransport in the extreme quantum limit*, Phys. Rev. Lett. **48**, 1559 (1982).

[18] J. K. JAIN, *Composite–Fermion approach for the fractional quantum Hall effect,* Phys. Rev. Lett. **63**, 199 (1989).

[19] D. PFANNKUCHE, private communication.

[20] W. PAN, H. L. STORMER, D. C. TSUI, L. N. PFEIFFER, K. W. BALDWIN, and K. W. WEST, *Transition from an electron solid to the sequence of fractional quantum Hall states at very low Landau level filling factor,* Phys. Rev. Lett. **88**, 176802 (2002).

[21] J. H. SMET, D. WEISS, R. H. BLICK, G. LÜTJERING, K. VON KLITZING, R. FLEISCHMANN, R. KETZMERICK, T. GEISEL, and G. WEIMANN, *Magnetic focusing of composite fermions through arrays of cavities,* Phys. Rev. Lett. **77**, 2272 (1996).

[22] R. L. WILLETT, H. L. STORMER, D. C. TSUI, A. C. GOSSARD, and J. H. ENGLISH, *Quantitative experimental test for the theoretical gap energies in the fractional quantum Hall effect,* Phys. Rev. **B 37**, 8476 (1988).

[23] O. N. MAKAROVSKII, L. SMIRČKA, P. VAŠEK, T. JUNGWIRTH, M. CUKR, and L. JANSEN, *Magnetoresistance and electronic structure of asymmetric* $GaAs/Al_{0.3}Ga_{0.7}As$ *double quantum wells in an in–plane or tilted magnetic field,* Phys. Rev. **B 62**, 10908 (2000).

[24] J. P. EISENSTEIN, L. N. PFEIFFER, and K. W. WEST, *Independently contacted two–dimensional electron systems in double quantum wells,* Appl. Phys. Lett. **57**, 2324 (1990).

[25] K. MURAKI, N. KUMADA, T. SAKU, and Y. HIRAYAMA, *n^+-GaAs back–gated double–quantum–well structures with full density control*, Jpn. J. Appl. Phys. **39**, 2444 (2000).

[26] A. R. HAMILTON, E. H. LINFIELD, M. J. KELLY, D. A. RITCHIE, G. A. C. JONES, and M. PEPPER, *Transition from one- to two–subband occupancy in the 2DEG of back–gated modulation–doped GaAs-Al_xGa_{1-x}As heterostructures*, Phys. Rev. **B 51**, 17600 (1995).

[27] A. G. DAVIES, C. H. W. BARNES, K. R. ZOLLEIS, J. T. NICHOLLS, M. Y. SIMMONS, and D. A. RITCHIE, *Hybridization of single- and double–layer behaviour in a double–quantum–well structure*, Phys. Rev. **B 54**, R17331 (1996).

[28] A. R. HAMILTON, M. Y. SIMMONS, C. B. HANNA, J. C. DÍAZ-VÉLEZ, M. PEPPER, and D. A. RITCHIE, *Exchange-driven bilayer-to-monolayer charge transfer in an asymmetric double-quantum-well*, Physica E **12**, 304 (2002).

[29] J. A. SIMMONS, S. K. LYO, J. F. KLEM, M. E. SHERWIN, and J. R. WENDT, *Submicrometer control of two–dimensional – two–dimensional magnetotunneling in double–well heterostructures*, Phys. Rev. **B 47**, 15741 (1993).

[30] M. P. LILLY, J. P. EISENSTEIN, L. N. PFEIFFER, and K. W. WEST, *Coulomb drag in the extreme quantum limit*, Phys. Rev. Lett. **80**, 1714 (1998).

[31] M. SHAYEGAN, J. JO, Y. W. SUEN, M. SANTOS, and V. J. GOLDMAN, *Collapse of the fractional quantum Hall effect in an electron system with large layer thickness*, Phys. Rev. Lett. **65**, 2916 (1990).

[32] Y. W. SUEN, L. W. ENGEL, M. B. SANTOS, M. SHAYEGAN, and D. C. TSUI, *Observation of a $\nu = 1/2$ fractional quantum Hall state in a double–layer electron system*, Phys. Rev. Lett. **68**, 1379 (1992).

[33] Y. W. SUEN, H. C. MANOHARAN, X. YING, M. B. SANTOS, and M. SHAYEGAN, *Origin of the $\nu = 1/2$ fractional quantum Hall state in wide single quantum wells*, Phys. Rev. Lett. **72**, 3405 (1994).

[34] J. P. EISENSTEIN, G. S. BOEBINGER, L. N. PFEIFFER, K. W. WEST, and SONG HE, *New fractional quantum Hall state in double–layer two–dimensional electron systems*, Phys. Rev. Lett. **68**, 1383 (1992).

[35] K. MURAKI, T. SAKU, and Y. HIRAYAMA, *Charge excitations in easy–axis and easy–plane quantum Hall ferromagnets*, Phys. Rev. Lett. **87**, 196801 (2001).

[36] K. MURAKI, Presentation at the annual meeting of the department von Klitzing of the Max Planck Institut for Solid State Research at Castle Ringberg 2001.

[37] N. KUMADA, D. TERASAWA, Y. SHIMODA, H. AZUHATA, A. SAWADA, Z. F. EZAWA, K. MURAKI, T. SAKU, and Y. HIRAYAMA, *Phase diagram of interacting composite fermions in the bilayer $\nu = \frac{2}{3}$ quantum Hall effect*, Phys. Rev. Lett. **89**, 116802 (2002).

[38] K. MURAKI, T. SAKU, Y. HIRAYAMA, N. KUMADA, A. SAWADA, and Z. F. EZAWA, *Interlayer charge transfer in bilayer quantum Hall states at various filling factors*, Solid State Commun. **112**, 625 (1999).

[39] G. ERNST, *Zeitaufgelöste Transportmessungen zum Quanten–Hall–Effekt*, Ph.D. thesis, Max Planck Institut for Solid State Research and Univ. Stuttgart (1997).

[40] J. D. NAUD, L. P. PRYADKO, and S. L. SONDHI, *Edge dynamics in quantum Hall bilayers: Exact results with disorder and parallel fields*, Phys. Rev. **B 63**, 115301 (2001).

[41] H. RUBEL, A. FISCHER, W. DIETSCHE, K. VON KLITZING, and K. EBERL, *Fabrication of independently contacted and tuneable 2D-electron-hole systems in GaAs/AlGaAs double quantum wells*, Mater. Sci. Eng. B **51**, 207 (1998).

[42] Y.-W. SUEN, *Correlated electron states in wide single quantum wells*, Ph.D. thesis, Princeton University (1993).

[43] M. MURAKAMI, *Development of refractory ohmic contacts materials for gallium arsenide compound semiconductors*, Sci. Technol. Adv. Mater. **3**, 1 (2002).

[44] T.-J. KIM and P. H. HOLLOWAY, *Ohmic contacts to GaAs epitaxial layers*, Crit. Rev. Sol. Stat. Mat. Sci. **22**, 239 (1997).

[45] Y.-C. SHIH, M. MURAKAMI, E. L. WILKIE, and A. C. CALLEGARI, *Effects of interfacial microstructure on uniformity and thermal stability of AuNiGe ohmic contacts to n-type GaAs*, J. Appl. Phys. **62**, 582 (1987).

[46] B. E. KANE, L. N. PFEIFFER, and K. W. WEST, *Variable density high mobility two–dimensional electron and hole gases in a gated GaAs/Al$_x$Ga$_{1-x}$As heterostructure*, Appl. Phys. Lett. **63**, 2132 (1993).

[47] B. E. KANE, L. N. PFEIFFER, and K. W. WEST, *High mobility GaAs heterostructure field effect transistor for nanofabrication in which dopant–induced disorder is eliminated*, Appl. Phys. Lett. **67**, 1262 (1995).

[48] V. UMANSKY, R. DE PICCIOTTO, and M. HEIBLUM, *Extremely high–mobility two dimensional electron gas: Evaluation of scattering mechanisms*, Appl. Phys. Lett. **71**, 683 (1997).

[49] S. KRAUS, *Untersuchung von Wechselwirkungen in zweidimensionalen Elektronensystemen mit Transport- und Drag-Messungen*, Ph.D. thesis, Max Planck Institute for Solid State Research and Univ. Stuttgart (2003).

[50] D. REUTER, D. KÄHLER, U. KUNZE, and A. D. WIECK, *Layer-compensated selectively doped* $Al_xGa_{1-x}As$*/GaAs heterostructures as a base material for nanolithography*, Semicond. Sci. Technol. **16**, 603 (2001).

[51] D. KÄHLER, U. KUNZE, D. REUTER, and A. D. WIECK, *Quantum wire fabrication from compensating-layer GaAs-AlGaAs heterostructures*, Microelectron. Eng. **61-62**, 619 (2002).

[52] D. KÄHLER, U. KUNZE, D. REUTER, and A. D. WIECK, *Aharonov-Bohm effect in nanoscale quantum rings fabricated from compensating-layer GaAs/AlGaAs heterostructures*, Physica E **17**, 284 (2003).

[53] S. KRAUS, private communication.

[54] S. LOK, private communication.

[55] S. DOROZHKIN, private communication.

[56] V. A. VOLKOV and S. A. MIKHAILOV, *Edge magnetoplasmons: low frequency weakly damped excitations in inhomogeneous two–dimensional electron systems*, Sov. Phys. JETP **67**, 1639 (1988).

[57] D. W. SHAW, *Localized GaAs etching with acidic hydrogen peroxide solutions*, J. Electrochem. Soc. **128**, 874 (1981).

[58] H. P. MEIER, R. F. BROOM, P. W. EPPERLEIN, E. VAN GIESON, CH. HARDER, H. JÄCKEL, W. WALTER, and D. J. WEBB, *Problems related to the formation of lateral p–n junctions on channeled substrate (100) GaAs for lasers*, J. Vac. Sci. Technol. B **6**, 692 (1988).

[59] G. S. BOEBINGER, H. W. JIANG, L. N. PFEIFFER, and K. W. WEST, *Magnetic–field–driven destruction of quantum Hall states in a double quantum well*, Phys. Rev. Lett. **64**, 1793 (1990).

[60] Z. F. EZAWA, *Spin-pseudospin coherence and* CP^3 *Skyrmions in bilayer quantum Hall ferromagnets*, Phys. Rev. Lett. **82**, 3512 (1999).

[61] W. PAN, H. L. STORMER, D. C. TSUI, L. N. PFEIFFER, K. W. BALDWIN, and K. W. WEST, *Highly anisotropic transport in the integer quantum Hall effect*, Phys. Rev. **B 64**, 121305(R) (2001).

[62] S.-J. CHENG, *Collective excitations and Coulomb drag in two-dimensional semiconductor systems*, Ph.D. thesis, Max Planck Institute for Solid State Research and Univ. Würzburg (2001).

[63] S.-J. CHENG, private communication.

[64] C.-M. HU and D. HEITMANN, *Bilayer quantum transistor*, Appl. Phys. Lett. **77**, 1475 (2000).

[65] Z. F. EZAWA, *Quantum Hall Effects*, World Scientific, Singapore (2000).

[66] M. ABOLFATH, L. BELKHIR, and N. NAFARI, *Quantum Hall effect in single wide quantum wells*, Phys. Rev. **B 55**, 10643 (1997).

[67] Z. F. EZAWA, A. SAWADA, K. MURAKI, and Y. HIRAYAMA, *Quantum coherence and Skyrmion textures in bilayer quantum Hall systems*, Physica E **6**, 640 (2000).

[68] T. JUNGWIRTH, S. P. SHUKLA, L. SMRČKA, M. SHAYEGAN, and A. H. MACDONALD, *Magnetic anisotropy in quantum Hall ferromagnets*, Phys. Rev. Lett. **81**, 2328 (1998).

[69] Y. N. JOGLEKAR and A. H. MACDONALD, *Bias-voltage-induced phase transition in bilayer quantum Hall ferromagnets*, Phys. Rev. **B 65**, 235319 (2002).

[70] T. JUNGWIRTH and A. H. MACDONALD, *Resistance spikes and domain wall loops in Ising quantum Hall ferromagnets*, Phys. Rev. Lett. **87**, 216801 (2001).

[71] T. JUNGWIRTH and A. H. MACDONALD, *Pseudospin anisotropy classification of quantum Hall ferromagnets*, Phys. Rev. **B 63**, 035305 (2001).

[72] A. SCHMELLER, J. P. EISENSTEIN, L. N. PFEIFFER, and K. W. WEST, *Evidence for Skyrmions and single spin flips in the integer quantized Hall effect*, Phys. Rev. Lett. **75**, 4290 (1995).

[73] D. K. MAUDE, M. POTEMSKI, J. C. PORTAL, M. HENINI, L. EAVES, G. HILL, and M. A. PATE, *Spin excitations of a two–dimensional electron gas in the limit of vanishing Landé g factor*, Phys. Rev. Lett. **77**, 4604 (1996).

[74] S. E. BARRETT, G. DABBAGH, L. N. PFEIFFER, K. W. WEST, and R. TYCKO, *Optically pumped NMR evidence for finite–size Skyrmions in GaAs quantum wells near Landau level filling $\nu = 1$*, Phys. Rev. Lett. **74**, 5112 (1995).

[75] R. CÔTÉ, A. H. MACDONALD, L. BREY, H. A. FERTIG, S. M. GIRVIN, and H. T. C. STOOF, *Collective excitations, NMR, and phase transitions in Skyrme crystals*, Phys. Rev. Lett. **78**, 4825 (1997).

[76] W. DESRAT, D. K. MAUDE, M. POTEMSKI, J. C. PORTAL, Z. R. WASILEWSKI, and G. HILL, *Resistively detected nuclear magnetic resonance in the quantum Hall regime: possible evidence for a Skyrme crystal*, Phys. Rev. Lett. **88**, 256807 (2002).

[77] Z. F. EZAWA and K. HASEBE, *Interlayer exchange interactions, SU(4) soft waves, and Skyrmions in bilayer quantum Hall ferromagnets*, Phys. Rev. **B 65**, 075311 (2002).

[78] P. KHANDELWAL, A. E. DEMENTYEV, N. N. KUZMA, S. E. BARRETT, L. N. PFEIFFER, and K. W. WEST, *Spectroscopic evidence for the localization of Skyrmions near* $\nu = 1$ *as* $T \to 0$, Phys. Rev. Lett. **86**, 5353 (2001).

[79] N. KUMADA, A. SAWADA, Z. F. EZAWA, S. NAGAHAMA, H. AZUHATA, K. MURAKI, T. SAKU, and Y. HIRAYAMA, *Doubly enhanced Skyrmions in* $\nu = 2$ *bilayer quantum Hall states*, J. Phys. Soc. Jpn. **69**, 3178 (2000).

[80] N. KUMADA, A. SAWADA, Z. F. EZAWA, H. AZUHATA, S. NAGAHAMA, K. MURAKI, T. SAKU, and Y. HIRAYAMA, *Preferred number of flipped spins in Skyrmion excitation*, Physica B **298**, 169 (2001).

[81] D. LILLIEHÖÖK, *Inter–Landau–level Skyrmions versus quasielectrons in the* $\nu = 2$ *quantum Hall effect*, Phys. Rev. **B 62**, 7303 (2000).

[82] S. L. SONDHI, A. KARLHEDE, S. A. KIVELSON, and E. H. REZAYI, *Skyrmions and the crossover from the integer to fractional quantum Hall effect at small Zeeman energies*, Phys. Rev. **B 47**, 16419 (1993).

[83] S. KOCH, R. J. HAUG, K. V. KLITZING, and M. RAZEGHI, *Suppression of the Landau–level coincidence: a phase transition in tilted magnetic fields*, Phys. Rev. **B 47**, 4048 (1993).

[84] D. R. LEADLEY, R. J. NICHOLAS, D. K. MAUDE, A. N. UTJUZH, J. C. PORTAL, J. J. HARRIS, and C. T. FOXON, *Fractional quantum Hall effect measurements at zero* g *factor*, Phys. Rev. Lett. **79**, 4246 (1997).

[85] T. CHAKRABORTY, *Spin–reversed ground state and energy gap in the fractional quantum Hall effect*, Surf. Sci. **229**, 16 (1990).

[86] F. C. ZHANG and S. DAS SARMA, *Excitation gap in the fractional quantum Hall effect: finite layer thickness corrections*, Phys. Rev. **B 33**, 2903 (1986).

[87] A. H. MACDONALD, P. M. PLATZMAN, and G. S. BOEBINGER, *Collapse of integer Hall gaps in a double–quantum–well system*, Phys. Rev. Lett. **65**, 775 (1990).

[88] Y. W. SUEN, J. JO, M. B. SANTOS, L. W. ENGEL, S. W. HWANG, and M. SHAYEGAN, *Missing integral quantum Hall effect in a wide single quantum well*, Phys. Rev. **B 44**, 5947 (1991).

[89] I. B. SPIELMAN, J. P. EISENSTEIN, L. N. PFEIFFER, and K. W. WEST, *Resonantly enhanced tunneling in a double layer quantum Hall ferromagnet*, Phys. Rev. Lett. **84**, 5808 (2000).

[90] M. KELLOGG I. B. SPIELMAN, J. P. EISENSTEIN, L. N. PFEIFFER, and K. W. WEST, *Observation of quantized Hall drag in a strongly correlated bilayer electron system*, Phys. Rev. Lett. **88**, 126804 (2002).

[91] M. KELLOGG, J. P. EISENSTEIN, L. N. PFEIFFER, and K. W. WEST, *Bilayer quantum Hall systems at $\nu_T = 1$: Coulomb drag and the transition from weak to strong interlayer coupling*, Phys. Rev. Lett. **90**, 246801 (2003).

[92] S. M. GIRVIN, *The quantum Hall effect: novel excitations and broken symmetries*, cond-mat/9907002 (1998).

[93] J. P. EISENSTEIN, *The quantum Hall effect branches out*, Physics World **14**, 30 (June 2001).

[94] J. SCHLIEMANN, S. M. GIRVIN, and A. H. MACDONALD, *Strong correlation to weak correlation phase transition in bilayer quantum Hall systems*, Phys. Rev. Lett. **86**, 1849 (2001).

[95] R. J. NICHOLAS, R. J. HAUG, K. V. KLITZING, and G. WEIMANN, *Exchange enhancement of the spin splitting in a GaAs-Ga$_x$Al$_{1-x}$As heterojunction*, Phys. Rev. **B 37**, 1294 (1988).

[96] C. HERMANN and C. WEISBUCH, *$\vec{k} \cdot \vec{p}$ perturbation theory in III-V compounds and alloys: a reexamination*, Phys. Rev. **B 15**, 823 (1977).

[97] E. TUTUC, S. MELINTE, and M. SHAYEGAN, *Spin polarization and g factor of a dilute GaAs two–dimensional electron system*, Phys. Rev. Lett. **88**, 036805 (2002).

[98] T. CHAKRABORTY and P. PIETILÄINEN, *Fractional quantum Hall effect at half–filled Landau level in a multiple–layer electron system*, Phys. Rev. Lett. **59**, 2784 (1987).

[99] B. I. HALPERIN, *Theory of the quantized Hall conductance*, Helv. Phys. Acta **56**, 75 (1983).

[100] J. D. NAUD, L. P. PRYADKO, and S. L. SONDHI, *Quantum Hall bilayers and the chiral sine–Gordon equation*, Nucl. Phys. B **565**, 572 (2000).

[101] D. YOSHIOKA, A. H. MACDONALD, and S. M. GIRVIN, *Fractional quantum Hall effect in two–layered systems*, Phys. Rev. **B 39**, 1932 (1989).

[102] A. CAPPELLI, L. S. GEORGIEV, and I. T. TODOROV, *A unified conformal field theory description of paired quantum Hall states*, Commun. Math. Phys. **205**, 657 (1999).

[103] V. W. SCAROLA and J. K. JAIN, *Phase diagram of bilayer composite fermion states*, Phys. Rev. **B 64**, 085313 (2001).

[104] M. GREITER, X. G. WEN, and F. WILCZEK, *Paired Hall states in double–layer electron systems*, Phys. Rev. **B 46**, 9586 (1992).

[105] B. I. HALPERIN, *Theories for* $\nu = 1/2$ *in single- and double–layer systems*, Surf. Sci. **305**, 1 (1994).

[106] D. C. CABRA, A. LOPEZ, and G. L. ROSSINI, *Transition from Abelian to non–Abelian FQHE states*, Eur. Phys. J. B **19**, 21 (2001).

[107] T. MORINARI, *Tunneling effect on the composite fermion pairing state in bilayer quantum Hall systems*, Phys. Rev. **B 65**, 115319 (2002).

[108] E. FRADKIN, C. NAYAK, and K. SCHOUTENS, *Landau–Ginzburg theories for non–abelian quantum Hall states*, Nucl. Phys. B **546**, 711 (1999).

[109] G. MOORE and N. READ, *Nonabelions in the fractional quantum Hall effect*, Nucl. Phys. B **360**, 362 (1991).

[110] M. GREITER, X.-G. WEN, and F. WILCZEK, *Paired Hall state at half filling*, Phys. Rev. Lett. **66**, 3205 (1991).

[111] E. FRADKIN, C. NAYAK, A. TSVELIK, and F. WILCZEK, *A Chern–Simons effective field theory for the Pfaffian quantum Hall state*, Nucl. Phys. B **516**, 704 (1998).

[112] B. I. HALPERIN, P. A. LEE, and N. READ, *Theory of the half–filled Landau level*, Phys. Rev. **B 47**, 7312 (1993).

[113] H. C. MANOHARAN, Y. W. SUEN, T. S. LAY, M. B. SANTOS, and M. SHAYEGAN, *Spontaneous interlayer charge transfer near the magnetic quantum limit*, Phys. Rev. Lett. **79**, 2722 (1997).

[114] R. PRICE, P. M. PLATZMAN, and SONG HE, *Fractional quantum Hall liquid, Wigner solid phase boundary at finite density and magnetic field*, Phys. Rev. Lett. **70**, 339 (1993).

[115] R. PRICE, X. ZHU, S. DAS SARMA, and P. M. PLATZMAN, *Laughlin–liquid–Wigner–solid transition at high density in wide quantum wells*, Phys. Rev. **B 51**, 2017 (1995).

[116] L. ZHENG and H. A. FERTIG, *Wigner–crystal states for the two–dimensional electron gas in a double–quantum–well system*, Phys. Rev. **B 52**, 12282 (1995).

[117] S. NARASIMHAN and T.-L. HO, *Wigner–crystal phases in bilayer quantum Hall systems*, Phys. Rev. **B 52**, 12291 (1995).

[118] Y. W. SUEN, H. C. MANOHARAN, X. YING, M. B. SANTOS, and M. SHAYEGAN, *One–component to two–component transitions of fractional quantum Hall states in a wide quantum well*, Surf. Sci. **305**, 13 (1994).

[119] D. SCHUH, private communication.

[120] SONG HE, S. DAS SARMA, and X. C. XIE, *Quantized Hall effect and quantum phase transitions in coupled two–layer electron systems*, Phys. Rev. **B 47**, 4394 (1993).

[121] SONG HE, X. C. XIE, S. DAS SARMA, and F. C. ZHANG, *Quantum Hall effect in double–quantum–well systems*, Phys. Rev. **B 43**, 9339 (1991).

[122] S. R. RENN and B. W. ROBERTS, *Tunneling between a pair of parallel Hall droplets*, Phys. Rev. **B 50**, 7626 (1994).

[123] T. S. LAY, T. JUNGWIRTH, L. SMRČKA, and M. SHAYEGAN, *One–component to two–component transition of the $\nu = 2/3$ fractional quantum Hall effect in a wide quantum well induced by an in–plane magnetic field*, Phys. Rev. **B 56**, R7092 (1997).

[124] T. JUNGWIRTH, T. S. LAY, L. SMRČKA, and M. SHAYEGAN, *Resistance oscillation in wide single quantum wells subject to in–plane magnetic fields*, Phys. Rev. **B 56**, 1029 (1997).

[125] N. E. HARFF, J. A. SIMMONS, S. K. LYO, J. F. KLEM, G. S. BOEBINGER, L. N. PFEIFFER, and K. W. WEST, *Magnetic breakdown and Landau–level spectra of a tunable double–quantum–well Fermi surface*, Phys. Rev. **B 55**, R13405 (1997).

[126] S.-J. CHENG and R. R. GERHARDTS, *Coupled two–layer plasmon modes induced in a single quantum well by in–plane magnetic fields*, Phys. Rev. **B 65**, 085307 (2002).

[127] J. HU and A. H. MACDONALD, *Electronic structure of parallel two–dimensional electron systems in tilted magnetic fields*, Phys. Rev. **B 46**, 12554 (1992).

[128] T.-L. HO, *Broken symmetry of two–component $\nu = 1/2$ quantum Hall states*, Phys. Rev. Lett. **75**, 1186 (1995).

[129] S.-J. YANG, Y. YU, and J.-B. LIN, *Laughlin-type wave function of two-dimensional electrons in a tilted magnetic field*, Phys. Rev. **B 65**, 073302 (2002).

[130] V. HALONEN, P. PIETILÄINEN, and T. CHAKRABORTY, *Subband-Landau-level coupling in the fractional quantum Hall effect in tilted magnetic fields*, Phys. Rev. **B 41**, 10202 (1990).

[131] R. L. WILLETT, J. P. EISENSTEIN, H. L. STÖRMER, D. C. TSUI, A. C. GOSSARD, and J. H. ENGLISH, *Observation of en even–denominator quantum number in the fractional quantum Hall effect*, Phys. Rev. Lett. **59**, 1776 (1987).

[132] K. INO, *Pairing effects at the edge of paired quantum Hall states*, Phys. Rev. Lett. **81**, 1078 (1998).

[133] K. INO, *Modular invariants in the fractional quantum Hall effect*, Nucl. Phys. B **532**, 783 (1998).

[134] K. INO, *Persistent edge current in the fractional quantum Hall effect*, Phys. Rev. Lett. **81**, 5908 (1998).

[135] K. INO, *The Haldane–Rezayi quantum Hall state and magnetic flux*, Phys. Rev. Lett. **82**, 4902 (1999).

[136] K. INO, *Spin–singlet hierarchy in the fractional quantum Hall effect*, Phys. Rev. Lett. **83**, 3526 (1999).

[137] K. INO, *Persistent edge currents for paired quantum Hall states*, Phys. Rev. **B 62**, 6936 (2000).

[138] V. W. SCAROLA, J. K. JAIN, and E. H. REZAYI, *Possible pairing–induced even–denominator fractional quantum Hall effect in the lowest Landau level*, Phys. Rev. Lett. **88**, 216804 (2002).

[139] N. READ, *Paired fractional quantum Hall states and the $\nu = 5/2$ puzzle*, Physica B **298**, 121 (2001).

[140] V. W. SCAROLA, K. PARK, and J. K. JAIN, *Cooper instability of composite fermions*, Nature **406**, 863 (2000).

[141] N. READ and D. GREEN, *Paired states of fermions in two dimensions with breaking of parity and time–reversal symmetries and the fractional quantum Hall effect*, Phys. Rev. **B 61**, 10267 (2000).

[142] J. P. EISENSTEIN, R. WILLETT, H. L. STORMER, D. C. TSUI, A. C. GOSSARD, and J. H. ENGLISH, *Collapse of the even-denominator fractional quantum Hall effect in tilted fields*, Phys. Rev. Lett. **61**, 997 (1988).

[143] J. P. EISENSTEIN, H. L. STORMER, L. N. PFEIFFER, and K. W. WEST, *Evidence for a spin transition in the $\nu = 2/3$ fractional quantum Hall effect*, Phys. Rev. **B 41**, 7910 (1990).

[144] R. G. CLARK and P. MAKSYM, *???*, Phys. World **2**, 39 (1989).

[145] R. G. CLARK, S. R. HAYNES, J. V. BRANCH, A. M. SUCKLING, P. A. WRIGHT, P. M. W. OSWALD, J. J. HARRIS, and C. T. FOXON, *Spin configurations and quasiparticle fractional charge of fractional QHE ground states in the $N = 0$ Landau level*, Surf. Sci. **229**, 25 (1990).

[146] L. W. ENGEL, S. W. HWANG, T. SAJOTO, D. C. TSUI, and M. SHAYEGAN, *Fractional quantum Hall effect at $\nu = 2/3$ and $3/5$ in tilted magnetic fields*, Phys. Rev. **B 45**, 3418 (1992).

[147] H. CHO, J. B. YOUNG, W. KANG, K. L. CAMPMAN, A. C. GOSSARD, M. BICHLER, and W. WEGSCHEIDER, *Hysteresis and spin transitions in the fractional quantum Hall effect*, Phys. Rev. Lett. **81**, 2522 (1998).

[148] J. EOM, H. CHO, W. KANG, K. L. CAMPMAN, A. C. GOSSARD, M. BICHLER, and W. WEGSCHEIDER, *Quantum Hall ferromagnetism in a two–dimensional electron system*, Science **289**, 2320 (2000).

[149] W. KANG, J. B. YOUNG, S. T. HANNAHS, E. PALM, K. L. CAMPMAN, and A. C. GOSSARD, *Evidence for a spin transition in the* $\nu = 2/5$ *fractional quantum hall effect*, Phys. Rev. **B 56**, R12776 (1997).

[150] S. KRAUS, O. STERN, J. G. S. LOK, W. DIETSCHE, K. VON KLITZING, M. BICHLER, D. SCHUH, and W. WEGSCHEIDER, *From quantum Hall ferromagnetism to huge longitudinal resistance at the 2/3 fractional quantum Hall state*, Phys. Rev. Lett. **89**, 266801 (2002).

[151] S. KRONMÜLLER, W. DIETSCHE, J. WEIS, K. V. KLITZING, W. WEGSCHEIDER, and M. BICHLER, *New resistance maxima in the fractional quantum Hall effect regime*, Phys. Rev. Lett. **81**, 2526 (1998).

[152] S. KRONMÜLLER, W. DIETSCHE, K. V. KLITZING, G. DENNINGER, W. WEGSCHEIDER, and M. BICHLER, *New type of electron nuclear–spin interaction from resistively detected NMR in the fractional quantum Hall effect regime*, Phys. Rev. Lett. **82**, 4070 (1999).

[153] S. KRONMÜLLER, *Eigenschaften von Grund- und Anregungszuständen im FQHE-Regime*, Ph.D. thesis, Max Planck Institute for Solid State Research and Univ. Stuttgart (1999).

[154] O. STERN, *Spin phenomena in the fractional quantum Hall effect: NMR and magnetotransport studies*, Ph.D. thesis, Max Planck Institute for Solid State Research and Univ. Stuttgart (2004).

[155] A. H. MACDONALD and G. C. AERS, *Inversion–layer width, electron-electron interactions, and the fractional quantum Hall effect*, Phys. Rev. **B 29**, 5976 (1984).

[156] M. DOBERS, K. V. KLITZING, and G. WEIMANN, *Electron–spin resonance in the two–dimensional electron gas of GaAs-Al*$_x$*Ga*$_{1-x}$*As heterostructures*, Phys. Rev. **B 38**, 5453 (1988).

[157] T. CHAKRABORTY and P. PIETILÄINEN, *The quantum Hall effects*, Springer, Berlin (1995).

[158] E. F. SCHUBERT, L. N. PFEIFFER, K. W. WEST, and A. IZABELLE, *Dopant distribution for maximum carrier mobility in selectively doped* $Al_{0.30}Ga_{0.70}As$*/GaAs heterostructures*, Appl. Phys. Lett. **54**, 1350 (1989).

[159] K. HASHIMOTO, K. MURAKI, T. SAKU, and Y. HIRAYAMA, *Electrically–controlled nuclear spin polarization and relaxation by quantum–Hall states*, Phys. Rev. Lett. **88**, 176601 (2002).

[160] E. L. IVCHENKO and A. A. KISELEV, *Electron* g *factor of quantum wells and superlattices*, Sov. Phys. Semicond. **26**, 827 (1992).

[161] A. A. KISELEV, E. L. IVCHENKO, and U. RÖSSLER, *Electron* g *factor in one- and zero-dimensional semiconductor nanostructures*, Phys. Rev. **B 58**, 16353 (1998).

[162] E. L. IVCHENKO, A. A. KISELEV, and M. WILLANDER, *Electronic* g *factor in biased quantum wells*, Solid State Commun. **102**, 375 (1997).

[163] R. M. HANNAK, M. OESTREICH, A. P. HEBERLE, W. W. RÜHLE, and K. KÖHLER, *Electron g factor in quantum wells determined by spin quantum beats*, Solid State Commun. **93**, 313 (1995).

[164] P. LE JEUNE, D. ROBART, X. MARIE, T. AMAND, M. BROUSSEAU, J. BARRAU, V. KALEVICH, and D. RODICHEV, *Anisotropy of the electron Landé* g *factor in quantum wells*, Semicond. Sci. Technol. **12**, 380 (1997).

[165] G. SALIS, Y. KATO, K. ENSSLIN, D. C. DRISCOLL, A. C. GOSSARD, and D. D. AWSCHALOM, *Electrical control of spin coherence in semiconductor nanostructures*, Nature **414**, 619 (2001).

[166] H. W. JIANG and E. YABLONOVITCH, *Gate–controlled electron spin resonance in* $GaAs/Al_xGa_{1-x}As$ *heterostructures*, Phys. Rev. **B 64**, 041307(R) (2001).

[167] R. MEISELS, I. KULAC, F. KUCHAR, and M. KRIECHBAUM, *Electron spin resonance of the two–dimensional electron system in* $Al_xGa1-xAs/GaAs$ *at subunity filling factors*, Phys. Rev. **B 61**, 5637 (2000).

[168] G. LOMMER, F. MALCHER, and U. RÖSSLER, *Reduced* g *factor of subband Landau levels in AlGaAs/GaAs heterostructures*, Phys. Rev. **B 32**, 6965 (1985).

[169] T. MACHIDA, T. YAMAZAKI, S. KOMIYAMA, K. MURAKI, and Y. HIRAYAMA, *Dynamic nuclear–spin polarization induced by scattering between fractional quantum Hall edge channels*, Microelectron. Eng. **63**, 63 (2002).

[170] T. MACHIDA, S. ISHIZUKA, T. YAMAZAKI, S. KOMIYAMA, K. MURAKI, and Y. HIRAYAMA, *Spin polarization of fractional quantum Hall edge channels studied by dynamic nuclear polarization*, Phys. Rev. **B 65**, 233304 (2002).

[171] T Machida, S. Ishizuka, and K. Muraki, *Spin polarization in fractional quantum Hall edge channels*, Physica E **12**, 76 (2002).

[172] D. C. Dixon, K. R. Wald, P. L. McEuen, and M. R. Melloch, *Dynamic nuclear polarization at the edge of a two–dimensional electron gas*, Phys. Rev. **B 56**, 4743 (1997).

[173] A. Berg, M. Dobers, R. R. Gerhardts, and K. v. Klitzing, *Magnetoquantum oscillations of the nuclear–spin–lattice relaxation near a two–dimensional electron gas*, Phys. Rev. Lett. **64**, 2563 (1990).

[174] I. V. Kukushkin, K. v. Klitzing, and K. Eberl, *Enhancement of the skyrmionic excitations due to the suppression of Zeeman energy by optical orientation of nuclear spins*, Phys. Rev. **B 60**, 2554 (1999).

[175] G. Salis, D. T. Fuchs, J. M. Kikkawa, D. D. Awschalom, Y. Ohno, and H. Ohno, *Optical manipulation of nuclear spin by a two–dimensional electron gas*, Phys. Rev. Lett. **86**, 2677 (2001).

[176] D. Paget, G. Lampel, B. Sapoval, and V. I. Safarov, *Low field electron–nuclear spin coupling in gallium arsenide under optical pumping conditions*, Phys. Rev. **B 15**, 5780 (1977).

[177] S. A. Vitkalov, C. R. Bowers, J. A. Simmons, and J. L. Reno, *ESR detection of optical dynamic nuclear polarization in GaAs/Al$_x$Ga$_{1-x}$As quantum wells at unity filling factor in the quantum Hall effect*, Phys. Rev. **B 61**, 5447 (2000).

[178] S. A. Vitkalov, C. R. Bowers, J. A. Simmons, and J. L. Reno, *Effect of the nuclear hyperfine field on the 2D electron conductivity in the quantum Hall regime*, JETP Lett. **69**, 64 (1999).

[179] F. Malcher, G. Lommer, M. Dobers, and G. Weimann, *Electron–spin–resonance in an AlGaAs-GaAs single–side doped quantum–well*, Superlattice. Microst. **5**, 99 (1989).

[180] Song He, F. C. Zhang, X. C. Xie, and S. Das Sarma, *Destruction of fractional quantum Hall effects in thick systems*, Phys. Rev. **B 42**, 11376 (1990).

[181] M. Alatalo, M. A. Salmi, P. Pietiläinen, and T. Chakraborty, *Correlations in coupled electron and hole layers of finite thickness*, Phys. Rev. **B 52**, 7845 (1995).

[182] J. H. Smet, R. A. Deutschmann, W. Wegscheider, G. Abstreiter, and K. von Klitzing, *Ising ferromagnetism and domain morphology in the fractional quantum Hall regime*, Phys. Rev. Lett. **86**, 2412 (2001).

[183] L. N. Pfeiffer and K. W. West, *The role of MBE in recent quantum Hall effect physics discoveries*, Physica E **20**, 57 (2003).

[184] R. L. WILLETT, H. L. STORMER, D. C. TSUI, and A. C. GOSSARD J. H. ENGLISH, *Quantitative experimental test for the theoretical gap energies in the fractional quantum Hall effect*, Phys. Rev. **B 37**, 8476 (1988).

[185] N. FREYTAG, Y. TOKUNAGA, M. HORVATIĆ, C. BERTHIER, M. SHAYEGAN, and L. P. LÉVY, *New phase transition between partially and fully polarized quantum Hall states with charge and spin gaps at $\nu = 2/3$*, Phys. Rev. Lett. **87**, 136801 (2001).

[186] N. KUMADA, D. TERASAWA, Y. SHIMODA, H. AZUHATA, A. SAWADA, Z. F. EZAWA, K. MURAKI, T. SAKU, and Y. HIRAYAMA, *Various phase transitions in $\nu = \frac{2}{3}$ bilayer quantum Hall sates*, Physica E **12**, 32 (2002).

[187] J. M. MOISON, C. GUILLE, F. HOUZAY, F. BARTHE, and M. VAN ROMPAY, *Surfcae segregation of third-column atoms in group III-V arsenide compounds: ternary alloys and heterostructures*, Phys. Rev. **B 40**, 6149 (1989).

[188] M. YOSHITA, H. AKIYAMA, L. N. PFEIFFER, and K. W. WEST, *Quantum wells with atomically smooth interfaces*, cond-mat/0205183 (2002).

[189] V. BAYOT, E. GRIVEI, S. MELINTE, M. B. SANTOS, and M. SHAYEGAN, *Giant low temperature heat capacity of GaAs quantum wells near Landau level filling $\nu = 1$*, Phys. Rev. Lett. **76**, 4584 (1996).

[190] V. BAYOT, E. GRIVEI, J.-M. BEUKEN, S. MELINTE, and M. SHAYEGAN, *Critical behavior of nuclear-spin diffusion in GaAs/AlGaAs heterostructures near Landau level filling $\nu = 1$*, Phys. Rev. Lett. **79**, 1718 (1997).

[191] D. K. MAUDE, S. MARTY, L. B. RIGAL, M. POTEMSKI, J. C. PORTAL, ZB. WASILEWSKI, M. HENINI, L. EAVES, G. HILL, and M. A. PATE, *Skyrmion excitations in the limit of vanishing Landé g-factor*, Physica B **249-251**, 1 (1998).

[192] K. HASHIMOTO, K. MURAKI, T. SAKU, and Y. HIRAYAMA, *Longitudinal resistance anomaly around the 2/3 filling factor observed in a GaAs/AlGaAs single heterostructure*, Physica B **298**, 191 (2001).

[193] O. STERN, N. FREYTAG, A. FAY, J. H. SMET, S. KRAUS, S. LOK, W. DIETSCHE, K. VON KLITZING, M. BICHLER, and W. WEGSCHEIDER, *An NMR study of the electron spin polarization in the FQHE of a single quantum well: Spectroscopic evidence for domain formation.*, Phys. Rev. **B** p. in preparation (2004).

[194] J. H. SMET, R. A. DEUTSCHMANN, F. ERTL, W. WEGSCHEIDER, G. ABSTREITER, and K. VON KLITZING, *Gate–voltage tuned spin interactions between two–dimensional electrons and their host nuclear lattice*, Nature **415**, 281 (2002).

[195] J. H. Smet, R. A. Deutschmann, F. Ertl, W. Wegscheider, G. Abstreiter, and K. von Klitzing, *Anomalous-filling-factor-dependent nuclear-spin polarization in a 2D electron system,* Phys. Rev. Lett. **92**, 086802 (2004).

[196] E. V. Deviatov, A. Würtz, A. Lorke, M. Yu. Melnikov, V. T. Dolgopolov, D. Reuter, and A. D. Wieck, *Two relaxation mechanisms observed in transport between spin-split edge states at high imbalance,* Phys. Rev. **B 69**, 115330 (2004).

[197] A. J. Daneshvar, C. J. B. Ford, M. Y. Simmons, A. V. Khaetskii, A. R. Hamilton, M. Pepper, and D. A. Ritchie, *Magnetization instability in a two–dimensional system,* Phys. Rev. Lett. **79**, 4449 (1997).

[198] E. P. De Poortere, E. Tutuc, S. J. Papadakis, and M. Shayegan, *Resistance spikes at transitions between quantum Hall ferromagnets,* Science **290**, 1546 (2000).

[199] V. Piazza, V. Pellegrini, F. Beltram, W. Wegscheider, T. Jungwirth, and A. H. MacDonald, *First–order phase transitions in quantum Hall ferromagnets,* Nature **402**, 638 (1999).

[200] E. P. De Poortere, E. Tutuc, and M. Shayegan, *Critical resistance in the AlAs quantum Hall ferromagnet,* Phys. Rev. Lett. **91**, 216802 (2003).

[201] E. P. De Poortere, E. Tutuc, and M. Shayegan, *Hysteretic resistance spikes at transitions between quantum Hall ferromagnets in AlAs 2D electrons,* Physica E **12**, 36 (2002).

[202] W. Dietsche, private communication.

[203] J. Zhu, H. L. Stormer, L. N. Pfeiffer, K. W. Baldwin, and K. W. West, *Hysteresis and spikes in the quantum Hall effect,* Phys. Rev. **B 61**, R13361 (2000).

[204] G. Yusa, K. Hashimoto, K. Muraki, T. Saku, and Y. Hirayama, *Self-sustaining resistance oscillations: electron-nuclear spin coupling in mesoscopic quantum Hall devices,* Phys. Rev. **B 69**, 161302(R) (2004).

[205] J. G. S. Lok, S. Kraus, O. Stern, W. Dietsche, K. von Klitzing, W. Wegscheider, M. Bichler, and D. Schuh, *Time and current dependencies of transport at the* $\nu = \frac{2}{3}$ *phase transition in narrow quantum wells,* Physica E **22**, 138 (2004).

[206] E. P. De Poortere, E. Tutuc, R. Pillarisetty, S. Melinte, and M. Shayegan, *Magnetism and pseudo-magnetism in quantum Hall systems,* Physica E **20**, 123 (2003).

[207] E. Tutuc, R. Pillarisetty, S. Melinte, E. P. De Poortere, and M. Shayegan, *Layer-charge instability in unbalanced bilayer systems in the quantum Hall regime,* Phys. Rev. **B 68**, 201308 (2003).

[208] U. ZEITLER, H. W. SCHUMACHER, A. G. M. JANSEN, and R. J. HAUG, *Magnetoresistance anisotropy in Si/SiGe in tilted magnetic fields: Experimental evidence for a stripe–phase formation*, Phys. Rev. Lett. **86**, 866 (2001).

[209] M. LYNASS, Presentation at the annual meeting of the Dept. von Klitzing at Castle Ringberg 2003.

[210] J. T. CHALKER, D. G. POLYAKOV, F. EVERS, A. D. MIRLIN, and P. WÖLFLE, *Quantum Hall ferromagnets, cooperative transport anisotropy, and the random field Ising model*, Phys. Rev. **B 66**, 161317(R) (2002).

[211] C. B. HANNA, *Rippled state of double–layer quantum Hall systems*, Phys. Rev. **B 66**, 165325 (2002).

[212] S. H. SIMON, *Comment on "Evidence for an anisotropic state of two-dimensional electrons in high Landau levels"*, Phys. Rev. Lett. **83**, 4223 (2000).

[213] Y. G. CHAI and R. CHOW, *Source and elimination of oval defects on GaAs films grown by molecular beam epitaxy*, Appl. Phys. Lett. **38**, 796 (1981).

[214] S.-L. WENG, C. WEBB, Y. G. CHAI, and S. G. BANDY, *Particulates: An origin of GaAs oval defects grown by molecular beam epitaxy*, Appl. Phys. Lett. **47**, 391 (1985).

[215] K. AKIMOTO, M. DOHSEN, M. ARAI, and N. WATANABE, *Origin of oval defects in GaAs layers grown by molecular beam epitaxy*, J. Cryst. Growth **73**, 117 (1985).

[216] J. H. SMET, K. VON KLITZING, D. WEISS, and W. WEGSCHEIDER, *dc transport of composite fermions in weak periodic potentials*, Phys. Rev. Lett. **80**, 4538 (1998).

[217] C. ALBRECHT, *Quantenmechanische Transporteffekte in kurzperiodischen lateralen Übergittern*, Ph.D. thesis, Max Planck Institute for Solid State Research and Univ. Stuttgart (2000).

[218] G. SALIS, D.D. AWSCHALOM, Y. OHNO, and H. OHNO, *Origin of enhanced dynamic nuclear polarization and all–optical nuclear magnetic resonance in GaAs quantum wells*, Phys. Rev. **B 64**, 195304 (2001).

[219] M OESTREICH and W. W. RÜHLE, *Temperature dependence of the electron Landé g factor in GaAs*, Phys. Rev. Lett. **74**, 2315 (1995).

[220] M. OESTREICH, S. HALLSTEIN, A. P. HEBERLE, K. EBERL, E. BAUSER, and W. W. RÜHLE, *Temperature and density dependence of the electron Landé g factor in semiconductors*, Phys. Rev. **B 53**, 7911 (1996).

[221] R. WINKLER, private communication.

[222] F. Fischer, M. Grayson, E. Schuberth, D. Schuh, M. Bichler, and G. Abstreiter, *New anisotropy behavior of quantum Hall resistance in (110) GaAs heterostructures at mK temperatures and fractional filling factors*, cond-mat/0311454 (2004).

[223] E. S. Tok, J. H. Neave, M. J. Ashwin, B. A. Joyce, and T. S. Jones, *Growth of Si-doped GaAs(110) thin films by molecular beam epitaxy; Si site occupation and the role of arsenic*, J. Appl. Phys. **83**, 4160 (1998).

[224] M. J. Snelling, E. Blackwood, C. J. McDonagh, R. T. Harley, and C. T. B. Foxon, *Exciton, heavy–hole, and electron g factors in type-I GaAs/AlGa$_{1-x}$As$_x$ quantum wells*, Phys. Rev. **B 45**, 3922 (1992).

[225] R. Winkler, S. J. Papadakis, E. P. De Poortere, and M. Shayegan, *Anomalous magneto–oscillations in two–dimensional systems*, Phys. Rev. Lett. **84**, 713 (2000).

[226] K. Muraki and Y. Hirayama, *Re–entrant behavior of the $\nu = 4/3$ fractional quantum Hall effect in a front–and–back–gated 2D hole gas*, Physica B **256-258**, 86 (1998).

[227] J. P. Eisenstein, K. B. Cooper, L. N. Pfeiffer, and K. W. West, *Insulating and fractional quantum Hall states in the first excited Landau level*, Phys. Rev. Lett. **88**, 076801 (2002).

[228] I. A. McDonald and F. D. M. Haldane, *Topological phase transition in the $\nu = 2/3$ quantum Hall effect*, Phys. Rev. **B 53**, 15845 (1996).

[229] A. Sawada, Z. F. Ezawa, H. Ohno, Y. Horikoshi, Y. Ohno, S. Kishimoto, F. Matsukura, M. Yasumoto, and A. Urayama, *Phase transition in the $\nu = 2$ bilayer quantum Hall state*, Phys. Rev. Lett. **80**, 4534 (1998).

[230] K. Muraki, private communication.

[231] O. Stern, private communication.

[232] A. Sawada, Z. F. Ezawa, H. Ohno, Y. Horikoshi, S. Kishimoto, F. Matsukura, Y. Ohno, M. Yasumoto, and A. Urayama, *Interlayer quantum coherence and anomalous stability of $\nu = 1$ bilayer quantum Hall state*, Physica B **249-251**, 836 (1998).

[233] E. V. Deviatov, A. A. Shashkin, V. T. Dolgopolov, H.-J. Kutschera, A. Wixforth, K. L. Campman, and A. C. Gossard, *Shifting the quantum Hall plateau level in a double layer electron system*, JETP Lett. **75**, 34 (2002).

[234] A. R. Hamilton, M. Y. Simmons, F. M. Bolton, N. K. Patel, I. S. Millard, J. T. Nicholls, D. A. Ritchie, and M. Pepper, *Fractional quantum Hall effect in bilayer two–dimensional hole–gas systems*, Phys. Rev. **B 54**, R5259 (1996).

[235] K. ENSSLIN, A. WIXFORTH, M. SUNDARAM, P. F. HOPKINS, J. H. ENGLISH, and A. C. GOSSARD, *Single–particle subband spectroscopy in a parabolic quantum well via transport experiments*, Phys. Rev. **B 47**, 1366 (1993).

[236] X. Y. LEE, H. W. JIANG, and W. J. SCHAFF, *Topological phase diagram of a two–subband electron system*, Phys. Rev. Lett. **83**, 3701 (1999).

[237] C. A. RICHTER, R. G. WHEELER, and R. N. SACKS, *Overshoot of quantum Hall plateaus*, Surf. Sci. **263**, 270 (1992).

[238] R. L. WILLETT, H. L. STORMER, D. C. TSUI, L. N. PFEIFFER, K. W. WEST, and K. W. BALDWIN, *Termination of the series of fractional quantum Hall states at small filling factors*, Phys. Rev. **B 38**, 7881 (1988).

[239] P. GRAMBOW, *Technologie und Untersuchung nanostrukturierter Halbleitersysteme*, Ph.D. thesis, TH Darmstadt (1992).

[240] G. K. WHITE and P. J. MEESON, *Experimental techniques in low-temperature physics*, Clarendon Press, Oxford (2002).

Acknowledgment

I would like to thank the following people:

- Prof. Dr. Klaus von Klitzing for the opportunity to work in a scientific environment that excited and encouraged me and in particular for the way of discussing problems and results,
- Dr. habil. Jurgen Smet who advised me in a very productive way, supported me with his knowledge, gave me all the freedom one can ever wish, introduced me to a lot of techniques and aspects, and managed to inspire me for this wide spread field of research,
- Prof. Dr. Martin Dressel, who kindly accepted the co-reporting,
- Dr. Jürgen Weis for a lot of support independent of the actual request I directed to him and in particular for the allocation of the two dilution refrigerators in 3B10 for quite a long time each,
- Prof. Dr. Werner Dietsche for a lot of useful hints, comments, and support,
- Dr. Sjoerd Lok for a lot of discussions and very helpful support whenever I requested,
- Maik Hauser for some excellent samples,
- Monika Riek for the introduction to the clean room facilities and the continuous support throughout the hole work *e.g.* hints etc.,
- Ulrike Waizmann for the preparation of some samples by means of e-beam lithography,
- Thomas Reindl for patterning the modulated samples in a dry etch process,
- Manfred Schmid for the almost ever just in time support in the case of any technical problem,
- Jürgen Behring, who was heavily involved in the excellent design and manufacturing of all the used sample rods used for this thesis,
- Ingo Hagel, Kevin Pellizzer, and Walter Schmidt for excellent technical support,
- Dr. Shun-Jen Cheng for the allocation of his quantum mechanical program,

- Dr. Martin Griebel, my college in the office during the first almost three years, with whom I had numerous fruitful discussions and who always supported me in the most powerful way,
- Denis Maryenko, my college in the office since the beginning of the "hot phase" of the thesis, for helpful suggestions and revision,
- Jörn Göres for giving me deeper insight in fascinating many particle correlation effects and for a lot of useful technical hints,
- Martin Geisler for supporting me in particular with respect to all kinds of software problems and for a lot of continuative hits,
- Omar Stern for a lot of helpful discussions,
- Dr. Stefan Kraus for a lot of discussions and help in structure design,
- Armin Welker for the help with the dilution refrigerators in 3B10,
- Dr. David Quirion for a lot of helpful discussions,
- Dr. Nicolas Freytag for a lot of new viewpoints on several topics,
- Dr. Ulrich Zülicke (Univ. Karlsruhe) for a lot of very fruitful discussions about theoretical concepts,
- Dr. Koji Muraki (NTT Basic Research Laboratories, Japan) for a lot of discussions, fruitful hints about quantum hall ferromagnetism,
- Dr. Matthew Grayson (WSI, Garching) for a lot of discussions, hints, and advises, and in particular the allocation of some samples,
- Dr. Erich Zielinski (Alcatel Research Center, Stuttgart) and his colleges for the very kind support of realizing HF-circuits,
- Walter Neuberger and Sigurd Marks (Elekonta, Gerlingen) for very kind and in particular fast support of realizing sample carriers in the basis of Duroid,
- Thomas Schmid (Rosenberger, Tittmoning) for hints on HF-properties of interconnects and calculations of transmission characteristics,
- Wolfgang Philipp (RHE, Radeberg) for help on figuring out adhesion problems of Au on ceramics,
- numerous other people who I asked due to what ever and their help and support.

Resume

Lutz W. Höppel, born on March 24th 1973 in Nürnberg, Germany

09/1979 - 07/1983	Elementary school in Wolkersdorf
09/1983 - 07/1992	Adam–Kraft–Gymnasium in Schwabach
07/1992 - 06/1993	Military service in Kümmersbruck
10/1993 - 12/1998	Studies of physics at the Technical University Munich
02/1999 - 02/2000	Scientific coworker at the Walter Schottky Institut in Garching
since April 1st 2000	work on current PhD-thesis at the Max Planck Institute for Solid State Research in Stuttgart in the department of Prof. Klaus v. Klitzing